Author Manuscript
Accepted for publication in a peer-reviewed journal

NIST National Institute of Standards and Technology • U.S. Department of Commerce

Published in final edited form as:
Prog Mater Sci. 2021 August ; 121: . doi:10.1016/j.pmatsci.2021.100786.

Damage tolerant design of additively manufactured metallic components subjected to cyclic loading: State of the art and challenges

Uwe Zerbst[1], **Giovanni Bruno**[1], **Jean-Yves Buffiere**[2], **Thomas Wegener**[3], **Thomas Niendorf**[3], **Tao Wu**[3], **Xiang Zhang**[4], **Nikolai Kashaev**[5], **Giovanni Meneghetti**[6], **Nik Hrabe**[7], **Mauro Madia**[1], **Tiago Werner**[1], **Kai Hilgenberg**[1], **Martina Koukolíková**[8], **Radek Procházka**[8], **Jan Džugan**[8], **Benjamin Möller**[9], **Stefano Beretta**[10], **Alexander Evans**[1], **Rainer Wagener**[9], **Kai Schnabel**[9]

[1)]Bundesanstalt für Materialforschung und -prüfung (BAM), Unter den Eichen 87, D-12205 Berlin, Germany

[2)]INSA-Lyon, F-69621 Villeurbanne, France

[3)]University Kassel, Material Science, Sophie-Henschel-Haus 3, D-34125 Kassel, Germany

[4)]Coventry University, Priory Street, CV1 5FB Coventry. U.K.

[5)]Helmholtz-Zentrum Geesthacht, Max-Plank-Str. 1, D-21502 Geesthacht, Germany

[6)]University of Padova, via Venezia, 1, I-35131 Padova, Italy

[7)]National Institute of Standards and Technology (NIST) 325 Broadway, MS-647 Boulder CO 80305, U.S.A. (The part of Nik Hrabe is an official contribution of NIST and is not subject to the copyright of the United states.)

[8)]COMTES FHT, Průmyslová 995, 334 41 Dobřany, Czech Republic

[9)]Fraunhofer-Institut für Betriebsfestigkeit (LBF), Bartningstr. 47, D-64298 Darmstadt, Germany

[10)]Politecnico di Milano, via La Masa 1, 20156 Milan, Italy

Abstract

Undoubtedly, a better understanding and the further development of approaches for damage tolerant component design of AM parts are among the most significant challenges currently facing the use of these new technologies.

This article presents a thorough overview of the workshop discussions. It aims to provide a review of the parameters affecting the damage tolerance of parts produced by additive manufacturing

Declaration of interests
The authors declare that they have no known competing financial interests or personal relationships that could have appeared to influence the work reported in this paper.

(shortly, AM parts) with special emphasis on the process parameters intrinsic to the AM technologies, the resulting defects and the residual stresses. Based on these aspects, basic concepts are reviewed and critically discussed specifically for AM materials:

- Criteria for damage tolerant component design;
- Criteria for the determination of fatigue and fracture properties;
- Strategies for the determination of the fatigue life in dependence of different manufacturing conditions;
- Methods for the quantitative characterization of microstructure and defects;
- Methods for the determination of residual stresses;
- Effect of the defects and the residual stresses on the fatigue life and behaviour.

We see that many of the classic concepts need to be expanded in order to fit with the particular microstructure (grain size and shape, crystal texture) and defect distribution (spatial arrangement, size, shape, amount) present in AM (in particular laser powder bed fusion). For instance, 3D characterization of defects becomes essential, since the defect shapes in AM are diverse and impact the fatigue life in a different way than in the case of conventionally produced components. Such new concepts have immediate consequence on the way one should tackle the determination of the fatigue life of AM parts; for instance, since a classification of defects and a quantification of the tolerable shapes and sizes is still missing, a new strategy must be defined, whereby theoretical calculations (e.g. FEM) allow determining the maximum tolerable defect size, and non-destructive testing (NDT) techniques are required to detect whether such defects are indeed present in the component. Such examples show how component design, damage and failure criteria, and characterization (and/or NDT) become for AM parts fully interlinked. We conclude that the homogenization of these fields represents the current challenge for the engineer and the materials scientist.

Keywords

Additive manufacturing; fatigue loading; component assessment; damage tolerance; defects; residual stresses

1. Introduction

In general terms, additive manufacturing (AM; also commonly referred to as “3D printing”) designates processes by which three-dimensional components are (primarily) formed by progressively adding thin layers of material. The process is controlled by a digital computer model. Additive manufacturing can be applied to almost any class of materials. For metal AM, powders and wires are the most widely used as feedstock material. A high-power laser or electron beam is used to locally fuse metallic powder particles while wire material can also be fused by an electric arc. Typical examples of metals used in AM are titanium alloys, nickel-based alloys, cobalt chrome alloys, aluminum alloys and stainless steels however the range is constantly expanding; for more detailed description see [1–3].

When the development of the various AM technologies started about 30 years ago, they were commonly referred to as “rapid prototyping”. They were used to reduce the development time of new components. Based on computer-aided design (CAD) data, structures with very complex shapes could be built fast and easily. The prototypes were then used for the development of the design and for testing the functionality of a component. The optimized components were however, produced by conventional manufacturing technologies.

While rapid prototyping is still an application of additive manufacturing, progress in different fields such as computing hardware and software, laser technology and powder feedstock technology have extended its application field from a mere tool for design purposes to a forming process technology for end-use products. During the last years, this development seems to have reached a “critical acceptance level” [4] manifested in a significant increase in sales of commercial systems, industrial applications, as well as a growth of fundamental research and development in the field. Nevertheless, the development of the technologies seems to be still at the early stages, such that conventional materials and design principles are more or less transferred unchanged to the new AM technology. However, the establishment of new AM specific solutions for design and material selection is certainly required in the future.

Additive manufacturing enables completely new possibilities for the production of components from metals and alloys. The new possibilities include the following:

- The requirement for expensive component specific casting molds or forging dies are removed or reduced. Eliminated machining costs is particularly an advantage for complex geometries and bespoke or small production batches;
- Almost unlimited geometrical freedom with regard to the design of the components particularly for very complex shapes which are either at or beyond the capability of conventional forming and subtractive methods (e.g. [5]);
- Optimized design for both functionality of components and the minimization of local stresses using finite element-based stress-strain analyses as applied to computer models of the component geometry. (e.g. [6]);
- Material optimization, e.g. use of materials with graded properties (either via microstructure optimization or alloying changes) such that the regions of highest stresses in the component consist of materials with increased damage tolerance properties [7, 8], and also tailoring materials with respect to various functional properties (e.g. [9]);
- The forming of similar and dissimilar material compounds (e.g. [10–12];
- Incorporation of health monitoring sensors (e.g. [13]), see also [14];
- Fast and cost-effective production of spare parts within a narrow time frame (e.g. [15,16].

However, the new possibilities also are accompanied by additional risks for the applications. The common disadvantages, challenges and risks associated with the current state of the

art of metal AM involve: (a) The AM processing of metallic materials is still considered to be challenging and far more difficult than laser sintering of polymers [17]. (b) The reproducibility of the performance of the finished product seems to be limited which is particularly relevant for safety-critical, load carrying components. Bruna-Rosso et al. [18] characterized the present status of Laser Powder Bed Fusion (L-PBF, older designation: Selective Laser Melting, SLM) as the following: “The process still relies on trial-and-error learning and L-PBF produced parts are still quite often not qualified, which limits the industrial development of this technology.” The situation is particularly challenging for cyclic loading as the following observation illustrates. The “design of critical load carrying parts via AM is still at its infancy because the damage mechanism and evolution of AM metal under cyclic loading are not yet understood, particularly under complex multiaxial loading conditions.” [19].

It is the view of the present authors that the major AM related challenges are the following:

- Pronounced material inhomogeneity and property anisotropy, leading to problems with transferability of material properties from specimen to component;
- Sub-surface and bulk defects which may be localized along preferred planes;
- Pronounced surface roughness;
- Large levels of residual stresses characterized by complex spatial distributions and leading to geometrical distortions.
- Often significant scatter bands of both material properties and defect population.

The respective contribution of each of these points is also influenced by many process parameters and will differ from component to component.

Besides relatively high costs and the size limitation of the components due to the limited installation space in some AM processes, problems, above all, arise from sometimes insufficient and difficult to reproduce material properties. The reason for the lack of reproducibility and sometimes insufficient properties is that the manufacturing technology is controlled by many process parameters which affect the build process, including the local cooling and reheating conditions. Consequently, the local material properties may vary spatially within in a given component. In a review paper, Yadollahi and Shamsaei [20] wrote: “Current experimental evidence suggests that the mechanical properties of laboratory AM specimens may not be representative of those associated with parts, due primarily to differences in geometry/size which influence the thermal histories experienced during fabrication, and consequently, microstructural features, surface roughness, and more.” In addition to the problems of the material imperfections [21,22] and residual stresses [23] this variability constitutes the main current challenge to the adoption and regular use of AM technologies for safety-critical structural metallic components [24- 26].

The aim of the present study is to summarize the discussions of the workshop, reviewing and discussing various concepts for the improvement of the safe-life and damage tolerance design of AM metallic components. To this purpose, first a general introduction into the

principles of safe design and assessment is provided in Section 2. The problems of adequate material data in AM is addressed in Section 3 followed by discussions of the defect and residual stress issues in Section 4 and 5. Section 6 will provide a brief introduction into post-fabrication treatment of AM components and Section 7 will, also briefly address specific problems of non-destructive testing of AM components. Finally, Section 8 will provide a discussion of potential strategies for the fatigue assessment of AM processed parts.

2. Safe-life and damage tolerant design and assessment

2.1 Basic principles of safe component design

The safe design of a component can be based on three main philosophies (cf. [27,28]:

- ***Safe life design*:** No failure of the structure is allowed over the entire projected service life;
- ***Damage tolerant design*:** Damage, i.e. crack propagation cannot be completely prevented but a potential crack will be detected well before it causes component failure;
- ***Fail safe design*:** The failure of a substructure is allowed if it does not immediately cause the failure of the overall structure because it will be detected in sufficient time to intervene in the system or to take the component out of service.

Since each of these philosophies has its advantages and disadvantages, it makes sense to combine them in an overall scheme.

The primary safety level (*safe life*) is based on the stress vs. number of cycles (S-N) or strain vs. number of cycles (ε-N) curve of the material. Depending on the number of loading cycles N that the component must perform unscathed, it is distinguished between low cycle fatigue (LCF) up to $N = 10^3 - 10^4$, high cycle fatigue (HCF) up to $N = 10^6 - 10^7$ and very high cycle fatigue (VHCF) beyond that value.

The secondary safety level (*damage tolerance*) includes the assumption that fatigue cracks exist and can grow to a critical size in the component if no countermeasures are taken. The crucial aspect to this safety level is that potential cracks are detected before they become critical. In the classic damage tolerance concept, this aim is realized by regular inspections during service using non-destructive testing (NDT) techniques. While the length of the inspection interval is traditionally based on individual user experience, there is also the possibility to combine these inspections with a residual lifetime as specified by fracture mechanics. In a classic damage tolerance analysis, this is the time or number of loading cycles a potential crack of a fixed size needs to grow to its critical size. The critical size can refer to fracture but also to other failure criteria in connection with the loss of functionality of the component. The fixed initial crack size is given by the detection limit of the NDT method under in-service conditions. What counts in this context, is the largest crack that could escape detection [27]. If the detection of smaller cracks cannot be guaranteed with sufficiently high probability, they are assumed to exist.

Note that some of the general problems for performing reliable NDT, such as limited accessibility, high surface roughness or heterogeneous microstructure will usually be exacerbated in AM applications [29].

Damage tolerance design can also be realized by means of non-inspection techniques, e.g. overload or proof tests. In proof testing, a load higher than the service load is applied to a component. If the component survives this load, the component is regarded as safe. However, the overload by itself may have introduced some damage (i.e. a crack) and there is the risk that the component might prematurely fail due to the extension of this damage during service. By means of fracture mechanics, it is possible to specify the size of a crack that would only just not lead to failure under proof test loading. This can then be used as the initial crack size for crack propagation simulation under service load. Finally, the time or number of loading cycles up to failure defines the period up to the next overload test, for an example see [30].

The third safety level (*fail-safe*) can be defined by several different procedures. One of these, which is restricted to pressurized components, is a *leak-before-break* analysis. Starting with an assumed, e.g. semi-circular surface defect, a crack propagation analysis is performed by fracture mechanics until the crack breaks through the wall. This provides information on the geometry and length of the leak, which might subsequently extend further until the final failure of the component. This can also be simulated by means of fracture mechanics. The crucial question to be answered is whether there will be enough time to intervene in the system after the detection of the leak and before the final rupture.

As mentioned above, *leak-before-break* is just a special case of a *fail-safe* analysis. Further options are *redundant* design (*multi-path loading*) and temporary crack arrest at designed crack arresters in thin walled structures [27].

2.2 The input parameters

2.2.1 Loading—All relevant loads applied to a part or material must be taken into account in the analysis. These loads can include:

- Applied service loads (forces, bending moments, pressure, etc.),
- Dead weight and inertia loads,
- Thermal stresses,
- Residual stresses.

While the applied stresses, even for complicated geometries can be reliably determined, e.g., by finite element analysis when the external load is known, the residual stresses can constitute a significant challenge, particularly in L-PBF. This will be discussed in more detail in Section 5.

The negative effects of the residual stresses in the general case and those which in particular impact on AM are:

- Distortion leading to undesired shape deviations [31,32] and even to the build-up of defects and cracking during manufacturing [33–35], see also [36].
- The promotion of fatigue crack initiation and the acceleration of crack propagation [32,37]. Such phenomena have a direct influence on the fatigue life and strength, as well as on the residual lifetime of an AM component.

Both the determination of the magnitude of residual stresses and their distribution in the component as well as and their consideration in component life assessment is anything but trivial. Residual stresses which cannot be completely removed for whatever reason in the test specimens, can severely affect the material properties, particularly the fatigue and fatigue crack propagation behaviour (see Section 5.3).

On the other hand, one can use post processing (e.g. mechanical such as shot or shock peening [38], but also thermal such as hot isostatic pressing [39]) to induce (sub-) surface or bulk compressive stresses, thereby influencing the crack initiation or propagation behavior (respectively).

2.2.2 Material parameters—The range of material properties required for structural assessment depends on the loading of the component and the type of analysis to be performed. In the case of monotonic loading, the parameters are;

- The monotonic stress-strain curve;
- The fracture toughness.

Since monotonic loading is not the focus of the current work, this shall not be further discussed herein. If the loading is cyclic, further parameters need be added. These comprise, in case of total life approaches,

- The (stabilized) cyclic stress-strain curve;
- The fatigue strength and lives (the S-N or ε-N curves).

If fracture mechanics methods are involved further parameters are needed:

- The fatigue crack growth characteristics (da/dN-ΔK curve) including the fatigue crack propagation threshold ΔK_{th};
- The intrinsic fatigue crack propagation threshold $\Delta K_{th,eff}$ and the cyclic R curve (if fracture mechanics is applied to the total fatigue life and strength).

For long cracks (the term “long crack” will be explained in Section 2.3.1) the crack propagation analysis is based on the da/dN-ΔK curve or, better, on the da/dN-ΔK_{eff} curve, the da/dN-ΔK curve is shifted to higher crack growth rates for higher loading ratios R (= K_{min}/K_{max}), with R being associated with the mean stress or mean K, $\overline{K}$, by

$$\bar{\sigma} = \frac{1}{2}(1 + R)\sigma_{max} \quad (1)$$

or

$$\overline{K} = \frac{1}{2}(1 + R)K_{max}\,. \tag{2}$$

K_{max} and K_{min} are the upper and lower K values in the loading cycle.

It was mentioned above that the da/dN-ΔK (and even the da/dN-ΔK_{eff}) curve can only be applied to so-called long cracks.

The reason for the dependence on R is the crack closure phenomenon (Fig. 1) which means that a crack will prematurely close in the loading cycle, usually at a stress level above zero. This is important because the crack will grow only while it is open. Consequently, the crack propagation analysis needs to be based on $\Delta K_{eff} = K_{max} - K_{op}$ instead of $\Delta K = K_{max} - K_{min}$ such as illustrated in Fig. 1a. K_{op} is that K value at which the crack opens under a load increase.

Various mechanisms exist for crack closure. They are all based on geometrical miss-match between the corresponding crack faces. For the plasticity-induced mechanism (Fig. 1b) this is due to the plastic zone generated at the crack tip which is “shifted” into the crack wake when the crack propagates. The roughness-induced mechanism (Fig. 1c) is caused by the asperities on the crack faces (see [40]) which yields mixed mode loading at the micro scale. The effect can be enhanced by crack kinking or branching. The oxide-debris induced mechanism (Fig. 1d) is active in materials prone to corrosion. The crack faces are covered by a thin oxide layer. If the crack is loaded at a low R ratio (or mean stress), parts of the crack faces are furbished, locally removing the oxide scale, with the consequence that the blank metal will subsequently corrode again. Due to this, an oxide-debris layer grows thicker over the time and finally fills up the crack wake simultaneously shifting the crack closure stress to a higher value. The degree of crack closure generally depends on R, where it is higher at low R (and mean stresses) and decreases and finally disappears at high R. Note that further crack closure mechanisms may act in addition to those shown in Fig. 1. A common fit to the da/dN-ΔK curve, which considers crack closure, is provided by the NASGRO equation [41–43].

The crack closure phenomenon is mirrored by the fatigue crack propagation threshold ΔK_{th}. This parameter can be separated into two components

$$\Delta K_{th} = \Delta K_{th,eff} + \Delta K_{th,op}\,. \tag{3}$$

The first one, $\Delta K_{th,eff}$, is an intrinsic material parameter which depends only on the modulus of elasticity E and the lattice type (in terms of the amplitude of the Burgers vector $\|\vec{b}\|$) see, e.g., [44]. $\Delta K_{th,eff}$ is also the lower bound of the overall threshold when no crack closure occurs. The crack closure component, $\Delta K_{th,op}$, is influenced by material properties such as the grain size (which may influence the roughness-induced closure or the crack tip plastic zone size) and by the stress ratio R; for a discussion see [45].

2.2.3 Defects: input parameters or target information?—The term “defect” requires a bit of discussion since it is used inconsistently across different scientific communities. In failure analysis, a defect is “an imperfection … that can be shown to cause failure … that would not have occurred in the absence of the imperfection” [46]. According to this definition, a certain degree of roughness is a defect when it is not adequately considered in the design process and when one or more cracks initiated at a roughness groove are not arrested but grow to a critical size. While this definition is plausible, it only refers to the end of the life of the component, i.e., its failure. In other words: When an imperfection is found such as during quality control after manufacturing, it is not clear whether this is a defect according to the definition above. However, since an imperfection is present that is a clear deviation from the nominal condition, it is usually treated as a potential defect. Therefore, for the purposes of this work, the term defect will be referred to as such.

For a general discussion of different types of defect and the consequence for failure see [47–49]. They can be assigned to the following categories:

- Material defects such as unwanted non-metallic inclusions, pores, unwelded regions, micro-shrinkages, cold cracks, hot cracks and other unwanted microstructures features
- Micro-geometric defects such as scratches, indents, corrosion pits and others
- Defects that could belong to both categories above, such as surface roughness

With respect to the different types of material defects in AM, the reader is referred to Section 4. What needs to be emphasized at this point is that defects play a particular important role in AM, which means that they should explicitly be considered in component life assessment. Options for this are discussed in Section 8.4.

It is known that different types of defects compete with respect to their influence on fatigue. Usually the largest defect dominates but aside from its size, characteristics such as proximity to the surface, presence of a textured crystallographic microstructure, morphology and its occurrence as a single defect or within a defect cluster or stringer, play roles with respect to the harmfulness of the defect. Note that there exists a critical defect size below which no effect on the fatigue strength can be stated (cf. the overview in [47–49]). Researchers have shown that this critical defect size depends on the strength of the material, in that it becomes smaller with increasing strength. In [50] the authors report on a critical defect size in L-PBF produced AlSi10Mg, above which the fatigue limit is exclusively controlled by the defect, whilst, at smaller defect sizes, microstructure additionally comes into play.

In [51] the authors explain his phenomenon by a two-criteria approach for the initial crack size for fatigue crack propagation. As mentioned previously, fatigue cracks are usually initiated at locations of material defects. If the initial cracks are short, they will be arrested after some limited growth. The various mechanisms by which crack arrest is realized are discussed in Section 2.3.1. Conversely: if the initial crack size, is due to a large pre-existing material defect and is larger than the arrest crack size, there will be no crack arrest. In that case the critical crack size is immediately given by the size of the defect. The simulations

shown that the arrest size of a physically short crack depends on the strength of the material, such that it becomes smaller with materials of higher strength [47]. This phenomenon explains the higher defect sensitivity of high strength materials.

2.3 Defects and fatigue strength

2.3.1 Short fatigue crack propagation and crack arrest—In (nominally) defect-free materials, fatigue damage starts with the accumulation of local plastic deformation. In engineering materials this is rather unusual since they contain material defects such as inclusions or porosity. These defects generate both strain concentration zones due to their different stiffness compared to the matrix material and local stress concentrations. The magnitude of the local stress concentration depends on the defect size and morphology. Consequently, these defects act as crack initiation sites [47–49]. The crack nucleation stage is rather short, and the major part of the lifetime is usually spent at the stages of micro and short crack growth until it becomes a long crack. In that context, Polak [52] summarizes: “Numerous studies have shown that in the majority of materials and under normal loading conditions, the period of crack initiation in smooth specimens without defects amounts to less than 5-20% of the fatigue life. In materials containing defects, the fraction of life spent in crack initiation is even lower. The major part of the life is spent in the growth of cracks, namely in the growth of short cracks.” It is not difficult to imagine that this will certainly be the case for metal AM applications. The fatigue crack propagation and arrest can be distinguished by the three subsequent stages (as described in Fig. 2):

(a) Micro-crack propagation and arrest: The first stage is that of microstructurally short crack propagation (designated in the figure by “micro-crack”). The size of the crack is of the order of microstructural features such as the grain size, and its growth is heavily influenced by the local microstructure. Successive phases of crack acceleration, deceleration and even arrest can be identified. The stress level at which point the largest of a considerable number of growing micro-cracks just arrests, defines the plain or intrinsic fatigue limit of the material [53]. In other words: the fatigue limit is not defined by fatigue crack initiation but by crack arrest [54]. Crack arrest typically occurs at the grain boundaries of the material. When the fatigue crack is going to extend across the grain boundary, the build-up of its plastic zone is inferred by the differing crystal orientation of the grain. If its driving force is not sufficiently high, it will be arrested at the grain boundary. Since crystal orientations will usually be stochastically distributed in polycrystalline material, crack arrest will not occur at all grain boundaries. The crack size defining the limit of the micro crack regime is not given by one grain size but frequently of the order of three, although smaller and larger numbers are as well possible [55]. Note that it is the crack front length rather than its depth which defines a micro-crack (e.g., [56]) and that the definition loses its meaning for through or long and shallow surface cracks. In the case of corrosion (the effect of which will usually be time-dependent), the fatigue limit will disappear due to promotion of crack penetration through the microstructural barrier [53]. This is also the case in variable amplitude loading whereby a small number of interspersed loading events above the fatigue limit level generate what is known as *fatigue damage accumulation* [57].

(b) Mechanically/physically short crack propagation and arrest: A micro-crack that is not arrested will subsequently grow to a size up to the plastic zone. It is then denoted as mechanically/physically short crack. Note that the distinction between “mechanically” and “physically” is not by the crack size but by the different mechanisms. Mechanically short means that small scale yielding conditions are not valid (the crack length is comparable to the extension of the plastic zone) and therefore elastic-plastic concepts, such as a cyclic J integral, ΔJ, must be used to determine the crack driving force. This will not be addressed here, see instead [58–60].

Physically short means that the crack closure phenomenon is still gradually building-up at this stage. It is not acting at the beginning of crack propagation since it requires some extent of the crack wake but it will increase with crack extension Δa until it reaches a stationary, crack depth independent state. This marks the transition to the long crack propagation stage as illustrated in Fig. 3.

As discussed above in Section 2.3.1(a), at the micro crack stage, the crack arrest occurs because the crack is unable to penetrate a microstructural barrier, e.g. a grain boundary. Now, at the mechanically/ physically short crack stage, a further arrest mechanism is active. Usually the crack driving force ΔK will increase with the growing crack. However, at the same time, the effective crack driving force ΔK_{eff} can decrease due to the build-up of the crack closure phenomenon. When ΔK falls below the fatigue crack propagation threshold ΔK_{th}, crack arrest will happen. Note that the threshold will simultaneously increase at the physically short crack stage (Section 2.2.2). Of course, the microstructure continues to play a role, but this is superimposed onto the mechanical effect and is “averaged out” because the crack front extends over a large number of grains at that stage.

(c) Crack arrest at notches: In engineering components, cracks usually initiate at notches (shoulders, holes, threads, etc.). This adds a further element to the discussion of crack arrest: the role of the stress gradient. Particularly, at sharp notches a mechanism is observed which is sometimes designated by the term “anomalous” crack growth behavior (e.g. [61]). First, the crack grows at a high propagation rate, then it decelerates due to the decreasing stresses in the wall thickness direction and the gradual build-up of the crack closure phenomenon. Finally, the crack arrests or accelerates again, depending on whether or not the crack driving force becomes smaller than the fatigue crack propagation threshold ΔK_{th}. Both crack arrest at micromechanical obstacles at the microcrack stage and crack arrest due to crack closure at notches determine the fatigue or endurance level. However, the former relates to the plain or materials fatigue limit and the latter controls the fatigue limit of the component, which is smaller due to notch effects, surface roughness etc.

For the sake of completeness, it must be mentioned that there exist further crack arrest mechanisms in addition to those discussed above and that these could also play a role in AM applications.

- First, a crack can arrest when it grows into a stress shielded area. Even for constant, crack depth independent crack closure, the crack driving force decreases even though the crack becomes larger. This is a typical scenario in thin

walled structures with designed stiffeners (cf. [62]) and is somewhat comparable with the effect of notches as discussed above.

- Second, crack arrest can happen when a crack grows into a region of higher threshold ΔK_{th} as compared to those of its origin. An example is crack advance in a weldment from the weld metal into the heat affected zone (HAZ). Note that the grain size in the HAZ, at least in its coarse-grained part, is usually larger than those in the base and weld metals. The larger grain size can be associated with more pronounced roughness-induced crack closure which in turn lowers ΔK_{eff} and increases ΔK_{th} (more exactly its closure part $\Delta K_{th,op}$).
- Third, there can be an influence of type I and II residual stresses. A common option for post-fabrication treatment of weldments and other components is the introduction of compressive residual stresses by surface tempering, peening, deep rolling etc. Residual stresses have usually no influence on the cyclic crack driving force ΔK but they shift R (and the mean stress) to higher (in the case of tensile) and lower (in the case of compressive residual stress) values. The overall fatigue propagation threshold ΔK_{th}, driven by its closure component $\Delta K_{th,op}$, depends on R in that it becomes smaller for high and larger for low R ratios respectively. In other words: compressive residual stresses increase ΔK_{th} because of which they can contribute to crack arrest.
- Fourth, phase transformation. It is well known that some austenitic steels including 316L can exhibit stress induced martensitic deformation, e.g. [63–65]. This was also found in L-PBF material where, as it seems, there is a connection between inhomogeneous martensite formation and crack branching (T. Werner, unpublished results).

A final note is necessary in this context: The term “short crack” has been discussed at the background of the gradual build-up of the crack closure phenomenon. This definition, in a certain way, “uncouples” it from the definition by the crack depth. However, it is conceivable that even a deep crack can have the characteristics of a short one, such that it does not show any or reduced crack closure at the start of its growth.

2.3.2 Monotonic versus cyclic strength—

The basic mechanical properties of a metallic material, its stiffness, strength, ductility, monotonic and cyclic crack resistance and fatigue strength are affected in different ways by the three underlying material characteristics: crystal lattice, microstructure and material defects (Fig. 4). In practice, these characteristics are given as specific parameters, such as the modulus of elasticity, the yield strength, parameters of fracture toughness, the fatigue limit. Some of these characteristics describe what may be designated as “global” (or “averaged”) properties whilst others are controlled by “local” features, e.g., stress concentrations at micro-notches. Whether we are dealing with a “global” or a “local” parameter depends not least on the ductility of the material, which might enable the material to overcome the harmfulness of the micro-notches such that local stress peaks are reduced by plastic yielding.

The monotonic strength parameters are “global” such that the stresses are related to the tensile specimen’s cross section. The cyclic (or fatigue) strength is strongly controlled

by local defects and heterogeneities, for HCF usually at or just below the specimen or component surface. This is because the fatigue cracks will be initiated at imperfections from where they subsequently grow into the cross section. The fracture toughness is controlled by local material imperfections at the lower shelf and the ductile-to-brittle transition stages, but it becomes a kind of “global” property at the upper shelf where the ligament ahead of the crack is fully plastic. For a detailed discussion of this issue see [66].

An example for the effect of material imperfections on both the monotonic strength (in terms of the hardness which corresponds to the ultimate tensile strength) and the cyclic strength, i.e., the fatigue limit, is shown in Fig. 5 for various steels and for an L-PBF manufactured Ni-based super alloy Inconel 718. The common relationship between Vickers hardness HV and the fatigue limit σ_w is given by

$$\sigma_w[MPa] = 1.6\,HV \pm 0.1\,HV \tag{4}$$

for a stress ratio R ($= \sigma_{min}/\sigma_{max}$) = −1 [54]. For hardness values HV > 400, it loses its validity due to small material defects, e.g., non-metallic inclusions in steel. The size of these material defects controls the fatigue limit in that hardness range. The mechanism behind the change at approximately HV = 400 has already been discussed at the end of Section 2.2.3. At a certain strength/hardness value, the size of the arrested crack falls below the size of crack-like defects, which pre-exist in the material from manufacturing. The limit value defines the critical size above which a harmful effect of the imperfection on the fatigue limit is to be expected.

While the critical defect size is roughly in the order of 10 to 25 μm for steels and aluminum [48,49], the imperfections found in two batches of the L-PBF material were in the order of 19 to 179 μm (average: 85 μm, batch A) and even 53 to 254 μm (average: 149 μm, batch B) [69]. In other words: they were significantly larger than the expected non-propagating crack size.

This in turn means that the fatigue strength is expected to be controlled by the defects even at low monotonic strengths. The consequence is that Eqn. (4) must not be applied to the investigated AM material and probably this statement can be extended to metallic AM materials in general, at least if no post-fabrication treatment is carried out. Murakami et al. [70], carrying out a comparable study, conclude that the relationship of Eqn. (4) and Fig. 5 can be used for AM materials only if a combination of hot isostatic pressing and surface polish is performed.

In contrast to the fatigue strength, the monotonic strength is usually not or only slightly affected by defects in ductile materials. This, for instance, shows up in Fig. 6 where an AM manufactured Ti6Al4V titanium alloy with different porosity (size, special distribution, etc.) is investigated and compared with samples without pores (marked as reference specimens) [26]. As it can be seen, the variance in the monotonic ultimate tensile strength is less than 5% between the two variants, whereas the difference in the fatigue strength is of the order of 30 to 40%. In contrast, the difference in the elongation at fracture is almost two-thirds between the sample types. This raises the question of how the connection between (cyclic)

fatigue strength and (monotonic) elongation at fracture can be rationalised. A possible explanation is that a potential material defect at or close to the surface will serve as initial site for fatigue crack propagation, but it will also trigger the necking instability of the tensile specimen. It is a well-known phenomenon that the presence of pre-existing defects affects the ductility of a material, which can trigger premature failure [71]. Zhang et al. [72] even propose a correlation between the fatigue limit and the elongation at fracture instead of Eqn. (4).

The following discussion will concentrate on fatigue damage, however, monotonic properties such as the ductility (in terms of the elongation or reduction of area at fracture) will be considered occasionally. These mechanical properties can be determined using sub-size specimens, which makes them a potential indicator of material gradients and scatter in toughness and fatigue strength. Note, however, that the elongation at fracture is not an intrinsic material property but also depends on the geometry and dimension of the tensile specimen [72]. Since elongation at fracture is affected by defects, some statistical size effect is expected. This will be observed through a higher scatter band than those of the strength parameters.

An example for the scatter in the elongation at fracture is provided in Fig. 7 where an array of miniaturized tensile specimens (gauge cross section: 1×1 mm^2) made of a precipitation-hardening alloy 17-4PH were tested. The two statistical distributions for AM refer to two commercial AM vendors. They are additionally compared with the statistical distribution of conventionally manufactured material. A number of observations can be made from Fig. 7. First, the elongation at fracture is not only different from vendor to vendor but it is also substantially smaller compared to the conventional wrought material, and, second, it shows a much wider scatter band. However, it is noted that only Vendor 2 used protective structural sidewalls and did not perform surface finish. Note that the geometry and dimensions of the conventionally manufactured and the AM tensile specimens were identical which means that no statistical size effect between the specimen sets is expected (width and thickness of the specimen gauge section were 1 mm).

Whilst the complete data set included 104 data points, the authors used the first 5 tests of both AM versions to plot Gaussian distributions (blue curves). In addition, they fitted 3-parameter Weibull distributions to the complete data sets (red curves).

The authors concluded that five specimens were not enough to statistically characterize the scatter bands. This is certainly correct, but even if one uses the complete data sets (red curves), the lower tails of the distribution functions seem not to be well fitted. A question arises due to the wide scatter bands. If we assume material defects such as pores particularly those close to the specimen surface as trigger points for necking instability, the defect characteristics are considered influential. These characteristics include the defect size, its proximity to surface and (for non-spherical voids) its orientation with respect to the loading direction on the elongation at fracture. In the case of the Vendor 2 distribution, the surface roughness is likely to have played an additional role in the level of elongation to fracture.

It is interesting to observe that the minimum values of elongation at fracture were associated with the presence of ‘rare’ interconnecting defects [74]. It is also worth remarking that AM materials also show a non-uniform deformation, together with a brittle behaviour of ‘as-built’ surfaces. These compete with the ductile behaviour of the underlying material [75].

3. Process parameters affecting the mechanical material properties

3.1. Brief overview

In the multitude of additive manufacturing processes for metals, two process categories are currently of greatest economic importance: power bed fusion (PBF) and directed energy deposition (DED) [76–79]. In the case of PBF, the most widely used techniques are laser and electron-beam energy sourced referred to as L-PBF and EB-PBF respectively. DED processes such as wire arc additive manufacturing (WAAM) and the laser metal deposition (LMD) are the main focus for potential industrial applications. Fig. 8 illustrates the different characteristics of the technologies mentioned. As mentioned above, a key motivation for using additive manufacturing is the ability to manufacture the components with freedom of design using CAD models. With respect to this aspect, the L-PBF technology should provide the largest benefit. However, with respect to safety critical components, WAAM offers the best conditions for achieving the targeted mechanical properties. Therefore, it is not a simple task to generally state which of the technologies is most preferable for industrial applications. This depends on the application case.

As L-PBF accounts for more than 80% of the market (in 2016) [23]), the main focus of the present review will be on PBF processes, where the biggest challenges need to be overcome in order to achieve sufficiently high mechanical performance of manufactured components. However, most of the aspects discussed in the current paper can also be applied to the other methods. Note that the residual stress problem (Section 5) is much more severe in L-PBF than in EB-PBF or DED.

A selection of important technological parameters which affect materials properties of L-PBF components is given in Fig. 9. A detailed discussion of the most important parameters will be provided in this section.

In addition to controlling the microstructure development, the local energy density, which is comprised of the combination of power and scan speed, as well as other features such as the scan pattern also have an influence on both the development of material defects and residual stresses.

3.2 Energy density

There are three main types of additive manufacturing material defects: lack of fusion porosity, keyhole porosity, and gas porosity [82], see also Section 4. Lack-of-fusion porosity occurs when the energy density of the beam is not high enough to fully melt the newly added layers of powder, thereby leaving partially melted and/or unmelted powder to be deposited upon during the next layer of deposition and melting [83]. The resulting unwelded regions have a flat shape with relatively large length extension perpendicular to the build

direction, and they primarily form between successive layers such that their orientation is parallel to the layers [84]. Another type of defects caused by too little energy density are so-called balling defects [85], see Section 4.2.4.1. Note that it is not only insufficient energy density but also too much heat dissipation in the bulk which can cause lack-of-fusion. The latter might occur if the initial temperature in the existing layer is rather low due to a large inter-layer time interval, see Section 3.3.2, or if too much heat flows into the support configuration.

Too high of an energy density yields great melt pool depth and may cause so-called key-hole porosity and spatter particles adhering to the surface [83], see also [21,86], cf. Section 4.2.4.1. Keyhole porosity can be easily distinguished from lack of fusion porosity through morphology, as keyhole porosity has a spherical morphology. High temperature gradients generate secondary stresses which, as a consequence, can cause thermal cracking [83].

Gas porosity resulting from powder feedstock, is less sensitive to additive manufacturing processing conditions, and can therefore exist across a broader range of energy densities. The most common additive manufacturing powder production method is atomization, and this technique results in some powder particles that contain closed pores. It has been shown that these powder pores can become entrained and remain in solidified additively manufactured metals [87]. Another source of gas porosity is the release of dissolved gases which, due to rapid cooling, cannot rise and escape in time. This can be observed particularly with aluminum alloys and is well known from welding processes. Gas pores have a spherical morphology, which can make it difficult to distinguish from keyhole pores. However, gas pores are limited in size to the maximum powder size, whereas keyholes pores can be much larger.

Fig. 10 shows the correlation between energy density (i.e. combinations of power and scan speed) and type of defect formation. Lack of fusion pores form at lower energy density due to under-melting, and keyholes pores form at higher energy density due to over-melting. The severity of these types of pores increases in size and number with increasing distance from the optimal processing region. It should be noted that gas porosity, being less process dependent, is observed in approximately equal size and quantity across this entire process space.

In order to increase the productivity of the L-PBF process, higher scan speeds are desirable. However, it has been largely observed that at high scan speeds, above a certain limit, there will be an increased level of porosity and reduced mechanical properties including those for fatigue [17,81,90]. While the porosity as an average value is less affected, higher scan speeds lead to larger pores with more irregular shape which means that the effect of increased scanning speed is comparable to that of lower laser power, i.e. under-melting.

Analogous to L-PBF, an increase of cooling rates through adjusting of laser beam irradiance (the ratio of laser power to focal spot area) in case of LMD can result in a more stable process which favorably influences the refinement of the solidification microstructure. Froend et al. [91] report, that in case of wire-based LMD of Al-alloy EN AW 5087 the use of low laser beam irradiances close to the lower limit of stable melting, results in structures

with a significantly refined microstructure. It was possible to reduce the degree of anisotropy of the microstructure and to increase the yield strength of up to 16 % in comparison to the structure manufactured at high laser beam irradiance. The latter was close to the transition to keyhole mode welding.

3.3 Energy dissipation and local thermal history

3.3.1 Cooling rate—In PBF-based AM, process characteristics lead to grain growth velocities being very high compared to other forms of solidification processing. These characteristics include high scan speeds (in L-PBF typically 0.5 – 2.0 m/s), (relatively) low temperatures of the chamber and base plate (< 200°C) in conjunction with a very small melt pool size due to small hatch spacing of 50 to 150 μm and layer thickness of 30 to 60 μm cause a cooling rates ranging from o 10^3 to 10^8 K/s [92]. Consequently, the highly localized, rapid solidification [93] causes unique microstructural features such as microscale segregation and very fine grain sizes [22,65,94]. The microstructures become even more complex due to the repeated heating-reheating cycles provided by successive laser tracks. Note that the microstructure is not only very fine but usually also highly metastable [92]. For example, Amine et al. [95], investigating L-PBF 304L austenitic steel, found significant changes in the microstructure after heat treatment at no more than 400°C and for 25 hours.

In addition to mechanical property anisotropy, the consequence of these AM microstructures is usually a higher monotonic strength and a lower ductility of the AM material as compared to its conventionally manufactured counterparts [65]. An example is provided in Fig. 11 [96]. In the as-built state, the yield and ultimate tensile strength values of the AM material were much higher than those of its wrought counterpart, while the ductility was significantly reduced (in the present case the reduction of area at failure). When annealed with heating to 1095°C with a holding time of one hour, the strength was reduced and was closer to the conventional material. In contrast, the ductility of the material with higher porosity, although also increased over the as-built state, was lower than in the wrought state. In that case, the failure of the specimens is expected to be defect controlled. What is not shown in the figure is the high scatter in the AM material properties of up to 120 MPa in strength and up to 20% in the reduction of area, which is much larger than in the conventional material.

Note, however, that the literature for PBF 316L also reports results with both the elastic limit and the elongation to fracture to be larger for the L-PBF version of the material [35,97]. This illustrates that some caution is necessary in view of the generalization of empirical trends.

The increase in monotonic strength can be due to martensitic transformation in titanium alloys [98–100], to a dendritic fine columnar sub-grain microstructure in 316L steel [96,101] and similar features in other materials (e.g., [102]). The explanation of an increase of both ductility and yield strength in the 316L steel is the presence of nano twins [97].

3.3.2 Inter-layer time interval—The local thermal history, i.e., the heating and cooling cycles upon a specific material point and its surrounding plays a major role with respect to both the local microstructure and the defect population in metallic AM materials. In that context, the time span between successive layer deposits at the same location, the inter-layer time interval, needs to be mentioned [103]. The development of the local temperature at the

position of the first laser track is illustrated by the example in Fig. 12. In this case, when the neighboring tracks are laid, the first one will be heated again, however, from track 3 onwards, the layers underneath will not be heated above the melting temperature anymore. Higher track numbers mean a larger vertical distance to the first track. Therefore, reheating becomes weaker of the bottom layers. The repeated heating and cooling will cause some annealing effect comparable to a multi-pass weld, and as in the latter case, the result will be a complex microstructure (e.g. [84]).

In general, longer inter-layer times result in higher ΔT and lower initial temperatures during the cycles while shorter ones show the opposite effect due to the increased bulk temperature. As a consequence, long inter-layer times tend to lead to a finer microstructure, a higher monotonic strength and a decreased elongation at fracture [20,105]. Fig. 13 provides an example for two different inter-layer times realized in single- and multiple bar configurations of 316L stainless steel. The effect of a parameter such as the number of parts placed on the platform [106], can be explained as an interlayer time effect.

Note that the longer inter-layer time in the example additionally resulted in lack-of-fusion defects. Due to a lower initial layer temperature, the laser induced melt pool depth was reduced such that the layers were not completely molten anymore [20,105].

Spranger et al. [107] also reported interdependencies between the inter-layer time and the melt pool geometry for laser metal deposition of Ti6Al4V. Low inter-layer times resulted in distinct heat accumulation, higher initial temperatures of the build plane, broader melt tracks and reduced layer heights. They also showed that the heat accumulation led to intensified tempering colors which indicated detrimental oxidation processes.

An example for the influence of the interlayer time in conjunction with varying laser power on the average grain size of 316L stainless steel in a L-PBF process is given in Fig. 14. It can be observed that an increase of the laser power and a shorter inter-layer time leads to significant grain coarsening. This is assumed to be due to increased heat accumulation and resulting lower cooling rates within the part. This effect is even more pronounced in the upper areas of the samples since they benefit less from higher heat dissipation into the baseplate. In these areas, also a significant deepening of the melt pool is reported to be accompanied by the occurrence of spherical pores. Note, that no support structures were used in this study, the specimens were built-up directly on the baseplate. Support structures, typically used for an easier removal of the build parts from the baseplate, will intensify the heat accumulation even further.

There is an effect of the inter-layer time on the fatigue strength as illustrated in Fig. 15. “Double-built” refers to a longer inter-layer time and a lower S-N curve, as expected. Note, however, that the data as shown in the figure might have a problem. Instead of the stress ratio R ($= \sigma_{min}/\sigma_{max}$) the authors provide a table with the mean stress and stress amplitude for each data point. Based on these, the R ratio not only varies between the single- and double-built series but also within the stress level for each curve. Unfortunately, the authors provide no indication whether the data shown in the diagram were finally mean stress corrected. Therefore, the curves must be analyzed with some caution.

3.4 The building orientation

3.4.1 Definition—What is actually meant by the term “building orientation” is the relative orientation of the building layer plane (which is parallel to the build plate) with respect to the applied loading direction of the component. The nomenclature is given in Fig. 16 for tensile and hourglass specimens as well as for fracture mechanics specimens. Note that the latter follows the nomenclature of ISO 12135 [109]. Alternative nomenclatures are provided by ASTM E 399 [110] and, specifically for AM, by Seifi et al. [111].

It has been empirically observed in metallic AM that the building orientation has an immense influence on the mechanical properties including fatigue [84,99,112]. Usually the horizontal specimens (i.e. 0° to the build plane) show superior mechanical behaviour than vertical ones (90° to the build plane). An example is provided by Fig. 17. With respect to fracture mechanics specimens, poorer properties are obtained for specimens with potential crack growth along the boundary between the built-up layers (z-x) compared to those with crack growth normal to the layer (x-y), which show better crack growth resistance. This trend was also found by Syed et al. [113] after relieving residual stresses in L-PBF Ti-6Al-4V.

In this context, it is important to consider the meaning of the term “loading direction” While the loading direction as expressed by the arrows are quite clear in Fig. 16, the reality will often be more complex. In the absence of certain constraints, e.g., a material texture or mixed mode loading conditions, a crack will always grow on a plane normal to the maximum principal stress. The direction of this, however, can change across the wall even if the global applied loading direction stays unchanged. As a consequence, a fatigue crack, during its growth, might change its direction of propagation. Due to their complex shape AM components are frequently subjected to complex multiaxial stress states [24] with changing directions [114], see [115] for thin-walled, net-like structures. A simplified example is shown in Fig. 18 for illustration. A hollow cylinder is subjected to internal pressure. Depending on the position along the perimeter, the loading direction (maximum principal stress) coincides with the horizontal or the vertical building direction, or a direction in-between the two, which means that both building directions are present in one and the same component.

Since the “local” building direction at the location of the highest local stresses and strains is of paramount importance with respect to the material properties, as demonstrated by the example of Fig. 17, the building orientation should be taken into account at an early stage in the design process. [116]. The building direction is also important for the surface roughness. It has been observed that for overhanging structures the top surface (upskin) exhibits lower surface roughness compared to the lower surface (downskin) [117], see also Section 4.2.3.

When surface machining is not possible, the building direction should therefore be optimized in order to have highly loaded surfaces corresponding to upskins/lower roughness.

3.4.2 Irregular defect pattern—In this section the effects of the building orientation will refer to the simplest case as shown in Fig. 16. These correspond to a heterogeneous formation of the microstructure and an uneven defect pattern. Considering first the defect

pattern: In particular, lack-of-fusion defects are characterized by an elongated shape (see Section 4.2.1.2). They form at the interface between two successive layers such that their orientation is perpendicular to the building and possibly the loading direction [114]. This condition is schematically illustrated in Fig. 19 along with the 2D stress concentration caused by an elliptical defect. Although the elliptical defect is certainly a simplification compared to the reality of a lack-of-fusion defect in an AM component, the tendency is clear. The elliptical defect is characterized by a large c/b ratio expressing the ratio of defect length to its height (a multiple of c/b = 1). This causes a stress concentration $K_t > 3$ for the vertical direction. At the surface such defects can commonly have a ratio c/b of the order of 5 and a very sharp radius of curvature in the as built state [117]. In the horizontal direction we have the opposite in that c/b is a fraction of 1 and K_t is smaller than 3. Therefore, local stresses at lack-of fusion-defects are expected to be much higher in the vertical than in the horizontal directions, and it is clear that this point combined with an unfavorable loading direction can adversely affect the damage tolerance capability.

3.4.3 Heterogeneous microstructures—The potential formation of heterogenous microstructures for the different building orientations is schematically illustrated in Fig. 20 [114]. During solidification, the grains elongate along the building direction because they grow in the direction of the maximum temperature gradient [93,119]. Since the latter also varies through the depth of the melt pool, there will as well be some heterogeneity in the grain structure in that direction [120]. If fatigue crack propagation is not transgranular but is at least partially intergranular, the result will be an increased asperity of the crack faces in the z-x configuration compared to the rather smooth x-z one. This will lead to the two following consequences: The roughness-induced crack closure effect (see Section 2.2.2) will be larger for the z-x specimen, thereby increasing the overall threshold ΔK_{th} and shifting the threshold regime of the da/dN-ΔK curve to lower crack propagation rates. Note, however, that this beneficial effect is expected only at lower R ratios ($R < 0.7$) and it will disappear at higher R ratios or for the da/dN-ΔK_{eff} curves. The effect of the local microstructure and to a lesser extent, defects (pores and lack-of fusion) on crack path deviation and branching is reported by [121] for L-PBF Ti-55511 alloy.

3.4.4 An indirect effect of the building orientation—An indirect effect of the building orientation relates to the *aspect ratio of the layer*. The term denotes the proportion of the area or length dimension, *d*, to the thickness, *t*, such as illustrated in Fig. 21. The important point is that the larger distance d (left) corresponds with a longer inter-layer time interval. As discussed in Section 3.3.2, this tends to lead to a finer microstructure, higher strength and reduced ductility. This does not necessarily imply that horizontal build orientations are disadvantageous for damage tolerant properties. What will be finally be the determining factor depends on other factors such as the defect pattern and on the orientation of the layers with respect to the loading direction.

3.5 Laser scanning strategy

3.5.1 Scanning strategies—Another process parameter that affects the mechanical properties of the metals produced is the scanning strategy. This describes the motion pattern of the beam over the surface of each layer. Common various scanning strategies as reported

in literature are illustrated in Fig. 22a. Scanning is important insofar as it significantly affects the local thermal history which in turn influences the evolution of the microstructure, the residual stresses and the defect configuration of the AM part [36,122–126], as well as the elastic anisotropy [127].

3.5.2 Effect on the microstructure and defect distribution—In Inconel 718 specimens manufactured by different laser scanning strategies, Fig. 22b, Liu et al. [129] found the continuous growth of columnar dendrites epitaxially along the deposition direction in single direction raster scanning to be inhibited in cross direction raster scanning. This resulted in finer grain sizes. For further reported results of these two scanning options, see also [130] and [131]. An example is shown in Fig. 23. The scan strategy in terms of chessboard, double exposure techniques etc. also has been shown to have an effect on the defect pattern, i.e., the local distribution of pores etc. [114,122,132].

3.5.3 Effect on residual stresses—There is an important effect of the scanning strategy on the residual stresses. In contrast to parameters such as the energy of the laser including the scan speed which primarily affect the amplitude of the residual stresses, the scanning pattern impacts both the magnitude [133] and local spatial distribution [23,123,134]. However, since the scan vector length influences the temperature gradient (the greatest stress component develops parallel to the scan vector [134]), a short scan vector can reduce the residual stresses at least in a single layer [23,135,136]. Lowering residual stresses can also be achieved by a smaller layer thickness [137]. For materials, which tend to form defects such as pores or microcracks, it may not always be possible to identify the processing strategy, that will result both in a defect-free microstructure and a more favorable distribution of residual stresses. Quite often the result will be a compromise between the two challenges of defect free microstructures and low residual stresses. Further discussion on the residual stress issue will be provided in Section 5.

3.6 Other parameters

3.6.1 Layer thickness—Layer thickness has an effect on the porosity level which tends to increase with larger layer thickness [138–140] and on surface roughness [141] for build-up directions deviating from the vertical case (see Section 4.2.3). Furthermore, reducing the layer thickness can be beneficial for reducing the residual stresses [4,137]. Laser beams allow for the use of smaller powder sizes than electron beams and therefore produce lower layer thicknesses.

3.6.2 Support configuration—The effect of solid and lattice support structures configuration on the microstructure and surface residual stresses of L-PBF Inconel 718 is reported in [142]. They found that due to different cooling rates, the presence of the support structure had an effect on the development of the microstructure. This was observed to be the finest in terms of grain size in the boundary regions separating the L-PBF and the support structures. The effect on the surface residual stresses was due to the different constraint conditions given by the support configuration. Reducing the temperature gradient by pre-heating the base plate will reduce thermal stresses and, as a consequence, also reduce residual stresses [4,135,143]. However, Mertens et al. [144], investigating L-PBF fabricated

H13 tool steel, report a change of the residual stresses from compressive to tensile with increasing preheat temperature, an information that is limited to the top surface. While the challenge of mapping the microstructure in whole components has been tackled [427], a complete picture on the pattern of the residual stresses in the whole structure is currently not yet available in literature.

3.6.3 Powder and powder reuse—For reasons of sustainability and cost effectiveness, it is common to reuse the surplus, unmelted powders in powder bed fusion processes. The powder is usually sieved before powder reuse in order to remove larger particle agglomerations. This raises the question of whether this reuse will influence the damage tolerance behaviour. Changes are to be expected with respect to the powder composition, morphology, particle size distribution and the rheological properties of the powder. Cordova et al. [145], investigating four commonly used AM powders after a long period of use, including measures for reprocessing the powders, found an increase in the mean particle size, which could be effectively controlled by sieving. However, reuse also resulted in modifications of the particle morphology where elongated particles and those containing satellites were observed. The flowability was, nevertheless, improved. The latter was also observed by [146,147] along with a narrower particle size distribution. These authors did not find any difference in the S-N diagrams between the new and the heavily used powders of Ti6Al4V in the as-build condition. They even reported a substantial improvement in the machined condition, which they ascribe to the lower cohesion and interparticle friction of the reused powders which, in conjunction with the better flowability could lead to smaller internal pores. On the other hand, Heiden et al. [148], investigating reused 316L stainless steel powders, argue for an adaption of the guidelines for feedstock quality. They not only found a slight increase in the powder particle diameter but also an increased roughness of the particles, an increase in surface oxygen content and an increase in δ ferrite. In particular, oxide formation is the main hindrance to reuse of powders.

4. Material defects in AM

4.1 General remarks

In Section 2.2.3, a rough classification of material defects, micro-geometrical defects and defects which might belong to both groups was provided. Here only defects of the first and the third classification will be discussed. Note, however, that other defects such as indents, scratches or corrosion pits might as well exist in an AM structure and, unlike material defects, these can be introduced not only at the manufacturing stage but also during service or maintenance.

The term critical defect size was introduced in Section 2.2.3. Below its size, the detrimental effect on the fatigue strength disappears. Finally, it was briefly discussed that there is some competition between different types of defects. Depending on its size and shape, its dispersion (e.g. clusters) and its proximity to surface the effect of defects on fatigue crack initiation will vary. As a rule, defects are more harmful when they are larger, when they are closer to the surface, when their stress concentration (with respect to the loading direction;

see Section 3.4.2, Fig. 19) is high and when they are clustered or occur somehow preferably orientated [47–49].

For example, Romano et al. [149], investigating additive manufactured AlSi10Mg, found lack-of-fusion porosity, to be much more detrimental for the fatigue behaviour than the microstructure. The same dominant effect was found by Le et al. [150] for Ti6Al4V alloys. Molaei and Fatemi [19], investigating the effect of Hot Isostatic Pressing (HIP) on the fatigue behaviour of Ti6Al4V and 17-4PH alloys, found that surface roughness was the dominant effect compared to porosity in samples with as-built, non-machined surface condition. Comparable observations were made by Kahlin et al. [78], see also [151]. Greitemeier et al. [152], investigating electron beam melted TiA16V4, found that voids dominated the fatigue properties in the absence of surface roughness. Tang et al. [153] found that pores smaller than 5 μm after HIP treatment of Ti6Al4V were irrelevant for crack initiation. This is not surprising, since this value is probably smaller than the critical defect size. Instead, the fatigue cracks were initiated at a small stress concentration at the surface. Beretta et al. (2020), investigating L-PBF formed AlSi10Mg, found surface defects such as local notches or undercuts are dominant compared with the surface roughness. Understanding the competition between different defects is important in order to anticipate the potential effect of the various options of post-fabrication treatment (Section 6).

Yadollahi and Shamsaei [20] reported a difference of the effect of defects on fatigue crack initiation with respect to the applied load level. While at high loading levels (at the finite life branch of the S-N curve) multiple crack initiations might prevail, near the fatigue limit it is just one defect and one crack which controls the fatigue life. This is also valid for metals obtained by other technologies than AM. Remember the definition of the plain fatigue limit given in Section 2.3. 1a which is the stress range at which the largest of a population of cracks just arrests. Or in other words: the fatigue limit defines the limit between the state at which all growing cracks are arrested and the state at which just one crack is able to further propagate. That the number of growing cracks, above the fatigue limit, increases with the stress level is also known from other applications such as weldments [155,156].

While in general defects reduce the mechanical properties, particularly those of fatigue (cf. Section 2.3.2, Fig. 5) their poorly predictable characteristic with respect to dispersion, the proximity to the surface and the occurrence in clusters. also generates substantial scatter. This has a consequence of a limited repeatability of these mechanical properties. As an example, Romano et al. [149] interpreted the variability in pore formation even under almost identical process conditions as the reason for the large scatter in S-N data on AM formed AlSi10Mg. Similar observations were made in [22,26,149,157–160], where the authors also considered the porosity responsible for the high observed scatter. Romano et al. [161] extend this statement to LCF. In the presence of designed deep V notches, the scatter in fatigue life was found to be reduced [162]. The probable reason is that the notch tip stress concentration factor ($K_t > 3$) was much greater than the pore stress concentration factor ($K_t \approx 2$) hence dominating the fatigue process. Li et al. [163], investigating AM Ti6Al4V specimens, found an influence of the density of near-surface build defects on the fatigue behavior which they could explain by a weakest-link model.

An attempt to classify defects has been made by Laquai et al. [164] using X-ray refraction techniques (see also [165–167]. Such techniques allow for the detection of extremely small defects (above around 1 nm), even below the resolution of synchrotron radiation computed tomography. X-ray refraction techniques permit empty pores to be distinguished from defects filled with unmelted powder, since they would scatter X-rays differently. This technique also allows the spatial arrangement of defects to be mapped in a planar sample (integrated through its thickness) over a large field-of-view (typically 10×10 mm).

4.2 Typical defects in AM

4.2.1 Voids

4.2.1.1 Gas pores: Gas pores are voids that result from entrapped gases in the molten pool. Gas bubbles do not have enough time to rise to and to escape from the surface, due to the rapid cooling in AM. Gas porosity can have several different physical origins. In Section 3.2, excessive laser power was found responsible for the creation of gas bubbles in the molten pool which are then trapped in the material during solidification. Another source of gas is associated with the metal powder, see Thiede et al. [168], particularly if the packing density of the latter is low [83]. There is an extensive range of process parameters which affect the degree of porosity, besides the above mentioned laser power and power density, these are scan speed, spot size, scan strategy, powder size, powder morphology and others [86,169].

The size of the gas pores is of the order of < 100 μm, [83]. Since their shape is approximately spherical, the stress concentration factor of an internal pore is rather small ($K_t \approx 2$), see Sobotka et al. [170], who provides an analytical solution for embedded pores and [26]. Note, however, that the stress concentration will increase when two adjacent pores are sufficiently close such that their stress-strain fields interact as illustrated in Fig. 24 [171], see also [170]). When the distance s between two adjacent pores decreases below the diameter D, K_t increases and almost doubles at a very short distance. Consequently, the pores will spontaneously coalesce, which increases their size, changes their shape and increases the stress concentration factor.

A similar effect of increasing stress concentration factor occurs when a pore is close to the free surface. For a brief review of literature data see [49]. When the structure is cyclically loaded, the plastic shear strain next to the pore increases dramatically below a certain distance from the surface, which is of the order of the pore radius [172] and the remaining material bridge reaches its plastic limit [173]. Consequently, the pore will immediately “snap through” this way forming a surface notch with a dimension much larger than that of the pore [69]. This is the reason why pores and other voids are most harmful when they are close to the surface [84]; for a brief review see [49].

There might also be the danger that voids may become surface defects when machining is performed to smooth the rough surface [20,174], an effect which was also reported for AM [84].

The effect is expected to be more pronounced for elongated lack-of-fusion defects (Section 4.2.1.2) which by themselves have a higher stress concentration factor. There is also an

interaction of cracks with pores which needs to be considered. In sintered steels, the pattern of porosity (pore clusters, chains etc.) affects fatigue crack propagation such that it can predetermine the path along which the cracks will grow [175–177]. This has also been numerically demonstrated for AM material, although for Nylon in that case [178].

Although it is occasionally reported in the literature that gas pores are randomly distributed in the volume, this does not seem to be generally the case, at least not at a smaller scale. Tammas-Williams et al. [132], see also [36,179] showed for Electron Beam Powder Bed Fusion (EB-PBF) Ti6Al4V that the location of the pores strongly correlated with the process parameters and scanning strategies used for contouring scanning and hatching. There was a tendency for clustering at the end and turning points of hatching infill scans.

Prithivirajan and Sangid [180] developed a crystal plasticity-based approach for investigating the effect of the pore size on the fatigue response of L-PBF Inconel 718. Cyclic simulations were performed varying the pore sizes, the locations of the pores relative to the surrounding microstructure and the proximity between adjacent pores. The microstructural characteristics, e.g., grain size, orientation and the type of grain boundary were obtained from Electron Backscatter Diffraction (EBSD). The authors obtained a critical size of single pores of 20 μm for the investigated L-PBF Inconel 718 with average grain size of 48 μm. However, in cases where the distance between adjacent pores was reduced to values less than 15 μm, even a pore size of 10 μm in diameter was able to cause fatigue failure.

4.2.1.2 Unmelted regions (lack of fusion): It has already been mentioned in Section 3.4.2 that lack-of fusion porosity is more harmful than gas porosity. The reasons for the severity of the lack of fusion defects are due to the elongated shape (“slit-shape”) and the more irregular morphology, which is associated with a higher stress concentration [20]. In addition, lack-of-fusion defects have a much larger extension. Tammas-Williams et al [132], reported defect lengths as high as 190 μm.

Under-melting can occur due to a too little laser energy or a too high energy absorption and dissipation in the setup. The powder is not fully melted to deposit the new layer and the energy is too low to penetrate deep enough into the molten pool (Section 3.2). Since the width of the molten pool is small, there will not be sufficient overlap between subsequent scan tracks. The consequences are poor interlayer bonding and lack-of-fusion defects between the scan tracks [83]. Materials prone to oxidation, e.g. aluminum alloys, tend to generate an oxide film at the built surfaces which decreases their wettability. Again, the consequence will be poor bonding and lack-of-fusion [83]. Gali et al [181] found the wettability of the AM aluminum material, to be the main causes for porosity and even for hot cracking. Other aspects to consider are the low absorption of laser energy and the presence of impurities.

Surface irregularities of the current build layer such as roughness at the sites of unmelted regions of a previous step [83] or due to insufficient spreading of the deposited powder [169] will also affect the bonding capability between the layers.

Unmelted regions and particularly those resulting from the poor bonding defects between the layers will lie in plane approximately perpendicular to the building direction, i.e. the stress concentration they induce is maximized in the vertical loading direction (see Section 3.4.2, Fig. 19). If the distance between the defects is small, clustering effects could be a potential consequence. Simultaneous multi-site crack initiation and growth at several lack-of-fusion defects could happen as this is observed in sinter metals [176,182]. When these defects coalesce at a later stage, the load carrying capacity of structures will be much lower than that in the case of single-site crack growth.

4.2.2 Cracks and crack-like features—The rapid solidification in AM affects the microstructure and the development of high residual stresses (see Section 5), but also may cause the formation of thermal cracks at the production stage (e.g., [83,92]). Due to a large solidification temperature range, high thermal expansion and extended shrinkage at solidification, L-PBF formed aluminum components are particularly prone to solidification cracking [17].

Crack-like defects can also be formed by the entrapment of surface oxide layers into the melt pool [17]. Bauereiß et al. [183] and Taheri et al. [184] have observed crack-like features in cases where the melted powder merged with surface contact points which were not melted to the previous layer. The result was a complex shape of the weld pool which was conserved after solidification.

4.2.3 Surface roughness—AM processed components in the as-built condition show much higher surface roughness than conventionally manufactured parts. The main reasons for this surface roughness are stepped layers in AM and partially melted powder at the surface due to an unstable melt pool [20,114], see Fig. 25. Especially in tilted build jobs and overhanging structures, partially attached particles and droplets of molten material create defects with a typical size above 50 μm; see [185]. There are some applications such as orthopedic implants where this might be beneficial for biocompatibility but in the general case high surface roughness is very detrimental for fatigue resistance (e.g., [20,78]). One problem is that post-fabrication surface treatment is sometimes difficult to achieve on AM components. It is a primary goal of AM to form the components geometrically as close as possible to the final state if possible without post-fabrication treatment; furthermore, the accessibility of conventional methods such as grinding and polishing is frequently limited due to the complex geometry of the AM components, e.g., hollow parts, lattice structures.

In L-PBF the magnitude of surface roughness is affected by various process parameters such as powder size and build orientation [20,186]. Another important factor is the scan speed. Increased scan speed is directly proportional to increased surface roughness [20,168]. This direct correlation is unwanted due to the need for higher scan speeds and therefore faster build times in production environments. However, this unfavorable correlation between scan speed and surface roughness can be partially mitigated via the use of a suitable scan strategy. A consequence of the dependency of the roughness on the process parameters is its variability along the component surface. Bagedorn et al. [186] have commented on the “irreproducible and inhomogeneous morphology after the manufacturing process”.

Specific aspects of surface roughness development are the “stair case” effect and the question of upward and downward facing surfaces with respect to the building direction. The consequence is non-uniformity of the roughness along the surface of an AM component.

Firstly, the staircase effect (Fig. 26) is due to the geometrical step between the sequential layers [187]. The roughness increases with the layer thickness [141] and depends on the build angle [188]. An average value for the surface roughness can be estimated by

$$R_a = 1000 \cdot t_i \cdot \sin\left(\frac{90-\theta}{4}\right) \cdot \tan(90-\theta) \quad (5)$$

[4] with t_i being the layer thickness and θ being the build angle. Thiede et al. [185] have found that the staircase effect (quantified through a “step function”) is however not predominant in the IN625 Ni-based superalloy.

Secondly, the upward and downward facing effects, Yadollahi and Shamsaei [20] provide an example in L-PBF Inconel 718 for a cylinder generated in 45° direction. They found a roughness of $R_a \approx 10$ μm at the upward-facing surface and $R_a \approx 25$ μm at the downward-facing surface and explained this difference by the more direct contact of the downwards side with the powder bed during manufacturing. Similar results were obtained for EB-PBF Ti6Al4V samples for 0 (R_a = 11 and 30 μm) and 45° (R_a = 32 and 36 μm) directions [117]. The authors also found a larger number of near-surface voids along the downward-facing side. As mentioned earlier in Section 4.2.1.1, there is the danger that such voids can become surface breaking by machining in order to reduce the roughness. Aside from the build angle, layer thickness is another parameter that effects the roughness in such a way that thicker layers correspond to higher roughness [190]. The diameter of the AM component can also have an effect on roughness as demonstrated by Pegues et al. [191]. The authors explain this observation with different heat dissipation rates in smaller and larger solidified volumes. Chen et al. [192] found that roughness was larger for surfaces built up in a direction away from the laser origin. Furthermore, Thiede et al. [185] have found that the higher roughness on the lower side (named downside) than on the upper side also causes an overestimation of the effective cross-sectional area of a cylindrical specimen. This implies an underestimation of the effective stress acting on the cross-section during uniaxial testing. Beretta et al. [154] found for L-PBF formed AlSi10Mg with different building directions the lowest fatigue strength for the lower (downward) side. However, they do not explain this as a roughness effect, but as an influence of the building direction on the residual stress state.

Surface roughness also depends on the basic technology used (see Fig. 25). For example, Balachandramurthi et al. [193] provided an example where the roughness of EB-PBF was three times higher than that of the same component formed by L-PBF. The reasons were the thicker layers and the coarser grain generated in EB-PBF.

One point to be mentioned in the context of roughness characterization is the agreement on its definition. Based on the surface roughness profile such as shown in Fig. 27, standards such as ISO 4287 [194] provide different measures for its specification. Usually, in AM papers the R_a parameter is used (e.g., [20,195]) which is the arithmetic average height parameter or centerline average. Provided that the parameter is only used for purpose of

comparison between different conditions, this does not matter. However, when it is used as an input parameter for fracture mechanics analyses, it is no longer a suitable parameter and should be replaced by R_z or R_{max} [196,197], cf. also the discussion by Schork et al. [156].

However, the description might be even more complex. Note that R_z refers to the maximum peak height R_p plus maximum valley R_v. However, from the point of view of the 'notch effect', the relevant parameter seems to be R_v and the protruding material does not have a significant effect. Gockel et al. [198] effectively found that R_v (or S_v if aeral measurements are adopted) is the roughness parameter that has the strongest correlation with fatigue life.

Generally, caution should be exercised in interpreting the relationship between surface roughness and fatigue strength. The surface integrity cannot be described by the measured parameters of surface roughness, since they do not sufficiently capture the presence of subsurface defects, partially open surface breaking defects or the presence of fine notches arising from irregularities of layer formation. For instance, AM surfaces are characterized by depressions and notches (see Fig. 25 or Notch 1 in Fig. 28) that are not likely to be covered by traditional measurement methods (either mechanical stylus or laser/optical methods). X-ray computed tomography (CT) potentially offers a more suitable means of control than conventional 2D or 3D profilometer for the characterization of the surface condition of AM parts [117,199–201]. Thiede et al. [185] call for a new paradigm in metrology when defining roughness, however an established procedure for this in connection to mechanical properties is not yet available.

The roughness-induced stress concentration reported by Kahlin et al. [78] was $K_t = 4.26$ for EB-PBF Ti6Al4V. Combined with a designed notch ($K_t = 2.5$), the authors estimated a fatigue notch factor of $K_f = 6.64$ such that the fatigue limit was reduced by almost a factor of seven. A similar magnitude of stress concentration due to roughness is presented in Fig. 28 originally reported by Vayssette et al. [202].

The examples comparing the effects of different surface finishing explain why surface roughness dominates the fatigue process if the component is not machined or otherwise surface treated after manufacturing. Surface roughness grooves are the most frequent locations for fatigue crack initiation in metallic AM components that are usually in conjunction with a designed notch. An example for the effect of surface roughness on the S-N curve is shown in Fig. 29. Note that, besides roughness there could be other effects of milling. The surface removal could have an influence on the residual stresses in the near-surface region.

Therefore, a question exists on how surface roughness should be addressed in component assessment. The conventional solution is correction factors to the plain fatigue limit. A variety of empirical correlations for these have been published, for reviews see Andrews and Sehitoglu [203]. Savaidis et al. [204] and Wormsen et al. [205]. However, Ås et al. [206] suggest that many of the empirical solutions are "notoriously inaccurate" and sometimes overly conservative.

A more recent example is provided by the German FKM guideline [207] where the fatigue strength reduction factor is given by following equation for normal stresses:

$$K_{R,\sigma} = 1 - a_{R,\sigma} \cdot log[R_z] \cdot log\left[\frac{2R_m}{R_{m,N,min}}\right] \quad R_z \text{ in } \mu m;\ R_m \text{ and } R_{m,N,min} \text{ in MPa} \tag{6}$$

.

The terms $a_{R,\sigma}$ and $R_{m,N,min}$ are empirical material constants given in the document.

The characteristic that the fatigue notch factor is not only affected by the roughness but also by the strength of the material (the ultimate tensile strength R_m in Eqn. 6) is known by the term “notch sensitivity”. Given the same roughness, the reduction in the fatigue strength becomes larger for higher strength materials. This general statement is also true for AM applications. As a summary of the literature, Solberg and Berto [208] state: “Especially for high strength metals, geometrical defects and surface roughness is a major factor determining the fatigue life.” This statement can be explained by the discussion provided in Section 2.3.2. The arrest size of a crack initiated at a defect becomes smaller with higher strength, until a point is reached where the size of the defect itself exceeds the arrest crack size such that no arrest occurs any longer. Beyond that point (above a Vickers hardness of HV = 400 in Fig. 5 and a much smaller value for AM), the fatigue strength is strongly affected by the defect, and it decreases with increasing HV (or strength).

An interesting point is made by Solberg and Berto [208] who claim that the notch sensitivity is not just a material property but a combined material and component property. Their observation that the effect decreases and, at the same time, the scatter in fatigue life becomes smaller for crack growth at narrow notches in AM-Inconel 718 can be easily explained by what was called “anomalous” crack growth in Section 2.3.1(c). The small tip radius of the designed notch, in conjunction with the stress decrease in the wall thickness direction and the gradual build-up of the crack closure phenomenon at the short crack stage prompts crack arrest independent of the depth of the secondary notch. The latter is provided by the roughness, which is responsible for the scatter when the crack is not arrested.

The reduction in fatigue strength due to roughness notches is strongest at the fatigue limit and it becomes smaller at the finite life branch of the S-N curve. McKelvey and Fatemi [209], investigating forged steels at different hardness levels found that difference disappeared below $N = 10^3$ loading cycles to failure. Borrego et al. [210] demonstrated the same effect for Ti6Al4V produced by L-PBF.

Beside of the empirical correction factors for K_f (or $K_{R,\sigma}$), the effect of surface roughness on the fatigue strength can also be obtained analytically by one of the two options:

- **a.** The roughness can be treated as notches as common in classic fatigue analysis [211].
- **b.** They can be treated as cracks (e.g., [54,58,139,196,212–216].

Due to the small notch root radii of the roughness groves such as that shown in Fig. 28, fracture mechanics calculations should yield appropriate results (see the discussion in [47,58,216] if the specific aspects of short crack propagation (Section 2.3.1) are taken into account. This can be realized by any method described in Section 8.4.

Pegues et al. [191], investigating L-PBF Ti6Al4V, reported on a size effect on the fatigue behaviour with respect to surface roughness which they explained by the different circumferences of their specimens. Their results are in line with the well-known size effect in fatigue strength which has a statistical component such that the probability of larger defects becomes larger with an increasing surface area [217].

4.2.4 Further defects

4.2.4.1 Balling defects and keyhole porosities: Balling effects are the consequence of poor wetting and are presented pictorially in Fig. 30a. Balling effects occur when the poor wetting causes the break-up of thin melt pools into spherical droplets with diameters of the order of the laser beam size [218]. The melted liquid peels the powder away from the surface. Reasons for the balling effect can be insufficient energy and/or too high laser speed or not enough material being available in the liquid phase [85]. At higher scan speeds, instabilities in the melted pool due to a capillary effect can be responsible [184]. The initial powder layers play a role as well [219]. For example, the oxygen content was found to cause balling initiation in stainless steel and nickel [85]. The consequences of the balling effect are rough, bead-shaped surfaces and the formation of discontinuous scan tracks and poor inter-line boding [220,221,222]. Li et al. [85], investigating stainless steel and nickel, found ellipsoidal balls up to a dimension of about 0.5 mm, see also [221].

Keyhole pores (Fig. 30b) are formed by a massive energy density. While the depth of the melt pool typically depends on the heat conduction of the underlying metal, in keyhole mode, this is controlled by the evaporation of metal [223]. The consequence is a deep and narrow melt pool which makes it difficult for the vapor bubbles inside to escape [224,225]. Keyhole pores can also be formed in laser welding. When keyholes collapse, they can leave an array of pores [226]. Cunningham et al. [227] have used high speed synchrotron imaging to produce beam velocity-beam power maps detailing the conditions of formation of keyholes and their morphologies for Ti6Al4V.

4.2.4.2 Non-metallic Inclusions: There exist critical defect sizes, below which the defects will not show an effect on the fatigue limit. There is a competition between different types of defects. Usually in AM, non-metallic inclusions will not play much of a role in this competition, simply because they are much smaller than defects due to unwelded regions or surface roughness. However, there are exceptions. Taheri et al. [184] report on large intermetallic particles (0.5 to 1 mm in size) such as oxides and sulphides which formed by chemical reaction of the material with the shielding gas.

Impurities in the powder can also influence the formation of inclusions. For example, Schmidtke et al. [228] found poorly bonded grains due to inclusions at the base of the grains in a scandium modified aluminum alloy and Brandão et al. [229] reported mostly spherical tungsten particles embedded in Ti6Al4V. Oxide contamination, by hindering wetting, can promote the balling effect [184,222]. Near surface carbide/oxide inclusions in addition to pores are regarded as fatigue crack initiation sites in Inconel 718 in [230].

4.2.4.3 Microstructure: Microstructural features (e.g. grain size/shape and crystallographic texture) are not normally considered defects in the context of fatigue

of engineering materials where the effect of defects dominates (Section 2.3.1). However, AM metals commonly exhibit non-traditional microstructures due to the complex thermal histories of the AM process, and these have been shown to have significant effect on fatigue behavior of these materials. For example, Hrabe et al. [231], achieved a large variation in crystallographic texture for EB-PBF Ti6Al4V by intelligent process parameter manipulation and showed significant effect on both fracture and fatigue crack growth rate (FCGR) behavior due to the texture variation. Another example is provided by Brenne and Niendorf [7] who successfully achieved crack arrest by manipulating grain size and morphology via AM process parameters for L-PBF 316L stainless steel. These two examples not only demonstrate the effect of microstructure on metal AM fatigue behavior. They also epitomize the potential for fatigue performance optimization through microstructure control.

4.2.5 Statistical issues—Aa a consequence of the complex morphology, the method of choice for sizing embedded defects in AM is X-ray computed tomography and this usually reveals a huge scatter band of defect sizes which requires statistical processing [24,111,149,159,199,232,233]. Fig. 31 shows scatter bands of defect diameters at the bottom, middle and top of an AM bar. Besides the lower and upper limits of the scatter, the authors report a large number of “outliers” which they define by defect sizes greater than 1.5 times above the third quantile. The large number brings up the question of whether these are really “outliers”. If not, their large size will control the failure of the component.

In fact, the whole issue is even more complicated because it is not only the size but also the morphology, the orientation with respect to the loading direction, the occurrence of clusters and, most important, the proximity to surface of a defect which matters with respect to its effect on fatigue (Section 4.1). Such information is not included in a “pure” size distribution. It has already been mentioned that cavities close to the surface are much more harmful than those located within the bulk (see the discussion in Section 4.2.1.1 and for an AM example [235]). This means that a small defect just beneath the surface can be much more dangerous than a larger one away from it.

If such observations are not taken into account, defect size statistics is at least conservative as long as it depicts correctly the upper tail of the distribution function. To that purpose, extreme value statistics can be applied, particularly the peaks-over-threshold method, which is explained by Murakami et al. [236] and ASTM E2283 [237]. This is applied to AM by Romano et al. [238,239]. An example of the extreme value statistics is shown in Fig. 32. Another approach is followed by Gorelik [25] who proposed the application of defect-exceedance curves to AM applications. The elaborate concept has been developed in the aerospace industry for turbine disks [240], see also [241]. An exceedance curve provides the dependency of the expected cumulative number of defects greater than a certain size on a given volume of material.

Thiede et al. [185] have quantified the amount and size of pores with respect to their distance to the surface. They have observed that pores concentrate close to the surface, but large pores are preferentially found in the bulk.

5. The problem of residual stresses in AM

5.1 Origin and classification

5.1.1 Residual stresses at component cross-section, microstructural and atomistic scales—Residual stresses are stresses that remain in a component after manufacturing or, later, following mechanical or thermal loading. Since they exist without applied load, their corresponding forces and moments must cancel out throughout the whole specimen or component volume and at any plane section. In other words: they are in internal equilibrium. With respect to the scale over which they balance out, residual stresses can be classified into different groups. A first classification distinguishes between the Type I, II and III residual stresses [242,243]. Type I or macroscopic residual stresses act on the scale of component geometry. When released, they cause the distortion of the component. Type II act on the scale of the microstructure, usually the grain size, and Type III at the atomic scale. It is usually the Type I stresses which matter with respect to fatigue and fracture, although Type II may also play a role with respect to microcracks [243].

There are different causes for the three types of residual stresses. Starting in reversed order, Type III stresses are the result of point and line defects in the lattice such as vacancies, dislocations, substitutional atoms etc. [23,242]. Type II residual stresses form due to the local difference in the slip behavior from grain to grain [23,242] or because of anisotropic thermal expansion and Young's modulus. Finally, Type I is caused by local geometrical misfit between different regions in the material/component as a consequence of (a) non-uniform plastic flow, (b) steep thermal gradients, or (c) phase transformations [242]. As described above (Section 3.3.1), a specific feature of AM is the presence of extreme thermal gradients leading to very high thermal stresses. These thermal stresses in combination with the lowered yield strength at elevated temperature can cause non-uniform plastic deformation which, after cooling, result in residual stresses. Note that the problem can be aggravated when dissimilar metals are joined due to strength mismatch resulting in strain concentration zones forming at the interface [4]. With respect to the effect of strength miss-match cf. section 1.9.3 of [216] and Annex C in [60].

Note that the measurement of Type II and III stresses, although possible in principle, is rather uncommon [244] because they are not usually considered in engineering assessments.

5.1.2 Long-, medium- and short-range Type I residual stresses—The following discussion will be limited to Type I residual stresses. In view of the classification in structural integrity, these can be differentiated further according to the length scale in which they operate. Referring to welding residual stresses, Green and Knowles [245] distinguished between long-, medium- and short-range residual stresses, see also [246,247].

a. Long-range (also called "reaction") residual stresses have their origin far away from the cross section which potentially carries the fatigue crack where they manifest as elastic stresses. Although they self-equilibrate overall within the structure this is not the case in this section. Reaction stresses are affected by many factors such as the overall geometry of the structure, the sequence of how the structure is built and other process parameters. When a detail is cut

from the structure, the long-range stresses are (partially) released. In fracture assessment, long-range residual stresses are treated as “primary stresses”, i.e., they are considered like mechanical applied stresses.

b. In contrast to the long-range residual stresses, the medium-range residual stresses self-equilibrate over the cross section containing the crack. This is because their origin is close to this plane. In fracture assessment they are considered as so-called “secondary stresses”. In contrast to the primary stresses, secondary stresses do not contribute to plastic collapse since larger plastic deformation overrides the eigenstrains associated with the secondary stresses [242].

c. Short-range residual stresses tend to play a role with respect to fatigue crack propagation only when a crack is greater than half the wall thickness [245,246]. This typically refers to the end-of-life stage of the structure with very limited contribution to residual and overall lifetime. They are, therefore, not relevant here.

Elastic follow up is a term sometimes used for distinguishing between the long- and medium-range residual stresses. This characterizes the ability of a structure to increase local strains by plastic (or creep) deformation while under constant load or displacement [248]. Long-range stresses show significant elastic follow-up, but medium-range stresses do not. Note that there might be some interaction between the long- and medium-range stresses which is usually explained by a bar-frame model. This will not be explained here, see, however [60,242,247] and, specifically for AM, [4].

It is important to note that even for welds, there are many cases where it is difficult to distinguish between long and medium range residual stresses. The same difficulty also applies to primary and secondary stresses. With respect to AM processed components this might even be the rule. As a consequence, residual stresses in AM components should generally be treated as “primary”, even at the risk of a conservative assessment in some cases. According to section 7.1.6 of BS 7910 [249] this is generally recommended when the spatial extent of the residual stresses is large compared with the crack size, which is the case for short cracks. An exception is low cycle fatigue (LCF) because of the effect of widespread plasticity on the residual stress state.

5.2 Residual stress distributions in AM structures

The magnitude as well as the distribution of residual stresses in AM depend on a wide range of parameters, presented in Fig. 33.

The most important parameters identified in literature can be grouped into:

(a) The thermal gradient along and across the scan direction—Thermal gradients pertaining to parameters such as the laser power, the scan speed, the layer thickness and its aspect ratio, but also by energy dissipation which can be influenced by, e.g., reheating the support configuration (e.g., [4,33,123,135,137,143,250]).

(b) The scanning strategy—The scanning strategy includes parameters such as a shorter deposition length, scanning in small islands etc. (e.g., [4,33,37,123,133,135,136,168,251,]).

(c) The use of support structures and the removal from the base plate—It has been observed in several works (see e.g. [252–254] that removal from the base plate relaxes residual stress and creates unwanted distortions in components. To avoid this issue, small support structures have been used, whereby only a certain number of contact points are allowed between the base plate and the component. Note, however, that residual stresses have been observed to not fully relax, leading to the conclusion that post-fabrication heat treatments are still necessary [254].

The development of the residual stresses also depends on the size and geometry of the component processed by AM, see, e.g., [250]. Bartlett et al. [255], investigating different geometries, found the highest residual stresses in purely cylindrical parts. Although AM processing is typically utilized for complex shaped components, the investigations available in the literature mostly refer to simple bar geometries. Thus, on the one hand they yield information of general value, however, on the other hand the results cannot be simply transferred to more complex structures but individual experimental investigations or simulations are necessary. On this specific point it has been shown by Edwards et al. [256] for EB-PBF Ti6Al4V, that components may have better fatigue properties than those predicted from standard specimens:

a. The magnitude in the residual stress of AM processed components can be very high, with peak values in the order of the yield strength of the material or even higher [23,257].

b. A quite typical spatial distribution found by many researchers (e.g., [113,137,168,244,252,257,258,259] is compressive residual stresses in the bulk and tensile residual stresses at the surface zone. An example is shown in Fig. 34. When loaded in the build direction, a potential crack would grow at a plane perpendicular to this, which implies that it is in between two layers. In the figure this refers to the z-x configuration which is usually the worst case for structural integrity (Section 3.4.1, Fig. 17 and Section 3.4.2, Fig. 19). An important part of this problem is residual stresses. However, it might not be the only issue, because other features such as anisotropic microstructure could play a role as well.

Tensile residual stresses are often observed at the surface. This is of importance since crack initiation and short crack propagation will usually occur in that region. Since the early stages of crack propagation control both the fatigue life and strength, this is of course detrimental for structural integrity.

Recall in Section 3.4.1, we identified the need to consider the building orientation with respect to the loading direction, which can be quite complex in real geometries. In Fig. 34 we have three different crack planes such that quite different residual stress distributions prevail at the perpendicular plane. While we have tension at the crack front in the x-z and (partially) in the z-x configuration, there is compression in the x-y one. It is therefore that stress

relieve annealing has a positive effect on the da/dN-ΔK curve in the first two cases (where tensile stresses are relieved) but a negative one in the third (x-y), where the beneficial compressive stresses are lowered. Positive effect means that the crack propagation rate da/dN for a given applied ΔK is lower, i.e. the red curve is below the blue one in Fig. 34. The example reveals how complicated the residual stress issue can be in component assessment. Syed et al. [113] reported a very similar trend and direction dependence of fatigue crack growth behaviour as the result of residual stresses.

Note, however, that a bit of caution is required in the interpretation of the results in the figure, since other potential influencing factors of the annealing, e.g. on the microstructure, are not considered.

c. There is also a residual stress gradient along the building direction such that the bottom and top regions of the bar are characterized by tensile stresses and the middle part by compressive stresses [23,33,142,2554,258,260]. In other words: the residual stresses vary from layer to layer. Note that the peak values of residual stresses always occur at the free surface of a layer at the upper surface of the bar [37,261]. However, when a new layer is added, the tensile stress in the previous layer changes to a compressive stress following the new thermal cycles.

d. After the component is cooled down, the largest (tensile) residual stresses are found at the end of the first track and at the last track [37,168,262]. The peak values of the residual stresses always occur at the onset of the scanning tracks where the first thermal cycle occurred [251,262].

e. Residual stresses are largest along the scan direction [37,134] and they increase with scan length [37,135], hence, a short scan vector is a method for reducing the magnitude of residual stresses, see Section 3.5.3.

Bartlett and Li [255], in a recent review paper on residual stresses in PBF, write: “The dependence of the residual stress formation on processing variables, material properties and part geometry has made it difficult to predict efficiently and has hindered widespread acceptance of AM techniques.” Definitely there remains significant potential for mitigating the residual stresses in AM by intelligent combinations of the process parameters listed in Fig. 33. In the meantime, the solution consists of post-fabrication stress relief using the methods which will be discussed in Section 6. It should, however, also be noted that stress relief may not be necessary for all AM techniques and material system combinations. EB-PBF utilizes layer preheating, which results in a high background temperature (400-800°C) throughout the entire process. This high background temperature has been found to sufficiently eliminate residual stress during the AM process as characterized by the neutron diffraction method [263].

A consequence of incomplete residual stress removal is demonstrated in Fig. 35 for a SEN(B) specimen subject to compression pre-cracking (see [264]). In Section 8.4.4, compression pre-cracking will be explained in the framework of cyclic R curve determination. What happens under such loading conditions is illustrated in Fig. 36. The specimen contains a narrow initial notch usually introduced by electro discharge machining

with the notch tip being additionally sharpened by a razor blade or other means. At the initial loading, the notch is compressed and due to this, a monotonic and a cyclic plastic zone remain after unloading (Fig. 36a). The plastic zone is characterized by tensile residual stresses such that the subsequent cyclic loading is realized by the difference between this residual and the applied stress. When the crack propagates, the cyclic plastic zone becomes smaller and it is shifted towards the boundary of the monotonic plastic zone generated from first loading cycle (Fig. 36b). Having reached the boundary of the plastic zone, the crack arrests (Fig. 36c). Depending on the yield strength of the material, crack arrest will usually happen after some ten or hundred microns. In Fig. 36a this is shown for conventionally processed 316L steel (red curve) where the crack stopped after a propagation of 183 μm. However, this did not happen in the AM processed 316L due to the remaining residual stresses from the L-PBF process (blue curve) for which crack propagation continued over 9 mm. Significant AM induced residual stresses remained in the test specimen after the stress relief annealing at 450 °C for 4 hours. Indications for residual stresses are also provided in Figs. 35c and d, where the crack is open in the unloaded state and the crack front is significantly irregular.

5.3 Effect of residual stresses on the cyclic crack growth driving force

Within the application range of the linear elastic ΔK concept and if crack closure effects are absent, the treatment of the residual stresses, in principle, is straightforward. They do not affect the K factor range ΔK but the mean value $\overline{K}$ or the R ratio (= K_{min}/K_{max}) as an indirect measure of the mean value. Consequently, they are simply added to both, the maximum and the minimum K, K_{max} and K_{min}, in the loading cycle:

$$\overline{K} = \frac{1}{2}\left[(K_{max} + K_r) + (K_{min} + K_r)\right] = \frac{1}{2}\left[K_{max} + K_{min}\right] + K_r, \tag{7}$$

$$R = \frac{K_{min} + K_r}{K_{max} + K_r}, \tag{8}$$

The R ratio is then understood as an effective ratio rather than the nominal value exclusively based on the applied loading. The crack propagation analysis in the structure must be carried out using the da/dN-ΔK curve obtained for this effective R ratio.

However, when fatigue crack closure comes into play, simple linear superposition is no longer adequate. In this case, a correction for crack closure has to be performed, see Section 2.2.2. Another restriction is in LCF, where ΔK does not adequately describe the cyclic crack growth driving force. Instead a plasticity-corrected factor, e.g. based on a cyclic J integral [58,214,266], cf. also [60], has to be determined. Note that the increase in the mean stress (when the residual stresses are tension) can potentially raise K_{max} such that it reaches the resistance against monotonic fracture or sustained failure. The consequence can be the premature failure of the component [243].

Even if the consideration of the residual stresses in fatigue crack propagation is straigthforward in principle, its practical implementation to AM processed components is

faced with serious challenges. This is due to the complex distribution of residual stresses across the section potentially containing the fatigue crack, which usually requires more sophisticated methods than two-dimensional weight or influence functions to determine the stress intensity factor. Even if such methods are available, the residual stress field must be known – and preferably in advance, i.e., from simulation – which is a significant challenge due to the wide range of influencing parameters. Note that considerable effort has been made in the field of residual stress simulation for many years now [23,31,33,134,137,250,259,261,262,267,424], for a comprehensive literature survey see [4].

5.4 Stability and relaxation of residual stresses

Not much has been reported about the stability of residual stresses in AM applications. Investigations have been carried out on weldments. We envisage a comparable situation in the case of AM. However, the effects may be more pronounced in AM because of the highly metastable conditions of the as-built state, arising from the high cooling rates, particularly for L-PBF processes. Residual stresses will be relaxed when the following condition is fulfilled:

$$\sigma^{p} + \sigma_{r} \geq \sigma_{Y} \tag{9}$$

where in Eq. (9), σ^{p} is the primary or applied (mechanical) stress, σ_{r} denotes the residual stress and σ_{Y} is the yield strength of the material. Keeping these three factors in mind, the following options are possible:

a. The residual stresses σ_{r} cannot be larger than the yield strength σ_{Y}, since plastic deformation causes stress relaxation. Of course, this statement is only approximately correct because it ignores the role of strain hardening. When the yield strength is lowered, such as at higher temperature, σ_{r} will be reduced. This is the basic principle of thermal stress relief. Note that σ_{Y} reduction can also occur under cyclic loading when the material shows cyclic softening. This has been shown to be the case in conventional as well as AM processed Ti6Al4V [195].

b. When the applied stress σ^{p} is increased beyond a certain limit, the sum of σ^{p} and σ_{r} will exceed the yield strength, with the consequence that the residual stress is lowered. This is the basic principle of mechanical residual stress relaxation, which can be realized by monotonic as well as by cyclic loading. It is known from weldments that even the first loading cycle can have a significant effect [268], for an overview see also [247]. In the case of cyclic softening materials the subsequent loading cycles will contribute to stress relaxation as well, until the stress-strain response has stabilized. Note that mechanical stress concentrations, e.g. due to notches, play an important role.

c. There is the possibility of intentionally introducing beneficial, i.e., compressive, residual stresses by peening or other methods onto the surface of the components after manufacturing. Since the residual stresses close to the surface in as-built AM tend to be tensile (Section 5.2), surface treatments will hinder the initiation and early growth of surface cracks. Of course, also the compressive residual

stresses will undergo relaxation under cyclic service loading such that the effect will reduce (see for instance [269]. An extensive overview on this topic is given by McClung [270]. It should be noted that tensile residual stresses will arise elsewhere to balance the compressive residual stresses. When shot peening is used on irregular/rough as-built surfaces the beneficial effect of surface compressive stresses can be somewhat counterbalanced by the presence of subsurface defects induced by the plastic deformation of the surface (see [117] for an example on EB-PBF Ti-6Al-4V).

The issue of residual stress stability plays a role in post-fabrication treatment (Section 6), where the mechanisms decribed above are used deliberately but it can also be relevant under service loading where both undesirable effects can occur.

Excursus: Threshold and Paris law regimes of the da/dN-ΔK curve of AM processed specimens—Although a considerable number of da/dN-ΔK curves for AM applications have been published during the recent years, no consistent picture can be provided. One contributing reason is the sometimes comparatively large scatter in the data typical for AM [122,271,272]. Note, however, that what is usually called “scatter” in da/dN-ΔK, in a large part, is only apparent. The sucession of acceleration and deceleration phases of crack propagation generates the apparent “scatter”, besides the techniques used for smoothing the raw data. Note that this is averaged out in residual or overal lifetime. For further explanation see [273] and section 2.3.2.4.2 in [60]. A similar conclusion was drawn by Konečná et al. [274] for laser sintered Ti6A14V who suspect that non-continuous crack propagation as observed at the specimen surface is the main source of the “scatter”.

Although a mixed picture arises with respect to the effect of the building orientation [65,100,122,275–278], some general conclusions can be drawn from the available studies:

- **a.** As a general rule, the threshold ΔK_{th} and the threshold range of the da/dN-ΔK curve is more strongly influenced by AM processing than the Paris law regime. There are, however, exceptions. For instance, Poulin et al. [278] report an effect of porosity and build orientation in Inconel 625 at higher ΔK values while there was no effect at lower ones. The effect was probably one on the crack growth path. (Note that the authors intentionally generated unusually large levels of porosity.)
- **b.** There are two effects which seem to affect the threshold regime but they are difficult to distinguish. These are residual stresses and roughness-induced crack closure. Examples provided in Fig. 37 show the threshold ranges of conventional and AM Inconel 718. The authors suspect the effects of residual stresses, a finer microstructure and a decreased content of boron as the reason for the lower threshold regime of the AM material.
- **c.** There are different features that might affect the tortuosity of the crack faces and, thus, indirectly crack closure in AM processed materials: It is well known that the crack closure increases with the grain size (and so does the crack propagation threshold ΔK_{th}, [280]. Relatively fine microstructures are typically observed for L-PBF due to the rapid solifdification of the melt pool. They should reduce

roughness-induced crack closure with the consequence of a low threshold. This is assumed by Konečná et al. [279], Galarraga et al. [281], Fergani et al. [282] and Poulin et al. [283]. An opposite effect, i.e. the increase of the crack closure effect can be caused by crack path deviation and crack branching triggered at different microstructural features in AM (e.g., [17,121,157,281, 284]). Nezhadfar et al. [272] observed crack paths along the columnar grain boundaries.

d. The effects of (c) can be overshadowed by the residual stresses. This is assumed (on the basis of experimental data) by Leuders et al. [285], Edwards and Ramulu [100], Becker and Dimitov [122], Seifi et al. [24] and Konečná et al. [279], by the latter authors as only a possibility. Mukherjee et al. [137], evaluating literature data, reported an almost linear relationship between the maximum residual stresses and the fatigue crack propagation rate da/dN in the range between da/dN = 2×10^{-5} and 2×10^{-4} mm/cycle.

e. Due to the residual stress distribution across the section of the AM specimens, the requirement for a straight crack front by the test standards, e.g., ASTM E 647 [286] and ISO 12108 [287] can be violated, see e.g. [272]. Likewise, an out-of-plane crack propagation was observed for specimens with a build angle of 45° whilst no deviation was found for the 0° orientation by Fergani et al. [282].

In cases where the Paris law exponent, i.e., the slope of the Paris line in double-logarithmic scaling becomes significantly higher than n = 4 (cf. Section 2.2.2), crack growth mechanisms others than fatigue will probably be temporarily operating. This could be the case with the R = 0.1 data for AM processed Ti6Al4V in [288].

Riemer and Richard [289], also investigating Ti6Al4V, found a decrease of the fatigue crack propagation threshold with increasing laser power (from 3.8 $MPam^{1/2}$ for 175 W to 2.4 $MPam^{1/2}$ for 950 W).

While nearly all literature studies are restricted to long crack conditions for which the ΔK concept is used, Romano et al. [161] additionally based their investigation on the elastic-plastic ΔJ_{eff} obtained by the P_J method of Vormwald [290]. To the same purpose, the application of the IBESS method to AM is in progress [58,60].

6. Post-fabrication treatment of AM components

6.1 General notes

As discussed in the sections above, structural integrity (and evaluation) is undermined mainly by the following features:

- Inhomogeneous microstructures and mechanical properties across the component;
- The anisotropy of these properties, i.e., their dependence on the build-up with respect to the loading direction;
- Defects such as porosity and unmelted regions;
- An unusual high surface roughness;

- High and inhomogeneous residual stresses.

The problem is further complicated by the fact that all these features are strongly influenced by a large variety of process parameters. Residual stresses will be observed with different magnitude, and sometimes also with different spatial distribution from component to component. Additionally, the material also plays a role.

The aim of post-fabrication treatment is to mitigate the effects of these features and to improve the component response to fatigue loading. These are not specifically for AM but are in use in the field of post-weld treatment (for a review see [291]). Some of the methods influence several features. In particular, Hot Isostatic Pressing (HIP) at the same time has an influence on (i) the microstructure (usually coarsening it and making it more homogenous), (ii) the defects by reducing pore size and closing unmelted regions, and (iii) the residual stresses, the magnitude of which are reduced through relaxation mechanisms.

Not every material will react to all treatments in the same way. The metastable microstructural conditions in the as-built state will play a role and also the framework of the component analysis must be considered such as whether the design is target safe life or a damage tolerance (see Section 2.1). In the first case, the fatigue strength is of importance. This is heavily influenced by surface or close-to-the-surface defects as well as surface roughness. In the second case, fatigue crack propagation is of primary interest. This is affected by the microstructure (including its inhomogenetity, anisotropy and coarseness) and by the residual stress state. The load level also plays an eminent role. If it is high, such as in low cycle fatigue, plasticity might reduce the harmfulness of defects and relieve residual stresses. This will, however, not be the case at lower loading levels in high cycle fatigue. Another question: Is there an expectation for multiple-site crack propagation or will fatigue damage probably occur at one site only? Not all these questions can properly be answered beforehand. Nevertheless, they should be kept in mind since the substantial goal of an individual post-fabrication treatment might depend on them.

6.2 Thermal treatment

6.2.1 Annealing—Annealing will have an influence on both the microstructure and the residual stress state. This effect depends on the material, the temperature, the holding time and the cooling rate. Usually, AM processed materials, particularly L-PBF, display an extraordinary fine but also metastable microstructure. Therefore, the result of annealing will be a coarsened microstructure, such as a larger grain size or other microstructural characteristics, such as dissolution or precipitation of phases. Note that annealing might result on contrasting effects on different properties. A well-known pattern is that an increased grain size tends to decrease the fatigue strength, whilst it improves the fatigue crack propagation behaviour in the threshold regime of the da/dN-ΔK curve (Fig. 38). Note further that sometimes depending on the material used process inherent characteristics may even pave the way for the elimination of post-fabrication heat treatment, see Wegener et al. [292].

In fatigue crack propagation the potential influence of the coarse microstructure on the roughness and tortuosity of the crack faces is evident. It promotes the roughness-induced

crack closure effect (Section 2.2.2) and, as a result of this, the fatigue crack propagation threshold is increased. This was found for AM processed materials, e.g., by Fergani et al. [282] and Yu et al. [293]. The grain size effect on the fatigue strength has another background in that a coarser grain reduces the monotonic strength (Hall-Petch effect).

It was shown for L-PBF processed AlSi10Mg that a heat treatment of 300°C for 30 min reduced the yield and tensile strength significantly but increased the elongation at fracture. Differences of yield and tensile strength in the as-built condition resulting from varying build-up strategies, scanning parameters, powder batches and machines were leveled out almost completely, with only differences in the elongation at fracture remaining. The tensile strength was correlated to the size of the sub-grain structure of separated eutectic Si particles, which seemed to be changed predominantly by this heat treatment [294].

The decreasing effect of stress-relief annealing on the fatigue strength is represented by the cyclic yield strength $R'_{p0,2}$ resulting from Incremental Step Tests of AlSi10Mg net-shaped small-scale specimens in Fig. 39. These were manufactured in various orientations – x, xz, y and z [295]. On the one hand, the figure shows that large variations in the cyclic yield strength can result for the net-shaped as-built state depending on the build orientation, specimen thickness and maximum strain amplitude. On the other hand, in the annealed state levels the cyclic yield strength to approximately 200 MPa independent of the built orientation, specimen thickness or maximum strain amplitude applied in the Incremental Step Tests.

Aside from a few exceptions, the general trend for AM processed materials is an improvement of fatigue strength with annealing [293,297]. Note that the same observation is made for Hot Isostatic Pressing (HIP) which also includes annealing, although at higher temperatures. After HIP treatment, a higher fatigue strength is generally observed [4,298]. Since the coarsening of the microstructure should cause the opposite effect, another explanation needs to be found for the fatigue strength improvement. The HIP cycle is expected to close internal pores and, depending on the temperature, it will lead to homogenization of the microstructure and relax the residual stress state. If tensile residual stresses at the surface are lowered or even removed there will be a beneficial effect on fatigue strength.

Hrabe et al. [263] were able to determine the fatigue strength improvement due to internal pore closure during HIP with no influence from residual stress. They accomplished this by studying EB-PBF Ti-6Al-4V where residual stresses (determined by neutron diffraction) were negligible even before HIP due to the consistently high background temperatures (400-800 °C) from layer preheating during the EB-PBF process.

In the literature it is often stated that residual stresses have limited effect on fatigue crack propagation in some materials, such as. Ti6Al4V [285] or 316L stainless steel [282]; Fig. 35 in Section 5.2 however demonstrates, that there is an effect on crack arrest. Of course, annealing temperature, holding time and cooling rate will play a role on the microstructure and residual stress state. The effect of different annealing conditions is impressively demonstrated by Fergani et al. [282]. They found that stress relieving at a

moderate temperature had no effect and annealing heat treament at 1050°C followed by furnace cooling only a limited effect on fatigue crack propagation in 316L stainless steel. In contrast, heat treatment at the same temperature followed by water quenching provided a significant improvement of crack growth resistance. The authors suspect the generation of compressive residual stresses as the reason.

However, for highly metastable material conditions, there can even be a detrimental effect. Examples are provided by Yadolahi et al. [299] for a 17-4 PH stainless steel and by Beevers et al. [138] as well as Zhang et al. [300] for AlSi10Mg. Note that in the first case for the 17-4 PH steel, the detrimental effect was only observed in high cycle fatigue, whereas, in the low cycle fatigue regime (where larger plasticity occurs) a beneficial effect was reported. There are also cases where annealing (and even HIP) seems to be of no effect on the fatigue strength [19,301]. A potential explanation for at least some of these examples is that the effect is overshadowed by the influence of the surface roughness which usually is the dominant factor with respect to the fatigue strength in the as-built state of AM components [4,19,302].

6.2.2 Hot isostatic pressing (HIP)—In Hot Isostatic Pressing, annealing (at relatively high temperature) is combined with a high isostatic gas pressure with the latter being applied in a high-pressure containment vessel. The effects combine the reduction of residual stresses with modifications of the microstructure (e.g., [4,234,303,304] and the densification of the material, i.e. the removal of pores and unwelded-regions or at least their reduction in size. A further effect is residual stress relief, except for AM techniques where the building plate temperature is large enough to sufficiently relieve any residual stresses that may form, e.g. EB-PBF [263]. The beneficial effect of a HIP treatment on the fatigue strength is illustrated for example in Fig. 40. and even though just few tests have been carried out, a general trend can be inferred. Günther et al. [151], investigating AM-Ti6Al4V, found the HIP treatment to reduce the pore size to a subcritical value. In addition, the failure mechanism changed such that crack initiation no longer occurred at defects, but instead was located at facets.

The effect of a HIP treatment on the threshold regime of the da/dN-ΔK curve is presented for Inconel 625 [283] in Fig. 41. The differences between the building directions in the as-built and heat treated state disappear after a HIP treatment. While the stress relief annealing was performed for one hour at a temperature of 870°C, in HIP the material was subjected to 1120°C for 4 hours. No residual stress analysis is provided in [283] since the authors assume the heat treatment to be effective in removing residual stresses, they suspect roughness-induced crack closure as the reason of the effect in Fig. 41b. Indeed, the authors found a coarser microstructure after HIP which they associated with the more tortuous crack paths observed.

Generally it is noted that both the material and the fatigue regime might influence the efficancy of a HIP treatment. In [306] the authors showed HIP being not so effective as in Fig. 40 in Inconel 718 because of microstructural aspects such as (a) the evolution of delta phase promoting localized damage formation, (b) grain coarsening and – most importantly – (c) the dissolution of sub-grains during HIP.

The reduction of the size of cavities such as pores or unmelted regions by HIP to below the detection limit of NDT is attested for many AM applications [174,215,234,298,302,307,308,]. The fact that cavities open to the surface cannot be eliminated is clear, but there is a question of embedded pores close to the surface. Whilst Masuto et al. [215] report on their removal in Ti6Al4V, Shamsaei and Simsiriwong [34] found this not necessarily to be the case. Perhaps an explanation could be microcracks from the pore to the surface which are too small to be detected [307]. Entrapped argon gas in internal pores is suspected to not be removed by HIP [303]. As a consequence, HIP can close pores, but cannot fuse the material since entrapped gas cannot escape. Tammas-Williams et al. [302] report X-ray CT observations, which show that some of the "eliminated" pores reappeared during subsequent heat treatment, probably driven by the high internal gas pressure inside the pores. Wu and Lai [309] report that a HIP treatment can also remove or reduce the influence of the build direction.

6.3 Mechanical treatment

The introduction of plastic deformation into the surface layer, in order to generate compressive residual stresses is a common method of post-fabrication treatment in welding. Typical methods include blasting, shot, laser and ultrasonic peening and deep cold rolling. Applications to AM are found in [117,186,310,311,422].

In principle, the mechanical treatment of additively manufactured structures can have different goals. The principal ones are (1) the removal of residual stresses and distortion, (2) grain size refinement and (3) the introduction of beneficial compressive residual stresses in fatigue critical areas or areas with high defect population. Whilst deep rolling is more efficient for grain refinement, laser shock peening (LSP) can introduce deep compressive residual stresses. It is assumed, that LSP-induced residual stresses are more stable with respect to stress relaxation due to cyclic loading compared to the well-established shot peening process or deep rolling, where significant plastic deformation of the surface occurs. Mechanical treatment can be applied during the additive manufacturing process, e.g. after each deposited layer or after several deposited layers, or as a final post-fabrication treatment to the generated structure.

A successful application of cold deep rolling for residual stress removal and microstructure refinement was demonstrated in large structural metallic components made by WAAM [312,313]. Successful distortion reduction of a WAAM Al-structure due to cold deep rolling applied during the additive manufacturing process (inter-pass rolling) as well as on the side surface (side rolling) is reported by Hönnige et al. [314]. The effect of inter-pass cold deep rolling on microstructure refinement of WAAM-Ti6Al4V was shown by McAndrew et al. [315]. Mechanical treatment can also be advantageous for notch sensitivity due to surface roughness reduction.

6.4 Surface finishing

6.4.1 Surface integrity—Since fatigue cracks are usually initiated at the surface; surface condition plays an important role for fatigue strength and short crack propagation while it is of low importance for long fatigue crack propagation. What is of paramount

importance in AM applications, is the unusually high roughness in the as-built state which sometimes overshadows other effects on fatigue strength (e.g. [4,19,139,301]). Therefore, smoothing and, in general terms, improving the surface quality is an important goal of post-fabrication treatment of AM components.

Note that it is not only roughness that defines the quality of a surface. Half a century ago, Field and Kahles [316] have introduced the term “surface integrity”. According to Murakami [54], the fatigue strength of a cyclically loaded component is influenced by four surface-relevant factors: (i) surface roughness which acts by local stress concentration, (ii) residual stresses close to the surface, (iii) work hardening (or softening) when the surface layer is plastically deformed, and (iv) potential transformations of the microstructure due the plastic deformation. It should be added, that these factors are also important for short crack propagation since this is closely related to fatigue strength.

6.4.2 Methods of surface finishing—In principle, the methods of surface finishing are not specific to AM parts, but they are also applied to components processed by many other methods, such as welding. However, what makes the situation in AM more complex is the frequently limited accessibility to geometrically complex components such as hollow structures or lattices. The methods can be distinguished between those which smoothen the surface and those that introduce compressive residual stresses. Note, that the effects will, sometimes unintentionally, be combined in some cases.

Methods primarily devoted to smoothening are: (a) mechanical machining (milling, grinding, polishing, etc.), (b) chemical and electropolishing, and (c) surface remelting.

a. Examples for the mechanical machining of AM surfaces are published, e.g., by Bagehorn et al. [186], Elangeswaran et al. [301], Nezhadfar et al. [297] and Yu et al. [293]. Note that sometimes machining is performed in order to satisfy the (high) requirements of design guidelines in an application field independent of AM, e.g. [179]. Usually, the scatter in fatigue strength is reduced due to the smoothing of the surface. For example, Nezhadfar et al. [297] associated the higher fatigue strength of the machined condition where only one fatigue crack was initiated compared to the specimens without post-fabrication treatment which exhibited multiple crack initiation. Likewise, Yu et al. [293] observed that crack initiated from embedded pores after polishing, in contrast to surface initiation by the other surface treatments which resulted in less surface smoothing, see also Beevers et al. [138]. Care should be taken to sufficient layer removal in order to avoid the risk that existing subsurface imperfections become surface flaws after final machining [19,84]. Note that there is also the danger of inducing unintended residual stresses by grinding.

b. Chemo- and electropolishing plays a more important role in AM post-fabrication than in other applications because of the complicated geometries and the poor accessibility making the application of mechanical methods impossible. Whilst chemopolishing can be used to almost any component shape, electropolishing is more limited insofar as the counter electrode needs to be positioned in the proximity of the surface to be treated [317]. Chemical etching of EB-PBF

Ti-6Al-4V has been found to be a very effective way of improving the poor fatigue strength of the as built material. A considerable reduction of the surface roughness/defects is observed which drastically reduces the probability of crack initiation. However, the etching process cannot completely remove the deepest surface defects (unless a very long etching time is used which is unpractical from an industrial point of view and/or for thin components) and therefore a relatively large scatter is observed at low stress levels [318].

c. Re-melting the surface is usually realized by laser treatment. Whilst it can be applied at each layer during production, it is more economic to restrict it to the final surfaces of the component [186,319,320].

Other surface treatment methods aimed at introducing compression residual stresses in the surface layer, besides smoothing the surface; would prevent or at least retard surface crack initiation, see Section 6.3. Note that, besides the generation of compressive residual stresses in the surface layer, there might also be further ramifications of the plastic deformation such as cyclic softening which will reduce the residual stress effect [195].

7. Non-destructive testing (NDT) of AM components

7.1 General aspects

In terms of the basic concept of NDT, a principal distinction can be made between two strategies designated as “good workmanship” or “quality control” and “fit-for-purpose” or “fitness-for service”. What is the difference?

a. The aim of “good workmanship” is to produce components as flawless as possible. Instead of an individual evaluation of the harmfulness of the flaws with respect to structural integrity, the criteria are set by the sensitivity of the NDT method. If, for some applications, defects below a certain size cannot be detected they are simply not taken into account.

b. In contrast, “fitness-for purpose” is based on an analysis of the effect of individual defects on structural integrity, e.g., critical crack sizes. This information then sets the goals for NDT, e.g., which defect size at which position in the component must absolutely be avoided or which defect size must be found with sufficiently high probability in inspection.

Obviously the two strategies differ in terms of their requirements to NDT. Comparable to the situation in the development of other new production technologies, NDT of AM, as it currently stands, concentrates on good workmanship. An expression of this point is the development of defect catalogues by ASTM [321] and ISO [322] which include imperfections such as porosity, unmelted material, layer defects, stop-start flaws, inclusions etc. [24,167]. The situation is reminiscent to the development of such catalogues for welds and castings. However, since the classification is based on the worst option from the long list of the potential flaw characteristics, the consequence might be extended conservatism in component assessment. In order to improve this situation, proposals have been made (Annex C in the most recent ISO 5817 version [323], VOLVO STD 181-0004 [324]) to combine the ISO quality system with the FAT class approach. The defect catalogue is moved towards a

fitness-for-service strategy. Eventually, this will also become necessary with the AM defect catalogues.

7.2 Specific challenges and requirements

AM provides specific challenges for non-destructive testing [24,325]:

- **a.** AM geometries will often be complex since the possibility to form such structures is one of the main advantages of the new technology. AM parts might have an internal structure with limited or even no accessibility for NDT.
- **b.** AM parts possess high roughness in the as-built states.
- **c.** AM materials often have metastable microstructures, and they show some anisotropy of the microstructure and defect configuration.

As a consequence of the problems listed above there is a trend towards non-contact, remote inspection. Methods currently under development for AM application, amongst others, comprise optical tomography, non-contact ultrasonic testing such as laser ultrasound (e.g. [184,326], and most of all, X-ray computed tomography (CT). X-ray CT is superior to others (including metallography) in that (i) it is able to visualize even complex defect geometries such as elongated non-welded areas, and (ii) it provides a volume scan which allows the generation of a defect size distribution, the quantification of its volume fraction and provides an information on the spatial distribution of the defects (e.g., [24,159,132,199,232,233,327]. A very informative up-to-date overview on NDT of metal AM by X-ray tomography is provided by du Plessis et al. [328]. However, the method also has disadvantages: when performed with laboratory X ray sources/detectors, CT is not well suited for crack and crack-like defect detection, the sensitivity will degrade with increasing wall thickness and the method, in general, is restricted to rather small component sizes [325] as the spatial resolution scales with the sample (large samples being visualized at low resolution and vice versa).

In practice the question is often that of the size of a “killer defect“, which highlights the problem of the biggest defect that can go undetected in the component or its highest loaded section [24]. Additionally, in the sense of a fitness-for-service strategy, the effect of defect type, size and distribution on the performance of the part has to be known. Therefore, NDT should not be considered independent of an overall strategy of component assessment as will be discussed in Section 8. Anyway, NDT has to be applied individually depending on the geometry of the structure, its surface finish etc. Sometimes multiple NDT techniques might be required to achieve full coverage [24,324]. Fig. 42 provides an overview on various NDT methods with respect to the spatial resolution and the potential location of the defects. While rather large defects of the order of millimeters are considered in a damage tolerance analysis, much smaller defects ranging from tens of micrometers play a role in safe life (see Section 2.1). A property that must be measured in any case is surface roughness [329].

An additional X-ray based technique for the characterization of defects in materials is X-ray refraction [165,330,331]. These are radiographic and tomographic techniques that combine a large field of view (of the order of several mm) with an exceptional detectability of small defects. While the spatial resolution is limited by the beam size in the laboratory (typically

50×1000 μm), and by the camera pixel size at a synchrotron (typically 1-5 μm), they are able to detect objects around 1 nm [166,332]. Moreover, by means of X-ray refraction techniques it is possible to detect the orientation dependence of the features investigated (in the AM case pores, but in general all “defects” such as grain boundaries, cracks, inclusions, etc.) [333]. X-ray refraction techniques have already been successfully used to distinguish pore shapes in L-PBF Ti-6Al-4V [164].

Finally, in-process NDT shall be mentioned as this type of process monitoring plays an increasing role in quality assurance for AM (e.g., [169,184,325,327,334–338,423]. Its aim is the detection of defects already during the production process, in order to immediately allow for corrective actions. In particular, infrared thermography and optical tomography were proven to be useful to identify ‘hot spots’ (i.e. possible defects and stress concentrators), as reported by Mohr et al. [327]. It is, however, still unclear whether such defects also appear in the final part. Another purpose of NDT is to monitor parameters such as layer-to-layer height or surface roughness. This can be done visually, by laser profilometer, or by other methods such as laser ultrasound, the signals of which are correlated with the target information. Acoustic emission or laser thermography can also provide information on crack initiation during the process.

8. Strategies for AM component assessment

8.1 Defect tolerant assessment by fatigue design approaches

Fatigue design concepts have been established and introduced to rules, regulations and standards even in the presence of defects. Independent of the choice of the design concept, fatigue failure with respect to defects is related to the notch effect (internal and/or external notches). For instance, in the case of the assessment of welds, these concepts are categorized into global and local approaches, stress-based (linear-elastic) approaches, strain-based (elasto-plastic) approaches, and fracture mechanics approaches [339,340]. This is summarized in Fig. 43.

(a) Nominal stress concept—Within the nominal stress approach, every type of defect needs to be considered separately. In most cases, the characteristics (dimensions etc.) of the defects are linked to the fatigue strength, e.g. by classification of the surface roughness, geometrical notches or internal imperfections. As an example, the notch effect of the additively manufactured aluminum alloy AlSi10Mg for small-scale flat specimens in net shape (as-built) and built in z-direction is discussed by Scurria et al. [341] and Möller et al. [342].

(b) Structural stress (or strain) concepts—Different options of structural stress and strain concepts exist, which estimate the fatigue life for hot spots, such as geometrical notches, where the cracks are initiated [340]. Originally, structural stress and strain concepts are based on strain measurements at a certain distance from the critical spots. Note, however, that the local fatigue character of AM components with defect is neither directly covered by the use of the nominal stress (or strain) concepts nor by the structural stress (or strain) concept.

(c) Local concepts—Local concepts consider the local shape of a notch. Notch support effects and the stress-strain response of the material can be included. The local notch stress concepts evaluate fictitious local stresses by linear-elastic (numerical) simulation. This information is then related to fatigue resistance S-N curves that depend on the choice of the notch radius in the finite element model as the representative of a potential defect and the material properties. These properties include the modulus of elasticity and the Poisson's ratio. These are then used in combination with an appropriate stress hypothesis and survival probability.

The direct transfer of the notch stress approach to AM components requires the modelling of fatigue relevant defects as described in Section 4, such as porosity or surface roughness. Locally distributed porosity and surface roughness of AM components or specimens need to be modelled by finite elements methods such as shown in Fig. 44. For models that include roughness see also Section 8.2.2.2.

The stress-fields resulting from linear-elastic simulations display stress concentrations at notches, such as those associated with pores and peaks in surface roughness. In Fig. 44a, an "ideal" specimen without imperfections is compared to a specimen with modelled spherical pores near the surface (Fig. 44b) and a specimen without imperfections, but with a surface layer with reduced modulus of elasticity (Fig. 44c). The rationale behind the last option is that the stiffness of a specimen with porosity can be approximated by a layer of continuous material with reduced modulus of elasticity compared to the "ideal" specimen. Since critical defects are not easy to determine due to variations in their position, size and distribution, this is an important simplification. Even though porosity can be modelled in order to detect critical locations, the computational effort increases drastically when considering a detailed representation of an entire component or system. Here, the technique of Representative Volume Elements or Representative Structure Elements can be used, see [344].

Representative Volume Elements can be of different complexity [344,345]. An example for PBF-LB AlSi10Mg is given in Fig. 45. It includes both core and contour material due to different parameter sets used during manufacturing.

In contrast to the notch stress concept, the notch strain concept, considers the elastic-plastic deformation behavior at the critical location with the notch geometry [346]. This approach also allows for the application to low cycle fatigue. An example for an application of the notch strain approach to a real AM component is presented in [347] and [348].

As with conventional materials, very high cycle fatigue (VHCF; more than 10^7 to 10^8 loading cycles) can play a role in AM applications. Experimental studies on this are reported for various materials such as Ti-6Al-4V, AlSi10Mg, AlSi7Mg, Inconel 718 and 316L stainless steel [151,382,388,389,425,426]. The essential characteristic of AM materials does not differ from what is otherwise known. VHCF is usually associated with a shift from surface to internal crack initiation. The fatigue crack initiates at defects and the first crack propagation stage is characterized by a fine granular area surrounding this defect ("fish-eye"). Depending on the material, the endurance limit, if it exists at all, is lowered compared to the classical limit under high cycle conditions (up to 10^6 to 10^7 loading cycles).

8.2 Numerical approaches

8.2.1 Application range of numerical tools in AM—Numerical simulation tools can be applied to many aspects of AM, including for lightweight design, topology optimization or lattice structure design. The constraints related to AM technologies such as overhang angles, minimum wall thicknesses or minimum feature sizes need to be included in the analysis. For more information on these considerations see Han et al. [349] and Wang et al. [115]. There are many physical phenomena occurring in AM which act over multiple length and time scales. Numerical simulations can model and understand these physical phenomena at the different scales [350]. For instance, the macroscale residual stresses induced in the AM process can be numerically predicted through thermo-mechanical finite element modelling applying the inherent strain method [351]. The physical phenomena occurring in the melt pool, such as rapid melting and re-solidification, melt pool dynamics and diffusive conduction among others, can be described by powder bed simulations using various models. These models include the Lattice Boltzmann method [352] or the discrete element method [353] etc. Based on the temperature gradient and the solidification velocity, the evolution of the microstructure in the AM process can be simulated by a phase field model [354], a Monte Carlo method [355].

In a multiscale framework, crystal plasticity finite element modeling and homogenization schemes can be used to create the link between the macroscale mechanical performance and microstructural features [180,356].

8.2.2 Numerical simulation of fatigue life

8.2.2.1 Empirical models: The most common methods for numerical fatigue life prediction are empirical models based on the data of a large number of experimental tests. They can generally be subdivided into three categories: (a) stress-life methods, (b) strain-life methods and (c) energy-based methods [357,358].

- **a.** In the stress-life method, the S-N curve is used to describe the fatigue life. It is generally used for high cycle fatigue (HCF) where the material response is mostly elastic. The prediction accuracy strongly depends on the evaluation of the nominal stress range and the stress concentrations at the structural details [359].
- **b.** In the strain-life method, the fatigue life is depicted by the relation between the strain amplitude and the number of the cycles to failure. This is applicable for a wide range of problems including low-cycle and high-cycle fatigue with the localized plastic strain and large stress concentration at critical locations, e.g. a notch and voids, which dominantly control the fatigue life [358,359].
- **c.** The energy-based models combine the effect of stress and strain on the energy. They are frequently used for materials with nonlinear deformation behavior in the low-cycle fatigue regime under proportional and non-proportional loading. In addition, energy-based damage models are capable of including mean stress and multiaxial loading [357].

These “safe-life” models are always coupled with rules of linear cumulative damage based on an assumption of a continuous damage evolution during each cycle. Because of its

intrinsic simplicity, the so-called Palmgren-Miner linear damage rule is widely applied, but it shows a main deficit in that it does not consider load sequence effects which significantly affect the accuracy of the prediction in some cases (see, e.g. [360]. In order to improve the prediction accuracy, corrected damage models and semi-empirical models were developed, for details see [357,358].

8.2.2.2 A local stress-strain method: Defects, pores and surface roughness all act as stress raisers, which greatly influence the fatigue life of the metallic samples.

In [202], the effect of the surface roughness of Ti-6Al-4V parts fabricated by L-PBF on high cycle fatigue was investigated through numerical simulations, see also Section 4.2.3. Three sets of specimens were tested in tension-compression: hot-rolled (reference), L-PBF HIP machined and L-PBF HIP as-built. For each set, the surface topology of the samples was obtained by 3D optical profilometer and 3D X-ray tomography respectively. These data then were transferred to finite element meshes (Fig. 46) and used for strength prediction based on statistics of a nonlocal fatigue indicator parameter.

Vayssette et al. [202] concluded that the surface roughness measurements from computed tomography (CT) worked better than those of profilometry for predicting the fatigue behavior of the sample with micro-notches and small pores on the surface. It was found that the numerical simulations were in good agreement with the experimental data. Moreover, it could be seen that the reduction of surface roughness can improve the HCF life.

An application of finite element-based modelling of the surface roughness within the frame of the notch stress concept is provided in Fig. 47. In particular the influence of the finite element mesh size on the local stresses is studied.

8.2.2.3 Continuum damage mechanics: Continuum damage mechanics provides in-depth insights into fatigue problems by describing the process of fatigue crack initiation and development. The fatigue life is predicted by cycle by cycle computing of a cumulative damage parameter, which is based on the theory of continuum mechanics and irreversible thermodynamics. Chaboche and Lesne [361] were the first who applied damage mechanics to fatigue life prediction. By combining measured changes in the tensile load-carrying capacity with the effective stress concept, they developed a nonlinear damage evolution approach. Based on this pioneering work, the models have been advanced in the following decades, see [358,359] for detailed information.

Wan et al. [362] developed a multi-scale model for describing the fatigue performance of AM Ti6Al4V structures, which incorporated the effects of building orientation and gas porosity. Their numerical results showed good agreement with experimental data. One conclusion was that the building direction greatly affected the fatigue performance of the additively manufactured samples. In addition, it was shown that the fatigue life of AM materials increased quickly for a porosity density smaller than 1%. However, the transferability problem in multiscale modeling needs improved understanding and consistency. In the work of Pei et al. [363], a plastic strain energy based low cycle fatigue damage model was developed for the mechanical and fatigue performance of L-PBF Inconel

718 under both monotonic and cyclic loading conditions. The results were compared with those for forged Inconel 718 alloy. The microstructural characteristics included in the analysis were pore defects and precipitate particles. The differences in the mechanical properties and fatigue performance between L-PBF and forged samples were discussed. It was found that by adding the microstructural characteristics to the modeling process, the results showed better agreement with experiments [363].

Zhan et al. [364] developed a fatigue damage model for the fatigue life of three commonly used AM alloys (SS316L, Ti-6Al-4V and AlSi10Mg) with consideration of AM defects. In this model, the hatch-spacing and the powder layer thickness were integrated in terms of the volumetric energy density in order to ensure the dimensionless consistency, but also to physically reflect the relationship between the fatigue behavior and the AM process parameters. A larger number of parameters, such as the volumetric energy density, the maximum stresses and the stress ratio R, were investigated. The numerical results showed good agreement with experimental data from the literature.

8.2.2.4 Probabilistic fatigue life prediction: Physical phenomena associated with additive manufacturing processes are complex and they include a number of sources for uncertainty at each step of the AM process, which affect the mechanical properties as well as their reproducibility [365]. As mentioned in Section 4, the process-induced defects cause large scatter bands in fatigue properties. Conventional design methods are deterministic, they are not able to cope with uncertainties in design, or they circumvent these restrictions by incorporating safety factors. In contrast, the probabilistic design approach allows for risk assessment to be incorporated in the design process. This can be crucial for a fatigue life prediction already at the design stage [366].

Based on a weakest-link theory which makes use of the Weibull probability density of defects (such as porosity and surface roughness), Siddique et al. [367], developed a procedure for the fatigue life of L-PBF manufactured AlSi12. In this context they used various destructive and non-destructive techniques for characterizing the amount, size and location of the defects under consideration. A comparison of the statistical effect of different defect types on the predicted fatigue life was provided.

8.3 Small scale testing

The determination of mechanical properties with sub-sized specimens is a topic of significant interest, particularly for AM, since there is often only a limited volume of material available for testing. This limitation can necessitate the need to extract test specimens from fine and intricate structures or slow building rates to produce monolithic material for full scale testing. In addition, miniaturized test specimens are more cost effective. While no official test standards exist currently, considerable work has been published on miniaturized specimen testing [368–372]. As a result, guidance on scale testing is already available, however standardization efforts are still currently a work in progress.

In the context of component assessment, the most important properties refer to tensile, fatigue, fracture and creep. First tier mechanical assessment typically begins with uniaxial tension testing, as the tensile data can be used to plan for subsequent fracture toughness

and fatigue tests. It is generally accepted that for the material behaviour representative of the bulk, the specimens must be large enough to include at least 10 grain sizes over the thickness [373–376]. This criterion is often fulfilled for AM parts with powders grain sizes of the order of 50 μm, used for producing 0.5 mm thick specimens. Of course, this requires that post-processing does not lead to larger grain growth for the relevancy of the test. The test specimen geometries and procedures, which are presently in use in literature, have been shown to provide reproducible results with respect to the properties of the AM materials. For instance, the application of miniature specimens to tensile and fatigue test has been successfully demonstrated by Dzugan et al. [377]. The miniature specimens have been machined from AM bars by turning and electro discharge machining (EDM). The specimen surfaces are treated by a combined procedure of grinding and polishing in order to remove a thin surface layer affected by thermal erosion and a recast layer with micro-cracks at the machined surface [378]. Preliminary LCF and HCF investigations showed that the miniature specimens could be used for testing at room temperature as well as at elevated temperatures [75]. The specimen geometries applied for small-scale fatigue and tensile testing are shown in Fig. 48. They were designed to satisfy, as good as possible, the recommendations of the ASTM E606 standard [379].

The micro-tensile testing procedure for the M-TT specimens is derived from ISO 6892-1 [380] and satisfies the demand to obtain reliable material characteristics with a minimum use of material. The strain can be measured using the digital image correlation system Aramis with a random speckle pattern applied to the specimen surface. This allows for a high measurement accuracy with gauge areas from some square millimeters to square meters depending on the optical camera system. The miniaturized specimen geometries for HCF and LCF tests are also derived from standard specimen geometries. An example for an S-N and an ε-N curve obtained by sub-sized specimens is shown in Fig. 49. The material tested was Inconel 718 deposited by Laser Powder Bed Fusion (L-PBF).

8.4 Fracture mechanics-based defect tolerant assessment

8.4.1 Requirements—Because of the major role that material defects play in the fatigue behaviour of AM processed components, fatigue design must be defect tolerant. There might be cases where the materials have been homogenized thoroughly by a very elaborate post-fabrication process, but these will probably be exceptions. In the majority of the cases, the analyses have to account for the presence of defects as well as for the inhomogeneity of the microstructure and material properties across the components. The consequence is a number of requirements which will be addressed in the following sections:

- **a.** The aim of a defect tolerant assessment is the determination of the load carrying capacity of the AM components in the presence of defects. This requires the application of fracture mechanics. Approaches which have been applied to AM comprise (i) the Kitagawa-Takahashi diagram; (ii) Murakami's $\sqrt{\text{area}}$ approach, (iii) cyclic R-curve analysis and (iv) Newman's modified strip yield model. An introduction will be provided in Sections 8.4.2 to 8.4.5.
- **b.** Due to the inhomogeneity of the microstructure and material properties across the component, the assessment needs to concentrate on specific hot spots. This

is usual practice in the design process. In AM, the assessment is complicated further by the large number of influencing factors that finally determine which locations in a component are potential crack initiation sites. This topic will be addressed in Section 8.5.

c. Due to the high process sensitivity in AM, a pronounced anisotropy of the mechanical properties must be considered. This brings up what is called the "similitude" problem. It is essential for component assessment that the properties determined on material specimens can be transferred to the component This is exactly the challenge in AM application. What matters, is that the information obtained by the specimens is relevant with respect to the areas and volumes in the structure on which the assessment is based (point b). A brief discussion on this is provided in Sections 8.6.

d. Fracture mechanics-based defect tolerant assessment requires the knowledge of a representative defect size. While the methods discussed in Sections 8.4.2 to 8.4.5 specify the relation between the defect size and the sustainable load of the component as a general function, specific defect sizes are required for the evaluation of a specific structure. How such values can be obtained is the topic of Section 8.7.

e. Finally, Section 8.8 will briefly address the residual stress problem as by now the most obscure problem in the structural assessment of AM components.

8.4.2 The Kitagawa-Takahashi diagram—The Kitagawa-Takahashi (KT) diagram [381] is a double-logarithmic plot of the fatigue limit (in general terms designated as $\Delta\sigma_{th}$ with "th" standing for "threshold") versus crack depth a (Fig. 50). The diagram can be split into three regions, separated by crack depths d_1 and d_2, which correspond to the stages of crack propagation discussed in section 2.3.1. Region I refers to micro-crack propagation, Region II to mechanically/physically short crack propagation and Region III to long crack propagation. Note that the curve is dependent on the stress ratio ($R = \sigma_{min}/\sigma_{max}$) of cyclic loading.

Note that the KT diagram provides a limit line not for crack initiation but for crack arrest, and that d_1 is what is designated as "critical defects size" in other contexts [47–49], i.e., it is the defect size below which no harmful effect on the fatigue limit is expected anymore; see Section 2.2.3. Note again that this depends on the strength of the material such that the critical defect size becomes smaller with increasing strength.

A KT diagram can be obtained by empirical investigation on sets of specimens with well-defined initial defects, i.e., artificially introduced, narrow notches. Note, however, that this technique might be problematic when the notch effect is not adequately considered in the determination of the threshold stress.

The KT diagram, as a first approximation, can also be constructed, when the fatigue limit of the defect free material $\Delta\sigma_{th}$ and the long crack threshold $\Delta K_{th,LC}$ are known. This is illustrated in Fig. 51 in case of a through crack in an infinite plate in tension, where Region I is given by

$$\Delta\sigma_{th} = \Delta\sigma_e \tag{10}$$

with $\Delta\sigma_e$ being the plain fatigue limit of the material obtained by testing smooth specimens. The right side of the diagram is characterized by long crack fracture mechanics as

$$\Delta\sigma_{th} = \Delta K_{th,LC}/\sqrt{\pi a} \tag{11}$$

with $\Delta K_{th,LC}$ being the long fatigue crack propagation threshold. Both equations form straight lines in double-logarithmic scaling. They intersect at a crack depth a_0 which can easily be determined by

$$a_0 = \frac{1}{\pi}\left(\frac{\Delta K_{th,LC}}{\Delta\sigma_e}\right)^2 \tag{12}$$

or, if one considers geometries deviating from the infinite plate in tension with a through crack, by

$$a_0 = \frac{1}{\pi}\left(\frac{\Delta K_{th,LC}}{Y \cdot \Delta\sigma_e}\right)^2 \tag{13}$$

with Y being the boundary correction factor which, e.g. for semi-circular surface cracks in tension loaded plates, is Y = 0.728 [427].

An efficient way to account for real geometries is to include the shape factor Y in the physical crack size “a”, [213,383].

$$\Delta\sigma_{th} = \frac{\Delta K_{th,\,LC}}{\sqrt{Y^2 a + a_0}} \tag{14}$$

where Y^2a can be considered as an equivalent crack size calculated by using the stress intensity factor equality:

$$Y^2 a = \frac{1}{\pi}\left(\frac{K_I}{\sigma}\right)^2 \tag{15}$$

and a_0 is kept as a material parameter, according to Eqn. (12).

Note that the value a_0, although nowadays even available from compendia for various materials (e.g., [383]) might be a problematic parameter as it makes use of the long fatigue crack propagation threshold $\Delta K_{th,LC}$. For lower R, the latter can depend on the method applied for its determination. This is the case when the oxide-debris-induced crack closure mechanism comes into play. An example of different threshold values obtained by different techniques is provided in Fig. 52. For a detailed discussion of this issue see Zerbst et al. [45]. In cases where the AM material is more prone to corrosion than the conventional material this effect can be expected to be exacerbated.

While Regions I and III of the KT diagram, in principle, can be adequately described by Eqs. (10) and (11), things are more complicated with respect to Region II which refers to the stage of the mechanically/physically short crack propagation (Section 2.3.1). Four methods have been applied to this:

(a) Region II of the KT diagram: Empirical determination based on tests with artificial notches: Although this is potentially the best method, it can be problematic when the cracks at arrest are still affected by the stress-strain fields of the notches and when these are not adequately considered in stress determination. Actually, this problem occurs in Region II of the KT diagram, and one can speculate that it could frequently have happened in older data sets. Since the artificial notches are used as substitutes for cracks they are prepared as narrow as possible. However due to the steep stress gradient, there is a tendency for "self-arrest" of the cracks initiating from the notch roots (see Section 2.3.1.c). The consequence is that the arrested cracks will not be deep enough from the notch root, and therefore be influenced by the notches.

(b) Region II of the KT diagram: Empirical determination based on El Haddad's approach: An empirical description of Region II is provided by El Haddad et al. [421] who base it on a fictitious crack depth $a + a_0$:

$$\Delta\sigma_{th} = \Delta K_{th,LC}/\sqrt{\pi(a+a_0)}\,. \tag{16}$$

with a_0 being obtained by Eqs. (12) or (23), see Fig. 51.

The KT diagram is finally given by

$$\Delta\sigma_{th} = \Delta\sigma_e \cdot \left[\frac{a_0}{a+a_0}\right]^{1/2}. \tag{17}$$

Complementarity, the fatigue crack propagation threshold ΔK_{th} is obtained as

$$\Delta K_{th} = \Delta K_{th,LC} \cdot \left[\frac{a}{a+a_0}\right]^{1/2} \tag{18}$$

(c) Region II of the KT diagram: Theoretical determination based on cyclic R curve analyses: Using the cyclic R curve analysis, the KT diagram is obtained by crack arrest considerations. This will be introduced in more detail in Section 8.4.4. Fig. 53 gives a schematic comparison with the methods discussed above. It has been confirmed by a number of authors [382,385–387] that the R curve method provides lower fatigue strengths in Region II. Akinawa et al. [385] have experimentally shown that the R curve analysis provided results which are more correct for the example they had investigated.

(d) *Region II of the KT diagram: Semi-empirical determination based on Murakami's $\sqrt{\text{area}}$ approach*: As in the case of the cyclic R-curve analysis this will be separately

discussed in Section 8.4.3. Different from the other approaches this method is restricted to the Region II of the KT diagram, i.e., of crack size range $d_1 < a < d_2$.

KT diagrams based on literature data have been provided for AM manufactured AlSi10Mg and Ti6Al4V by Beretta and Romano [390], see also [161], Fig. 54. These have been obtained by Eqn. (16) with reported data of $\Delta\sigma_e$ and $\Delta K_{th,LC}$. The crack size a_0 was based on Eqn. (13) with the geometry function being Y = 0.65 for surface crack initiation and Y = 0.5 for internal crack initiation. At the abscissa, the crack depth was replaced by the square root of the crack area, $\sqrt{\text{area}}$, in accordance with Murakami's approach introduced in Section 8.4.3. A similar philosophy was followed by Ngnekou et al. [391]. KT diagrams have also been applied to AM in [26,117,139,392,154].

In the approach of Beretta and Romano [390], see also [161], the general scheme is shown in Fig. 55, the KT diagram is not derived theoretically such as in the cyclic R-curve analysis (Section 8.4.4). Instead it needs to be known a priori or to be empirically determined, such as in Fig. 54.

8.4.3 Murakami's $\sqrt{\text{area}}$ approach—Murakami has shown that the maximum K factor along the front of small surface cracks, independent of the individual shapes of these cracks, can roughly be correlated with the square root of their projected areas, $\sqrt{\text{area}}$, perpendicular to the loading axle with an accuracy within 10%.

$$K_{I,max} \approx 0.65 \cdot \sigma \cdot \sqrt{\pi\sqrt{\text{area}}}\,. \tag{19}$$

Furthermore, he has obtained a general correlation for the fatigue crack propagation threshold ΔK_{th}:

$$\Delta K_{th} \propto \left(\sqrt{\text{area}}\right)^{1/3} \tag{20}$$

Note that the term $\sqrt{\text{area}}$ is not only used for cracks, but for defects in general, e.g., also for inclusions (which might detach from the matrix material already during manufacturing or at an early stage of the lifetime), see also [48]. Eqn. (20) was shown to be valid for 20 μm < $\sqrt{area}$ < 1 mm.

As with the fatigue limit (Eqn. 4 in Section 2.3.2), also ΔK_{th} can be empirically correlated with the Vickers hardness HV

$$\Delta K_{th} \propto (HV + 120)\,. \tag{21}$$

Combining the above equations, Murakami finally obtained an expression

$$\Delta K_{th} = 3.3 \cdot 10^{-3} \cdot (HV + 120) \cdot \left(\sqrt{\text{area}}\right)^{1/3} \cdot \left(\frac{1-R}{2}\right)^{\alpha} \tag{22}$$

with $\alpha = 0.226 + HV \cdot 10^{-4}$. The error band around Eqn. (22) is given as ± 20%.

Substituting K_{max} by ΔK_{th} and σ by the R ratio dependent fatigue limit $\Delta\sigma_{th}$ in Eqn. (22) a KT diagram type expression is obtained:

$$\Delta\sigma_{th} = 2.86 \cdot (HV + 120) \cdot \left(\sqrt{area}\right)^{-\frac{1}{6}} \cdot \left(\frac{1-R}{2}\right)^{\alpha} \quad (23)$$

for surface defects. For embedded defects the factor 2.86 must be replaced by 3.12. Note that the validity of Eqn. (23) is limited to the range between the maximum lengths of non-propagating cracks d_1 and the short-long crack transition d_2, i.e. Region II in the KT diagram. Any application beyond these limits would yield incorrect results [38].

There is also a trend to use the $\sqrt{\text{area}}$ parameter in the KT diagram replacing the crack depth a at the abscissa as in Fig. 54 (e.g., [390,393], Murakami's $\sqrt{\text{area}}$ parameter is applied to AM in [69,150,154,160,238,288,298,391,394–396].

8.4.4 The cyclic R curve approach—The cyclic R curve has been introduced in Section 2.2.2. It is a complementary approach to the KT diagram, as schematically illustrated in Fig. 56. An option for the experimental determination of the cyclic R-curve is provided in Fig. 57, for a detailed discussion see [397]. To ensure the absence of any initial crack closure effect, the fatigue pre-crack is introduced in compression pre-cracking, i.e., the upper and the lower stress level in the cycle are below zero, cf. also Figs. 35 and 36 in Section 5.2. Then, the cyclic stress level is stepwise increased at a constant R. As soon as ΔK becomes larger than $\Delta K_{th,eff}$, the crack will start to grow but will eventually stop due to the gradual build-up of the crack closure phenomenon. After the crack has been arrested, the load level is increased and the crack can grow again. When ΔK has reached a value above the long fatigue crack propagation threshold $\Delta K_{th.LC}$, no crack arrest can occur any longer. Finally, the cyclic R curve is plotted though the crack arrest points. In addition, an information on the intrinsic and the long crack thresholds is provided by the test.

In the frame of a cyclic R curve analysis, the cyclic R-curve can be used to determine crack arrest load levels (i.e., fatigue limits) for plain surfaces as well as for notched geometries. This is schematically illustrated in Fig. 58. The transition from arrest to propagation is given by the crack driving force curve (for load $\Delta\sigma_2$ in the example) that is tangential to the cyclic R-curve and the corresponding arrest crack depth $a_{arret.}$ Note that the initial crack depth a_i is smaller because the crack still will have to grow for a certain amount until it is arrested. As is highlighted in Fig. 58, the length of the non-propagating crack is not a material property, but it depends of the shape of the applied load curve ($\Delta\sigma_2$ in the example), that in turn depends on the notch geometry, see also the remarks on crack arrest in notches in Section 2.3.1 (c). Note further that the crack depth, both in terms of a_i and a_{arrest}, as it is discussed here, starts from the tip of the pre-existing notch or crack/defect and does not include this.

Since both the KT diagram and the cyclic R curve analysis describe crack arrest, the cyclic R curve, in principle, can be used to determine KT diagrams, see Fig. 53 in Section 8.4.2. The modified a_0 value a_0' according to Tanaka and Nakai [398] is based on the intrinsic fatigue propagation threshold $\Delta K_{th,eff}$ (Section 2.2.2; Eqn. 3) and determined by

$$a_0' = \frac{1}{\pi}\left(\frac{\Delta K_{th,eff}}{Y \cdot \Delta\sigma_e}\right)^2; \quad (24)$$

cf. also [399].

The principle of the cyclic R-curve analysis was first introduced by Tanaka and Akinawa [401], with more recent examples are found in [402–405], see also Madia et al. [58] and Zerbst et al. [60]. The approaches differ in their approximation of the cyclic R-curve and in the specification of the initial crack size a_i (cf. [399]) but they all follow the scheme described above. Madia et al. [58], see also Zerbst et al. [60], applied the method to different weld geometries; they determined both the finite life S-N curve and the fatigue limits for two different steels. Like Murakami's $\sqrt{area}$ approach, the cyclic R curve method can be applied both independently or in the framework of a KT analysis.

Note that the application of the cyclic R curve concept to the determination of the KT diagram has a great potential. Not only can the diagram be determined for any component geometry, but it can also consider features such as multiple crack propagation. There is ongoing work on the development of a concept for the assessment of AM components based on the cyclic R-curve method.

8.4.5 Modified strip yield model—The application of the FASTRAN computer code to the assessment of an AM structure is reported by Yadollahi et al. [406]. In the following, the basic principle will be briefly explained. FASTRAN uses the modified strip yield model in the version developed by Newman [407]. It is illustrated in Fig. 59. The model considers a plate subjected to remote tension. Three regions need to be distinguished in the vicinity of the crack, in the figure designated by (1), (2) and (3). Region (1) is an elastic continuum, Region (2) a strip ahead of the crack tip which consists of bar elements of perfect plastic material modelling the plastic zone. Region (3), in the wake of the crack, also contains bars, but these are split because of which they can only transfer compressive but not tensile stresses.

What is essential, is that the strip yield model is able to predict the gradual build-up of the plasticity-induced crack closure mechanism. When the crack propagates, the bars in Region 2 closest to the crack tip are cut and they get shifted into Region 3 (the crack wake) where they stay stretched, thereby increasing the crack opening load. Similar to the other models discussed in Section 8.4, the approach provides a fatigue crack growth analysis starting from a pre-existing crack (or defect) and includes the short as well as the long crack propagation stages. Note that the NASGRO equations have been derived as an approximation of results obtained by the modified strip yield model.

8.5 Identification of potentially critical sites in a component

The component assessment based on critical sections or zones in an AM structure has been introduced by Gorelik [25] who calls this a "zone-based approach". Yadollahi and Shamsaei [20] use the term "critical location". In a complex geometry, this is the site from which the failure of the structure is expected, see also Meneghin et al. [408]. In an AM structure it

is not just the location of the highest local stresses and strains under isotropic conditions which determines the failure site, but this also might be affected by features such as the build-orientation with respect to the local loading direction (i.e., the direction of the highest principal stress, see Section 3.4.1, Fig. 18), material anisotropy, inhomogeneous roughness, defect spatial distributions or a combination of several of those factors.

Consequently, some classification of the potential critical sites is needed so that separate analyses are performed for these classes. Following Gorelik [25] each prospective zone should be characterized as far as possible by

- uniform material properties (microstructure, material parameters, defect distribution);
- distinct geometrical features (e.g. thin wall);
- a similar residual stress state;
- a similar feasibility with respect to NDT, and
- the same post-fabrication treatment.

With respect to the applied loading, two aspects shall be added here:

a. First, it is not just the stress concentration at the surface but also the stress profile through the thickness that defines the criticality of potential crack initiation sites. In common fatigue analysis this is considered by a support factor. Alternatively, a fracture mechanics analysis, based on the linear elastic stress intensity factor can be performed using the stress profile along the wall thickness direction. The criticality of the site is then evaluated by the values of the respective K factors.

b. Another factor that will affect the criticality of a site is what could be designated as local stiffness. In the case of a crack this is usually called constraint. A parameter for characterizing this is the stress triaxiality usually given as the ratio of the hydrostatic to the equivalent (e.g. von Mises) stress.

It is clear, that the information required will rarely be completely available. Of particular importance is the build orientation. The demand of Leutenecker-Twelsiek et al. [116] to consider this aspect before the final design of the component has already been mentioned. In principle, this requirement can be extended to the other aspects listed above.

In practice, classification of potentially critical sites in AM applications will rather be based on qualitative than strictly quantitative criteria. As far as the authors are aware, concrete guidance on this aspect still needs to be provided. Some basic ideas could be transferred from other applications. As an example, a guideline for hazardous goods containers subjected to impact loading [409], using a rather coarse FEM mesh, first identifies all sites where the local stress exceeds half the yield strength. These sites are then compared and classified using criteria such as the local stiffness and the stress profiles in wall thickness direction. In AM, further criteria need to be added to these considerations, such as those outlined above. As the result, the one or two most critical cases in each class are identified for which the final assessment is carried out.

8.6 Representative material properties

The material properties needed in component assessment have been briefly introduced in Section 2.2.2. In the following sections, the similitude problem, i.e., the determination of component- (or section-) representative material parameters turns out to be of paramount importance for AM. As a consequence of the high sensitivity to the large number of process parameters, such as the build orientation, the local geometry, the scanning strategy, the pre-heat temperature of the build platform or the inter-layer time interval, which all contribute to the thermal history (see Section 3); the material properties tend to be different from site to site in the component. In order to avoid non-representative information, an in-depth understanding of the correlation between process, structure and material properties is required. This is the case even if test coupons are taken from the component itself or an attached section, because it cannot simply be assumed that these have experienced the same thermal history as the potentially critical location in the structure.

Similar observations have been made for other component types such as welds or castings. For example, in a fusion weld, the material properties of the base metal, the weld metal and the heat affected zone (HAZ) will be significantly different due to the different local thermal history, see., e.g., [410]. An example is provided by Kucharczyk et al. [411]. A possible option to deal with this problem is the reproduction of the local microstructure in appropriate purpose-generated witness coupons. Of primary importance is the reproduction of the cooling curve which the HAZ or other sections have experienced. In welding, this is usually expressed as the $t_{8/5}$ time which is the time the weld needs to cool down from 800°C to 500°C. As long as the thermal history is appropriately simulated, other parameters such as the specimen dimensions do not play a role. This simplifies the determination of fracture mechanics parameters which requires a minimum specimen size. For HAZ material, the thermal simulation is achieved by using a combination of measured data and numerical simulation. The information required comprises the temperature field in the weld during manufacturing, which is usually determined at the surface, the component geometry, information on the welding process (single or multiple layers, etc.) and the time-temperature-transition diagram (TTT) of the material. Afterwards the result had to be evaluated based on the distribution of microstructural features and the hardness [411].

A similar approach is needed for AM which will be more challenging than that for a fusion weld because of the larger number of relevant process parameters and more complex geometries. Consequently, Komi and Kokkonen [394] identify the numerical simulation of the L-PBF process including post-fabrication as a key issue in their concept of defect tolerant design of AM components. A degree of simplification will be required by concentrating on the main parameters.

A numerical simulation of the build-up of a L-PBF complete component is challenging, since the melt pool size is ~10^{-4} m, while typical components are in the order of 10^{-2} m to 10^{-1} m. A fine mesh, which is needed for describing the fast moving and localized heat input by the laser beam, would result in an unmanageable number of elements for the whole component. Therefore, different approaches for simplification of the models and reduction of numbers of elements have been introduced by several authors. Khan et al. [412] used a dynamic remeshing method for thermal calculations in order to limit the overall number

of elements: In the heat input zone and within a defined surrounding volume, a fine mesh is used while at greater distances the mesh is dynamically coarsened. They were able to simulate multiple tracks adjacent to each other and also a few subsequent layers. These results were in good agreement to measured temperatures.

Other authors have used a multi-scale approach: A simplified build-up model with a comparably coarse mesh is set up to describe a whole part, while subsequent layers are described as layer compounds. The heat input for this model is validated by data derived from a single layer model that uses a heat source, which itself was validated by a single laser track simulation. By using the results of the build-up model as thermal load for mechanical simulations, the calculation of residual stresses and distortions could be demonstrated [413]. An approach using an even more simplified build-up model was used by Illies et al. [414]. They activated layer by layer in a thermal calculation, neglecting any thermal gradients in the lateral directions. Due to the achieved reduction of number of elements, there were able to calculate the thermal history of a simple part. They state that by knowing the thermal field in a component, the laser process parameters can be adapted to the local requirements of certain geometrical features.

Knowing the temperature cycle of a certain region of a component, approaches to the transfer of this temperature cycle onto representative specimens must be developed. It can be assumed that not only the use of the same process parameters and local hatching strategies, but also the same inter-layer time is necessary to achieve a comparable heat input. The heat conduction and, therefore, the resulting cooling rates can be adjusted to a certain extent by adequate pre-heating temperatures as well as by additional geometrical features acting as heat sinks. Such an approach needs to be validated. Therefore, real temperature data from the build jobs of components and specimens are inevitably required. While in fusion welding processes, the measurement of temperatures alongside the weld track is possible by using thermocouples, the recording of temperatures is challenging in L-PBF processes. The component is stepwise buried isolating powder bed, which makes it impossible to attach thermocouples. The most promising approach for temperature measurements are thermographic cameras giving lateral information on the temperature distribution of the top build layer. The further development of accurate temperature measurement techniques is therefore an important prerequisite for developing representative specimens.

8.7 Critical defect size

In respect to defect tolerant component assessment, the defect size which is assumed to exist, a_i, can be introduced as statistic or deterministic information. The first option can be based on extreme value statistics or, if available, a defect exceedance curve, see Section 4.2.5. The deterministic approach uses a conservative upper bound as design parameter which can be obtained from statistical information. The following approaches have been used for AM applications:

a. Romano et al. [149] used the extreme value distribution of Fig. 32 (Section 4.2.5) in order to specify an upper bound defect size a_i according to the percentile value of P = 97.5%. This was then used as an artificial notch which they then realized as an artificial notch in conjunction with a Kitagawa-Takahashi diagram.

b. An approach frequently applied in the aerospace industry is the equivalent initial flaw size (EIFS) method. By this method, the initial defect size is determined by fracture mechanics-based back-calculation to a time or number of loading cycles of zero. Greitemeier et al. [415] obtained an initial crack size of ca. 250 μm and 490 μm for AM processed Ti6Al4V by this method. An application to L-PBF AlSi10Mg is published by Beretta et al. [154]. Note, that the EIFS a_i is a model parameter rather than a physical one due to potential shortcomings in the applied fracture mechanics model. This is usually the linear elastic da/dN-ΔK curve even for short cracks and it is also simplified with respect to other aspects such as crack closure.

c. A similar approach is the iterative successive approximation of a_i such that the calculation reproduces the experimental S-N curve. Yadollahi et al. [406] have applied this to AM processed Inconel 718 in conjunction with their modified strip yield model (Section 8.4.5). As a result, they have obtained a_i values of 8 μm and 20 μm for the non-defective state and 120 μm for the defective state.

d. In the aerospace industry a fixed value of $a_i = 1.27$ mm (0.05 inch) is used as an upper bound to the experimental EIFS data [16,408,416,].

Some additional notes shall finally be added to conclude this section:

i. Usually, the initial defects are considered as semicircular cracks.

ii. It has already been mentioned that it is not just the size but also characteristics such as the proximity to surface which determine whether a defect will act as a crack initiation site. A method for revealing the real “killer defects” is fractography. The fracture surfaces are analyzed postmortem to identify the crack initiation sites and to measure the sizes of the defects which caused initiation. There is a tendency that a_i values identified this way are larger than those identified by metallography [417,418]. Note, however, that this observation has been made for non-metallic inclusions and that it does not have to be the same for X-ray computed tomography (CT).

The advantage of the X-ray CT as a method to identify the “killer defect” is that it covers all defects above a certain size limit in the measured volume which needs to be rather small for measurement purposes (see Section 7.2). Therefore, it makes sense to compare X-ray CT and fractographic results. Such an investigation has been performed by Leuders et al [235], who showed a discrepancy between apparently dominant defects used for predictions and defects found at the surface, which cause the relevant fatigue damage. It was found that the location of a defect had a far greater influence than currently expected. Likewise, Persenot et al. [318] have shown for EB-PBF Ti-6Al-4V that high resolution laboratory X-ray CT (voxel size 2.5 μm) underestimated the size of surface killer defects and therefore its criticality.

iii. In Section 2.2.3, the so-called fracture mechanics triangle has been introduced in conjunction with the question of whether the initial defects should be treated as input parameters or as target information of a defect tolerant assessment. Both

are possible. If the size of a_i is known or conservatively specified, the maximum cyclic stress that the component can tolerate without failure can be determined. Alternatively, the fracture mechanics-based analysis (Section 8.4) can be used to specify a maximum allowable defect size for a given applied load. It is then the task of non-destructive testing to ensure with a high probability that defects of that size are detected in time.

iv. Finally, it must be pointed out again that surface roughness, when given as R_z or R_{max} values (Section 4.2.3) needs to be treated as a stress concentration or as an initial defect. Such as the other defect parameters, it can vary from site to site in the component. Greitemeier et al. [415] have also applied the EIFS principle to surface roughness. As a consequence of the general shortcomings of the EIFS approach (see above) and also due to the definition of the roughness (the authors have used R_t for characterizing this) it should not be expected to receive the same results as by surface measurement.

8.8 Residual stresses

Residual stresses are perhaps the weakest link in component assessment as it currently stands. The general principle how to deal with them in a fracture mechanics analysis is rather easy: their effect on the stress ratio R is taken into account (Section 5.3). The main problem is to gather the information on their magnitude and distribution across the section, since these depend on a number of geometrical and process parameters. An open question is also the potential relaxation of residual stresses under cyclic loading (Section 5.4). An example for the consideration of residual stresses in component assessment, although in a simplified way, is presented by Gumpinger et al. [139] for AM processed AlSi10Mg.

Recent results by Beretta et al. [154] for the fatigue strength of as-built surfaces manufactured in different orientations show that residual stresses play a role as equally important as surface defects detected at the fracture origin (Fig. 60). In fact, the S-N diagrams at R = 0.1 for the specimens printed in different orientations were very different (see Fig. 61). The reason for this difference were attributed to the defects detected at the crack origin for the different orientations as well as the residual stresses (series C: σ_r= 140 MPa; series D: σ_r= 72 MPa), that made the effective R ratio R_{eff} = 0.55 – 0.6 for series C and D. In case of series C, the sum $\sigma_r + \Delta\sigma_{appl}$ would have exceeded the yield strength of the material, so the estimation of stress relaxation based onto the limit of elastic shakedown was a conservative assumption.

The fact that real defects are not centered on the estimated KT diagram can be due to different reasons: (i) the simple estimation of stress relaxation together with scatter of residual stress measurements, (ii) the too simple description of the KT diagram with the El-Haddad model especially at different R ratios, (iii) the effect of “shielding” due to the roughness profile and surface texture that makes the effect of a sequence of surface depressions less detrimental (in terms of the K factor at the prospective cracks) than the effect of a single notch.

More often, residual stress fields are evaluated by FEM simulations (see several examples the last paragraph in Section 5.3), so that information concerning part integrity during and post-fabrication can be obtained. However, much work is still necessary to determine the material parameters (see Section 8.6 and Thiede et al, [185]) to input into models. Some metrological problems need still to be solved when dealing with the experimental determination of residual stresses in AM parts. In fact, currently available standards (e.g., ISO 21432 [419] and EN 15305 [420]) do not encompass AM materials and components. The further link between residual stresses and fatigue life is being addressed at present (Section 5.3), but still needs a global vision to be established.

9. Concluding remarks and recommendations

The present study provides an overview on backgrounds, problems and their possible solutions, as well as perspectives in the field of fatigue design of additively manufactured (AM) metallic materials and structures. The paper shows that AM materials behave as a new class of alloys and require tailored solutions to the classic materials science problems such as determination of lifetime, fracture and fatigue behavior, influence of the microstructure and of the defects on the performance (residual stress, mechanical properties).

AM metallic parts are needed in market segments such as aerospace, automotive, and medical because of the freedom of design and of the decreased time-to-market of additive technologies (such technologies allow for instance non-series production of tailored implants without enormous extra costs). In order to facilitate the penetration of additive technologies into the above-mentioned market segments, a thorough understanding of the mechanical performance of AM materials is needed. The unexpected behavior of “classic” materials, when manufactured via additive technologies, stems from their peculiar microstructure and defect distribution. In fact, due to their specific crystallographic texture, the amount, distribution, and type of defects, the surface roughness, classic metallic alloys (such as Ti6Al4V, 316L, IN718) become AM-alloys when processed by additive techniques.

We show that a lot of work has been and is being done in the fields of

- Definition of crack initiation and propagation criteria for AM materials. Here the classic tools seem to be suited to tackle the specific problems raised by this new class of materials. However, the specific morphological texture (surface roughness, pore and microcrack distribution and shape) of such materials lowers their performance, so that much research is dedicated to post-treatments to improve toughness and fatigue life;
- Definition of fatigue resistance criteria (in all fatigue regimes). Again, classic instruments such as the Kitagawa-Takahashi diagram show their usefulness to qualify AM alloys, and identify the effect of the “new” kinds of defects (lack-of-fusion, air bubbles, keyholes, unmolten powder) on the fatigue behavior, spanning the whole range from LCF to VHCF. In spite of this, new universal laws still need to be defined, which can characterize similar alloys (for instance Nickel based). Moreover, since a classification of defects and a quantification of the tolerable shapes and sizes is still missing, a new strategy must be

defined, whereby theoretical calculations (e.g. FEM) allow determining the maximum tolerable defect size, and non-destructive testing (NDT) techniques are required to detect whether such defects are indeed present in the component. Such examples show how component design, damage and failure criteria, and characterization (and/or NDT) become for AM parts fully interlinked.

- Quantification and classification of the defects. A great deal of 2D and 3D methods has been deployed to fully characterize the peculiar defects and surface texture of AM alloys. In particular 3D X-ray computed tomography has become a standard tool to assess the integrity of materials and parts, since more than the amount, the shape and the spatial distribution of defects have become decisive in the determination of the mechanical properties of AM alloys. Trivially, the tendency is now to monitor the defect formation *during* the process (e.g. through thermography, on-line experiments) and observe the influence of defects *during* operation (in-situ diffraction or imaging experiments).
- Determination of the residual stress (RS) and identification of stress-relief treatments. AM (especially laser powder bed fused, LPBF) metallic alloys always contain residual stress locked in the (sometimes unstable) microstructure. Therefore, RS has consistently become a “material parameter” to identify; alternatively, post-processing treatments must be applied to release such manufacturing-RS. Both the RS determination methods and the search for optimal heat treatments (HT) have proven to be major challenges, again due to the peculiar microstructure (especially crystallographic texture).

Undoubtedly, the lack of viable concepts in all the above-mentioned fields is a main challenge to the adaption and regular use of AM for safety-critical applications, or in other words to the market penetration of AM parts. The main issues which have been identified can be summarized as the following:

a. Aspects of safety-critical (or damage tolerance) design with fracture mechanics being at the center, but classic fatigue, damage mechanics and empirical testing using sub-sized specimens are briefly addressed. We have shown, for instance, that a systematic understanding of the anisotropy of the mechanical properties and damage behavior of AM metallic alloys is still underway, and the scale-up from small test specimens to full parts will still require a great deal of investigations. In particular, factors such as the position of the part on the build plate in LPBF jobs play a decisive role on the final performance of the material, so that care must be taken to ensure reproducibility and scalability of the experimental results.

b. The influence of the manufacturing technology on the material properties including their scatter and spatial distribution has been thoroughly discussed. We have seen that large differences may rise in materials properties when using electron beam melting (EBM) or LPBF (for instance EBM does not induce RS). As mentioned above, AM processed materials acquire a particular footprint depending on their processing technology, so that one should rather talk about LPBF-IN718, EBM-Ti64 etc. This imposes a larger burden on the

materials scientist, since the materials behaviour cannot be made universal in a straightforward manner: the classic triangle or materials science (process/ microstructure/ properties) becomes now much smaller and it is incredibly easy to influence one corner by touching the other. This paradigm shift also implies that simulations need to be run using materials properties specific to the processing technique, and general properties (tabulated for classically produced materials) cannot be used as input parameters.

c. Particular emphasis is placed on material defects, which are known to play a significant role for the damage tolerance behavior of AM parts. These include pores and un-melted regions, cracks and crack-like features, balling effects, keyholes and non-metallic inclusions, but also the surface roughness of the as-built components. While for welding technologies (the classic process closest to AM) defect classifications are even standardized and criteria for quantification of tolerable defect size and form already exist, the aspects of defect classification and above all of quantification of critical defects (in terms of form and size) are still in their infancy for AM. Novel and advanced characterization techniques, such as X-ray refraction radiography and Computed Tomography, are now becoming essential and even routinary, so that the classic microstructural characterization tools such as optical and scanning electron microscopy must be updated to tackle the challenge of detecting and quantifying defects in 3D. Fundamental understanding of defect formation is also necessary, so that on-line techniques (optical tomography, laser thermography) are being utilized to monitor discontinuities and possibly feedback the process parameters. This axis of research is extremely important but represents only the beginning of the challenge; in fact, some of the defects observed on-line will not necessarily be found in the final part. This implies that the connection between the microstructure during the process and that after fabrication is still unclear. The behavior of the detected defects under operating conditions represents the next question of the challenge, and, for instance, in-situ imaging or diffraction experiments are being developed to answer such questions. Only the synergy between simulation tools, on-line monitoring and advanced characterization can tackle the whole challenge.

d. In the context of defect and RS management, post-fabrication treatments have been discussed. These include thermal treatment as well as HIP and surface finish. It is now clear that some materials (e.g. IN718 and Ti64) processed by routes (such as LPBF) whereby large thermal gradients and cooling rates occur need post processing thermal and eventually mechanical treatments to relieve stresses and improve the morphological texture (defects, surface roughness). These post-processes strongly limit the predicated advantage of AM to shorten the time-to-market of parts. They also impose reflexions on both the suitability of additive techniques for the production of particular components and on the necessity of full characterization and qualification programs of AM components. Linked to the simulation activities mentioned above, it is now also clear that such post-processing treatments induce a change of microstructure (e.g. grain growth

and a more equiaxed orientation) and properties. Therefore, different materials properties than those valid for the as-built materials must be used in calculations. One can see that the level of complexity of a lifetime prediction dramatically raises for AM materials.

e. Unlike in the case of some classic processing routes, residual stresses play in AM materials and components a major role. In fact, most of the additive processes feature large temperature gradient and cooling rates, i.e. induce large internal stresses during fabrication. These stresses trivially depend on many factors (e.g. position on the build plate, size of the specimen) and processing parameters (e.g. laser power but also build plate pre-heat). These factors cause quite different and always complex spatial RS distributions, so that embedding RS as a factor in component assessment constitutes a particularly difficult problem. The situation can be seen analogous to welding, whereby a large body of literature on RS determination is already available, but with a significantly larger degree of difficulty for additive manufacturing, due to the intrinsically 3D nature of the stress fields and the scale of variation of such stresses. It has been seen that surface and sub-surface RS as high as the yield strength of the material often occur (in the as-built state) for LPBF components, so that the full spatial RS distribution in the part is necessary for its integrity assessment. In this direction, advanced characterization techniques (such as synchrotron X-ray and neutron diffraction) have become paramount for the qualification of the parts. Moreover, the classic methods for RS determination are being critically reviewed for AM parts, since some of the assumptions (e.g. that the stress principal axes coincide with the geometrical axes of the part) made for standard components are no longer valid.

f. Thoughts for a component evaluation concept are developed. They include, besides classical fatigue and fracture mechanics considerations with the emphasis on short crack propagation, the identification of safety-critical locations, for which representative material properties have to be determined, and questions of non-destructive testing – all this in view of the specific features which have to be considered when dealing with additive manufacturing. It becomes clear that non-destructive testing becomes a part of the design strategy of components: in view of the complex shape of AM components (especially powder based manufactured), access to the critical location must be guaranteed, and the design freedom must not only be used to save weight and scrap but also to guarantee testability. In this context, the effect of the use of support structures on the properties is also discussed. The possible elimination of such structures remains a goal, since their removal from the final part is time consuming and requires manual intervention in the production chain; however, it has been shown that not only the dimensional tolerances cannot be guaranteed without support structures (and even macroscopic distortions appear), but also the part integrity strongly suffers and sometime even the RS increases if support structures are not used in the production process. All these facts call for a closer collaboration between the designers and the materials scientists, and we see that AM poses

problems that need to be tackled in a global manner: one cannot develop a manufacturing process if the materials integrity is not taken into account.

Acknowledgement

This article is an outcome of the workshop on Fatigue of Additive Manufactured Metallic Components jointly organized by the Bundesanstalt für Materialforschung und -prüfung (Federal Institute for Materials Research and Testing), BAM Berlin, Germany and the National Institute of Standards and Technology (NIST) Boulder, CO, U.S.A, held in Berlin 15-16.5.2019. The aim of the workshop was a comprehensive discussion of the specific aspects of additively manufactured (AM) components in regard to failure under cyclic loading.

We thank all participants to the workshop for the inspiring discussion.

CV of Authors

Prof. Uwe Zerbst works as a research associate at Bundesanstalt für Materialforschung und – prüfung (BAM), Germany. He received his PhD degree from the University of Magdeburg, Germany. His research interest is fracture mechanics where he has more than 35 years experience in material parameter determination and analytical assessment of components under monotonic and cyclic loading. His focus during the last years was the utilization of fracture mechanics to the determination of the fatigue strength and total life prediction of cyclically loaded components. He published about 120 technical papers and two textbooks in the field.

Prof. Dr. Giovanni Bruno has a degree in Nuclear Engineering and a Ph.D. in Materials Science. Successively, he also got a degree in Solid State Physics at the University of Bologna, Italy. After Post-Doctorates in the UK and in Germany, he became project leader in France. He then moved to industry, as group head and then as project leader at Corning Incorporated. He is now division head at BAM, Berlin, and Professor at the University of Potsdam, Germany. His research interests span from residual stress analysis with neutrons and X-rays, quantitative microstructural characterization by means of Computed Tomography and X-ray refraction, and micromechanical models of elastic properties and stress, especially applied to additively manufactured metals and ceramics.

Prof. Jean-Yves Buffiere received his PhD in Materials Science from INP Grenoble in 1993, he is currently Professor at INSA Lyon. He has pioneered the use of synchrotron X-ray tomography for the 3D characterization of damage mechanisms in metallic alloys. On that topic, he is the co-author of more than a hundred papers (h index 48, ~8000 citations in google scholar), he has organized several international symposia and conferences and coedited a book on 3D characterisation. He has co-supervised 27 PhD and received the Prix RIST (1999) and Médaille Réaumur (2018) from the French Society of Metals and Materials (SF2M) and the Grand Prix Pechiney from the French Académie des Sciences (2003).

Prof. Dr. Thomas Niendorf is Full Professor at the Institute of Materials Engineering at University of Kassel (Germany). Dr. Niendorf studied Mechanical Engineering at University of Paderborn (Germany). In 2010 he did his doctorate. Dr. Niendorf's research interests are in the interrelationships of process, microstructure, mechanical properties and reliability of metallic materials. Analysis of residual stresses, microstructure evolution and fatigue performance are key aspects of research projects conducted. Research activities in the field of additive manufacturing (AM) comprise powder bed techniques (EBM and SLM) as well as laser metal deposition. Dr. Niendorf published more than 150 peer-reviewed papers in renowned journals. For his young career achievements he received several distinguished awards, e.g. the Heinz Maier-Leibnitz-Award by German Research Foundation.

M.Sc. Thomas Wegener received his M.Sc. degree in Industrial Engineering from University of Paderborn, Germany. Currently, he is a Ph.D student at the Institute of Materials Engineering at the University of Kassel, Germany. His research interest is focused on fatigue and crack-growth in high manganese steels and additive manufacturing.

Dr. Tao Wu received his PhD degree in computational mechanics from Leibniz Universität Hannover in Germany. Currently, he is working as a postdoctoral researcher at the Institute of Materials Engineering at Kassel Universität in Germany, with research focus on residual stress measurement, hybrid component, additive manufacturing and numerical simulations.

Prof. Dr. Xiang Zhang received her PhD degree from Imperial College London. She works at Coventry University as Professor in Structural Integrity. Prior to her current position, she worked at Imperial College London and Cranfield University. Her research interest is focused on the fatigue and fracture problems in lightweight metallic alloys and polymer composite materials, and their applications in the aerospace structures. She is a Fellow of the Royal Aeronautical Society and member of the Society's specialist group in materials and structures. She currently serves as an Associate Editor for the Journal of Aerospace Engineering and on the editorial boards of a number of international scientific journals.

Dr. Nikolai Kashaev concluded his studies in energy-related mechanical engineering with the advanced subject of electrical aerospace engines and power plants at the Bauman University of Technology in Moscow in 2001. Subsequently, he worked as a scientific employee at the Foundation Institute for Materials Technology in Bremen for four years. In 2005, he obtained his doctoral degree in materials engineering. After various activities in industry, he has been the head of the Laser Processing and Structural Assessment department at the Institute for Materials Research, Materials Mechanics at the Helmholtz Centre in Geesthacht since 2010. His research interests are laser welding and processing of lightweight metallic materials, residual stress engineering, laser shock peening, damage tolerance assessment, fatigue life prediction of welded and additively manufactured components and structures.

Prof.Giovanni Meneghetti received the PhD from the University of Padova. Presently he is full professor in Machine Design at the Department of Industrial Engineering of the University of Padova. He has published around 100 peer-reviewed papers on local approaches for structural durability analysis of welded components and structures, fatigue design of structures in metallic materials, experimental analysis of strains, in-field load data acquisition, development of design methodologies for structural integrity.

Dr. Nik Hrabe received his PhD degree from University of Washington. He is a staff metallurgist and project leader at the National Institute of Standards and Technology (NIST). His research interest is focused on fatigue and fracture behavior of additive manufacturing metals.

Dr. Mauro Madia received his PhD degree from Politecnico di Milano, Italy. He works as research associate in Bundesanstalt für Materialforschung und –prüfung (BAM), Germany. His research interest is focused on the fracture mechanics-based modelling of the fatigue strength of metallic components, the experimental determination and analytical modelling of the short-crack fatigue threshold and the structural integrity assessment of metallic components. He has been awarded the Silver Badge of Honour by the German Association for Materials Research and Testing (DVM).

Tiago Werner studied Mechanical Engineering at Technische Universität Berlin, Germany. Since October 2018 he is doing a doctorate on the assessment of components under cyclic loading considering short fatigue crack propagation as a research assistant at Bundesanstalt für Materialforschung und –prüfung (BAM), Germany. The focus of his experimental work is on the determination of fatigue properties in additively manufactured steel.

Prof. Dr.-Ing. Kai Hilgenberg received his Ph.D. in mechanical engineering from the University of Kassel for his work on a new laser-based surface treatment technology for metal forming tools. He works currently as Junior Professor at the Technical University of Berlin and leads a working group at BAM Bundesanstalt für Materialforschung und -prüfung. His research focuses on metal-process interactions during laser beam welding and additive manufacturing.

Dr. Martina Koukolíková received her Ph.D. in Materials Science from the University of West Bohemia, Czech Republic in 2007. She has worked in COMTES FHT from 2007 as an expert and research scientist in materials science in the Department of Materials Analysis. Her research interest is focused on the research and development of progressive steels and superalloys for power and chemical industry, additive manufacturing and determination of causes of operational and manufacturing failures of components. Dr. Koukolíková has experience in national and European research programs.

Dr. Radek Prochazka received his Ph.D. degree in Material Science and Engineering from University of West Bohemia in Pilsen, Czech Republic. He is currently working in the private research organization COMTES FHT in Dobrany. His research interest is focused on mechanical properties evaluation of sub and full-size samples for static and dynamic testing of metals and their application in a residual life assessment of large engineering components.

Prof. Dzugan obtained his Ph.D. in the field of Materials at West Bohemian University in Pilsen, Czech Republic He was employed at SKODA Research institute in Pilsen where he was dealing mechanical testing. He was a post-doc at the Helmholtz Dresden-Rossendorf, Germany and then at Tohoku University in Japan. From 2006 he joined COMTES FHT in Pilsen, Czech Republic, where he established mechanical testing laboratory and later become R&D Director. He co-author of over 200 scientific papers. He has been involved in over 30 publically funded projects. He is lecturing at West Bohemian University in Pilsen. His main scientific interest are: mechanical testing and additive manufacturing. He is

member of many international technical organizations. He is also member of ASTM, where he is leader of E28.04.01 Task group on small specimens group F42-JG61 on Orientation and Location Dependence Mechanical Properties for Metal Additive Manufacturing.

Dr.-Ing. Benjamin Möller, born in 1982, studied Mechanical Engineering at the Technische Universität Darmstadt, Germany. After working as a research assistant in the research group ‘System Reliability, Adaptive Structures, and Machine Acoustics SAM’, he joined the Fraunhofer LBF in Darmstadt in 2016 and finished his doctoral thesis in the field of fatigue of welds in 2019. His research within the fatigue assessment has been extended to recent material developments and joining technologies, such as laser beam welding or additive manufacturing.

Prof.Stefano Beretta got his PhD at Kyushu University in 1997 and since then he has been making his career at the Politecnico di Milano, where he became Full Professor in 2002. S. Beretta is a member of the Editorial Board of *Eng. Fract. Mechanics.* His main research interests are: fatigue and damage tolerance assessment of railway components; development of probabilistic methods for defect analysis and assessment under LCF and HCF; the fatigue and integrity assessment of AM materials and metamaterials.

Dr. Alexander Evans received his PhD degree in Materials Science and Engineering from The University of Manchester. He works at the Bundesanstalt für Materialforschung und –prüfung (BAM), in the department of Non-Destructive Testing. His research interest is focused on the development of residual stress analysis in additively manufactured materials using diffraction techniques.

Rainer Wagener:

Dr.-Ing. Rainer Wagener, born in 1975, studied Mechanical Engineering at Clausthal University of Technology, Germany, where he presented his doctoral thesis on “The Cyclic Material Behaviour under Constant and Variable Amplitude Loading” in 2007. He worked for one year with a German automobile-supplier in the area of component fatigue testing using road load data. In 2008 he joined the Fraunhofer LBF in Darmstadt, where he is the group manager of ‘Component-Related Material Behavior’ since 2012.

Kai Schnabel:

Kai Schnabel, M.Sc., born in 1989, studied Mechanics at the Technische Universität Darmstadt, Germany. He is a research assistant in the working group for ‘Numerical Methods and Component Design’ of the Fraunhofer LBF in Darmstadt. His focus is the fatigue assessment of additively manufactured metallic components and nodular cast iron.

Nomenclature

a
crack length (crack depth for surface cracks)

a_{arrest}
crack depth at crack arrest, Fig. 58

a_0
fit parameter of the El Haddad approach

a_0'
modified El Haddad parameter based on $\Delta K_{th,eff}$

b,c
pore dimensions (Fig. 19)

C, n
constants for describing the da/dN–ΔK curve in the Paris range

d
length dimension of an AM layer (Fig. 21)

d_1, d_2
length scales (crack length/depth) in the Kitagawa-Takahashi diagram (Fig. 50)

D
pore diameter (Fig. 24)

E, G, n
elastic constants (Fig. 4)

da/dN
fatigue crack propagation rate

HV
Vickers hardness

J
J-integral (crack driving force parameter)

J_c
critical *J*-integral (Fig. 4)

J_i
J-integral at initiation (Fig. 4)

K
stress intensity factor (*K*-factor) (crack driving force parameter)

K_f
fatigue notch factor

K_{mat}
fracture resistance under monotonic loading (general term)

K_{max}
maximum *K*-factor in a loading cycle

K_{min}
minimum *K*-factor in a loading cycle

K_{op}
K-factor above which the crack is open

K_t
stress concentration factor

$K_{I,imax}$
maximum K factor along the front of a small surface crack (Eqn. 19)

$\overline{K}$
mean value of *K* in a loading cycle [= $0.5(K_{max} + K_{min})$]

N
number of loading cycles

N_f

number of loading cycles up to fracture

P
probability

R
loading ratio (= $\sigma_{min}/\sigma_{max}$ or K_{min}/K_{max})

$\boldsymbol{R_{eff}}$
effective loading ratio taking into account the effect of residual stresses

$\boldsymbol{R_a;R_z;R_{max};\ R_v}$
surface roughness parameters

$\boldsymbol{R_{eL}}$
lower yield strength (materials showing a Lüders' plateau)

$\boldsymbol{R_{p\ 0.2}}$
0.2 % proof strength (materials without Lüders' plateau)

$\boldsymbol{R'_{p0.2}}$
cyclic yield strength

s
distance between two pores (Fig. 24)

t
layer thickness (Fig. 21)

U
crack closure parameter ($\Delta K_{eff}/\Delta K$)

$\boldsymbol{U_{LC}}$
crack closure parameter for *long* cracks, independent of the crack depth a

$\boldsymbol{U_{SC}}$
crack closure parameter for *short* cracks (function of the crack extension Δa)

x,y,z
coordinates in longitudinal, transverse and thickness direction, Fig. 16

Y
boundary correction function in the K factor solution

α
constraint factor (modified strip yield model Section 8.4.5

Δ*a*
crack extension

ΔJ
cyclic *J*-integral (cyclic loading)

ΔJ_{eff}
effective cyclic *J*-integral (taking into account crack closure)

ΔK
K-factor range (K_{max} - K_{min}), cyclic *K*-factor

ΔK_{eff}
effective *K*-factor range (= K_{max} - K_{op})

ΔK_{p}
plasticity corrected *K*-factor range

ΔK_{th}
fatigue crack propagation threshold

$\Delta K_{th,eff}$
intrinsic fatigue crack propagation threshold (no crack closure effect)

$\Delta K_{th,LC}$
fatigue crack propagation threshold in the long crack regime

$\Delta K_{th,op}$
extrinsic part of ΔK_{th} due to the crack closure phenomenon

$\Delta K_{th,SC}$
fatigue crack propagation threshold in the (physically) short crack regime

$\Delta \sigma$
stress range ($\sigma_{max} - \sigma_{min}$)

$\Delta \sigma_{appl}$
applied $\Delta \sigma$ (by mechanical loading)

$\Delta \sigma_{th}$;$\Delta \sigma_{e}$
endurance limit based on stress range

σ
stress

σ_{a}
stress amplitude (= ½ $\Delta \sigma$)

σ_{e}
fatigue limit based on stress amplitude

σ_{f}

flow stress given by the average between yield and tensile strength

σ_r
residual stress

σ_{op}
stress above which the crack is open

σ_w
fatigue limit (stress amplitude) for $R = -1$

σ_Y
yield strength, general (either R_{eL} or $R_{p0.2}$)

σ^p
primary stress (due to mechanical loading)

$\bar{\sigma}$
mean stress given by 0.5 ($\sigma_{max} + \sigma_{min}$)

$\sqrt{area}$
square root of defect (or crack) area normal to the loading direction; given in μm; Murakami's approach, see Section 8.4.3

Abbreviations:

AM	Additive Manufacturing
ASTM	American Society for Testing and Materials
CAD	Computer Aided Design
CT	Computed Tomography
Cyclic R curve	Fatigue crack propagation threshold ΔK_{th} as a function of crack extension Δa in the physically short crack propagation regime
DED	Direct Energy Deposition
EB-PBF	Electron Beam Powder Bed Fusion
EDM	Electro Discharging Machining
EIFS	equivalent initial flaw size
FAT	fatigue classes, stress range referring to $2x10^6$ loading cycles
FEM	Finite Element Method
FCGR	fatigue crack growth rate

HCF	high cycle fatigue
HIP	Hot Isostatic Pressing
GS	grain size (Fig. 38)
ISO	International Standardization Organisation
KT	Kitagawa-Takahashi diagram (Section 8.4.2)
LC	long crack
LCF	low cycle fatigue
LMD	Laser Metal Deposition
L-PBF	Laser Powder Bed Fusion (formerly: SLM)
LSP	Laser Shock Peening
NASGRO	approach and computer program for fatigue crack propagation, provided by NASA
NDT	Non-Destructive Testing
PBF	Powder Bed Fusion
PoD	Probability of Detection (of a crack by NDT)
PoND	Probability of Non-detection
SC	short crack
SLM	Selected Laser Melting (now preferred: L-PBF)
S-N curve	stress (amplitude) versus number of loading cycles to failure
VHCF	very high cycle fatigue (more than $10^7/10^8$ loading cycles)
WAAM	Wire Arc Additive Manufacturing
ε-N curve	total strain (amplitude) versus number of loading cycles to failure
2D	two dimensional
3D	three dimensional

11. References

[1]. Herzog D, Seyda V, Wycisk E, Emmelmann C. Additive manufacturing of metals. Acta Mat2016;117:371–392.

[2]. Bourell D, Kruth JP, Leu M, Levy G, Rosen D, Beese AM, Clare A. Materials for additive manufacturing. CIRP Annals – Manufact Technol2017;66:659–681.

[3]. Bajaj P, Hariharan A, Kini A, Kürnsteiner P, Raabe D, Jägle EA. Steels in additive manufacturing A review of their microstructure and properties. Mat Sci Engng A2020;722:138633.

[4]. DebRoy T, Wie HL, Zuback JS, Mukherjee T, Elmer JW, Milewski JO, Beese AM, Wilson-Heid A, De A, Zhang W. Additive manufacturing of metallic components – process, structure and properties. Progress in Mat Sci2018;92:112–224.

[5]. Thomas DS. Costs, benefits, and adoption of additive manufacturing: a supply chain perspective. Int J Adv Manufact Techn2016;85:1857–1876.

[6]. Lippert RB, Lachmayer R. A design method for SLM-parts using internal structures in an extended design space. In: Meboldt M, Klahn C (eds) Industrializing additive manufacturing. Proc of Additive Manufacturing in Products and Applications – AMPA201770-81. Springer Int. Publ, 14–23, 2018.

[7]. Brenne F, Niendorf T. Damage tolerant design by microstructural gradation – Influence of processing parameters and build orientation on crack growth within additively processed 316L. Mat Sci Engng A2019;764:138186.

[8]. Zhang C, Chen F, Huang Z, Jia M, Chen G, Ye Y, Lin Y, Liu W, Chen B, Shen Q, Zhang L, Lavernia EJ. Additive manufacturing of functionally graded materials: A review. Mat Sci Engng A2019;764:138209.

[9]. Hoefer K, Nitsche A, Abstoss KG, Ertugrul G, Haelsig A, Mayr P. Multi-material additive manufacturing by 3D plasma metal deposition for graded structures of super duplex alloy 1.4410 and the austenitic corrosion resistant alloy 1.4404. JOM, J Minerals, Met Mat Soc2019;71:1554–1559.

[10]. Kim H, Cong W, Zhang H-C, Liu Z. Laser engineered net shaping of nickel-based superalloy Inconel 718 powders onto AISI 4140 alloy steel substrates: Interface bond and fracture failure mechanism. Materials2017;10:341.

[11]. Yan LChen XZhang YNewkirk JWLiou F. Fabrication of functionally graded Ti and γ-TiAl by laser metal deposition. JOM, J Minerals, Met Mat Soc2017;69:2756–2761.

[12]. Bandyopadhyay A, Heer B. Additive manufacturing of multi-material structures. Mat Sci Engng R2018;129:1–16.

[13]. Töppel T, Lausch H, Brand M, Hensel E, Arnold M, Rotsch C. Structural integration of sensors/actuators by laser beam melting for tailored smart components. JOM, J Minerals, Met Mat Soc2018;70:321–327.

[14]. Hehr A, Norfolk M, Wenning J, Sheridian J, Leser P, Leser P, Newman JA. Integrating fiber optic strain sensors into metal using ultrasonic additive manufacturing. JOM, J Minerals, Met Mat Soc2018;70:315–320.

[15]. Ya W, Hamilton K. On-demand spare parts for the marine industry with directed energy deposition: propeller use case. In: Meboldt M, Klahn C (eds) Industrializing additive manufacturing. Proc of Additive Manufacturing in Products and Applications – AMP A201770-81. Springer Int Publ, 70–81, 2018.

[16]. Jones R, Singh Raman RK, Iliopoulos AP, Michopoulos JG, Phan N, Peng D. Additively manufactures To-6Al-4V replacement parts for military aircraft. Int J Fatigue2019; 124:227–235.

[17]. Olakanmi EO, Cochrane RF, Dalgarno KW. A review on selective laser sintering/melting (SLS/SLM) of aluminium alloy powders: Processing, microstructure, and properties. Progress in Mat Sci2015;74:401–477.

[18]. Bruna-Rosso C, Demir AG, Previtali B. Selective laser melting finite element modelling: Validation with high-speed imaging and lack of fusion defects prediction. Mater Design2018;156:143–153.

[19]. Molaei R, Fatemi A. Crack paths in additive manufactured materials subjected to multiaxial cyclic loads including surface roughness, HIP, and notch effects. Int J Fatigue2019;124:558–570.

[20]. Yadollahi A, Shamsaei N. Additive manufacturing of fatigue resistant materials: Challenges and opportunities. Int J Fatigue2017;98:14–31.

[21]. Darwish K, Chen ZW, Pasang T. Reducing lack of fusion during selective laser melting of CoCrMo alloy: Effect of laser power on geometrical features of tracks. Mat Design2016;112:357–366.

[22]. Torries B, Imandoust A, Beretta S, Shao S, Schamsaei N. Overview on microstructure and defect-sensitive fatigue modeling of additively manufactured materials. JOM, J Minerals, Met Mat Soc2018;70:1853–1862.

[23]. Bartlett JL, Li X. An overview of residual stresses in metal power bed fusion. Additive Manufact2019;27:131–149.

[24]. Seifi M, Gorelik M, Wallner J, Hrabe N, Shamsaei N, Daniewicz S, Lewandowski JJ. Progress towards metal active manufacturing standardization to support qualification and certification. JOM, J Minerals, Met Mat Soc2017;69:439–455.

[25]. Gorelik MAdditive manufacturing in the context of structural integrity. Int J Fatigue2017;94:168–177.

[26]. Biswal R, Zhang X, Syed AK, Awd M, Ding J, Walther F, Williams S. Critically of porosity defects on the fatigue performance of wire + arc additive manufactured titanium alloy. Int J Fatigue2019;122:308–217.

[27]. Broek DPractical application of fracture mechanics. Kluwer Academic Publ., Dordrecht/Boston/ London, 1988.

[28]. Zerbst U, Schwalbe K-H, Ainsworth RA. An overview of failure assessment methods in codes and standards. In: Schwalbe K-H, Ainsworth RA (eds) Comprehensive Structural Integrity; Volume 7: Practical Failure Assessment Methods; Elsevier, 4–48, 2003.

[29]. Koester LW, Bond LJ, Taheri H, Collins PC. Nondestructive evaluation of additively manufactures metallic parts: in-situ and post deposition. In: Froes F, Boyer R (eds) Additive Manufacturing for the Aerospace Industry. Elsevier Amsterdam/Oxford/ Cambridge MA, 401–417, 2019.

[30]. Zerbst U, Stadie-Frohbös G, Plonski T, Jury J. The problem of adequate yield load solutions in the context of proof tests on a damaged subsea umbilical. Engng Failure Anal2009;16:1062–1073.

[31]. Mercelis P, Kruth J-P. Residual stresses in selective laser melting. Rapid Prototyping J2006;12:254–256.

[32]. Zhang Y, Wu L, Gou X, Kane S, Deng Y, Jung Y-G, Lee J-H, Zhang J. Additive manufacturing of metallic materials: a review. J Mat Engng Perfom2017;27:1–13.

[33]. Yadroitsev I, Yadroitsava I. Evaluation of residual stress in stainless steel 316Land Ti6Al4V samples produced by selective laser melting. Virtual Phys Prototyping2015;10:67–76.

[34]. Shamsaei N, Simsiriwong J. Fatigue behavior of additively-manufactured metallic parts. Procedia Struct Integrity2017;7:3–10.

[35]. Liu L, Zhong Y, Zou J, Wu J, Chiu JY, Shen JZ. Dislocation network in additive manufactured steel breaks strength-ductility trade-off. Mat Today2018;21:354–361.

[36]. Mishurova T, Artzt K, Haubrich J, Requena G, Bruno G. New aspects about the research for the most relevant parameters optimizing SLM materials. Add Manufact2019;25:325–334.

[37]. Liu S, Shin YC. Additive manufacturing of Ti6Al4V: a review. Mat Design2019;164:107552.

[38]. Evans AD, King A, Pirling T, Bruno G, Withers PJ. Near surface residual stress determination of laser shock peening by neutron diffraction. MECA SENS III Conf, Manchester, UK, Sept. 2003, J Neutr Res11;2004:229–234.

[39]. Mishurova T, Artzt K, Rehmer B, Haubrich J, Ávila L, Schoenstein F, Serrano-Munoz I, Requena G, Bruno G. Separation of the impact of residual stress and microstructure on the mechanical performance of LPBF Ti-6Al-4V at elevated temperature. Int J Fatigue, 2021, under review.

[40]. Bruno G, Kachanov M, Sevostianov I, Shyam A. Micromechanical modeling of non-linear stress-strain behavior of polycrystalline microcracked materials under tension. Acta Mat2019;164:50–59.

[41]. Newman JC Jr.A crack opening stress equation for fatigue crack growth. Int J Fracture1984;24:R131–R135.

[42]. Forman RG, Mettu RR. Behaviour of surface and corner cracks subjected to tensile and bending loads in Ti-6Al-4V alloy. ASTM STP 1131, American Society for Testing and Materials (ASTM), Philadelphia, 519–546, 1992.

[43]. NASGRO, Fatigue crack growth computer program “NASGRO” Version 3, Houston, Texas: NASA, 2000.

[44]. Pokluda J, Pippan R, Vojtek T, Hohenwarter A. Near-threshold behavior of shear-mode fatigue cracks in metallic materials. Fatigue Fracture Engng Mat Struct2014;37:232–254.

[45]. Zerbst U, Vormwald M, Pippan R, Gänser H-P, Sarrazin-Baudoux C, Madia M. About the fatigue crack propagation threshold of metals as a design criterion – a review. Engng Fracture Mech2016;153:190–243.

[46]. Aliya D, Becker WT. (2002) Glossary to Becker, W T, Shipley RJ. (eds.) ASM Handbook, Vol. 11, Failure Analysis and Prevention, American Society for Metals, ASM International, 1061–1077.

[47]. Zerbst U, Madia M, Klinger C, Bettge D, Murakami Y. Defects as the root cause of fatigue failure of metallic components. Part I: Basic aspects. Engng Failure Anal2019;97:777–792.

[48]. Zerbst U, Madia M, Klinger C, Bettge D, Murakami Y. Defects as the root cause of fatigue failure of metallic components. Part II: Non-metallic inclusions. Engng Failure Anal, 2019;98:228–239.

[49]. Zerbst U, Madia M, Klinger C, Bettge D, Murakami Y. Defects as the root cause of fatigue failure of metallic components. Part III: Cavities, dents, corrosion pits, scratches. Engng Failure Anal2019;97:759–776.

[50]. Ngnekou JND, Nadot Y, Henhaff G, Nicolai J, Ridosz L. Influence of defect size on the fatigue resistance of AlSi10Mg alloy elaborated by selective laser melting (SLM). Procedia Struct Integrity2017;7:75–83.

[51]. Zerbst U, Madia M, Vormwald M, Beier HTh. Fatigue strength and fracture mechanics – a general perspective. Engng Fracture Mech2018;198:2–23.

[52]. Polak JCyclic deformation, crack initiation, and low-cycle fatigue. In: Ritchie RO, Mursakami Y (eds) Comprehensive Structural Integrity; Volume 4: Cyclic loading and Fracture; Elsevier, 1–39, 2003.

[53]. Miller KJ. The two thresholds of fatigue behavior. Fatigue Fracture Engng Mat Struct1993;16:931–939.

[54]. Murakami YMetal fatigue. Effects of small defects and nonmetallic inclusions. Elsevier. Oxford, 2002.

[55]. Vincent M, Nadot Y, Nadot-Martin C, Dragon A. Interaction between a surface defect and grain size under high cycle fatigue loading: Experimental approach for Armco iron, Int J Fatigue2016;87:81–90.

[56]. Capelli MD, Carlson RL, Kardomates GA. The transition between small and long fatigue crack behavior and its relation to microstructure. Int J Fatigue2008;30:1473–1478.

[57]. Kondo YFatigue under variable amplitude loading, In: Ritchie RO, Murakami Y (eds) Comprehensive Structural Integrity; Volume 4: Cyclic loading and fracture; Elsevier, 253–279, 2003.

[58]. Madia M, Zerbst U, Beier HTh, Schork B. The IBESS model – elements, realisation and validation. Engng Fracture Mech2018;198:171–208.

[59]. Tchoffo Ngoula D, Madia M, Beier HTh, Vormwald M, Zerbst U. Cyclic J-integral: Numerical and analytical investigations for surface cracks in weldments. Engng Fracture Mech2018;198:24–44.

[60]. Zerbst U, Madia M, Schork B, Hensel J, Kucharczyk P, Tchoffo Ngoula D, Tchuindjang D, Bernhard J, Beckmann C. Fatigue and fracture of weldments. The IBESS approach for the determination of the fatigue life and strength of weldments by fracture mechanics analysis. Springer Nature Switzerland AG, Cham, Switzerland, 2019.

[61]. Ding F, Feng M, Jiang Y. Modeling of fatigue crack growth from a notch. Int J Plasticity2007;23:1167–1188.

[62]. Zerbst U, Heinimann M, Dalle Donne C, Steglich D. Fracture and damage modelling of thin-walled structures – an overview. Engng Fracture Mech2009;76:5–43.

[63]. Miller A, Estrin Y, Hu XZ. Magnetic force microscopy of fatigue crack tip region in a 316L austenitic stainless steel. Scripta Mat2002;47:441–446.

[64]. Ganesh P, Kaul R, Sasikala G, Kumar H, Venugopal S, Tiwari P, Rai S, Prasad R, Kukreja L. Fatigue crack propagation and fracture toughness of laser rapid manufactured structures of AISI 316L stainless steel. Metallogr Microstruct Anal2014;1:36–45.

[65]. Suryawanshi J, Prashanth KG, Ramamurty U. Mechanical behavior of selective laser melted 316L stainless steel. Mat Sci Engng A2017;696:113–121.

[66]. Zerbst U, Hilgenberg K. Damage development and damage tolerance of structures manufactured by selective laser melting – a review. Procedia Struct Integrity2017;7:141–148.

[67]. Garwood MF, Zurburg HH, Erickson M. Correlation of laboratory tests and service performance interpretation of tests and correlation with service. American Society of Metals (ASM), Philadelphia, 1951;1–77.

[68]. Nishijama SStatistical analysis of fatigue test data. J Soc Mater Sci Japan1980;29 (316):24–29.

[69]. Yamashita Y, Murakami T, Mihara R, Okada M, Murakami Y. Defect analysis and fatigue design basis for Ni-based superalloy 718 manufactured by selective laser melting. Int J Fatigue2018;117:485–495.

[70]. Murakami Y, Masuo H, Tanaka Y, Nakatani M. Defect analysis for additively manufactured materials in fatigue from a viewpoint of quality control and statistics of extremes. Procedia Struct Integrity2019;19:113–122.

[71]. Sharon JA, Padilla HA, Boyce BLInterpreting the ductility of nanocrystalline metals. J Mat Res2013;28:1539–1552.

[72]. Zhang M, Sun C-N, Zhang X, Goh PC, Wei J, Li H, Hardacre D. Elucidating the relations between monotonic and fatigue properties of laser powder bed fusion stainless steel 316L. JOM, J Minerals, Met Mat Soc2018;70:390–395.

[73]. Salzbrenner BC, Rodelas JM, Madison JD, Jared BH, Swiler LP, Shen Y-L, Boyce BL. High-throughput stochastic tensile performance of additively manufactured stainless steel. J Mater Proc Techn2017;241:1–12.

[74]. Boyce BL, Salzbrenner BC, Rodelas JM, Swiler LP, Madison JD, Jared BH, Shen YL. Extreme-value statistics reveal rare failure-critical defects in Additive Manufacturing. Adv Engng Mat2017;19(8):1700102.

[75]. Dzugan J, Seifi M, Prochazka R, Rund M, Podany P, Konopik P, Lewandowski JJ. Effects of thickness and orientation on the small-scale fracture behaviour of additively manufactured Ti-6Al-4V. Mat Charact2018;143:94–109.

[76]. Frazier WE. Metal additive manufacturing: a review. J Mater Engng Perform2014;23:1917–1928.

[77]. Beese AM, Carroll BE. Review of mechanical properties of Ti-6Al-4V made by laser-based additive manufacturing using powder feedstock. JOM, J Minerals, Met Mat Soc2016;68:724–734.

[78]. Kahlin M, Ansell H, Moverare JJ. Fatigue behaviour of notched additive manufactured Ti6Al4V with as-build surfaces. Int J Fatigue2017;101:51–60.

[79]. ISO/ASTM 52900 - Additive manufacturing – General principles – Terminology. International Organization for Standardization (ISO), Geneva, Switzerland, 2017.

[80]. Garcia-Colomo A, Wood D, Filomeno M, Stewart WW. A comparison framework to support the selection of the best additive manufacturing process for specific aerospace applications. Int J Rapid Manuf9, 2019.

[81]. Aboulkhair NT, Everitt NM, Ashcroft I, Tuck C. Reducing porosity in AlSi10Mg parts processed by selective laser melting. Additive Manufact2014; 1-4:77–86.

[82]. Cunningham R, Narra SP, Montgomery C, Beuth J, Rollett AD. Synchrotron-based x-ray microtomography characterization of the effect of processing variables on porosity formation in laser power-bed additive manufacturing of Ti-6Al-4V. JOM. J Minerals, Met Mat Soc2017;69:479–484.

[83]. Zhang B, Li Y, Bai Q. Defect formation mechanisms in selective laser melting: a review. Chin J Mech Engng2017;30:515–527.

[84]. Brandi E, Heckenberger U, Holzinger V, Buchbinder D. Additive manufactured AlSi10Mg samples using Selective Laser Melting (SLM): Microstructure, high cycle fatigue, and fracture behavior. Mat Design2012;34:159–169.

[85]. Li R, Liu J, Shi Y, Wang L, Jiang W. Balling behavior of stainless steel and nickel powder during selective laser melting process. Int J Adv Manuf Technol2012;59:1025–1035.

[86]. Kasperovic G, Haubrich J, Gussone J, Requena G. Correlation between porosity and processing parameters in TiAl6V4 produced by selective laser melting. Mat Design2016;105:160–170.

[87]. Cunningham RDefect formation mechanisms in powder-bed metal additive manufacturing. PhD Thesis.Carnegie Mellon University, 2018.

[88]. Zhang M, Sun C-N, Zhang X, Goh PC, Wei J, Hardacre D. Fatigue and fracture behaviour of laser powder bed fusion stainless steel 316L: Influence of processing parameters. Mat Sci Engng A2017;703:251–261.

[89]. Gong H, Rafi K, Gu H, Starr T, Stucker B. Analysis of defect generation in Ti6Al-4V parts made using powder bed fusion additive manufacturing processes. Addit Manufact, 2014;1:87–98.

[90]. Santos LMS, Fereira JAM, Jesus JS, Costa JM, Capela C. Fatigue behaviour of selective laser melting steel components. Theor Appl Facture Mech2016;85:9–15.

[91]. Froend M, Ventzke V, Dorn F, Kashaev N, Klusemann B, Enz J. Microstructure by design: An approach of grain refinement and isotropy improvement in multi-layer wire-based laser metal deposition. Mat Sci Engng A2020;772:138635.

[92]. Gu D, Hagedorn Y-C, Meiners W, Meng G, Batista RJS, Wissenbach K, Poprawe R. Densification behavior, microstructure evolution, and wear performance of selective laser melting processed commercially pure titanium. Acta Mat2012;60:3849–3860.

[93]. Chen ZW, Guraya T, Darvish K, Phan MAL, Pasang T. Solidification during selective laser melting of Co-29Cr-6Mo alloy. JOM, J Minerals, Met Mat Soc2019;71:691–696.

[94]. Thompson SM, Bian L, Shamsaei N, Yadollahi A. An overview of direct laser deposits for additive manufacturing; Part I: Transport phenomena, modelling and diagnostics. Additive Manufact2015;8:36–62.

[95]. Amine T, Kriewall CS, Newkirk JW. Long-term effects of temperature exposure on SLM 304L stainless steel. JOM, J Minerals, Met Mat Soc2018;70:384–389.

[96]. Carlton HD, Haboub A, Gallegos GF, Parkinson DY, MacDowell AA. Damage evolution and failure mechanisms in additively manufactured stainless steel. Mat Sci Engng A2016;651:406–414.

[97]. Wang YM, Voisin T, McKeown JT, Ye J, Calta NP, Li Z, Zeng Z, Zhang Y, Chen W, Roehling TT, Ott RT, Santala MK, Depond PJ, Matthews MJ, Hamza AV, Zhu TR. Additively manufactured hierarchical stainless steels with high strength and ductility. Nat Mat2018;17:53–71.

[98]. Vrancken B, Cain V, Knutsen R, van Humbeeck J. Residual stress via the contour method in compact tension specimens produced via selective laser melting. Scripta Mat2014;87:29–32.

[99]. Edwards P, Ramulu M. Fatigue performance evaluation of selective laser melted Ti-6Al-4V. Mat Sci Engng2014;598:327–337.

[100]. Edwards P, Ramulu M. Effect of build direction on the fracture toughness and fatigue crack growth in selective laser melted Ti-6Al-4V. Fatigue Fracture Engng Mat Struct2015;38:1228–1236.

[101]. Saeidi K, Gao X, Zhong Y, Shen ZJ. Hardened austenite steel with columnar sub-gain structure formed by laser melting. Mat Sci Engng A2015;625:221–229.

[102]. Kajima Y, Takaichi A, Nakamoto T, Kimura T, Yogo Y, Ashida M, Doi H, Nomura N, Takahashi H, Hanawa T, Wakabayashi N. Fatigue strength of Co-Cr-Mo alloy clasps prepared by selective laser melting. J Mech Behav Biomedical Mat2016;59:446–458.

[103]. Torries B, Shamsaei N. Fatigue behavior and modelling of additively manufactures Ti-6Al-4V including interlayer time interval effects. JOM, J Minerals, Met Mat Soc2017;69:2698–2705.

[104]. Hussain A, Hao L, Yan C, Everson R. Finite element simulation of the temperature and stress fields in single layers built without-support in selective laser melting. Mat Design2013;52:638–647.

[105]. Yadollahi A, Shamsaei N, Thompson SM, Seely DW. Effects of process time interval and heat treatment on the mechanical and microstructural properties of direct laser deposited 316L stainless steel. Mat Sci Engng A2015;644:171–183.

[106]. Gu D, Chen H. Selective laser melting of high strength and toughness stainless steel parts: The roles of laser hatch style and part placement strategy. Mat Sci Engng A2018;725:419–427.

[107]. Spranger F, Graf B, Schuch M, Hilgenberg K, Rehtmeier M. Build-up strategies for additive manufacturing of three dimensional Ti-6Al-4V-parts produced by laser metal deposition. J Laser Appl2018;30:022001.

[108]. Mohr G, Altenburg SJ, Hilgenberg K. Effects of inter layer time and build height on resulting properties of 316L stainless steel processed by laser powder bed fusion. Add Manufact2020;32:101080.

[109]. ISO 12135Metallic materials – Unified method of test for the determination of quasistatic fracture toughness. International Organization for Standardization (ISO), Geneva, Switzerland, 2002.

[110]. ASTM E399Standard test method for linear-elastic plane-strain fracture toughness K_{Ic} of metallic materials. American Society for Testing and Materials (ASTM), ASTM International. West Conshohocken, PA, 2012.

[111]. Seifi M, Salem A, Beuth J, Harrysson O, Lewandowski JJ. Overview of materials qualification needs for metal additive manufacturing. JOM, J Minerals, Met Mat Soc2016;68:747–764.

[112]. Yadollahi A, Simsiriwong JThompson SMShamsaei N. Data demonstrating the effects of build orientation and heat treatment on fatigue behavior of selective laser melted 17-4 PH stainless steel. Data in Brief2016;7:89–92. [PubMed: 26955653]

[113]. Syed AK, Ahmad B, Guo H, Machry T, Eatock D, Meyer J, Fitzpatrick ME, Zhang X. An experimental study of residual stress and direction-dependence of fatigue crack growth behaviour in as-built and stress-relieved selective-laser-melted Ti6Al4V. Mat Sci Engng A, 2019;775:246–257.

[114]. Afkhami S, Dabiri M, Alavi SH, Björk T, Salminen A. Fatigue characteristics of steels manufactured by selective laser melting. Int J Fatigue2019;122:72–83.

[115]. Wang Y, Zhang L, Daynes S, Zhang H, Feih S, Wang MY. Design of graded lattice structure with optimized mesostructures for additive manufacturing. Mat Design2018;142:114–123.

[116]. Leutenecker-Twelsiek B, Klahn C, Meboldt M. Considering part orientation in design for additive manufacturing. Procedia CIPR2016;50:408–413.

[117]. Persenot T, Burr A, Martin G, Buffiere JY, Dendievel R, Maire E. Effect of build orientation on the fatigue properties of as-built Electron Beam Melted Ti-6Al-4V alloy. Int J Fatigue2019;118:65–76.

[118]. Peterson PE. Stress concentration factors. John Wiley & Sons, New Yorket al., 1973.

[119]. He K, Zhao X. 3D thermal finite element analysis of the SLM 316L parts with microstructural correlations. Complexity, Article ID 6910187, 2018.

[120]. Gockel J, Sheridan L, Narra SP, Klingbeil NW, Beuth J. Trends in solidification grain size and morphology for additive manufacturing of Ti-6Al-4V. JOM, J Minerals, Met Mat Soc2017;69:2706–2710.

[121]. Wang K, Bao R, Thang T, Liu B, Yang Z, Jiang B. Fatigue crack branching in laser deposited Ti-55511 alloy. Int J Fatigue2019;124:217–226.

[122]. Becker TH, Dimitrov D. The achievable mechanical properties of SLM produced maraging steel 300 components. Rapid Prototyping J2016;22:487–494.

[123]. Cheng B, Shrestha S, Chou K. Stress and deformation evaluations of scanning strategy effect in selective laser melting. Additive Manufact2016;12:240–251.

[124]. Kurzynowski T, Gruber K, Stopyra W, Kuznicka B, Chlebus E. Correlation between process parameters, microstructure and properties of 316L stainless steel processed by selective laser melting. Mat Sci Engng A2018;718:64–73.

[125]. Parry L, Ashcroft IA, Wildman RD. Geometrical effects on residual stress in selective laser melting. Additive Manufact2019;25:166–175.

[126]. Wan HY, Zhou ZJ, Li CP, Chen GF, Zhang GP. Effect of scanning strategy on mechanical properties of selective laser melted Inconel 718. Mat Sci Engng A2019;753:42–48.

[127]. Geiger F, Kunze K, Etter TZ. Tailoring the texture of IN738LC processed by selective laser melting (SLM) by specific scanning strategies. Mat Sci Engng A2016;661:240–246.

[128]. Yakout M, Elbestawi MA, Veldhuis SC. On the characterization of stainless steel 316L parts produced by selective laser melting. Int J Adv Manuf Technol2018;95:1953–1974.

[129]. Liu F, Lin X, Huang C, Song M, Yang G, Chen J, Huang W. The effect of laser scanning path on microstructures and mechanical properties of laser solid formed nickel-base superalloy Inconel 718. J Alloys Compounds2011;509:4505–4509.

[130]. Simonelly M, Tse YY, Tuck C. On the texture formation of selective melted Ti-6Al-4V. Met Mat Trans A2014;45:2863–2872.

[131]. Nadammal N, Cabeza S, Mishurova T, Thiede T, Kromm A, Seyfert Ch, Farahbod L, Haberland Ch, Schneider JA, Dolabella Portella P, Bruno G. Effect of hatch length on the development of microstructure texture and residual stresses in selective laser melted superalloy Inconel 718. Mat Design2017;134:139–150.

[132]. Tammas-Williams S, Zhao H, Leonard F, Derguti F, Todd I, Prangnell PB. XCT analysis of their influence of melt strategies on defect population in Ti-6Al-4V components manufactured by Selective Electron Beam Melting. Mat Charact2015;102:47–61.

[133]. Mugwagua L, Dimitrov D, Matope S, Yadroitsev I. Evaluation of the impact of scanning strategies on residual stresses in selective laser melting. Int J Adv Manuf Technol2019;102:2441–2450.

[134]. Parry L, Ashcroft IA, Wildman RD. Understanding the effect of laser scan strategy on residual stress in selective laser melting through thermo-mechanical simulation. Additive Manufact2016;12:1–15.

[135]. Kruth J-P, Deckers J, Yasa E, Wauthle R. Assessing and comparing influencing factors of residual stresses in selective laser melting using a novel analysis method. J Engng Manufact2012;226:980–991.

[136]. Ali H, Ghadbeigi H, Mumtaz K. Effect of scanning strategies on residual stress and mechanical properties of Selective Laser Melted Ti-6Al-4V. Mat Sci Engng A2018;712:175–187.

[137]. Mukherjee T, Zhang W, BebRoy T. An improved prediction of residual stresses and distortion in additive manufacturing. Comp Mat Sci2017;126:360–372.

[138]. Beevers E, Brandão AD, Gumpinger J, Gschweitl M, Seyfert C, Hofbauer P, Rohr T, Ghidini T. Fatigue properties and material characteristics of additively manufactured AlSi10Mg – Effect of the contour parameter on the microstructure, density, residual stress, roughness and mechanical properties. Int J Fatigue2018;117:148–162.

[139]. Gumpinger J, Brandão AD, Beevers ERohr T, Ghidini T, Beretta S, Romano S. Expression of additive manufacturing surfaced irregularities through a flaw-based assessment. ASTM Symp on Structural Integrity of Additive Manufactured Parts. November 6-8, 2018, Washington DC, ASTM International., 2018.

[140]. Mugwagua L, Dimitrov D, Matope S, Yadroitsev I. Influence of process parameters on residual stress related distortions in selective laser melting. Procedia Manufact2018;21:92–99.

[141]. Qiu C, Panwisawas C, Ward M, Basoalto HC, Brooks JW, Attallah MM. On the role of melt flow into the surface structure and porosity development during selective laser melting. Acta Mat2015;96:72–79.

[142]. Nadammal N, Kromm A, Saliwan-Neumann R, Farahbvod L, Haberland C, Portella PD. Influence of support configurations on the charactzeristics of selective laser-melted Inconel 718. JOM, J Minerals, Met Mat Soc2018;70:343–348.

[143]. Molaei R, Fatemi AFatigue design with additive manufactured metals: Issues to consider and perspective for future research. Procedia Engng2018;213:5–16.

[144]. Mertens R, Vrancken B, Holmstock N, Kinds Y, Kruth J-P, van Humbeeck J. Influence of powder bed preheating on microstructure and mechanical properties of H13 tool steel SLM parts. Physics Procedia2016;83:882–890.

[145]. Cordova L, Campos M, Tinga T. Revealing the effects of powder reuse for selective laser melting by powder characterization. JOM, J Minerals, Met Mat Soc2019;71:1062–1072.

[146]. Quintana OA, Alvarez J, McMillan R, Tong W, Tomonto C. Effects of reusing Ti-6Al-4V powder in a selective laser melting additive system operated in an industrial setting. JOM, J Minerals, Met Mat Soc2018;70:1863–1869.

[147]. Carrion PE, Soltani-Tehrani A, Phan N, Shamsaei N. Powder recycling effects on the tensile and fatigue behavior of additively manufactured Ti-6Al-4V parts. JOM, J Minerals, Met Mat Soc2019;71:1963–973.

[148]. Heiden MJ, Deibler LA, Rodelas JM, Koepke JR, Tung DJ, Saiz DJ, Jared BH. Evolution of 316L stainless steel feedstock due to laser powder bed fusion process. Add Manufact2019;25:84–103.

[149]. Romano S, Brückner-Foit A, Brandão A, Gumpinger J, Ghidini T, Beretta S. Fatigue properties of AlSi10Mg obtained by additive manufacturing: Defect-based modelling and prediction of fatigue strength. Engng Fracture Mech2018;187:165–189.

[150]. Le V-D, Pessard E, Morel F, Edy F. Interpretation of the fatigue anisotropy of additively manufactured TA6V alloys via a fracture mechanics approach. Engng Fracture Mech2019;214:410–426.

[151]. Günther J, Krewerth D, Lippmann T, Leuders S, Tröster T, Weidner A, Biermann H, Niendorf T. Fatigue life of additively manufactured Ti-6Al-4V in the very high cycle fatigue regime. Int J Fatigue2017;94:236–245.

[152]. Greitemeier D, Palm F, Syassen F, Melz T. Fatigue performance of additive manufactured TiAl6V4 using electron and laser beam melting. Int J Fatigue2017;94:211–217.

[153]. Tang HP, Wang J, Song CN, Liu N, Elambasseril J, Qian M. Microstructure, mechanical properties, and flatness of SEMB Ti-6Al-4V sheet in as-built and hot isostatically pressed conditions. JOM, J Minerals, Met Mat Soc2017;69:466–471.

[154]. Beretta S, Gargourimotlagh M, Folletti S, Rigoni L, Riccio M. Fatigue strength assessment and surface rating for “as built” AlSi10Mg manufactured by SLM with different build directions. Subm. to Int J Fatigue, 2020.

[155]. Lecsek RL, Yee R, Lambert SB, Burns DJ. A probabilistic model for initiation and propagation of surface cracks in welded joints. Fatigue Fracture Engng Mat Struct1955;18:821–831.

[156]. Schork B, Kucharczyk P, Madia M, Zerbst U, Hensel J, Bernhard J, Tchuindjang D, Kaffenberger M, Oechsner M. The effect of the local and global weld geometry as well as material defects on crack initiation and fatigue strength. Engng Fracture Mech2018;198:103–122.

[157]. Greitemeier D, Dalle Donne C, Schoberth A, Jürgens M, Eufinger J, Melz T. Uncertainty of additive manufactured Ti-6Al-4V: chemistry, microstructure and mechanical properties. Appl Mech Mat2015;807:169–180.

[158]. Greitemeier D, Holzinger V, Dalle Donne C, Eufinger Jund Melz T. Fatigue prediction of additive manufactured Ti-6Al-4V for aerospace: Effect of defects surface roughness. 28th ICAF Symp Helsinki, 2015.

[159]. Siddique S, Imran M, Rauer M, Kaloudis M, Wycisk E, Emmelmann C, Walther F. Computed tomography for characterization of fatigue performance of selective laser melted parts. Mat Design2015;83:661–669.

[160]. Meneghetti G, Rigon D, Gennari C. An analysis of defects influence on axial fatigue strength of maraging steel specimens produced by addititive manufacturing. Int J Fatigue2019;118:54–64.

[161]. Romano S, Beretta S, Miccoli S, Gschweitl M. Probabilistic framework for defect tolerant fatigue assessment of AM parts applied to a space component. ASTM Symp on Structural Integrity of Additive Manufactured Parts. November 6-8, 2018, Washington DC, ASTM International.

[162]. Solberg K, Torgersen J, Berto F. Fatigue behaviour of additively manufactured Inconel 718 produced by selective laser melting. Procedia Struct Int2018;13:1762–1767.

[163]. Li P, Warner DH, Pegues JW, Roach MD, Shamsaei N, Phan N. Towards predicting differences in fatigue performance of laser powder bed fused Ti-6Al-4V coupons from the same build. Int J Fatigue2019;126:284–296.

[164]. Laquai R, Müller BR, Kasperovich G, Haubrich J, Requena G, Bruno G. X-ray refraction distinguishes unprocessed powder from empty pores in selective laser melting Ti-6Al-4V. Mat Res Letters2018;6:130–135.

[165]. Hentschel MP, Hosemann R, Lange A, Uther B, Brückner R. Röntgenkleinwinkelbrechung an Metalldrähten, Glasfäden und hartelastischem Polyproplen. Acta Cryst A1987;43:506–513, in German.

[166]. Kupsch A, Müller BR, Lange A, Bruno G. Microstructure characterization of ceramics via 2D and 3D X-ray refraction techniques. J Eur Ceram Soc2017;37:1879–1889.

[167]. Laquai R, Müller BR, Kasperovich G, Requena G, Haubrich J, Bruno G. Classification of defect types in SLM Ti-6Al-4V by x-ray refraction topography. Mater Perf Char (MPC)9:82–93. ASTM International, 2020.

[168]. Thiede T, Mishurova T, Evsevleev S, Serrano-Muñoz I, Gollwitzer C, Bruno G. 3D shape analysis of powder for laser beam melting by synchrotron X-ray CT. Quantum Beam Sci2019;3:3.

[169]. Malekipour E, El-Mounayri H. Common defects and contributing parameters in powder bed fusion AM process and their classification for online monitoring and control: a review. Int J Adv Manuf Technol2018;95:527–550.

[170]. Sobotka JC, Enright MP, McClung PC. Application of critical distances to fatigue at pores. Fatigue Fracture Eng Mat Struct2019;42, 1646–1661.

[171]. Tammas-Williams S, Withers PJ, Todd I, Prangnell PB. The influence of porosity on fatigue crack initiation in additively manufactured titanium components. Sci Rep2017;7(1):7308, 84. [PubMed: 28779073]

[172]. Borbely A, Mughrabi H, Eisenmeier G, Höppel H. A finite element modelling study of strain localization in the vicinity of near-surface cavities as a cause of subsurface fatigue crack initiation. Int J Fracture2002;115:227–22.

[173]. Fan J, McDowell DL, Horstemeyer MF, Gall K. Cyclic plasticity at pores and inclusions in cast Al–Si alloys, Engng Frature Mech2003;70:1281–1302.

[174]. Mishurova T, Rehmer B, Artzt K, Haubrich J, Schoenstein F, Serrano-Munoz I, Requena G, Bruno G. Influence of residual stress and microstructure on mechanical performance on LPBF Ti-6Al-4V, 2020. In preparation.

[175]. Sudhakar KV. Fatigue behavior of a high-density powder metallurgy steel. Int J Fatigue2000;22:729–724.

[176]. Wang Y, Bergström J, Burman C. Four-point bending fatigue behaviour of an iron-based laser sintered material. Int J Fatigue2006;28:1705–1715.

[177]. Romero C, Yang F, Bolzoni L. Fatigue and fracture properties of Ti alloys from powder-based processes – a review. Int J Fatigue2018;117:407–419.

[178]. Ibbett J, Tafazzolimoghaddam B, Delgadillo H, Curiel-Sosa JL. What triggers a microcrack in printed engineering parts produced by selective laser sintering on the first place?Mat Design2015;88:588–597.

[179]. Chern AH, Nandwana P, Yuan T, Kirka MM, Dehoff RR, Liaw PK, Duty CE. A review on the fatigue behaviour of Ti-6Al-4V fabricated by electron beam melting additive manufacturing. Int J Fatigue2019;119:173–184.

[180]. Prithivirajan V, Sangid MD. The role of defects and critical pore size analysis in the fatigue response of additively manufactured IN718 via crystal plasticity. Mat Design2018;150:139–153.

[181]. Gali C, Le Guen E, Lacoste E, Arvieu C. Main defects observed in aluminum alloy parts produced by SLM: from causes to consequences. Add Manufact2018;22:165–175.

[182]. Danninger H, Weiss B. The influence of defects on high cycle fatigue of metallic materials, J Mat Process Techn2003;143-144:179–184.

[183]. Bauereiß A, Scharowsky T, Körner C. Defect generation and propagation mechanisms during additive manufacturing by selective beam melting. J Mat Process Technol2014;214:2522–2528.

[184]. Taheri H, Shoaib MRSB, Koestner LW, Bigelow TA, Collins PC, Bond LJ. Powder-based additive manufacturing – a review of types of defects, generation mechanisms, detection, property evaluation and metrology. Int J Addit Subtract Mat Manuf2017;1:172–209.

[185]. Thiede T, Farahbod-Sternahl L, Serrano-Munoz I, Léonard F, Haberland C, Bruno G. Additively manufactured IN625 struts at the microscale: comprehensive understanding of surface roughness and bulk porosity. J Mat Res Tech, Submitted, 2020.

[186]. Bagehorn S, Wehr J, Maier HJ. Application of mechanical surface finishing processes for roughness reduction and fatigue improvement of additively manufactured Ti-6Al-4V parts. Int J Fatigue2017;102:135–142.

[187]. Chen Z, Cao S, Wu X, Davies HJ. Surface roughness and fatigue properties of selective laser melted Ti-6Al-4V alloy. In: Froes F, Boyer R (eds.) Additive manufacturing for the aerospace industry. Elsevier, Amsterdam/Oxford/Cambridge MA, 2019:283–299.

[188]. Covarrubias EE, Eshraghi M. Effect of build angle on surface properties of nickel superalloys processed by selective laser melting. JOM, J Minerals, Met Mat Soc2018;70:336–342.

[189]. Sikder S, Barani A, Kishawy HA. Effect of adaptive slicing on surface integrity in additive manufacturing. Proc ASME 2014 Int Design Engng Techn Conf Computers Inform in Engng Conf, Buffalo, NY, 2014.

[190]. Barari A, Kishawy HA, Kaji F, Elbestawi MA. On the surface quality of adaptive manufactured parts. Int J Adv Manuf Technol2017;89:1969–1974.

[191]. Pegues J, Roach M, Williamson RS, Shamsaei N. Surface roughness effects on the fatigue strength of additively manufactured Ti-6Al-4V. Int J Fatigue2018;116:543–552.

[192]. Chen Z, Wu X, Tomus D, Davies CHJ. Surface roughness of selective laser melted Ti-6Al-4V alloy components. Add Manufact2018;21:91–103.

[193]. Balachandramurthi AR, Moverare J, Dixit N, Pederson R. Influence of defects and as-built surface roughness on fatigue properties of additively manufactured Alloy 718. Mat Sci Engng A2018;735:463–474.

[194]. ISO 4287Geometrical product specifications (GPS) - Surface texture: profile method - terms, definitions and surface texture parameters, International Organization for Standardization (ISO), Geneva, Switzerland, 2010.

[195]. Fatemi A, Molaei R, Sharifimehr S, Phan N, Shamsaei N. Multiaxial fatigue behavior of wrought and additive manufactured Ti-6Al-4V including surface finish effect. Int J Fatigue2017;100:347–366.

[196]. Taylor D, Clancy OM. The fatigue performance of machined surfaces. Fatigue Fracture Engng Mat Struct1991;14:329–336.

[197]. Novovic D, Dewes RC, Aspinwall DK, Voice W, Bowen P. The effect of machined topography and integrity on fatigue life, Int J of Machine Tools Manufact2004;44:125–134.

[198]. Gockel J, Sheridan L, Koerper B, Whip B. The influence of additive manufacturing processing parameters on surface roughness and fatigue life. Int J Fatigue2019;124:380–388.

[199]. Du Plessis A, le Roux SG. Standardized X-ray tomography testing of additively manufactured parts: A round robin test. Additive Manufact2018;24:125–136.

[200]. Du Plessis A, Glaser D, Moller H, Mathe N, Tshabalala L, Mfusi B, Mostert R. Pore closure effect of laser shock peening of additively manufactured AlSi10Mg. *3D* Printing Add Manuf2019;6:245–252.

[201]. Persenot T, Burr A, Martin G, Buffiere JY, Dendievel R, Maire E. Effect of build orientation on the fatigue properties of as-built Electron Beam Melted Ti-6Al-4V alloy. Int J Fatigue, 2019;118:65–76.

[202]. Vayssette B, Saintier N, Brugger C, El May M, Pessard E. Numerical modelling of surface roughness effect on the fatigue behaviour of Ti-6Al-4V obtained by additive manufacturing. Int J Fatigue2019;123:180–195.

[203]. Andrews S, Sehitoglu H. Computer model for fatigue crack growth from rough surfaces, Int J Fatigue2000;22:619–630.

[204]. Savaidis G, Savaidis A, Tsamasphyros G, Zhang C. On size and technological effects in fatigue analysis and prediction of engineering materials and components. Int J Mech Sci2002;44:521–534.

[205]. Wormsen A, Fjeldstad A, Kirkemo F, Muff AD, Reinås L, Macdonald KA. Fatigue analysis of low alloy steel forgings used in the subsea industry. Int J Fatigue2017;96:43–66.

[206]. Ås SK, Skallerud B, Tveiten BW. Surface roughness characterization for fatigue life predictions using finite element analysis. Int J Fatigue2008;30:2200–2209.

[207]. Rennert D, Kullig E, Vormwald M, Esderts A, Siegele D. Analytical strength assessment of components made of steel, cast iron and aluminium materials in mechanical engineering, FKM Guideline, 6th ed, Forschungskuratorium Maschinenbau (FKM), Frankfurt/Main, Germany, 2013.

[208]. Solberg K, Berto F. Notch-effect interaction in additively manufactured Inconel 718. Int J Fatigue2019;122:35–45.

[209]. McKelvey SA, Fatemi A. Surface finish effect on fatigue behavior of forged steel. Int J Fatigue2012;36:130–145.

[210]. Borrego LP, Ferreira JAM, Costa JDM, Capela C, de Jesus J. A study of fatigue notch sensitivity on titanium alloy TiAl6V4 parts manufacture by selective laser melting. Procedia Struct Integrity2018;13:1000–1005.

[211]. Pegues JW, Shamsaei N, Roach MD, Williamson RS. Fatigue life estimate of additive manufactured parts in the as-built surface condition. Mat Design Process Comm2019;1:c36.

[212]. Vormwald MAnrißlebensdauervorhersage auf der Basis der Schwingbruchmechanik für kurze Risse. PhD Thesis, Institut fur Stahlbau und Werkstoffmechanik, Heft 47, T.H. Darmstadt, in German, 1989.

[213]. Atzori B, Lazzarin P, Meneghetti G. Fracture mechanics and notch sensitivity. Fatigue Fracture Engng Mat Struct2003;26:257–267.

[214]. Madia M, Zerbst U. Application of the cyclic R-curve method to notch fatigue analysis. Int J Fatigue2016;82:71–79.

[215]. Masuo H, Tanaka Y, Morokoshi S, Yaguzra H, Uchida T, Yamamoto Y, Murakami Y. Effects of defects, surface roughness and HIP on fatigue strength of Ti-6Al-4V manufactured by additive manufacturing. Procedia Struct Integrity2017;7:19–26.

[216]. Zerbst UApplication of fracture mechanics to welds with crack origin at the weld toe – A review. Part 1: Consequences of inhomogeneous microstructure for materials testing and failure assessment. Welding World2019;63:1715–1732.

[217]. Romano S, Miccoli SBeretta S. A new FE post-processor for probabilistic fatigue assessment in the presence of defects and its application to AM parts. Int J Fatigue2019;125:324–341.

[218]. Agarwala M, Bourell., Beaman J, Marcus H, Barlow J. Direct selective laser sintering of metals. Rapid Prototyping J1995;1:26–36.

[219]. Tolochko NK, Mozzharov SE, Yadroitsev IA, Laoui T, Froyen L, Tizov VI, Ignatiev ME. Balling process during selective laser treatment of powders. Rapid Prototyping J. 2004;10:78–87.

[220]. Shen YF, Gu DD, Pan YF. Balling process in selective laser sintering 216 stainless steel powder. Key Engng Mat2006;315-216:357–360.

[221]. Tan JH, Wong WLE, Dalgarno KW. An overview of powder granulometry on feedstock and part performance in the selective laser melting process. Add Manuf2017;18:228–225.

[222]. Promoppatum P, Yao S-C. Analytical evaluation of defect generation for selective laser melting of metals. Int J Adv Manuf Technol2019;103:1185–1198.

[223]. King WE, Barth C, Castillo VM, Gallegos GF, Gibbs JW, Hahn DE, Kamath C, Rubenchik AM. Observation of keyhole-mode laser melting in laser powder-bed fusion additive manufacturing. J Mat Process Technol2014;214:2915–2925.

[224]. Teng C, Pal D, Gomg H, Zeng K, Briggs K, Patil N, Stucker B. A review of defect modelling in laser material processing. Add Manufact2017;14:137–147.

[225]. Zhao C, Fezzaa K, Cunningham RW, Wen H, De Carlo FD, Chen L, Rollett AD, Sun T. Real-time monitoring of laser powder bed fusion process using high-speed X-ray imaging and diffraction. Sci Reports, 7, 3602, www.nature.com/scientific reports, 2017.

[226]. Cao X, Wallace W, Immarigeon J-P, Poon C. Research and progress in laser welding of wrought aluminum alloys. II. Metallurgical microstructures, defects and mechanical properties. Mat Manufact Processes2002;18:23–49.

[227]. Cunningham R, Zhao C, Parab N, Kantzos C, Pauza J, Fezzaa K, Sun T, Rollett AD. Keyhole threshold and morphology in Laser Melting revealed by ultrahigh-speed x-Ray imaging. Science2019;363:849–52. [PubMed: 30792298]

[228]. Schmidtke K, Palm F, Hawkins A, Emmelmann C. Process and mechanical properties: Applicability of a scandium modified Al-alloy for laser additive manufacturing. Phys Procedia2011;12:369–374.

[229]. Brandão AD, Gerard R, Gumpinger J, Beretta S, Makaya A, Pambaguian L, Ghidini T. Challenges in additive manufacturing of space parts: Powder feedstock cross-contamination and its impact on end products. Materials2017;10:522.

[230]. Johnson AS, Shao S, Shamsaei N, Thompson SM, Bian L. Microstructure, fatigue behavior, and failure mechanisms of direct laser-deposited Inconel 718. JOM, J Minerals, Met Mat Soc2017;69:597–603.

[231]. Hrabe N, White R, Lucon E. Effects of internal porosity and crystallographic texture on Charpy absorbed energy of electron beam melting titanium alloy (Ti-6Al-4V). Mat Sci Engng A2019;742:269–277.

[232]. Ziolkowski G, Chlebus E, Szymczyk P, Kurzac J. Application of x-ray CT method for discontinuity and porosity detection in 316L stainless steel parts produced with SLM technology. Archives Civil Mech Engng2014;14:608–614.

[233]. Maskery I, Aboilkhair NT, Corfield MR, Tuck C, Clare AT, Leach RK, Wildman RD, Ashcroft IA, Hague RJM. Quantification and characterization of porosity in selectively laser melted Al-Si10-Mg using X-ray computed tomography. Mat Charact2016;111:193–204.

[234]. Seifi M, Salem A, Satko D, Shaffer J, Lewandowski JJ. Defect distribution and microstructure heterogeneity effects on fracture resistance and fatigue behavior of EBM Ti-6Al-4V. Int J Fatigue2017;94:263–287.

[235]. Leuders S, Vollmer M, Brenne F, Tröster T, Niendorf T. Fatigue strength prediction for titanium alloy TiAl6V4 manufactured by Selective Laser Melting. Met Mat Trans A2015;46A:3816–3823.

[236]. Murakami YBeretta S. Small defects and inhomogeneities in fatigue strength: experiments, models and statistical implications, Extremes1999;2:123–147.

[237]. ASTM. E2283-03 Standard practice for extreme value analysis of nonmetallic inclusions in steels and other microstructural features, American Society for Testing and Materials (ASTM), Philadelphia, 2003.

[238]. Romao S, Beretta S, Brandão A, Gumpinger J, Ghidini T. HCF resistance of AlSi10Mg produced by SLM in relation to the presence of defects. Procedia Struct Integrity2017;7:101–108.

[239]. Romano S, Brandão A, Gumpinger J, Gschweitl M, Beretta S. Qualification of AM parts: extreme value statistics applied to tomographic measurements. Mat Design2017;131:32–46.

[240]. FAA (Federal Aviation Adminmistration)Turbine Rotor Material Design. DOT/FAA/AR-00/64; Appendix A: The development of anomaly distributions for aircracft engine titanium disk alloys, Final Report, 2000.

[241]. McClung RC, Enright MP, Millwater HT, Leverant GR, Hudak SJ Jr, A software framework for probabilistic fatigue life assessment of gas turbine engine rotors. J ASTM Int2004;1:199–215.

[242]. Withers PJ. Residual stress and its role in failure. Rep Prog Phys2007;70:2211–2264.

[243]. Withers PJ., Bhadeshia HKDH. Residual stress. Part 1 – measurement techniques. Mat Sci Technol2001;17:355–375.

[244]. Li C, Liu ZY, Fang XY, Guo YB. Residual stress in metal additive manufacturing. Procedia CIRP2018;71:348–353.

[245]. Green D, Knowles J. The treatment of residual stress in fracture assessment of pressure vessels. ASME J Pressure Vessels Piping1992;233:237–247.

[246]. Budden PJ, Sharples JK. Treatment of secondary stresses. In: Ainsworth RA, Schwalbe K-H (eds) Comprehensive Structural Integrity; Volume 7: Practical Failure Assessment Methods. Elsevier, 2003:245–287.

[247]. Hensel J, Nitschke-Pagel T, Tchoffo-Ngoula D, Beier HTh, Tchuindjang D, Zerbst U. Welding residual stresses, fatigue crack propagation and fatigue strength. Engng Fracture Mech2018;198:123–141.

[248]. McClung RC, Chell GG, Lee Y-D, Russell DA, Orient GE. Development of a practical methodology for elastic-plastic and fully plastic fatigue crack growth. NASA Report NASA/CR-1999-209428, 1999.

[249]. BS7910Guide to methods for assessing the acceptability of flaws in metallic structures. Including Amendment (2015) and Corrigenda I-2. The British Standards Institution (BSI) Standards Publ., London, 2013.

[250]. Williams RJ, Hooper PA, Davies CM. Finite element prediction and validation of residual stress profiles in 316L samples manufactured by laser powder bed fusion. Procedia Struct Integrity2018;13:1353–1358.

[251]. Liu Y, Yang Y, Wang D. A study on the residual stress during selective laser melting (SLM) of metallic power. Int J Adv Manuf Technol2016;87:647–656.

[252]. Mishurova T, Cabeza S, Artzt K, Haubrich J, Klaus M, Genzel Ch, Requena G, Bruno G. An assessment of subsurface residual stress in SLM Ti-6Al-4V. Materials2017;10:348.

[253]. Mishurova T, Cabeza S, Thiede T, Nadammal N, Kromm A, Klaus M, Genzel Ch, Haberland Ch, Bruno G. The influence of the support structure on residual stress and distortion in SLM Inconel 718 parts. Met Mat Trans A2018;49:3038–3046.

[254]. Serrano-Munoz IMishurova T, Nadammal N, Thiede T, Trofimov A, Evans A, Ulbricht A, Kromm A, Bruno G. The subsurface residual stress distribution dependence on the scan strategy in L-BPF IN718 in as built and released conditions. Adv Eng Mater, Submitted2020.

[255]. Bartlett JL, Croom BP, Burdick J, Henkel D, Li X. Revealing mechanisms of residual stress development in additive manufacturing via digital image correlation. Additive Manufact2018;22:1–12.

[256]. Edwards P, O'Conner A, Ramulu M. Electron Beam Additive Manufacturing of titanium components: properties and performance. J Manufact Sci Engng2013;135 (6):061016-061016–17.

[257]. Wu AS, Brown DW, Kumar M, Gallegos G, King WE. An experimental investigation into additive manufacturing induced residual stresses in 316L stainless steel. Met Mat Transact A2014;45:6260–6270.

[258]. Shamsaei N, Yadollahi A, Bian L, Thompson SM. An overview of direct laser deposition for additive manufacturing; Part II: Mechanical behavior, process parameter optimization and control. Additive Manufact2015;8:12–35.

[259]. Ahmad B, van der Veen SO, Fitzpatrick ME, Guo H. Residual stress evaluation in selective-laser-melting additively manufactured titanium (Ti6Al4V) and Inconel 718 using the contour method and numerical simulation. Additive Manufact2018;22:571–582.

[260]. Serrano-Munoz I, Mishurova T, Thiede T, Sprengel M, Nadammal N, Nolze G, Saliwan-Neumann R, Evans A, Bruno G. The residual stress in as-built Laser Powder Bed Fusion IN718 alloy as a consequence of the microstructure induced by the scan strategy. Sci Rep, Submitted2020.

[261]. Li C, Liu JF, Guo YB. Prediction of residual stress and part distortion in selective laser melting. Procedia CIRP2016;45:171–174.

[262]. Gu D, He B. Finite element simulation and experimental investigation of residual stresses in selective laser melted Ti-Ni shape memory alloy. Comp Mat Sci2016;117:221–232.

[263]. Hrabe N, Gnäupel-Herold T, Quinn T. Fatigue properties of a titanium alloy (Ti-6Al-4V) fabricated via electron beam melting (EBM): Effects of internal defects and residual stress. Int J Fatigue, 2017;94:202–210.

[264]. Werner T, Madia M, Zerbst U. Experimental investigation of cyclic R-curves for additively manufactured 316L steel. ESIAM 19, 9-119, Trondheim, Norway, 2019.

[265]. Tabernig B, Pippan R. Determination of the length dependence of the threshold for fatigue crack propagation. Engng Fract Mech2002;69, 899–907.

[266]. Zerbst U, Madia M, Hellmann D. An analytical fracture mechanics model for estimating of S-N curves of metallic alloys containing large second phase particles. Engng Fracture Mech2012;82:115–134.

[267]. Conti P, Cianetti F, Pilerci P. Parametric finite element model of SLM additive manufacturing process. Procedia Struct Integrity2018;8:410–421.

[268]. Farajian-Sohi M, Nitschke-Pagel Th, Dilger K. Residual stress relaxation of quasistatically and cyclically loaded steel welds. Welding World2010;54:R49–R60.

[269]. Evans A, Kim S-B, Shackleton J, Bruno G, Preuss M, Withers PJ. Relaxation of residual stress in shot peened Udimet 720li submitted to solely thermal loads and high temperature low-cycle fatigue. Metall Mater Trans A2005;36:3041–3053.

[270]. McClung RC. A literature survey on the stability and significance of residual stresses during fatigue. Fatigue Fracture Engng Mat Struct2007;30:173–205.

[271]. Walker KF, Liu Q, Brandt M. Evaluation of fatigue crack propagation behaviour in Ti-6Al-4V. Int J Fatigue2017;104:302–308.

[272]. Nezhadfar PD, Burford E, Anderson-Wedge K, Zhang B, Shao S, Daniewicz SR, Shamsaei N. Fatigue crack growth behavior aof additively manufactures 17-4 PH stainless steel: Effects of build orientetion and microstructure. Int J Fatigue2019;123:168–179.

[273]. Miedlar PC, Berens AP, Gunderson A, Gallagher JP. USAF damage tolerant design handbook: Guidelines for the analysis and design of damage tolerant aircraft structures. AFRL-VA-WP-TTR-2003-3002, 2002.

[274]. Konečná R, Kunz L, Bača A, Nicoletto G. Resistance of direct metal laser sintered Ti6Al4V alloy against growth of fatigue cracks. Engng Fracture Mech2017;185:82–91.

[275]. Reschetnik W, Brüggemann J-P, Aydinöz ME, Grydin O, Hoyer K-P, Kullmer G, Richard HA. Fatigue crack growth behavior and mechanical properties of additively processed EN AW-7075 aluminium alloy. Procedia Struct Integrity2016;2:3040–3048.

[276]. Cao F, Zhang T, Ryder MA, Lados DA. A review of the fatigue properties of additively manufactured Ti-6Al-4V. JOM, J Minerals, Met Mat Soc2018;70:349–357.

[277]. Rans C, Michielssen J, Walker M, Wang W, Hoen-Velterop L. Beyond the orthogonal: on the influence of build orientation on fatigue crack growth in SLM Ti-6Al-4V. Int J Fatigue2018;116:344–354.

[278]. Poulin J-R, Kreiteberg A, Terriault P, Brailovski V. Long fatigue crack propagation behavior of laser powder bed-fused inconel 625 with intentionally-seeded porosity. Int J Fatigue2019;127:144–156.

[279]. Konečná R, Kunz L, Nicoletto G, Bača A. Long fatigue crack growth in Inconel 718 produced by selective laser melting. Int J Fatigue2016;92:499–506.

[280]. Plekhov O, Paggi M, Naimark O, Carpinteri A. A dimensional analysis interpretation to grain size and loading frequency dependencies of the Paris and Wohler curves. Int J Fatigue2011;33:477–483.

[281]. Galarraga H, Warren RJ, Lados DA, Dehoff RR, Kirka MM. Fatigue crack growth mechanisms at the microstructure scale in as-fabricated and heat treated Ti-6Al-4V ERLI manufactured by electron beam melting (EBM). Engng Fracture Mech2017;176:263–280.

[282]. Fergani O, Branti Wold A, Berto F, Brotan V, Bambach M. Study of the effect of heat treatment on fatigue crack growth behaviour of 316L stainless steel produced by selective laser merting. Fatigue Fracture Engng Mat Struct2018;41:1102–1119.

[283]. Poulin J-R, Brailovski V, Terriault P. Long fatigue crack propagation behavior of Inconel 625 processed by laser powder bed fusion: Influence of build orientation and post-processing conditions. Int J Fatigue2018;116:634–647.

[284]. Akita M, Uematsu Y, Kakiuchi T, Nakajima M, Kawaguchi R. Defect dominated fatigue behavior in type 630 stainless steel fabricated by selective laser melting. Mat Sci Engng A2016;666:19–26.

[285]. Leuders S, Thöne M, Riemer A, Niendorf T, Tröster T, Richard HA, Maier HJ. On the mechanical behaviour of titanium alloy TiAl6V4 manufactured by selective laser melting: Fatigue and crack growth performance. Int J Fatigue2013;48:300–307.

[286]. ASTM E647-11Standard test method for measurement of fatigue crack growth rates. American Society for Testing and Materials (ASTM), Philadelphia, 2011.

[287]. ISO 12108Metallic materials – Fatigue testing – Fatigue crack growth method. International Organization for Standardization (ISO), Geneva, Switzerland, 2012.

[288]. Benedetti M, Santus C. Notch fatigue and crack growth resistance of Ti-6Al-4V alloy additively manufactured via selective laser melting: A critical distance approach to defect sensitivity. Int J Fatigue2019;121:281–292.

[289]. Riemer A, Richard HA. Crack propagation in additive manufactured materials and structures. Procedia Struct Integrity2016;2:1229–1236.

[290]. Vormwald MElastic-plastic fatigue crack growth. In: Radaj D, Vormwald M (eds) Advanced Methods of Fatigue Assessment, Springer, Berlin/Heidelberg, Chapter 4:391–481, 2013.

[291]. Kirkhope KJ, Bell B, Caron L, Basu RI, Ma K-T. Weld detail fatigue life improvement techniques. Marine Struct1999;12:447–474.

[292]. Wegener T, Günther J, Brenne F, Niendorf T. Role of post fabrication heat treatment on the low-cycle fatigue behavior of electron beam melted Inconel 718 superalloy, accepted in in STP 1620 on ASTM Symposium on Structural Integrity of Additive Manufactured Parts, 2019.

[293]. Yu H, Li F, Wang Z, Zheng X. Fatigue performance of selective laser melted Ti-6Al-4V: Influence of surface finishing, hot isostatic pressing and heat treatments. Int J Fatigue2019;120:175–183.

[294]. Kempf A, Hilgenberg K. Influence of sub-cell structure on the mechanical properties of AlSi10Mg manufactured by laser powder bed fusion. Mater Sci Eng A2020;776:138976.

[295]. Wagener R, Scurria M, Möller B. Einflusse auf das zyklische Spannungs-Dehnungsverhalten von additiv gefertigten Strukturen aus AlSi10Mg. Conference proceedings of the 3rd Meeting of the DVM working group Additive Manufactured Components and Structures, 7 and 8 November 2018, Berlin, Report 403, 57–66; in German, 2018.

[296]. Wagener R, Scurria M, Schnabel K, Bein T. Einflüsse auf das zyklische Werkstoffverhalten von additiv gefertigten metallischen Strukturen und deren Berücksichtigung bei der Schwingfestigkeitsbewertung. In: Richard HA, Schramm B, Zipsner T (eds) Additive Fertigung von Bauteilen und Strukturen – Neue Erkenntnisse und Praxisbeispiele. Springer Vieweg, 101–126; in German, 2019.

[297]. Nezhadfar PD, Shrestha R, Phan N, Shamsai N. Fatigue behavior of additively manufactured 17-4 PH stainless steel: Synergetic effects of surface roughness and heat treatment. Int J Fatigue2019;124, 188–204.

[298]. Masuo H, Tanaka Y, Morokoshi S, Yagura H, Uchida T, Yamamoto Y, Murakami Y. Influence of defects, surface roughness and HIP on the fatigue strength of Ti-6Al-4V manufactured by additive manufacturing. Int J Fatigue2018;117:163–179.

[299]. Yadollahi A, Shamsaei N, Thompson SM, Elwany A, Bian L. Effects of building orientation and heat treatment on fatigue behaviour of selective laser melted 17-4 PH stainless steel. Int J Fatigue2017;94:218–235.

[300]. Zhang C, Zhu H, Liao H, Cheng Y, Hu Z, Zeng X. Effect of heat treatments of fatigue property of selective laser melting AlSi10Mg. Int J Fatigue2018;116:513–522.

[301]. Elangeswaran C, Cutolo A, Muralidharan GK, de Formanoit C, Berto F, Vanmeensel K, van Hooreweder B. Effect of post-treatments on the fatigfue behaviour of 316L stainless steel manufactured by laser powder bed fusion. Int J Fatigue2019;123:31–39.

[302]. Tammas-Williams S, Withers PJ, Todd I, Prangnell PB. Porosity regrow during heat treatment of hot isostatically pressed additively manufactured titanium components. Scripta Mat2016;122:72–76.

[303]. Tillmann W, Schaak C, Nellesen J, Schaper M, Aydinöz ME, Hoyer K-P. Hot isostatic pressing of IN718 components manufactured by selective laser melting. Additive Manufact2017;13:93–102.

[304]. Wang J, Tang HP, Yang K, Liu N, Jia L, Qian M. Selective electron beam manufacturing of Ti-6Al-4V strips: Effect of build orientation, columnar grain orientation, and hot isostatric pressing on tensile properties. JOM, J Minerals, Met Mat Soc2018;70:638–643.

[305]. Zhao X, Li S, Zhang MLiu YSercombe TBWang SHao YYang RMurr LE. Comparison of the microstructures and mechanical properties of Ti–6Al–4V fabricated by selective laser melting and electron beam melting. Mat Design2016;95:21–31.

[306]. Aydinöz ME, Brenne F, Schaper M, Schaak C, Tillmann W, Nellesen J, Niendorf T. On the microstructural and mechanical properties of post-treated additively manufactured Inconel 719 superalloy under quasi-static and cyclic loading. Mat Sci Engng A2016;669:246–258.

[307]. Tammas-Williams S, Withers PJ, Todd I, Prangnell PB. The effectiveness of hot isostatic pressing for closing porosity in titanium parts manufactured by selective electron beam melting. Met Mat Transact A2016;47:1939–1946.

[308]. Åsberg M, Frederiksson G, Hatami S, Frederiksson W, Krakhmalev P. Influence of port treatment on microstructure, porosity and mechanical properties of additive manufactured H13 tool steel. Mat Sci Engng A2019;742:584–589.

[309]. Wu M-W, Lai P-H. The positive effect of hot isostatic pressing on improving the anisotropies of bending and impact properties in selective laser melted Ti-6Al-4V alloy. Mat Sci Engng A2016;658:429–438.

[310]. Lv Y, Lei L, Sun L. Effect of microshot treatment on the fatigue behaviour of laser-melted W6Mo5Cr4V2 steel gear. Int J Fatigue2017;98:121–130.

[311]. Hackel L, Rankin JR, Rubenchik A, King WE, Matthews M. Laser peening: A tool for additive manufacturing post-processing. Additive Manufact2018;24:76–75.

[312]. Colegrove PA, Coules HE, Fairman J, Martina F, Kashoob T, Mamash H, Cozzolino LD. Microstructure and residual stress improvement in wire and arc additively manufactured parts through high-pressure rolling. J Mat Processing Tech2013;213:1782–1791.

[313]. Colegrove PA, Donoghue J, Martina F, Gu J, Prangnell P, Hönnige J. Application of bulk deformation methods for microstructural and material property improvement and residual stress and distortion control in additively manufactured components. ScriptaMat2017;135:111–118.

[314]. Hönnige JR, Colegrove PA, Ahmad B, Fitzpatrick ME, Canguly S, Lee TL, Williams SW. Residual stress and texture control in Ti-6Al-4V wire + arc additively manufactured intersections by stress relief and rolling. Mat Design2018;150:293–203.

[315]. McAndrew AR, Alvarez Rosales M, Colegrove PA, Hönnige JR, Ho A, Fayolle R, Eyitayo K, Stan I, Sukrongpang P, Crochemore A, Pinter Z. Interpass rolling of Ti-6Al-4V wire+arc additively manufactured features for microstructural refinement. Additive Manufact2018;21:340–349.

[316]. Field M, Kahles J. Review of surface integrity of machined components, Ann CIRP1971;20:153–163.

[317]. Tyagi P, Goulet T, Riso C, Stephenson R, Chuenprateep N, Schlitzer J, Benton C, Garcia-Moreno F. Reducing the roughness of internal surface of an additive manufacturing produced 316 steel component by chemopolishing and electropolishing. Additive Manufact2019;25:32–38.

[318]. Persenot T, Burr A, Martin G, Buffiere J-Y, Dendievel R, Maire E, Lachambre J. Fatigue performances of chemically etched thin struts built by selective electron beam melting: experiments and predictions. Materialia, in press, 2020.

[319]. Yasa E, Kruth J-P. Microstructural investigation of selective laser melting 316L stainless steel parts exposed to laser re-melting. Procedia Engng2011;19:389–395.

[320]. Gora WS, Tian Y, Cabo AP, Ardron M, Maier RRJ, Prangnell P, Weston NJ, Hand DP. Enhancing surface finish of additively manufactured titanium and cobalt chrome elements using laser-based finishing. Physics Procedia2016;83:258–263.

[321]. ASTM WK47031. Standard guide for post-process non-destructive testing of metal additively manufactured parts used in aerospace applications. ASTM International, West Conshohocken, PA, 2018.

[322]. ISO/ASTM DTR 52905Additive manufacturing – Non-destructive testing and evaluation – Standard guideline for defect detection in metallic parts. Joint project between ISO TC 261 and ASTM Committee F42; under development, 2019.

[323]. ISO 5817Welding – Fusion welded joints in steel, nickel, titanium and their alloys (beam welding excluded) – Quality levels for imperfections. International Organisation for Standardization (ISO), Geneva, 2014.

[324]. VOLVO Standard STD 181-0004 Volvo Group Weld Quality Standard, 2008.

[325]. Waller JM, Parker BH, Hodges KL, Burke ER, Walker JL. Nondestrutive evaluation of additive manufacturing. State-of-the discipline report. Report NASA/TM-2014-218560, Langley Research Center, Hampton, VA, 2014.

[326]. Everton S, Dickens P, Tuck C, Dutton B. Using laser ultrasound to detect subsurface defects in metal laser powder bed fusion components. JOM, J Minerals, Met Mat Soc2018;70:378–383.

[327]. Mohr G, Altenburg SJ, Ulbricht A, Heinrich P, Baum D, Maierhofer C, Hilgenberg K. (2020In-situ defect detection in laser powder bed fusion by using thermography and optical tomography —Comparison to computed tomography. Metals2020; 10 (1), 103.

[328]. Du Plessis A, Yadroitsava I, Yadroitsev I. Effects of defects on mechanical properties in metal additive manufacturing: A review focusing on X-ray tomography insights. Mat Design2020;187:108385.

[329]. Grimm T, Wiora G, Witt G. Quality control of laser-beam-melted parts by a correlation between their mechanical properties and a three-dimensional surface analysis. JOM, J Minerals, Met Mat Soc2017;69:544–550.

[330]. Müller BR, Lange A, Harwardt M, Hentschel MP. Synchrotron-based micro-CT and refraction-enhanced micro-CT for non-destructive materials characterization. Adv Engng Mat2009;11:435–440.

[331]. Müller BR, Hentschel MP. Micro-diagnostics: X-ray and synchrotron techniques, in: Czichos H (ed) Handbook of technical diagnostics - Fundamentals and application to structures and systems, Springer, Berlin (Germany), 287–300, 2013.

[332]. Müller BR, Cooper RC, Lange A, Kupsch A, Wheeler M, Hentschel MP, Staude A, Pandey A, Shyam A, Bruno G. Stress-induced microcrack density evolution in β-eucryptite ceramics: Experimental observations and possible route to strain hardening. Acta Mat2018; 144 (Supplement C):627–641.

[333]. Kupsch A, Lange A, Hentschel MP, Onel Y, Wolk T, Staude A, Ehrig K, Müller BR, Bruno G. Evaluating porosity in cordierite diesel particulate filter materials, part 1 X-ray refraction. J of Ceramic Sci Techn2013;4:169–176.

[334]. Everton SK, Hirsch M, Stravroulakis P, Leach RK, Clare AT. Review of in-situ monitoring and in-situ metrology for metal additive manufacturing. Mat Design2016;95:431–445.

[335]. Cerniglia D, Montinaro N. Defect detection in additively manufactured components: Laser ultrasound and laser thermography comparison. Procedia Struct Integrity2018;8:154–162.

[336]. DePond PJ, Guss G, Ly S, Calta NP, Deane D, Khairallah S, Matthews MJ. In situ measurements of layer roughness during laser powder bed fusion additively manufactured using low coherence scanning interferometry. Mat Design2018;154:347–359.

[337]. Stockman T, Knapp C, Henderson K, Carpenter J, Schneider J. Stainless steel 304L lens AM process monitoring using in-situ pyrometer data. JOM, J Minerals, Met Mat Soc2018;70:1835–1843.

[338]. Borish M, Post BK, Roschill A, Chesser PC, Love LJ, Gaul KT. Defect identification and mitigation via visual inspection in large scale additive manufacturing. JOM, J Minerals, Met Mat Soc2019;71:893–899.

[339]. Sonsino CM. Concepts and required materials data for fatigue design of PM components. Europ Congress Exhibition on Powder Metallurgy (PM 2001), 22nd to 24th October 2001, Nizza, 80–109.

[340]. Radaj D, Sonsino CM, Fricke W. Fatigue Assessment of Welded Joints by Local Approaches. Cambridge, 2nd ed, Woodhead Publ, 2006.

[341]. Scurria M, Möller B, Wagener R, Melz T. Interaction of geometrical notches and defects with the fatigue strength of additively manufactured AlSi10Mg. Proc First Europ Int Conf Struct Integrity of Additive Manufactured Mat (ESIAM19), 9-11 September 2019, Trondheim.

[342]. Möller B, Bernhard J, Scurria M, Schnabel K, Melz T. Fatigue strength of additively manufactured and laser beam welded AlSi10Mg. Proc First Europ Int Conf Struct Integrity of Additive Manufactured Mat (ESIAM19), 9th to 11th September 2019, Trondheim.

[343]. Schnabel K, Baumgartner J, Scurria M. Challenges in the fatigue strength analysis of additively manufactured metallic components based on finite-element simulations. Automotive CAE Grand Challenge 2019, 16–1742019, Hanau.

[344]. Wagener R, Möller B, Melz T, Scurria M. Deriving Strain Based Local Structural Element Concept for the Fatigue Assessment of Additively Manufactured Structures. SAE Techn Paper 2019-01-0525, 2019.

[345]. Schnabel K, Möller B, Baumgartner J. Fatigue Assessment of Additively Manufactured Metallic Structures Using Local Approaches Based on Finite-Element Simulations. 8th edition of the International conference on fatigue design (Fatigue Design 2019), 20-21 November 2019, Senlis.

[346]. Lawrence FV, Ho N-J. Mazumdar PK. Predicting the Fatigue Resistance of Welds. Annual Review Mat Sci1981;11:401–425.

[347]. Schnabel K, Baumgartner J, Wagener R. Strukturelemente zur Berücksichtigung von Anisotropie und Inhomogenitäten in der rechnerischen Lebensdauerabschätzung von additiv

gefertigten Bauteilen. Conf proc of the 4th Meeting of the DVM working group Additive Manufactured Components and Structures, 6-7 November 2019, Berlin.

[348]. Wagener R, Möller B, Scurria M, Bein T. A fatigue life approach for additively manufactured structures. TMS 2020, 149th Annual Meeting and Exhibition Supplemental Proc, San Diego2020, Springer, 2020:127–138.

[349]. Han Y, Zhuang H, Lu J. Deformation-induced ambient temperature α-to-β phase transition and na,nocrystallization in (α + β) titanium alloy. Mat Res2009;24:3439–3445.

[350]. Markl M, Körner C. Multiscale modeling of powder bed–based additive manufacturing. Ann Rev Mater Res2016;46:93–123.

[351]. Megahed M, Mindt HW, N'Dri N, Duan H, Desmaison O. Metal additive-manufacturing process and residual stress modeling. Integr Mater Manuf Innov2016;5:61–93.

[352]. Ammer R, Markl M, Ljungblad U, Körner C, Rüde U. Simulating fast electron beam melting with a parallel thermal free surface lattice Boltzmann method. Comput Math Appl2014;67:318–330.

[353]. Gu D, Xia V, Dai D. On the role of powder flow behavior in fluid thermodynamics and laser processability of Ni-based composites by selective laser melting. Int J Mach Tool Manuf2019;137:67–78.

[354]. Gong X, Chou K. Phase-field modeling of microstructure evolution in electron beam additive manufacturing. JOM, J Minerals, Met Mat Soc2015;67:1176–1182.

[355]. Rodgers TM, Madison JD, Tikare V. Simulation of metal additive manufacturing microstructures using kinetic Monte Carlo. Comput Mater Sci2017;135:78–89.

[356]. Zhang KS, Ju JW, Li Z, Bai YL, Brocks W. Micromechanics based fatigue life prediction of a polycrystalline metal applying crystal plasticity. Mech Mat2015;85:16–37.

[357]. Cui WAstate-of-the-art review on fatigue life prediction methods for metal structures. J Mar Sci Techn Japan2002;7:43–56.

[358]. Santecchia E, Hamouda AMS, Musharavati F, Zalnezhad E, Cabibbo M, El Mehtedi M, Spigarelli S. A review on fatigue life prediction methods for metals. ADV Mat Sci Engng2016:1–26.

[359]. Gaonkar NValidation of a computational model for predicting fatigue life. PhD Thesis, Carleton University, 2019.

[360]. Schijve JFatigue of structures and materials, Springer Science, & Business Media, 2001.

[361]. Chaboche JL, Lesne PM. A non-linear continuous fatigue damage model. Fatigue Fracture Engng Mat1988;11:1–17.

[362]. Wan H, Wang Q, Jia C, Zhang Z. Multi-scale damage mechanics method for fatigue life prediction of additive manufacture structures of Ti-6Al-4V. Mat Sci Engng A2016;669:269–278.

[363]. Pei CShi D, Yuan H, Li H. Assessment of mechanical properties and fatigue performance of the SLM manufactured nickel-based superalloy Inconel 718. Mat Sci Engng A2019;759:278–287.

[364]. Zhan Z, Li H, Lam KY. Development of a novel fatigue damage model with AM effects for life prediction of commonly used alloys in aerospace. Int J Mech Sci2019;155:110–124.

[365]. Hu Z, Mahadevan S. Uncertainty quantification and management in additive manufacturing: current status, needs, and opportunities. Int J Additive Manuf Techn2017;93:2855–2874.

[366]. Zhu SP, Huang HZ, Smith R, Ontiveros V, He LP , Modarres M. Bayesian framework for probabilistic low cycle fatigue life prediction and uncertainty modeling of aircraft turbine disk alloys. Pobabilistic Engng Mech 2013;34:114–122.

[367]. Siddique S, Awd M, Tenkamp J, Walther F. Development of a stochastic approach for fatigue life prediction of AlSi12 alloy processed by selective laser melting. Engng Fail Anal2017;79:34–50.

[368]. Gussev MN, Busby JT, Field KG, Sokolov MA, Gray SE. Role of Scale Factor During Tensile Testing of Small Specimens. ASTM STP 1576: Small specimen test techniques, 31–49, 2014.

[369]. Dzugan J, Prochazka R, Konopík P. Micro-tensile test technique development and application to mechanical property determination. Small specimen test techniques. In: Sokolov MA, Lucon E (eds) ASTM STP 1576:1–19, ASTM International, West Conshohocken, PA, 2014.

[370]. Rund M, Konopik P. Determination of local tensile and fatigue properties with the use of sub-sized specimens. Proceedings of the ASME 2015 Pres Ves Piping Conf PVP 2015-45958, 2015.

[371]. Rund M, Prochazka R, Konopik P, Dzugan J, Folgar H. Investigation of sample-size influence on tensile test results at different strain rates. Proc Eng2015;114:410–415.

[372]. Gussev MN, Howard RH, Terrani KA, Kevin G. Field: Sub-size tensile specimen design for in-reactor irradiation and post-irradiation testing. Nucl Engng Design2017;320:298–308.

[373]. Kumar K, Madhusoodanan K Rupani, B B. Miniature specimen technique as a tool for estimation of service life of operating pressure equipment, International Conference and Exhibition on Pressure Vessel and Piping (OPE), Chennal, February 7-9, 2006.

[374]. Kohno Y, Kohyama A, Hamilton ML, Hirose T, Katoh Y, Garner FA. Specimen size effects on the tensile properties of JPCA and JFMS. J Nucl Mat2000;283–287:1014–1017.

[375]. Chen F, Chen S, Dong XH, Li CY, Hong XT, Thang XP. Size effects on tensile strength of aluminum-bronze alloy at room temperature, Mat Design, 2015;778–784.

[376]. Haiting L, Yao S, Shuang Y, Pengfei Z, Lei ZAcomprehensive solution to miniaturized tensile testing: Specimen geometry optimization and extraction of constitutive behaviors using inverse FEM procedure. Fusion Engng Design2017;121:188–197.

[377]. Dzugan J, Prochazka R, Konopik P. Low cycle fatigue tests with the use of miniaturized test specimens. Pres Ves Piping (PVP-2017), Waikoloa, Hawaii, USA, 716-202017.

[378]. Dzugan J, Sindelarova M, Prochazka R, Konopik P. Specimens preparation influence on results of micro-tensile tests. Int Conf on Sustain Energy, Environment and Information Engng, Bangkok, 2016.

[379]. Procházka R, Džugan J. Strain controlled cyclic tests on miniaturized specimen. IOP Conf Series: Mat Sci Engng2017;179(1):012060.

[380]. ISO 6892-1Metallic materials - Tensile testing - Part 1: Method of test at room temperature. International Organization for Standardization (ISO), Geneva, Switzerland, 2016.

[381]. Kitagawa H, Takahashi S. Applicability of fracture mechanics to very small cracks or the cracks in the early stage. In: Proc 2nd Intern Conf Mech Behav Mater, Boston, ASM, Cleveland, Ohio, 627–631, 1976.

[382]. Wycsik E, Siddique S, Herzog D, Emmelmann C. Fatigue performance of laser additive manufactured Ti-6Al-4V in very high cycle fatigue regime up to 10^9 cycles. Front Mater2015;2:72.

[383]. Atzori B, Meneghetti G, Susmel L. Material fatigue properties for assessing mechanical components weakened by notches and defects. Fatigue Fracture Engng Mater Struct2005;28:83–97.

[384]. Carboni M, Regazzi D. Effect of the experimental technique onto R dependence of ΔK_{th}. Procedia Engng2011;10:2937–2942.

[385]. Akinawa Y, Zhang LM, Tanaka K. Prediction of the fatigue limit of cracks specimens based on the cyclic R curve method. Fatigue Fracture Engng Mat Struct1997;20:1387–1398.

[386]. Chapetti MD. Fatigue propagation threshold of short cracks under constant amplitude loading. Int J Fatigue2003;25:1319–1326.

[387]. Garb C, Leitner M, Stauder B, Schnubel D, Grün F. Application of modified Kitagawa-Takahashi diagram for fatigue strength assessment of cast Al-Si-Cu alloys. Int J Fatigue2018;111:256–265.

[388]. Siddique S, Awd M, Tencamp J, Walther F. High and very high cycle fatigue failure mechanisms in selective laser melted aluminum alloys. J Mater Res2017;32:4296–4304.

[389]. Frye P, Muhammad M, Simsiriwong J, Shansaei N. Very high cycle fatigue behavior of laser beam-powder bed fusion Inconel 718. Proc 30th Annual Solid Freeform Fabrication Symp – An Additive Manufact Conf. 2019.

[390]. Beretta S, Romano S. A comparison of fatigue strength sensitivity to defects for materials manufactured by AM or traditional processes. Int J Fatigue2017;94:178–191.

[391]. Ngnekou JND, Nadot Y, Henhaff G, Nicolai J, Kan WH, Cairney JM, Ridosz L. Fatigue properties of AlSi10Mg produced by Additive Layer Manufacturing. Int J Fatigue2019;119:160–172.

[392]. Wycisk E, Solbach A, Siddique S, Herzog D, Walther F, Emmelmann C. Effects of defects in laser adaptive manufactured Ti-6Al-4V on fatigue properties. Phys Procedia2014;56:317–378.

[393]. Beretta S, Ghidini A, Lombardo F. Fracture mechanics and scale effects in the fatigue of railway axles. Engng Fracture Mech2005;72:195–208.

[394]. Komi E, Kokkonen P. Inclusion of AM process simulation within the defect tolerant fatigue design concept of SLM manufactured components. Proc 1st ECCOMAS Thematic Conf on Simulation for Additive Manufacturing, 11-13 October 2017, Munich, Germany.

[395]. Benedetti M, Fontanari V, Banmdini M, Zanini F, Carmignato S. Low- and high-cycle fatigue resistance of Ti-6Al-4V ELI additively manufactured via selective laser melting: Mean stress and defect sensitivity. Int J Fatigue2018;107:96–109.

[396]. Nakatani M, Masuo H, Tanaka Y, Murakami Y. Effect of surface roughness on fatigue strength of Ti-6Al-4V alloy manufactured by additive manufacturing. Procedia Struct Integrity2019;19:294–301.

[397]. Maierhofer J, Kolitsch S, Pippan R, Gänser H-P, Madia M, Zerbst U. The cyclic R-curve – determination, problems, limitations and application. Engng Fracture Mech2018;198:45–64.

[398]. Tanaka K, Nakai Y. Propagation and non-propagation of short fatigue cracks at a sharp notch. Fatigue Engng Mat Struct1983;6:315–327.

[399]. Zerbst U, Madia M, Vormwald M. Applying fracture mechanics to fatigue strength determination – some basic considerations. Engng Fracture Mech2019;126:188–201.

[400]. Tridello A, Fioccgi J, Biffi CA, Chiandussi G, Rossetto M, Tuissi A, Paolino DS. Influence of the annealing and defects on the VHCF behavior of an SLM AlSi10Mg alloy. Fatigue Fracture Engng Mat Struct2019;42:2794–2107.

[401]. Tanaka K, Akiniwa Y. Resistance-curve method for predicting propagation threshold of short fatigue cracks at notches. Engng Fracture Mech. 1988;30:863–876.

[402]. McEvily AJ, Endo M, Murakami Y. On the $\sqrt{\text{area}}$ relationship and the short fatigue crack threshold. Fatigue Fracture Engng Mat Struct2003;26:269–278.

[403]. Chapetti MD, Belmonte J, Tagawa T, Miyata T. Integrated fracture mechanics approach to analyse fatigue behavior of welded joints. Sci Tech Welding Joining2004;9:430–438.

[404]. Endo M, McEvily AJ. Prediction of the behavior of small fatigue cracks. Mat Sci Engng A42007;68–470:51–58.

[405]. Zerbst U, Madia M. Fracture mechanics-based assessment of the fatigue strength: approach for the determination of the initial crack size. Fatigue Fracture Engng Mat Struct2015;38:1066–1075.

[406]. Yadollahi A, Mahtabi MJ, Doude HR, Newman JC Jr. (2017aPrediction of fatigue lifes in additively manufactured alloys based on the crack-growth concept. Proc 28th Annual Int Solid Freedom Fabrication Symp, Austin, TX39–47, 2017.

[407]. Newman JC Jr.FASTRAN-2: A fatigue crack growth structural analysis program. NASA TM-104159, 1992.

[408]. Meneghin I, Ivetic G, Stiller M, Molinari G, Ristori V, Della Rata S, Dumont F. Fatigue in additive manufactured aircraft: The long way to make it fly. In: Niepokolczycki A, Komorowski J (eds) ICAF 2019 – Structural Integrity in the Age of Additive Manufacturing. Proc 30th Symp of the Int Committee on Aeronautic Fatigue, Krakow, Poland, 16–30, 2019.

[409]. Komann S, Kiyak Y, Wille F, Zerbst U, Klingbeil D, Weber M. Licensing of German transport packages „CASTOR“: Fracture mechanics assessment. ASME Press Vess Piping Div Publ. PVP 3, 2012.

[410]. Moeini G, Sajadifar SV, Wegener T, Brenne F, Niendorf T, Böhm S. On the low-cycle fatigue behavior of friction stir welded Al-Si12 parts produced by selective laser melting. Mat Sci Engng A2019;764:138189.

[411]. Kucharczyk P, Madia M, Zerbst U, Schork B, Gerwin P, Münstermann S. Fracture-mechanics based prediction of the fatigue strength of weldments. Material aspects. Engng Fracture Mech2018;198:79–102.

[412]. Khan K, Mohr G, Hilgenberg K, De A. Probing a novel heat source model and adaptive remeshing technique to simulate laser powder bed fusion with experimental validation. Comput Mater Sci, revised version submitted, 2020.

[413]. Seidel C, Zaeh MF. Multi-scale Modelling Approach for Contributing to Reduced Distortion in Parts Made by Laser-based Powder Bed Fusion. Proc CIRP2018;67:197–202.

[414]. Illies O, Li G, Jürgens J-P, Ploshikhin V, Herzog D, Emmelmann C. Numerical modelling and experimental validation of thermal history of titanium alloys in laser beam melting. Proc CIRP2018;74:92–96.

[415]. Greitemeier D, Dalle Donne C, Syassen F, Eufinger J, Melz T. Effect of surface roughness in fatigue performance of additive manufactured Ti-6Al-4V. Mat Sci Technol2016;32:629–634.

[416]. Mardaras J, Emile P, Santgerma A. Airbus approach for F&DT stress justification of additive manufacturing parts. Procedia Struct Integrity2017;7:109–115.

[417]. Laz PJ, Hillberry BM. Fatigue life prediction from inclusion-initiated cracks. Int J Fatigue1998;20:263–270.

[418]. Thumser R, Kleemann S, Bergmann JW, Kleemann A. Investigation on defect distribution and its statistical evaluation for case hardened material states. Int J Fatigue2012;41:52–56.

[419]. ISO 21432 - Non-destructive testing — Standard test method for determining residual stresses by neutron diffraction. International Organization for Standardization (ISO), Geneva, Switzerland, 2019.

[420]. EN 15305-2009-1 - Non-destructive testing - Test method for residual stress analysis by X-ray diffraction. European Standard, 2009.

[421]. El Haddad MH, Smith KN., Topper TH. Fatigue crack propagation of short cracks. Trans. ASME, J Engng Mat Techn, 1979;101:42–46.

[422]. Persenot T, Burr A, Plancher E, Buffière J-Y, Dendievel R, Martin G. Effect of ultrasonic shot peening on the surface defects of thin struts built by electron beam melting: consequences on fatigue resistance. Additive Manufact2019;28:821–30.

[423]. Wasmer K, Kenel C, Leinenbach C, Shevchik SA. In situ and real-time monitoring of powder-bed AM by combining acoustic emission and artificial intelligence. In: Meboldt M, Klahn C (eds) Industrializing additive manufacturing. Proc of Additive Manufacturing in Products and Applications – AMPA201770-81. Springer Int Publ:200–209, 2018.

[424]. Zhang W, BebRoy T. An improved prediction of residual stresses and distortion in additive manufacturing. Comp Mat Sci2017;126:360–372.

[425]. Lesperance X, Ilie P, Ince A. Very high cycle fatigue characterization of additively manufactured AlSi10Mg and AlSi7Mg aluminium alloys based on ultrasonic fatigue testingFatigue Fracture Engng Mat Struct2020;1–9

[426]. Voloskov B, Evlashin S, Dagesyan S, Abimov S, Akhatov I, Sergeichev I. Very high cycle fatigue behavior of additively manufactured 316L stainless steel. Materials2020;13:3293.

[427]. Barriobero-Vila P, Artzt K, Stark A, Schell N, Siggel M, Gussone J, Kleinert J, Requena G, Haubrich J. Mapping the geometry of Ti-6Al-4V: From martensite decomposition to localized spheroidization during selective laser melting. Scripta Mat2020;182:48–52.

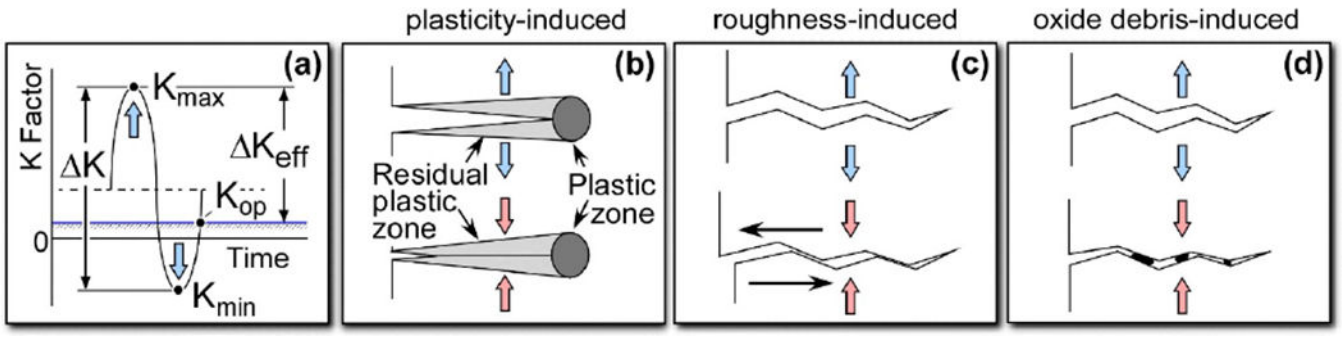

Fig. 1:

Important crack closure mechanisms. (a) Nomenclature for defining the cyclic crack driving force for crack closure; (b) plasticity-induced mechanism; (c) roughness-induced mechanism; (d) oxide debris-induced mechanism.

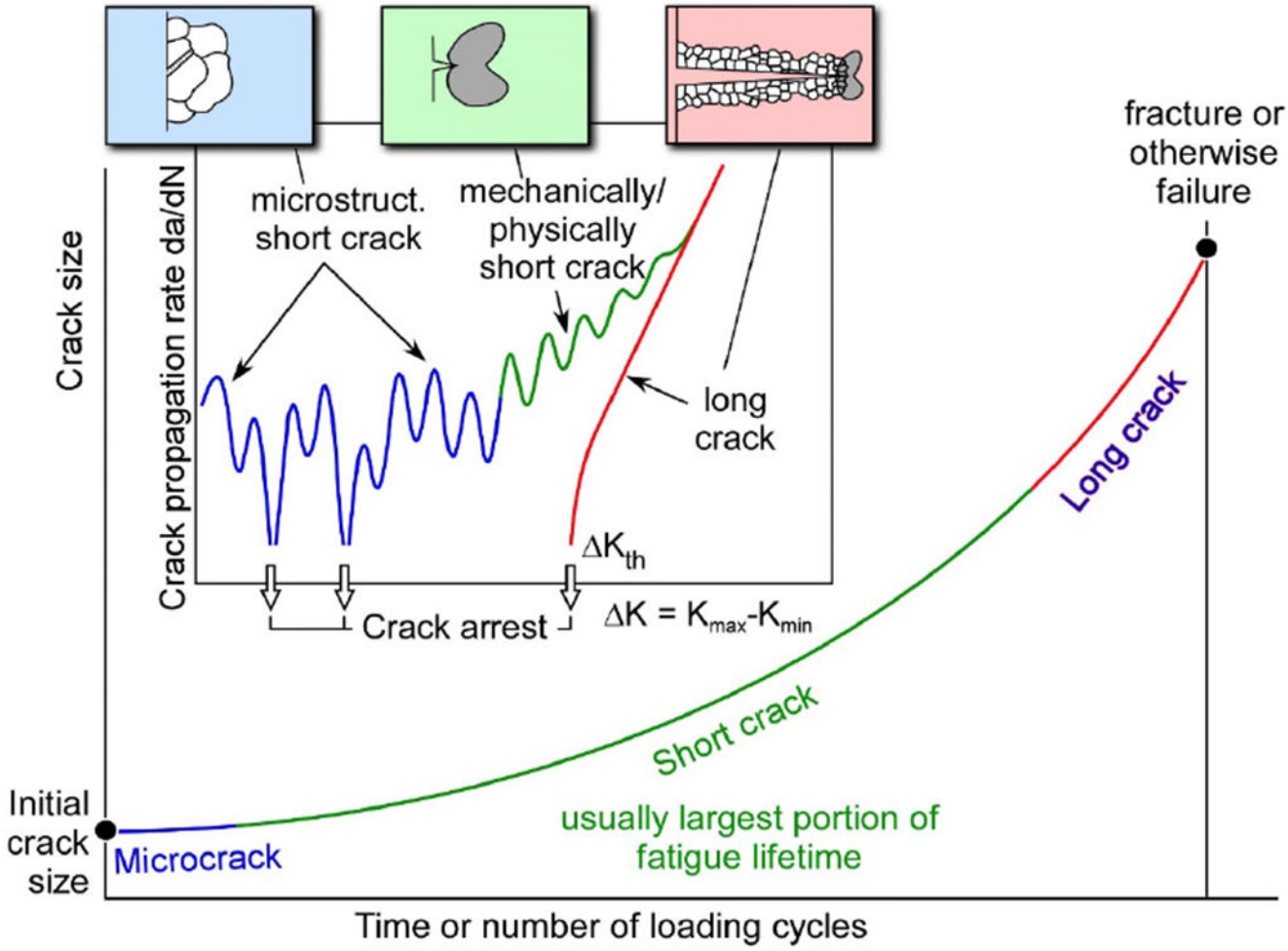

Fig. 2:
Schematic view of the subsequent fatigue crack propagation stages.

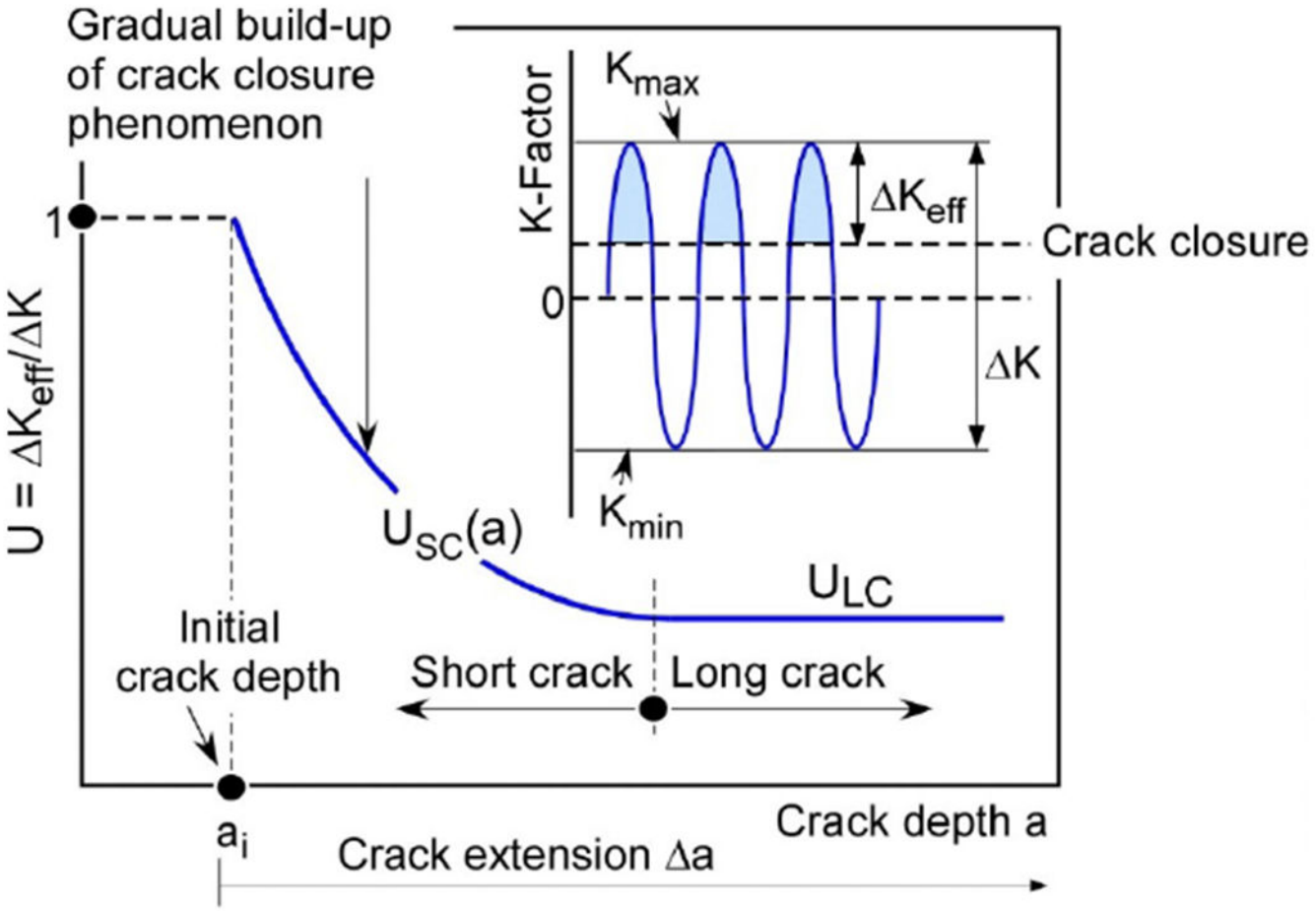

Fig. 3:
Gradual build-up of the crack closure phenomenon, schematic view.

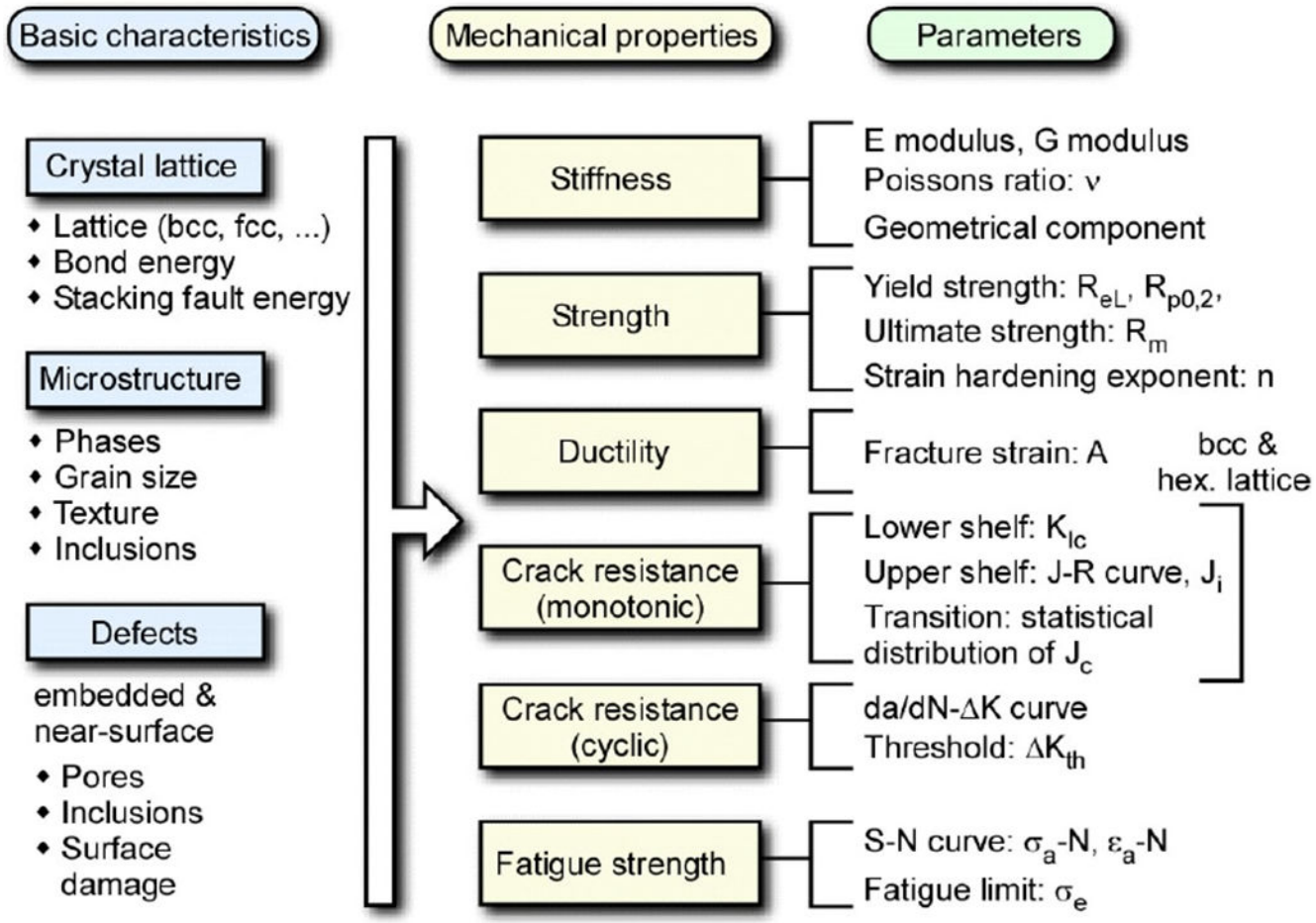

Fig. 4:

Relations between the basic characteristics, basic mechanical properties and the mechanical parameters in metallic materials; according to [66].

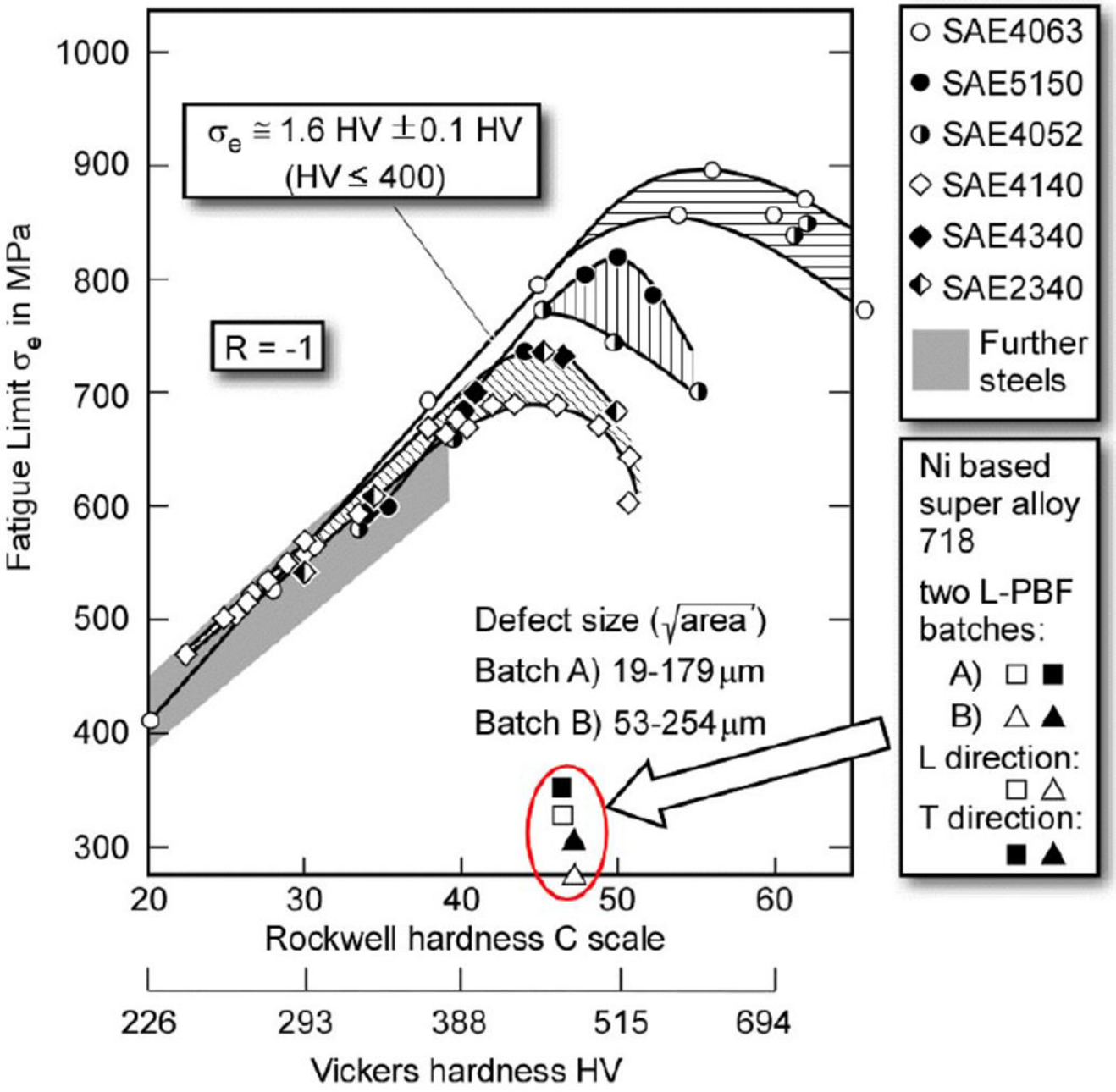

Fig. 5:
Relationship between hardness and fatigue limit. Empirical data: SAE steels: [67], further steels: [68], AM-L-PBF manufactured super alloy: [69].

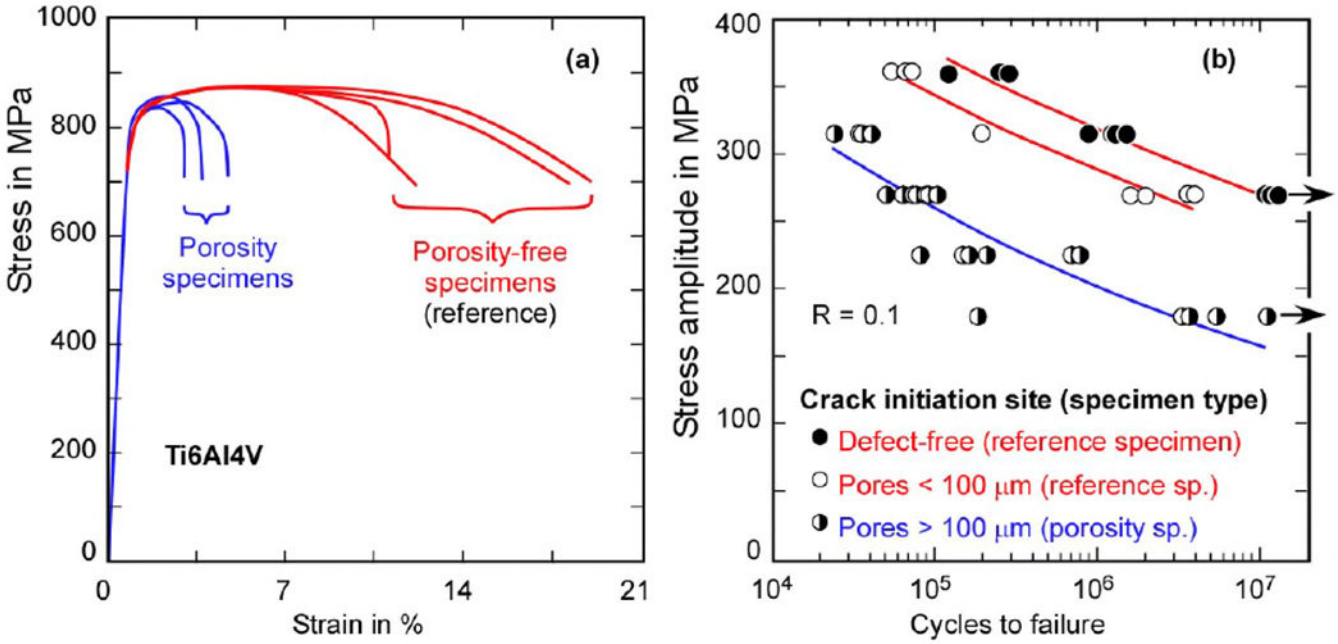

Fig. 6 :

Effect of porosity on the material behaviour of an AM generated Ti6Al4V; (a) Engineering stress-strain curves; (b) S-N curves; according to [26].

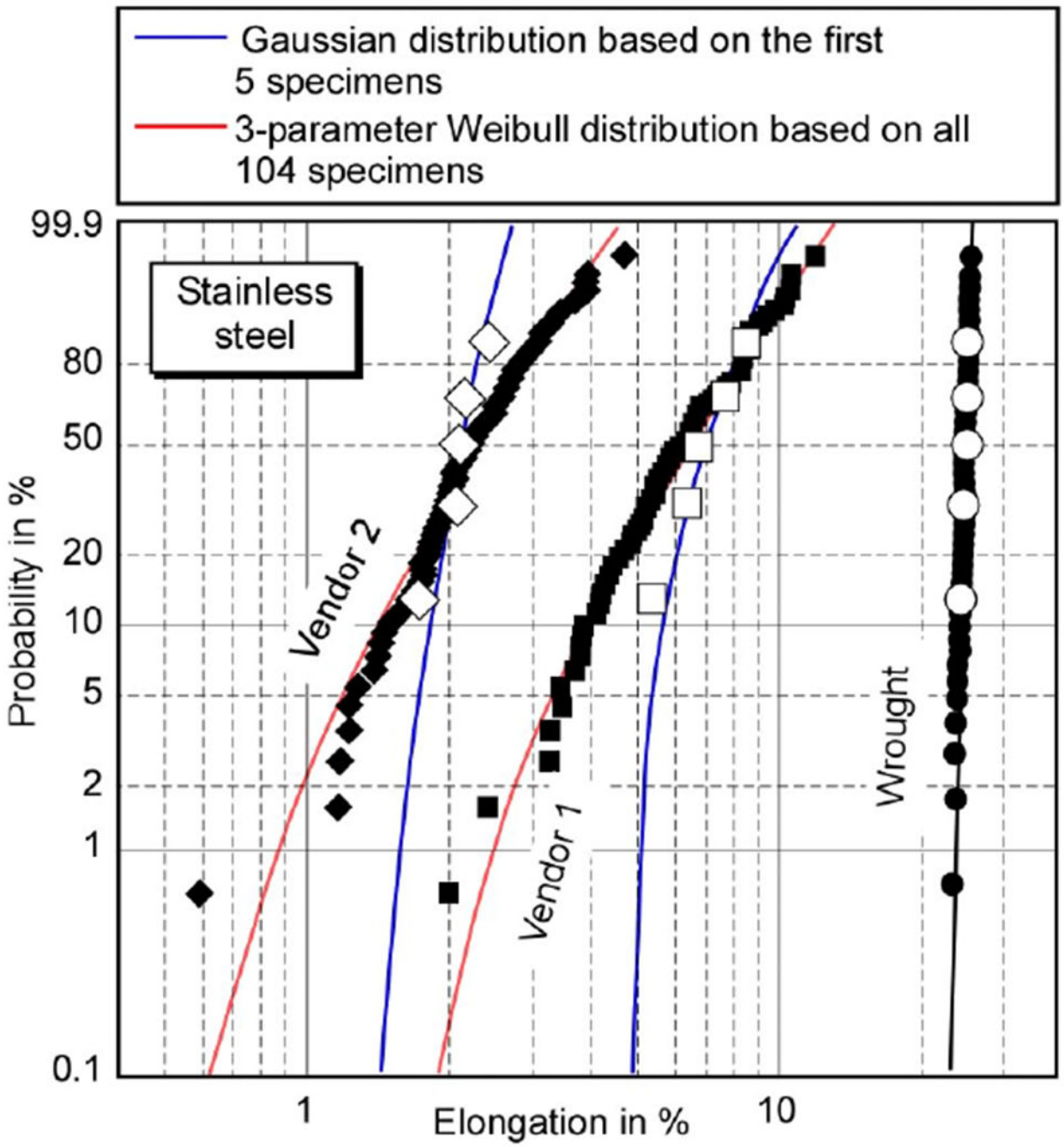

Fig. 7:

Statistical distributions of the elongation at failure of a precipitation-hardening alloy 17-4PH manufactured by a powder bed fusion process by two commercial vendors; comparison with conventionally generated material. The cumulative distribution functions are based on 5 specimens only (Gaussian, blue curves) and on the complete data sets (3-parameter Weibull, red curves); according to [73].

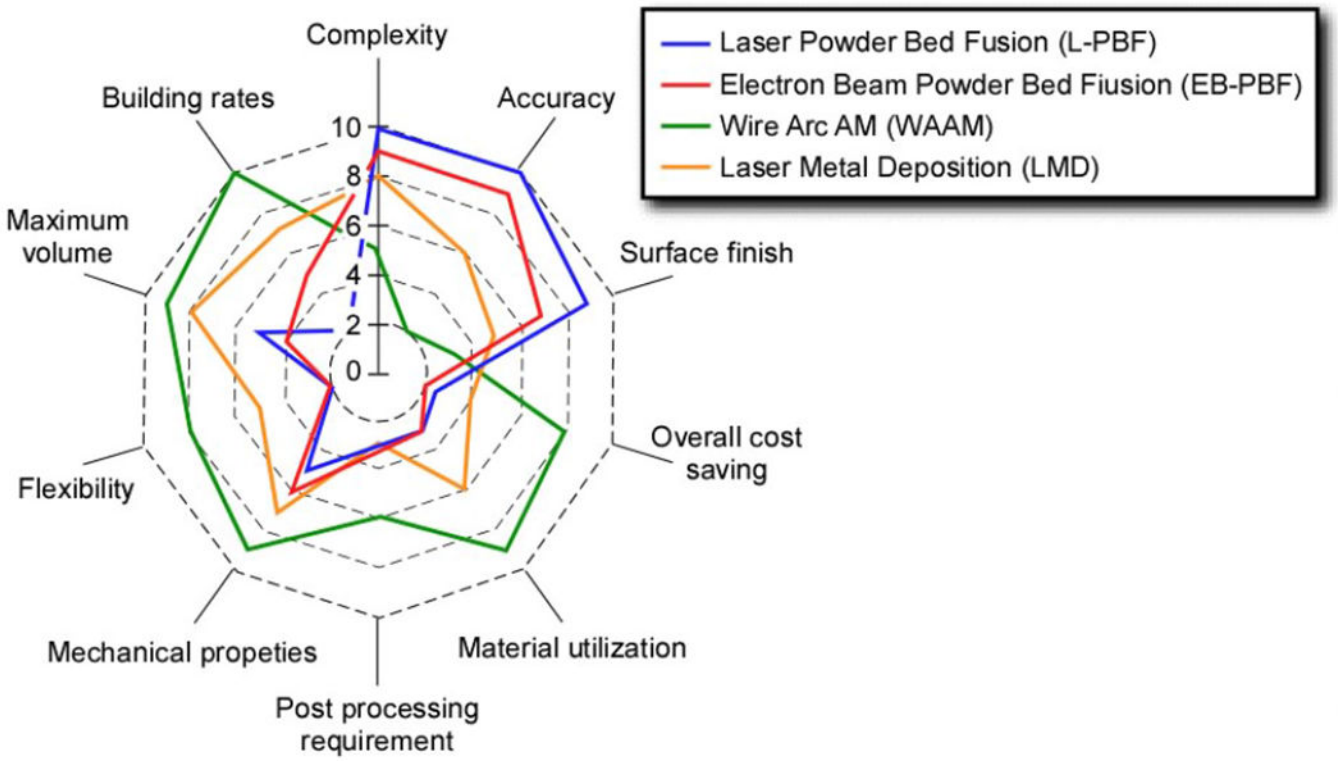

Fig. 8.

Comparison framework among different metal AM technologies used in the aerospace industry; according to [80].

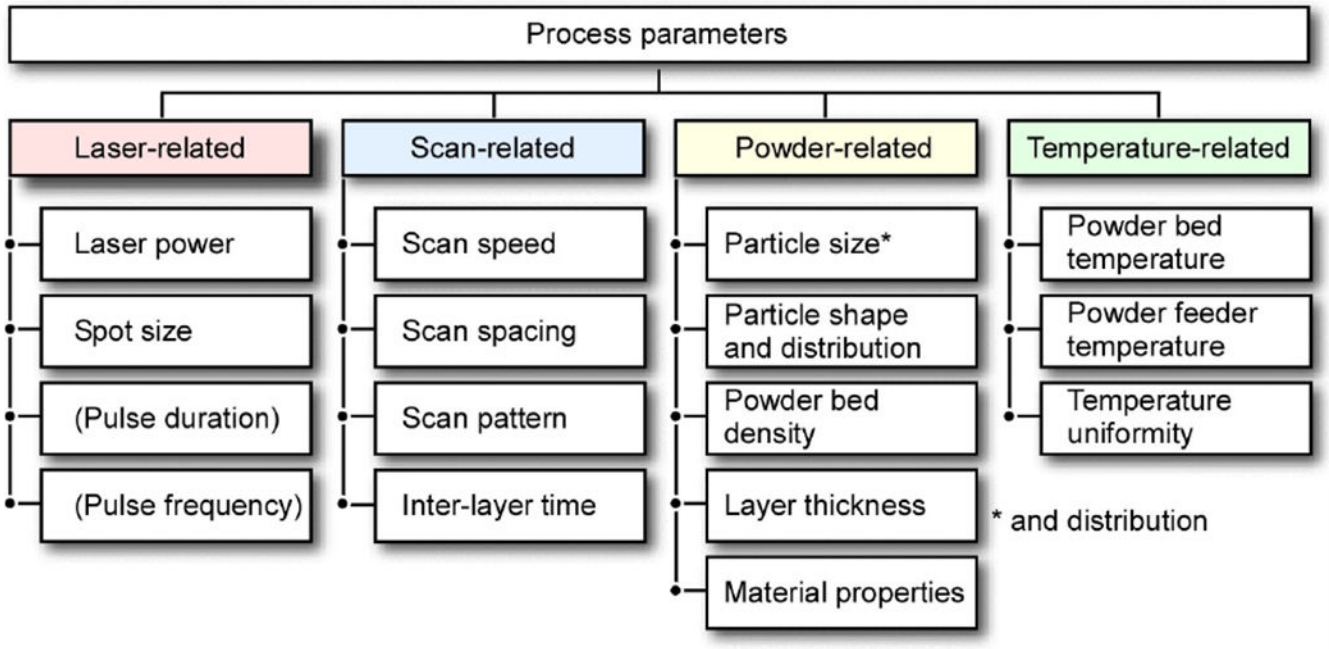

Fig. 9:

Process parameters in Laser Powder Bed Fusion (L-PBF) which control damage tolerance relevant material properties; according to [81], slightly modified.

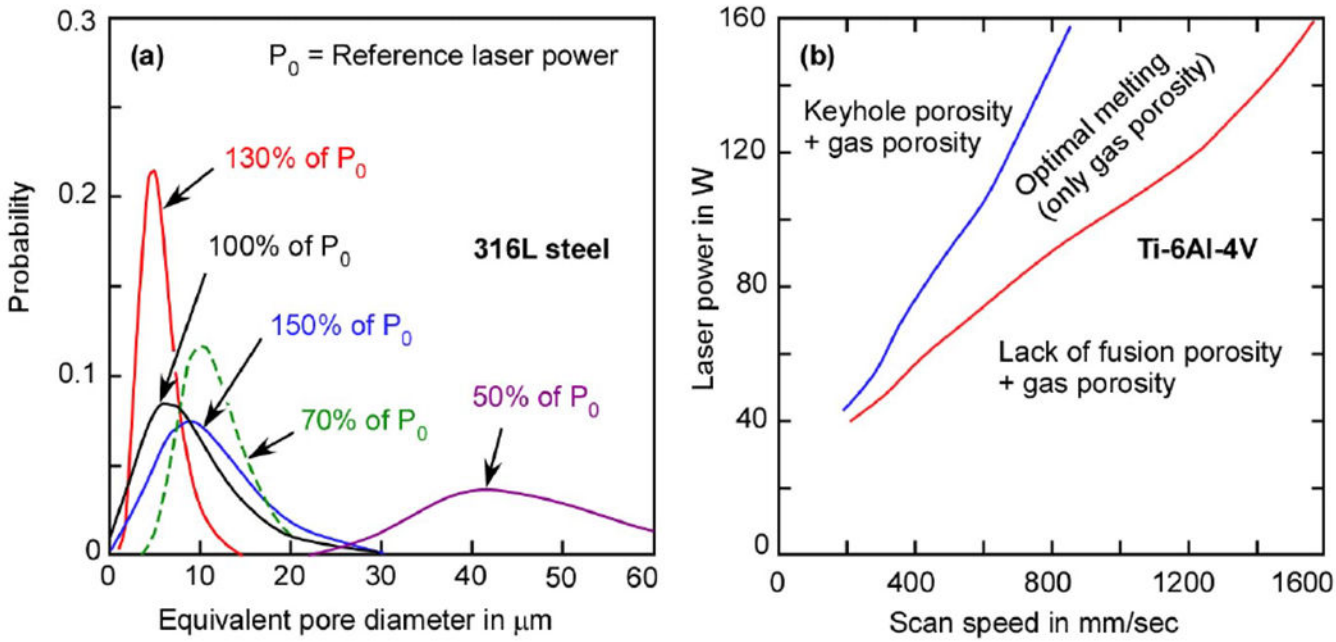

Fig. 10:

Effect of laser power and scan speed on the formation of defects in AM materials; (a) Gumbel extreme value distribution probability density function of the defect size in powder bed fusion manufactured 316L steel for varying laser power; according to [88]. (b) Processing window developed for L-PBF Ti-6Al-4V; according to [89].

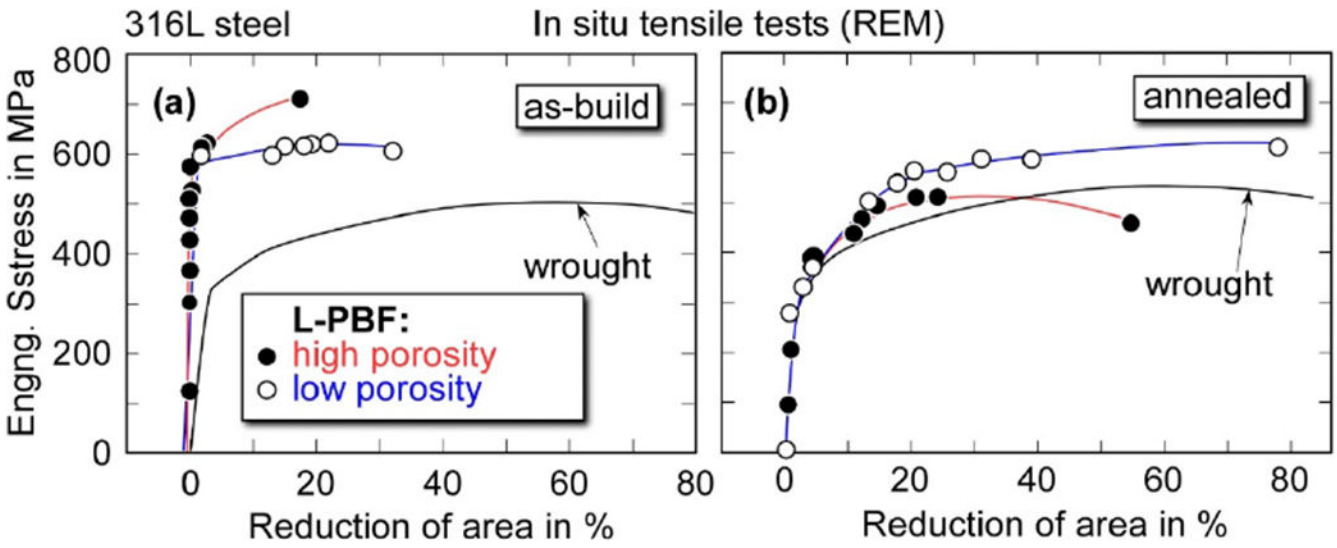

Fig. 11:

Engineering stress-strain curves of as-built and annealed 316L steel compared to its conventional manufactured equivalent; high porosity: 2.4 ± 0.7% with regions with maximum values up to 17%; low porosity: 0.1 ± 0.04% (maximum values < 2%); for comparison: wrought material: 0.004 ± 0.0015%; according to [96].

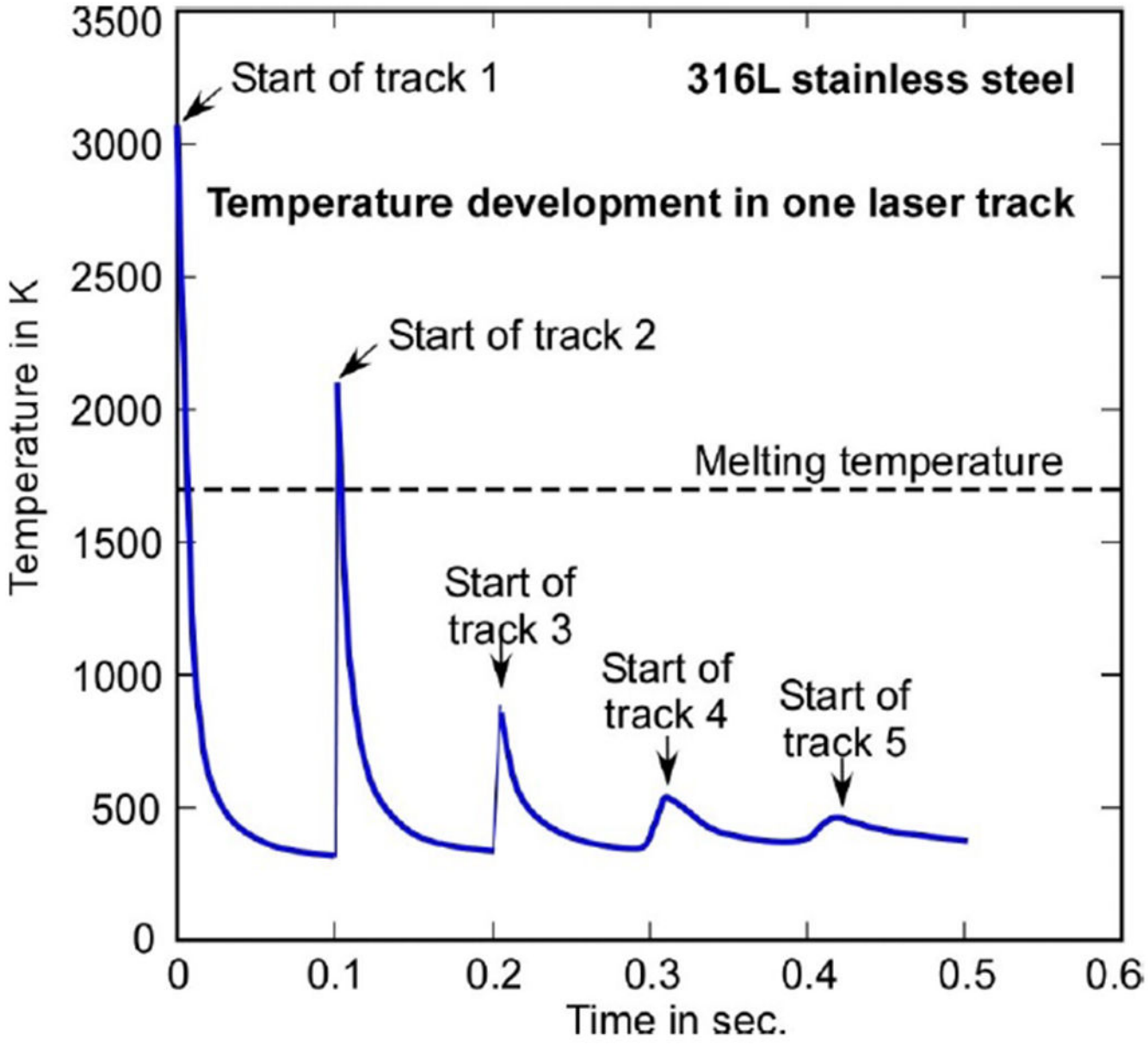

Fig. 12:

Example for a finite element simulation of the temperature development in the first track of a Laser Powder Bed Fusion (L-PBF) sub-structure; 316L stainless steel. The subsequent tracks (larger numbers refer to a larger lateral distance to the first one) cause the reheating of the first one; according to [104].

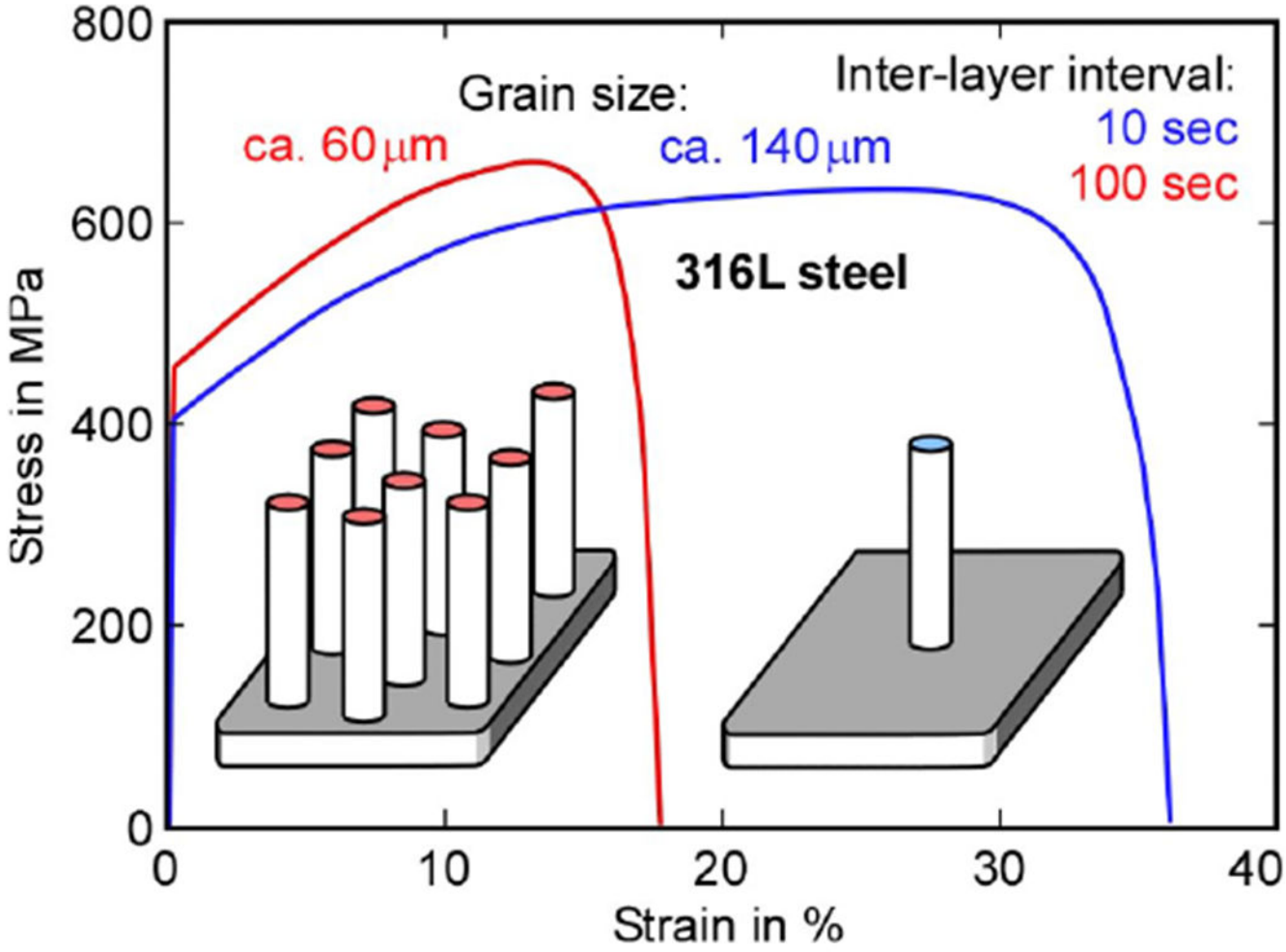

Fig. 13:
Example for the effect of different inter-layer times on the grain size and the stress-strain curve of 316 stainless steel processed by laser metal deposition; according to [20].

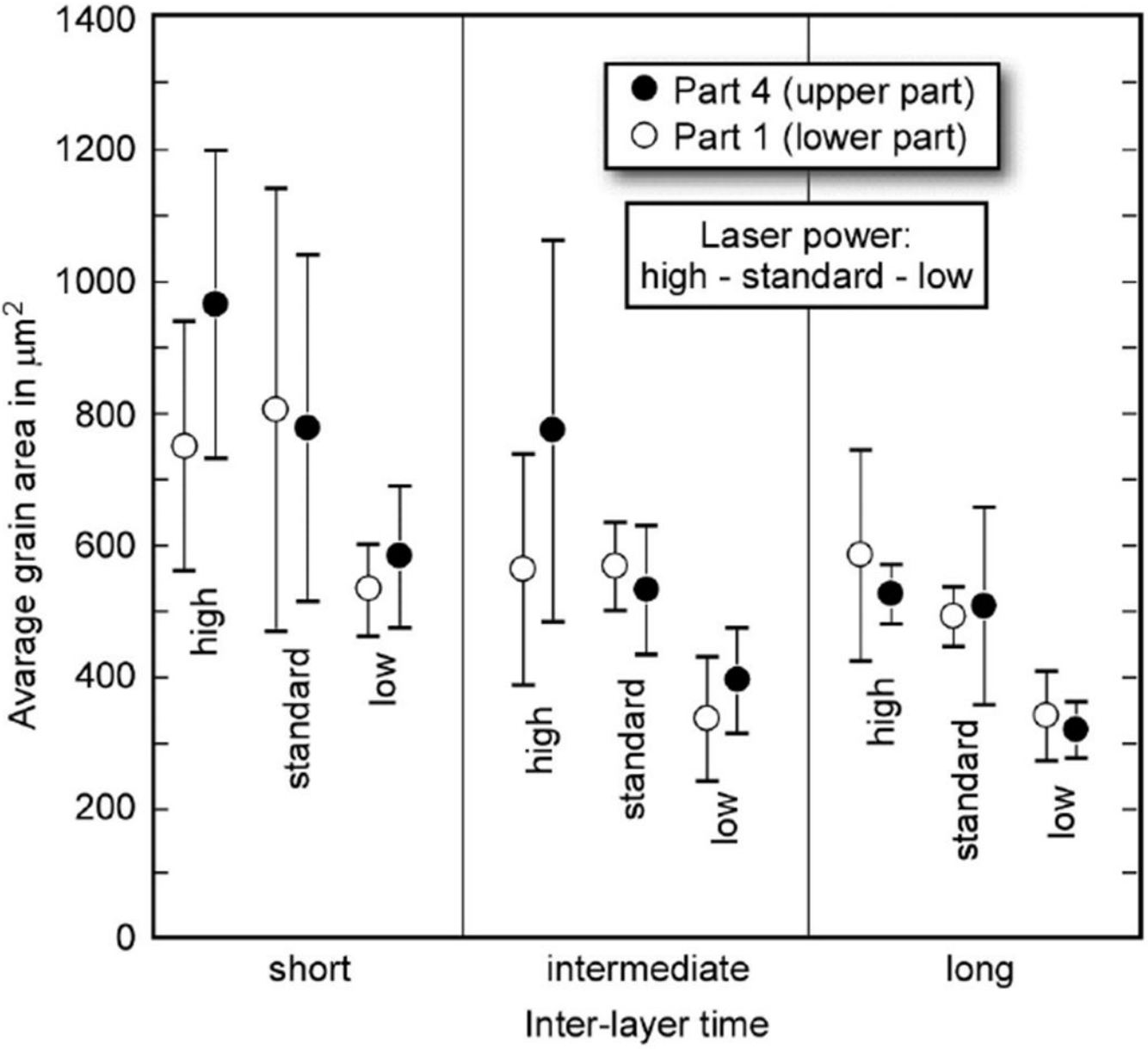

Fig. 14:

Effect of inter-layer time and laser power on the average grain size of 316L stainless steel cuboids at two different positions along the build direction (part 1: 7.5 mm, part 4: 100 mm). Error bars indicate the standard deviation of N = 5 measurements; according to [108].

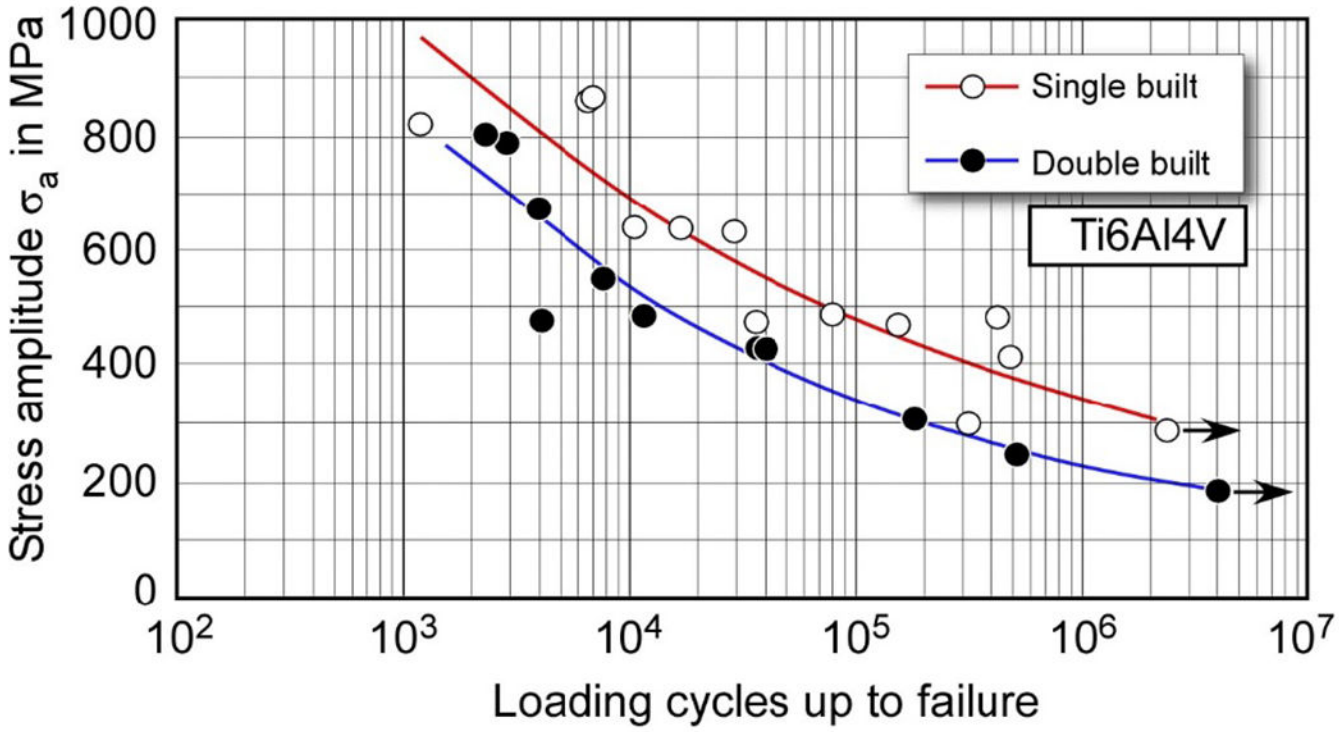

Fig. 15:

S-N curve data for single and double-built Ti6Al4V by laser metal deposition; according to [103]. Note that the data points in the diagram correspond to tests with varying R ratios. “Double built” means two columns versus one (“single built”) in a single build job.

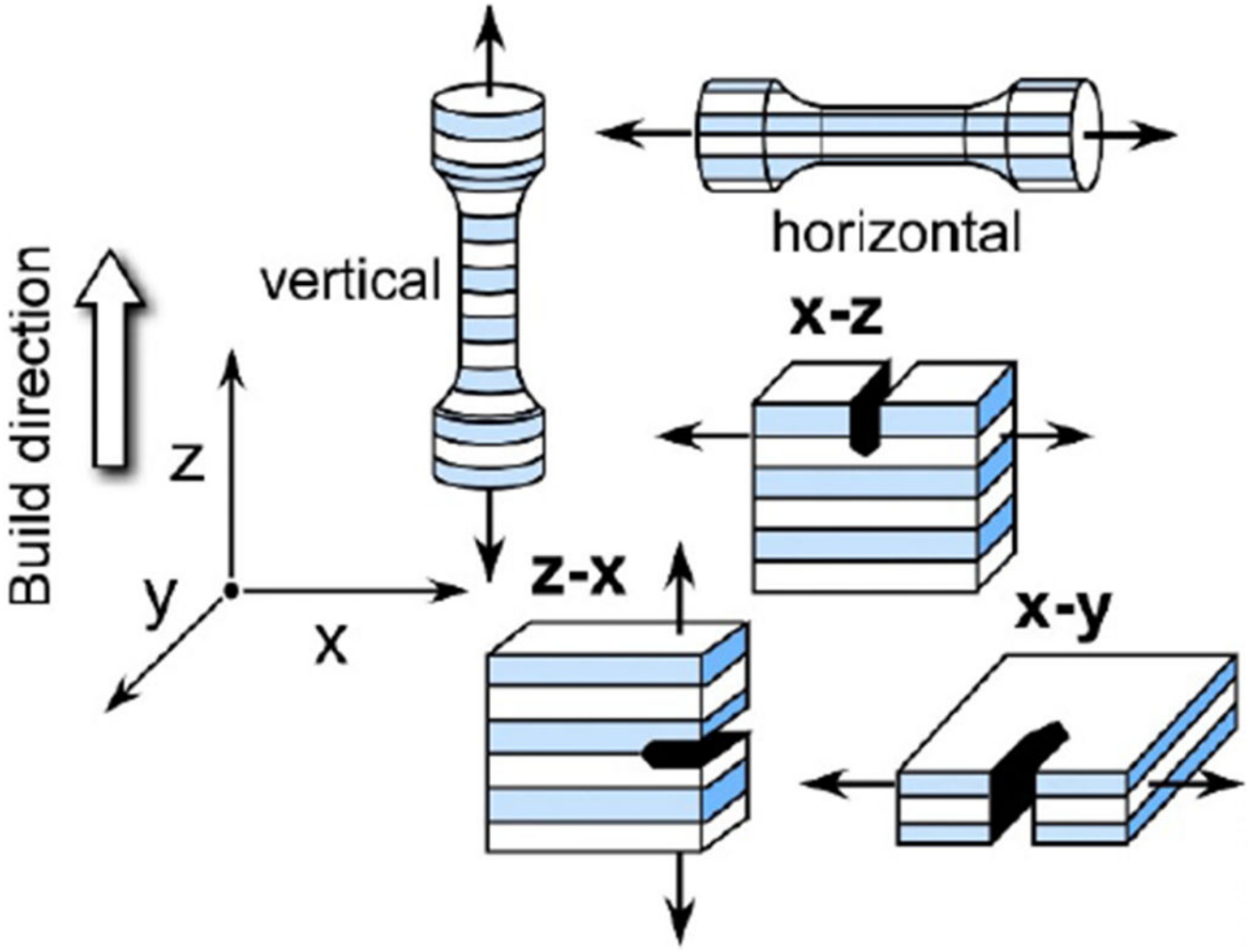

Fig. 16:

Nomenclature defining the building direction of tensile samples and crack orientation in the fracture mechanics specimens with respect to the loading direction. For the latter, the first letter refers to the loading direction and the second to the direction of crack growth.

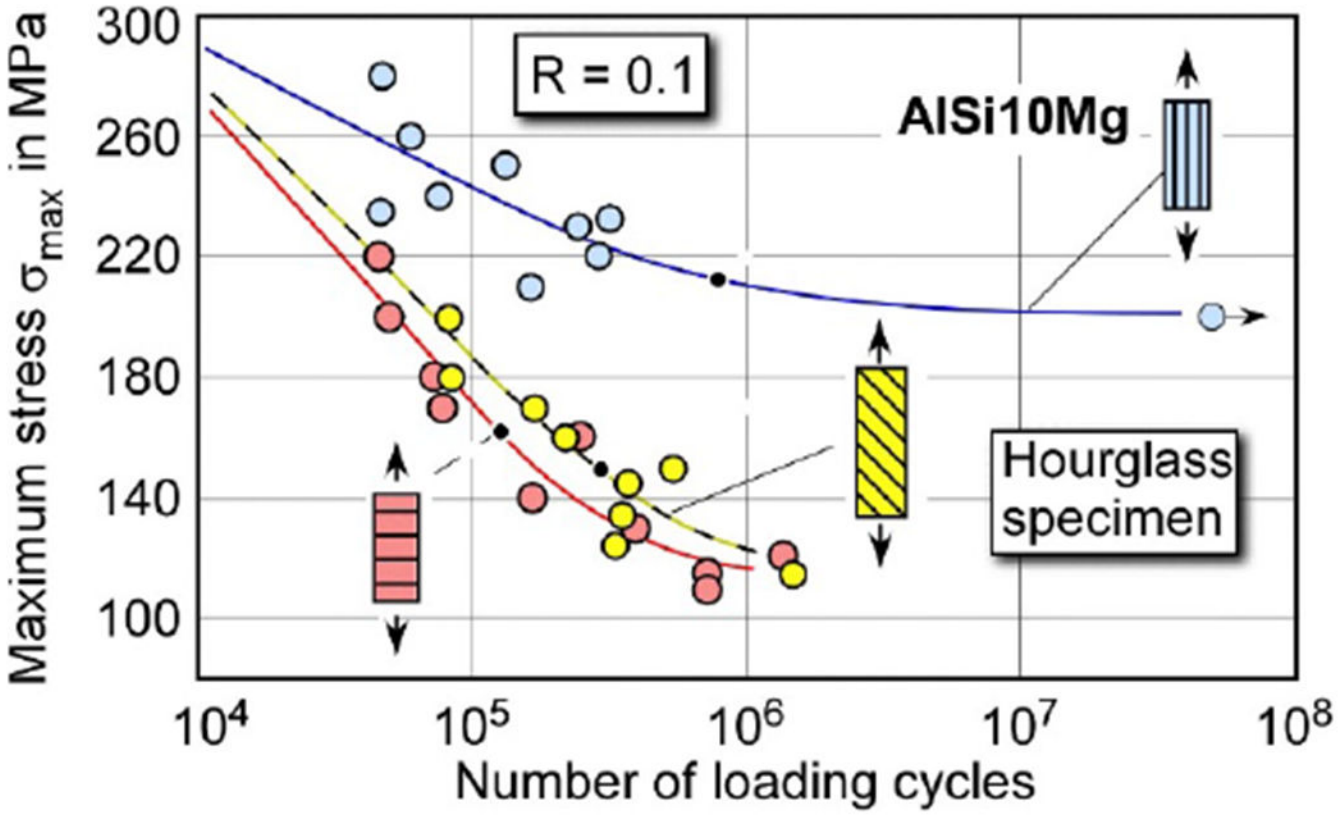

Fig. 17:
Example of the effect of the building orientation on the fatigue resistance (curves refer to 50% probability of failure), the test specimens were machined; according to [84].

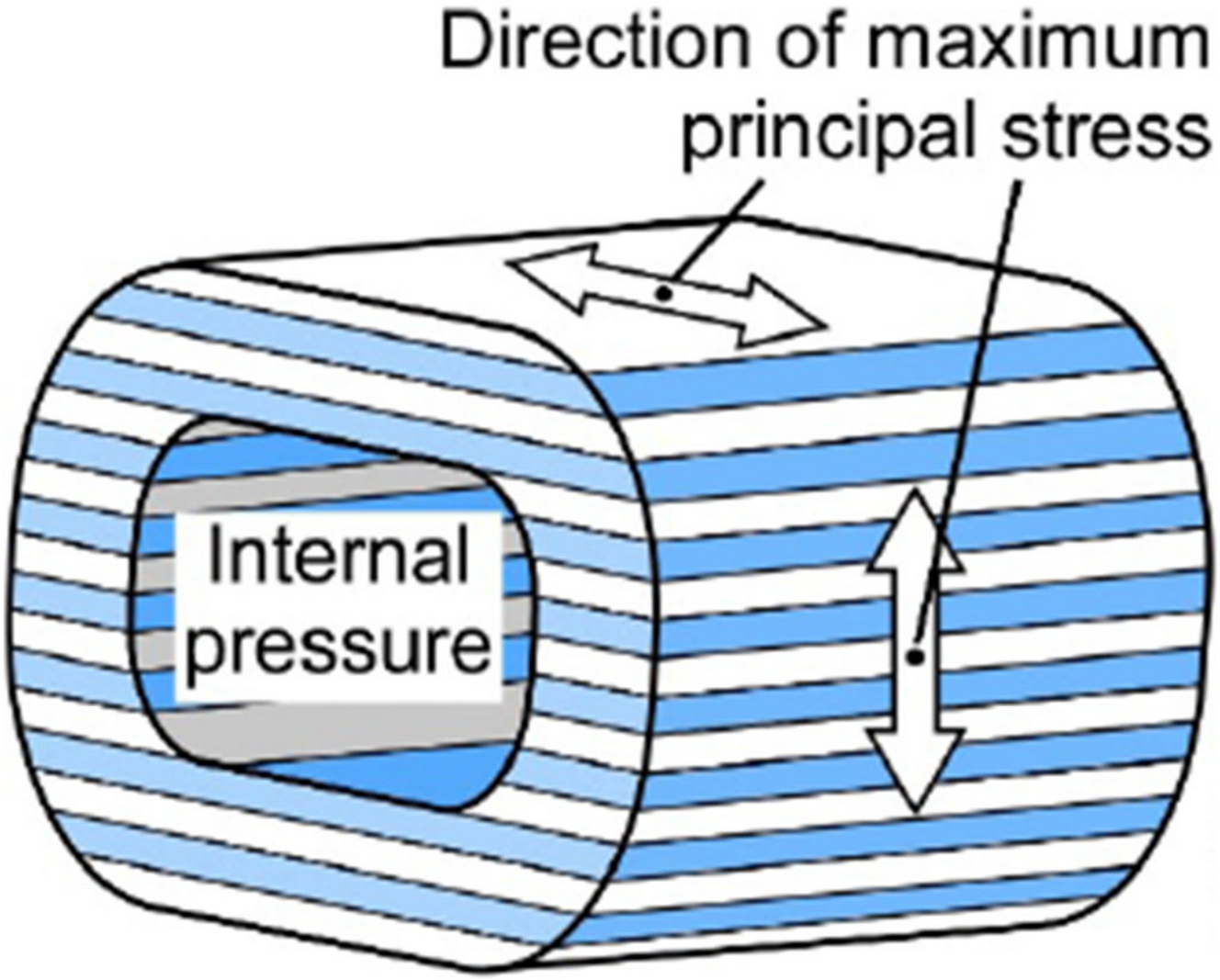

Fig. 18:
Illustration example for different building orientations with respect to the direction of the maximum principal stress within a simplified AM component.

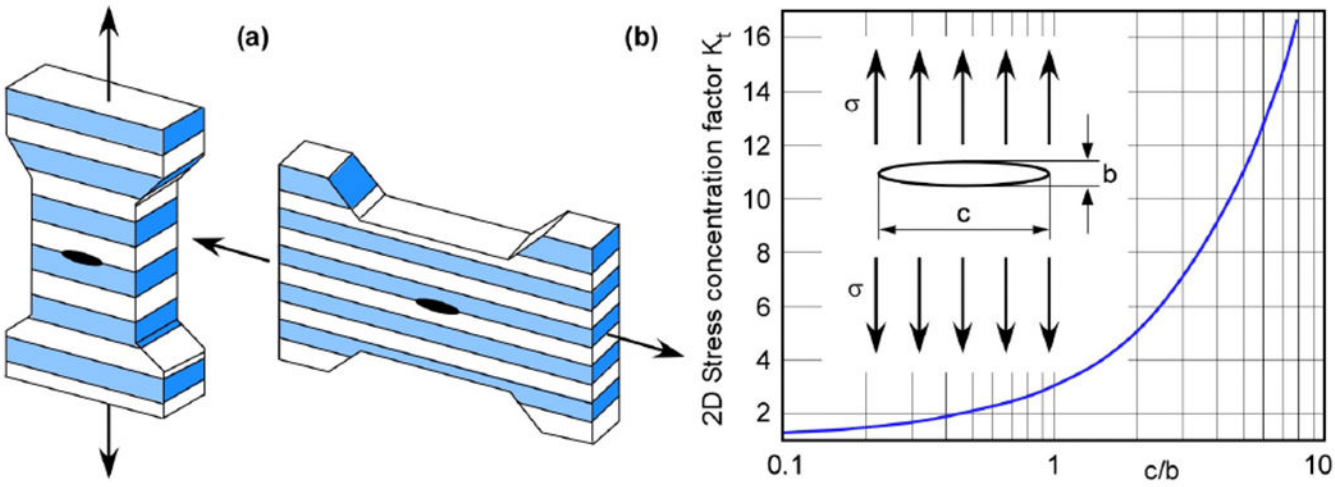

Fig. 19:

Effect of an elongated hole between two built-up layers. (a) Schematic view for the conditions in vertical and horizontal direction; (b) 2D stress concentration factor of an elliptical hole in an infinite plate as a function of the aspect ratio c/b; according to [118].

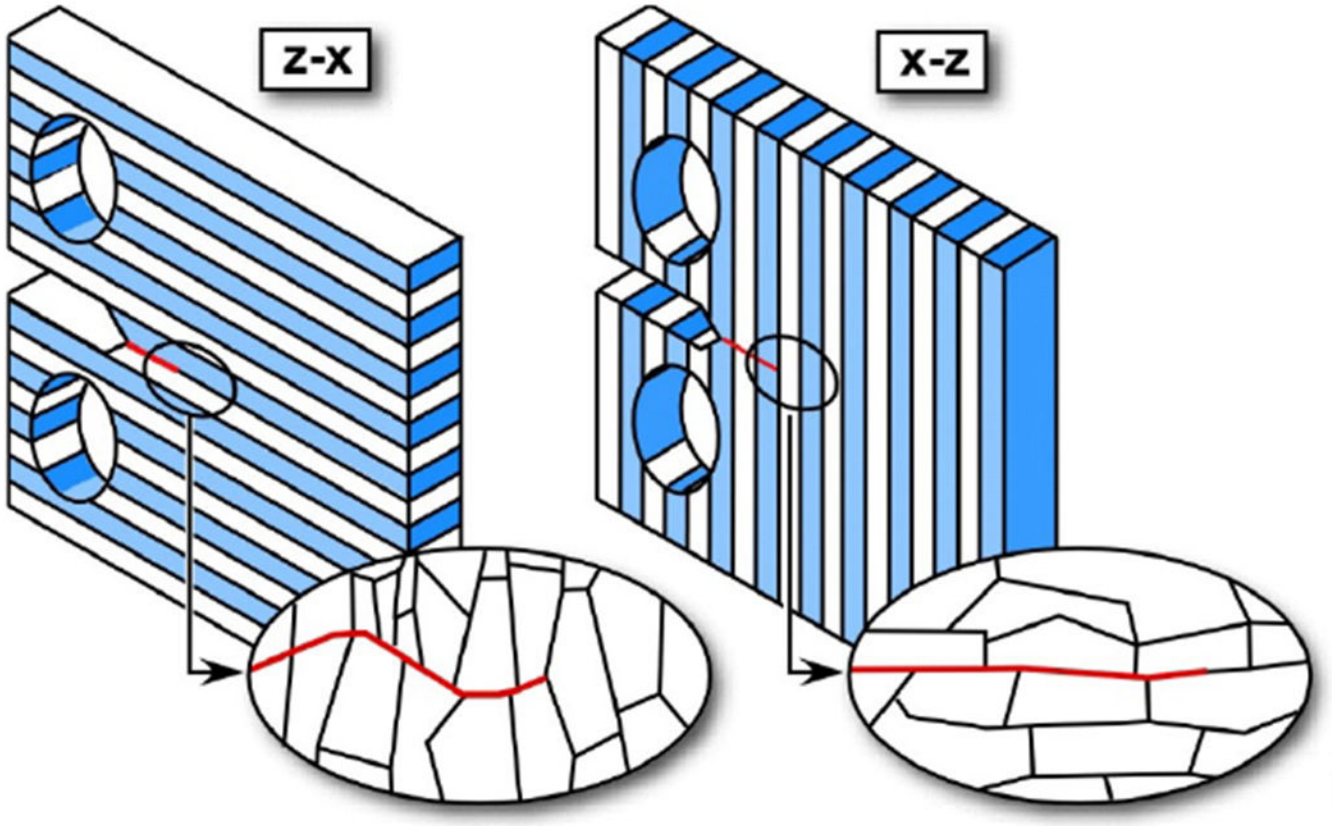

Fig. 20:
Potential effect of the alignment of the (along the building direction) elongated grains in z-x and x-z specimens on the potential fatigue crack propagation path and the expected asperity of the crack faces; according to [114].

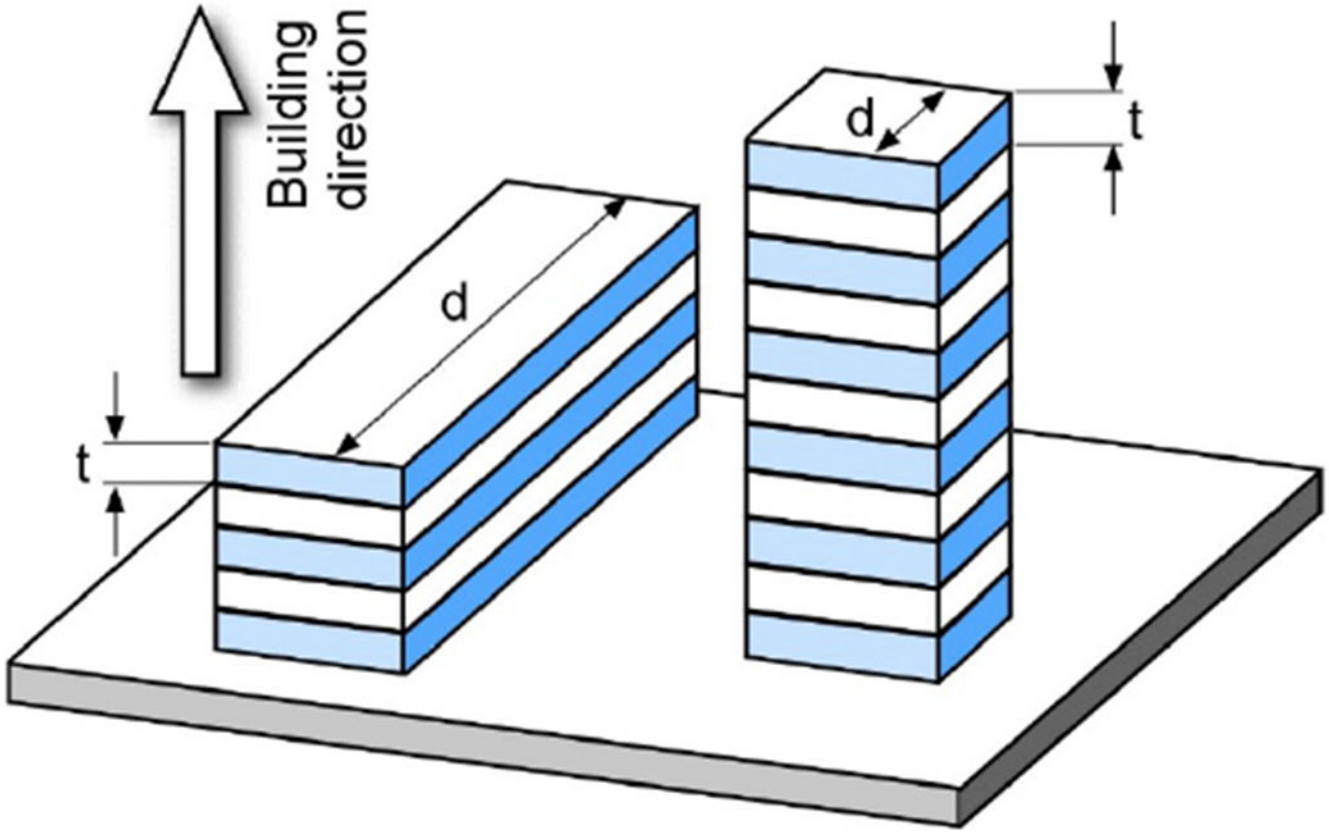

Fig. 21:
Example for different aspect ratios in horizontally (left) and vertically (right) build structures; according to [114].

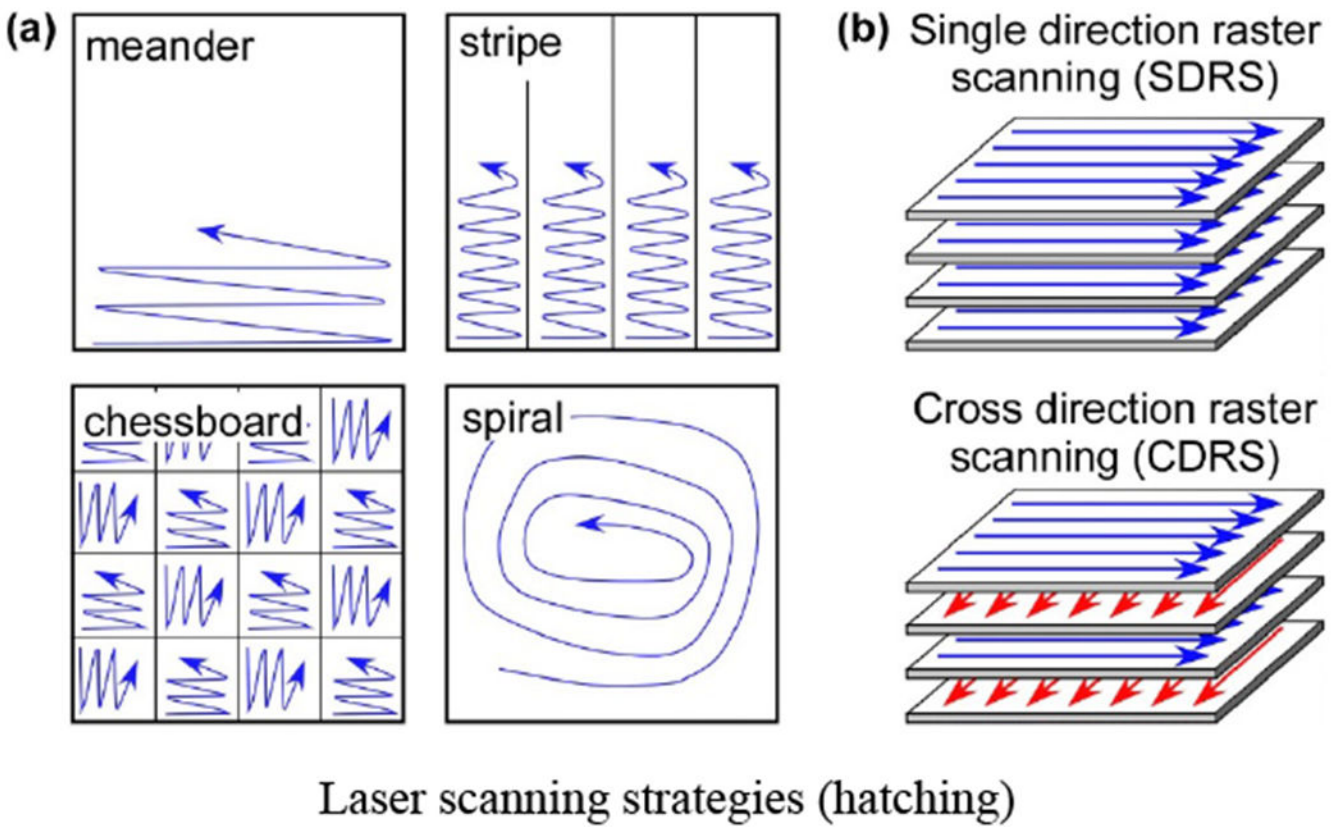

Fig. 22:
Laser scanning strategies (hatching). (a) Selected examples of scanning patterns; according to [128]; (b) Single direction and cross direction raster scanning; according to [129].

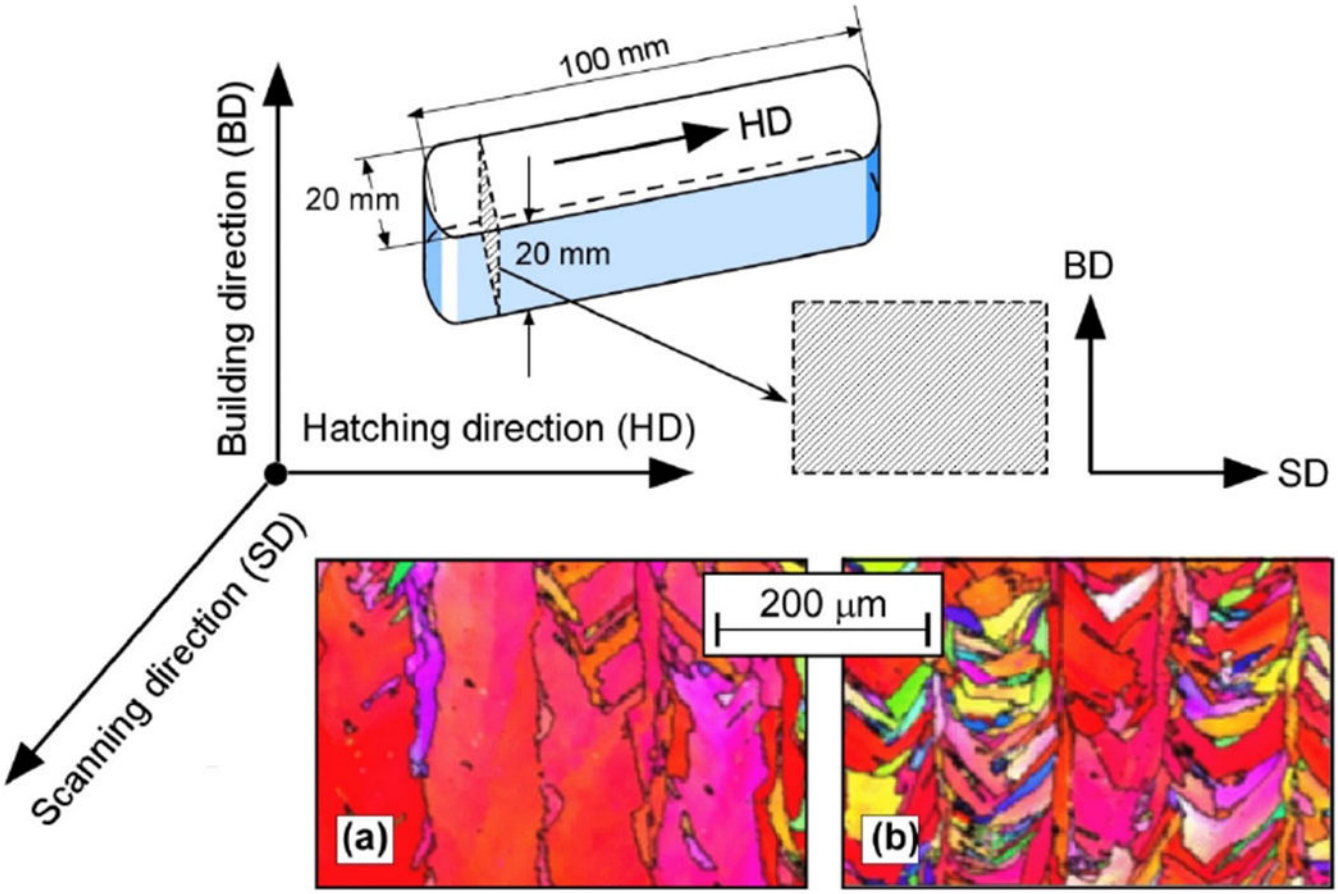

Fig. 23:

Microstructure of L-PBF Inconel 718; (a) short hatch length sample; (b) long hatch length sample (ten times the short hatch length); according to [131].

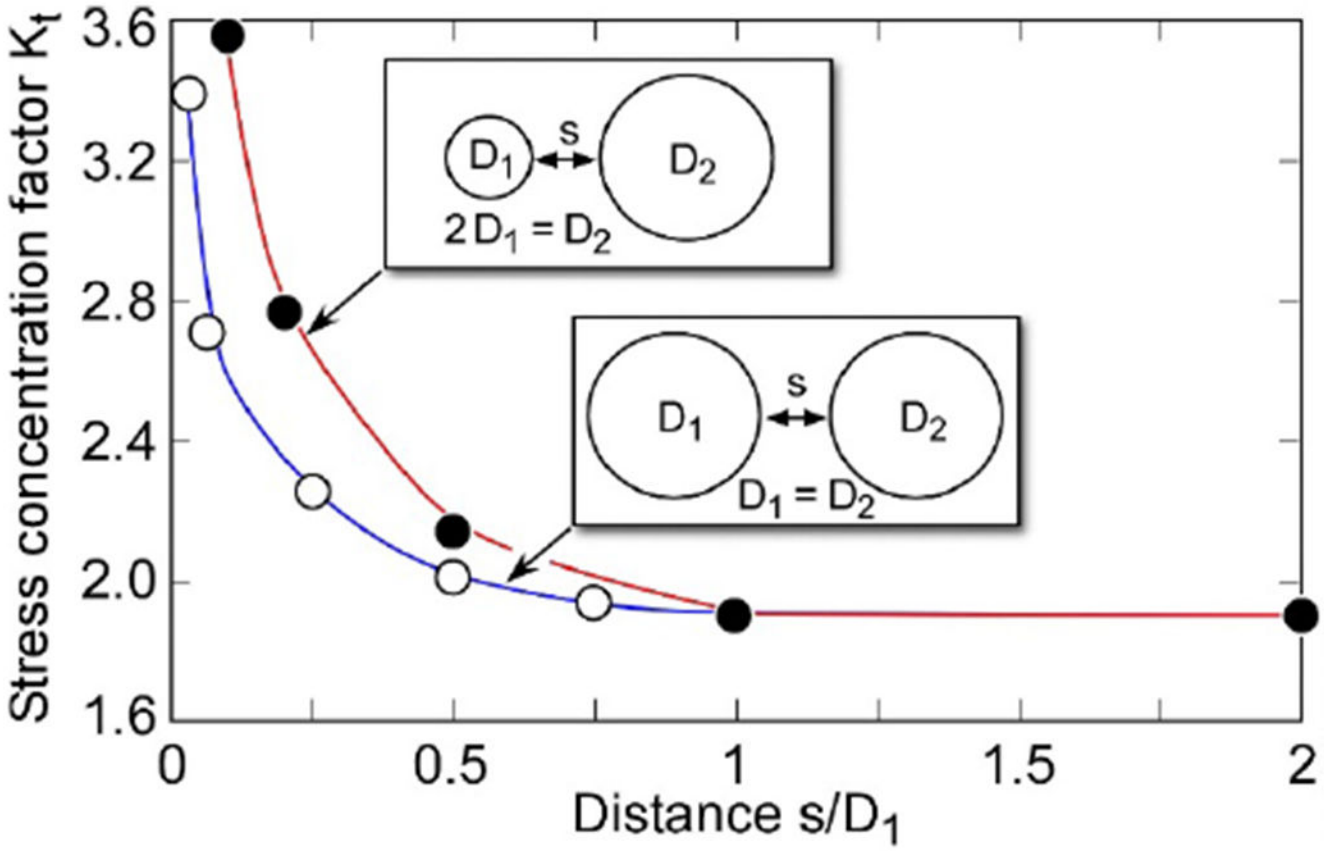

Fig. 24:
Effect of the distance between two spherical holes on the resulting stress concentration factor; according to [171].

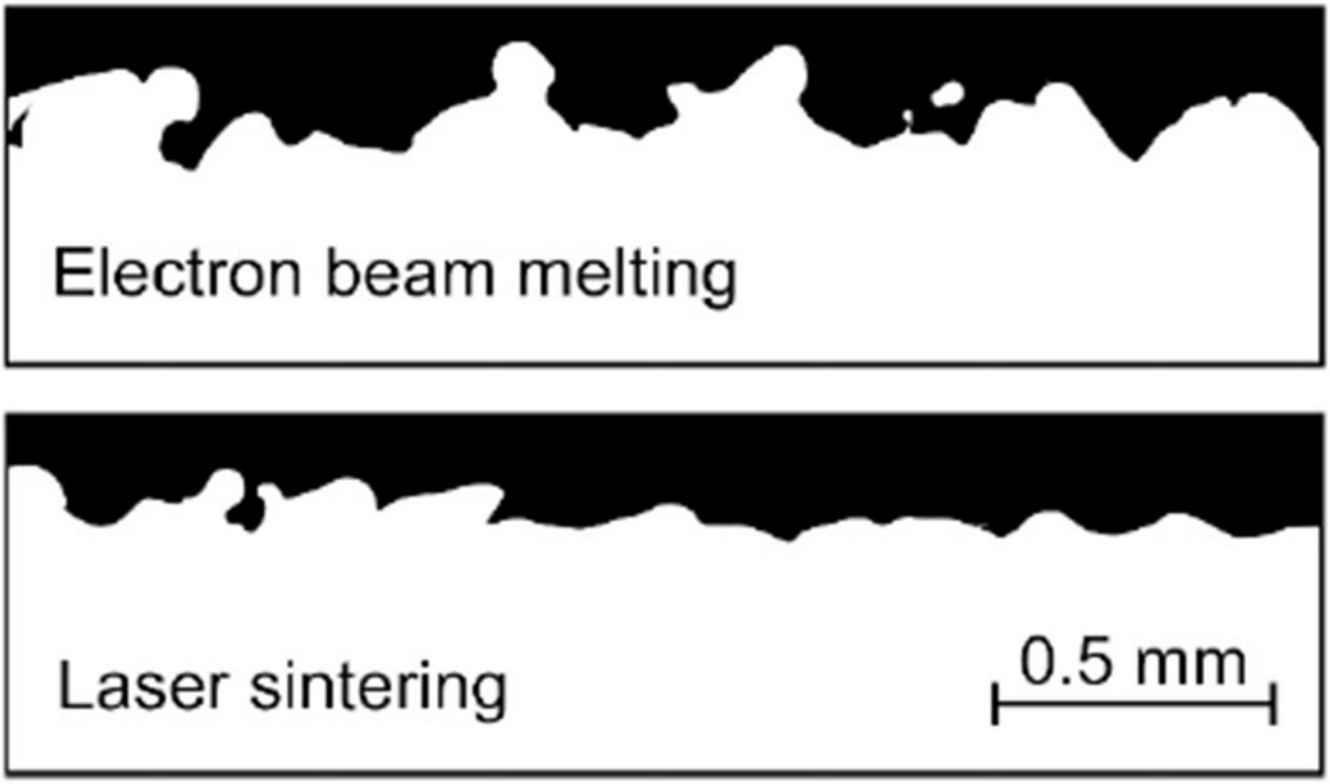

Fig. 25:
Examples of as-built surface roughness of AM-Ti6Al4V formed by two different technologies; according to [78].

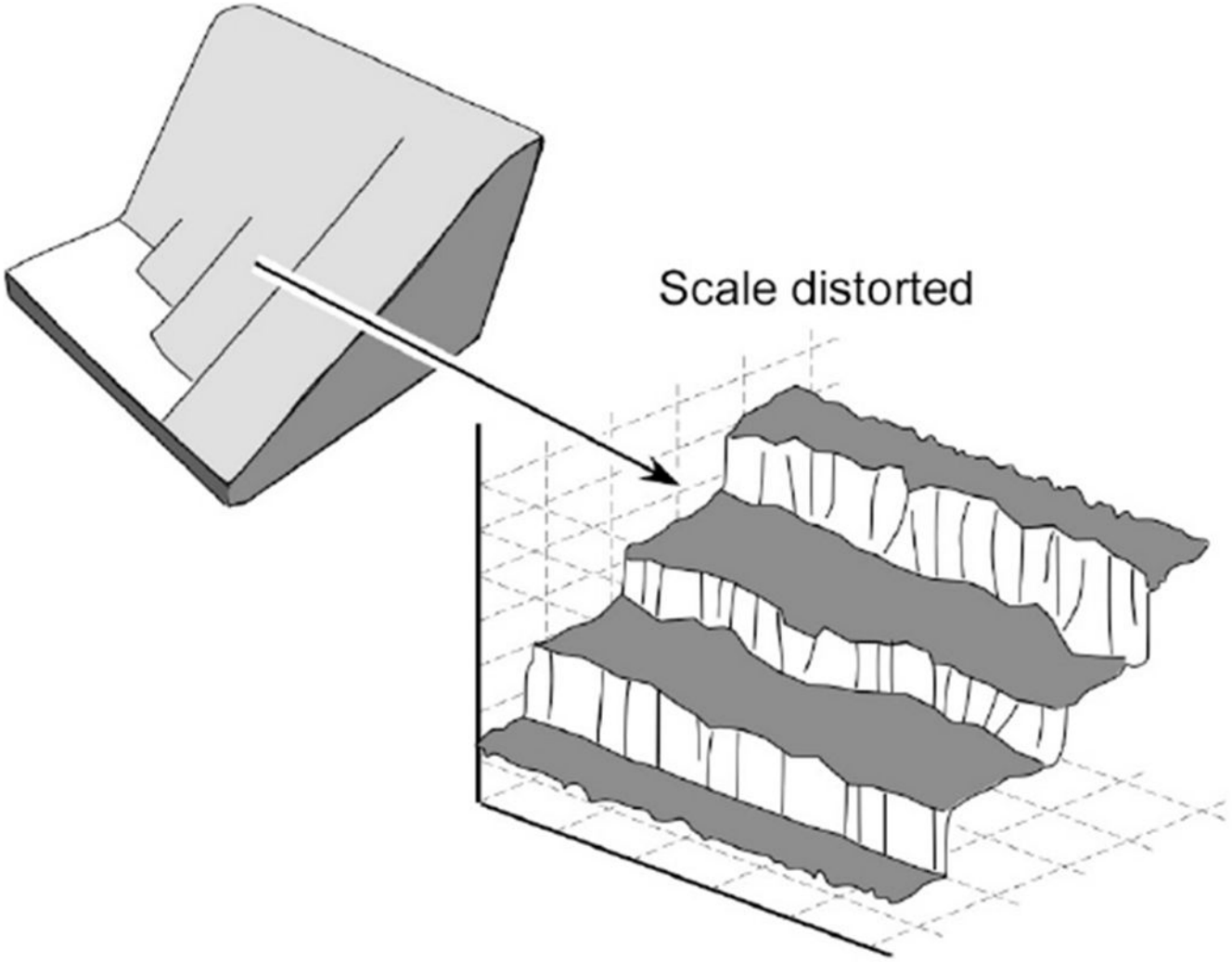

Fig. 26:
Examples of the staircase effect; according to [189]; Figure simplified.

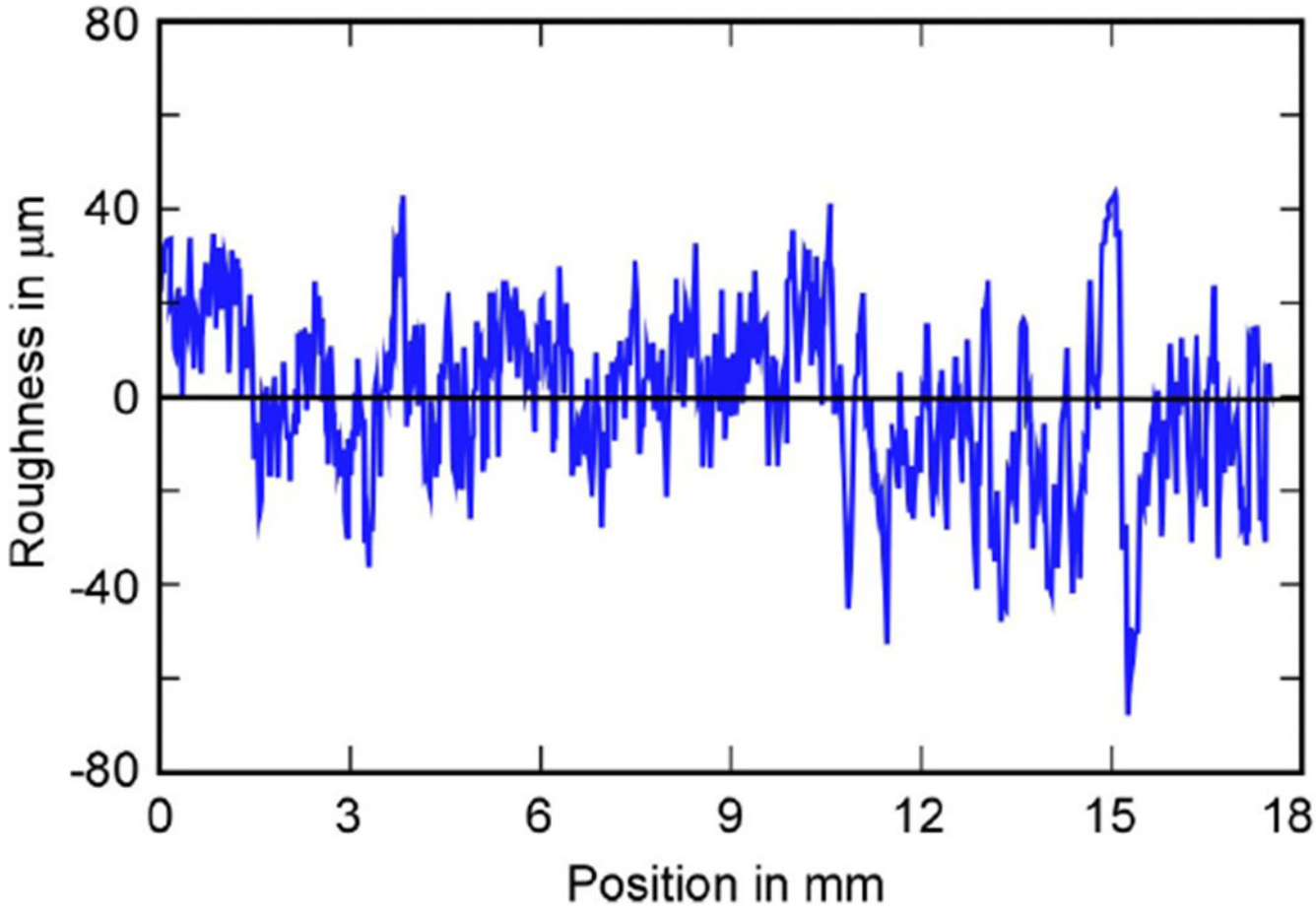

Fig. 27:
Example profile of as-built surface roughness of AM Ti6Al4V; originally presented in [195].

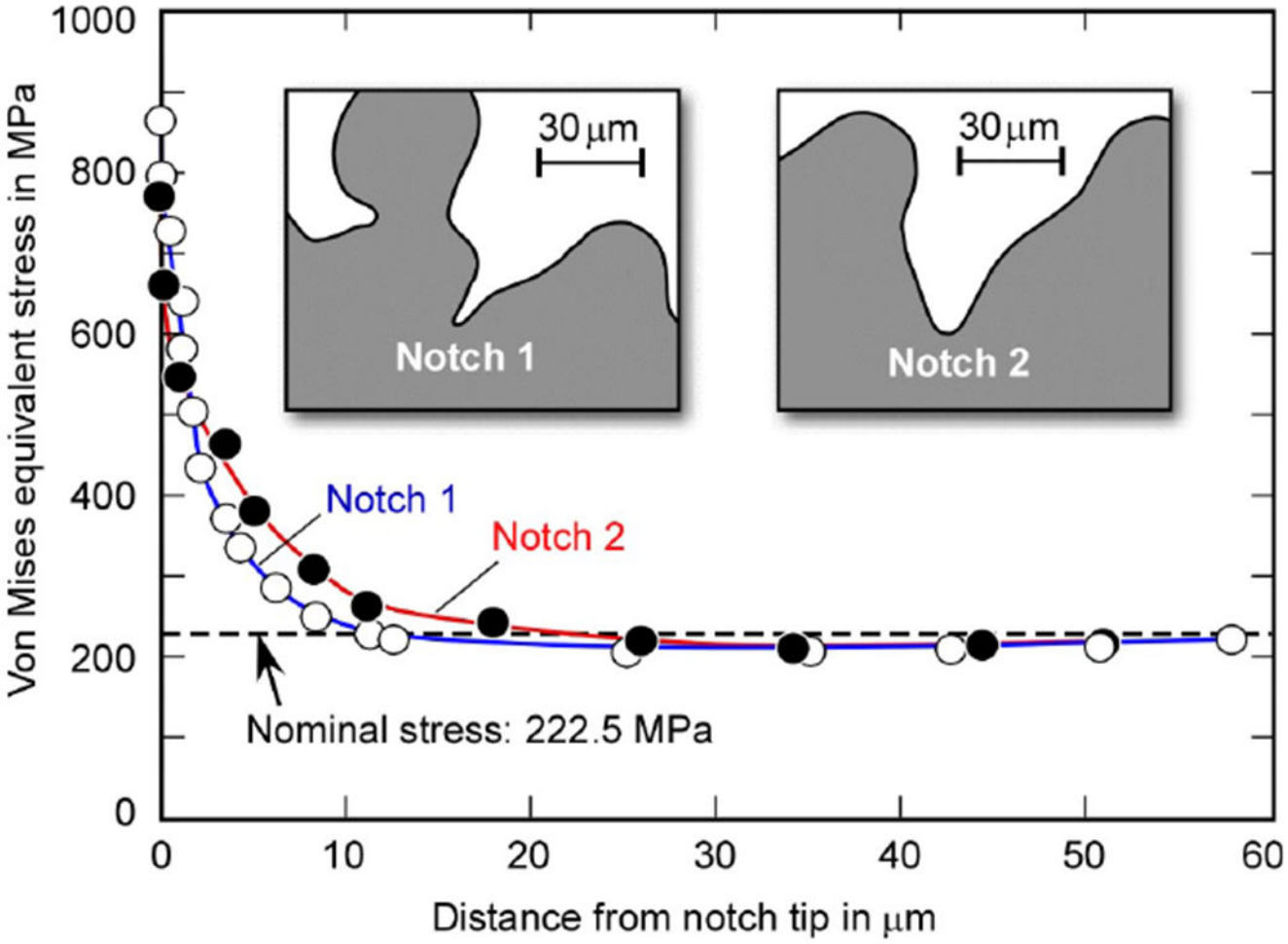

Fig. 28:
Examples of stress distributions in as-built surface roughness of AM-Ti6Al4V; according to [202].

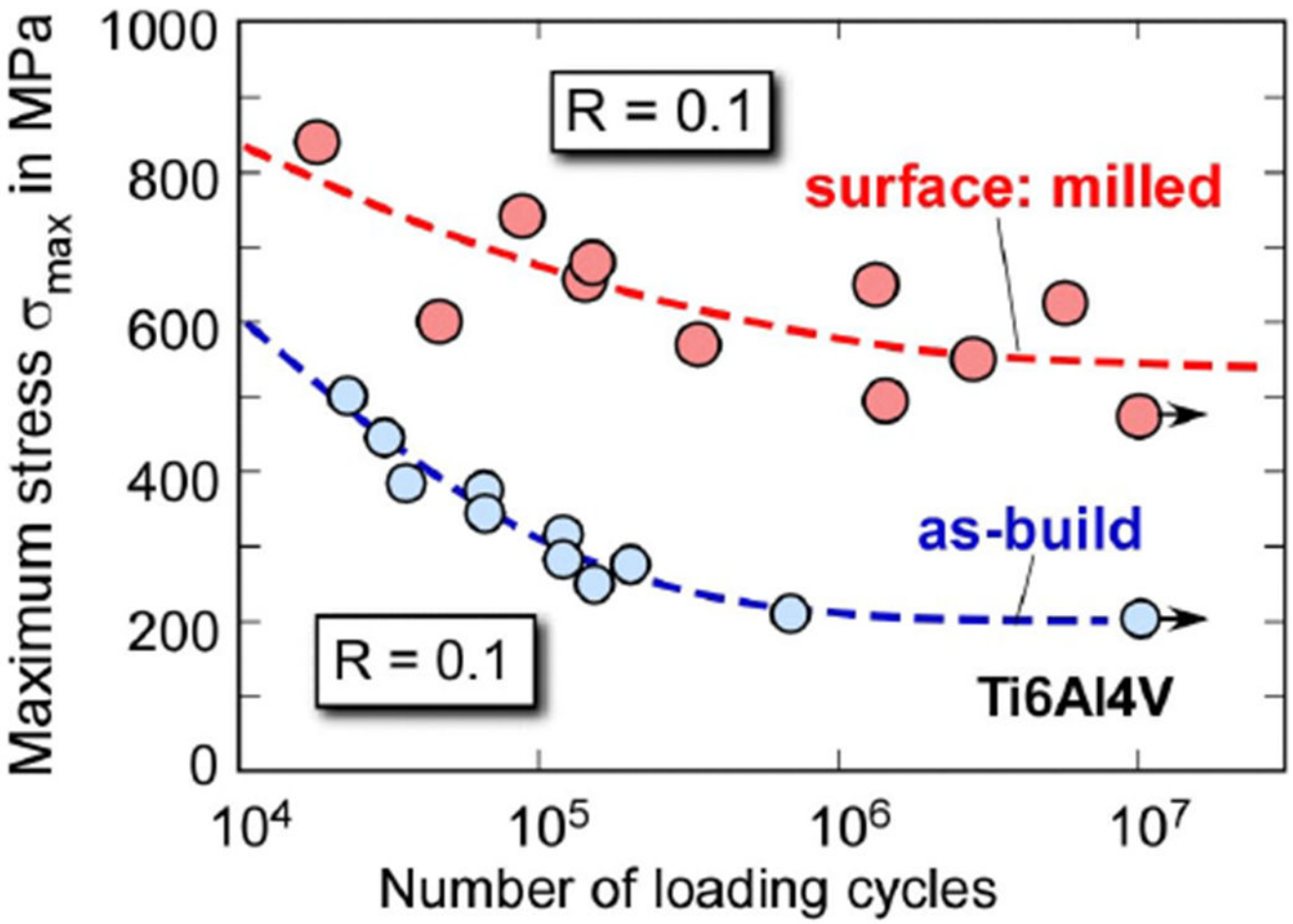

Fig. 29:
Example for the effect of surface treatment on the fatigue strength of L-PBF Ti6Al4V; according to [158].

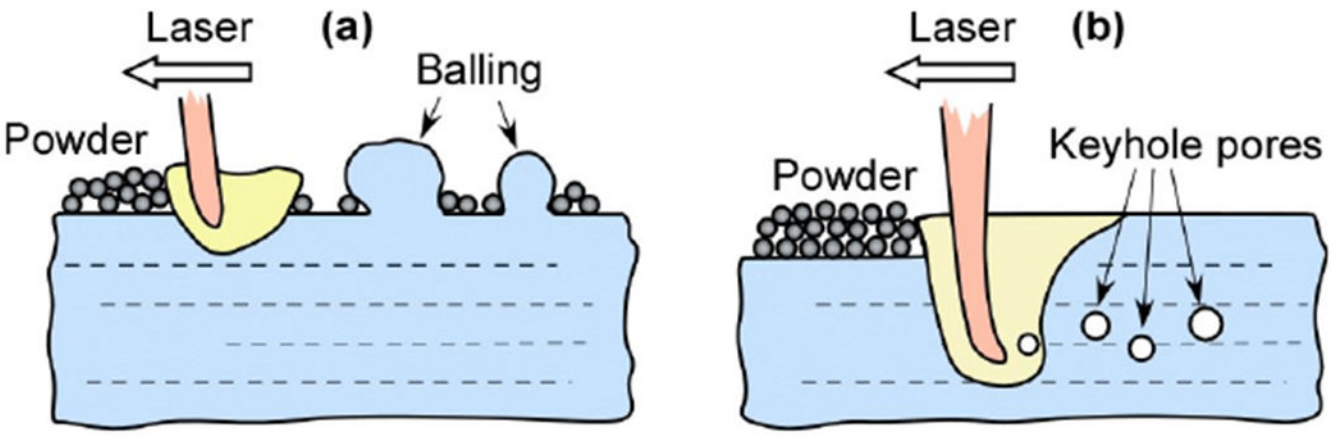

Fig. 30:
Schematic of (a) Balling defects; (c) Keyhole defects.

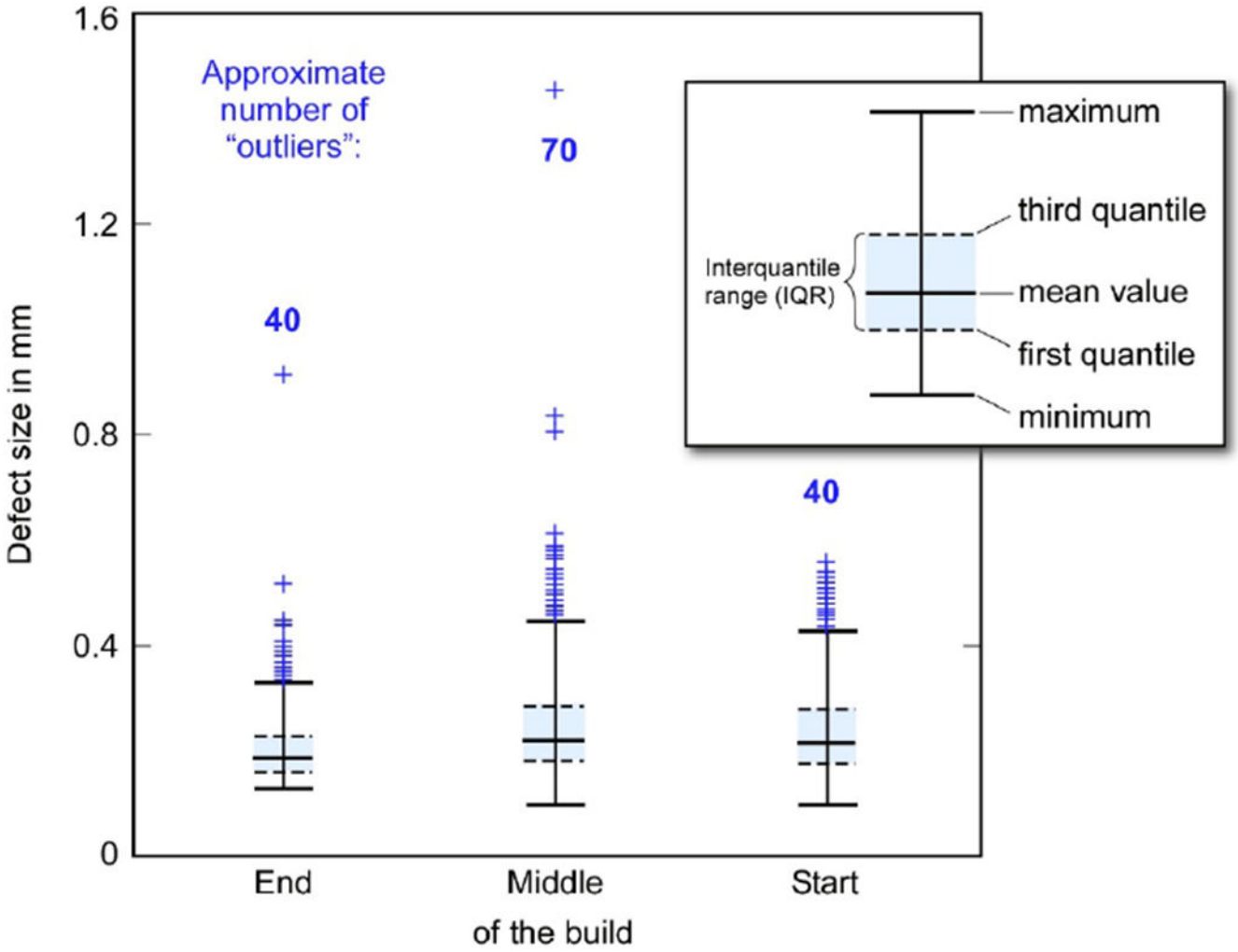

Fig. 31:
Scatter bands of pore diameters along the vertical dimension of an AM processed bar; according to [234].

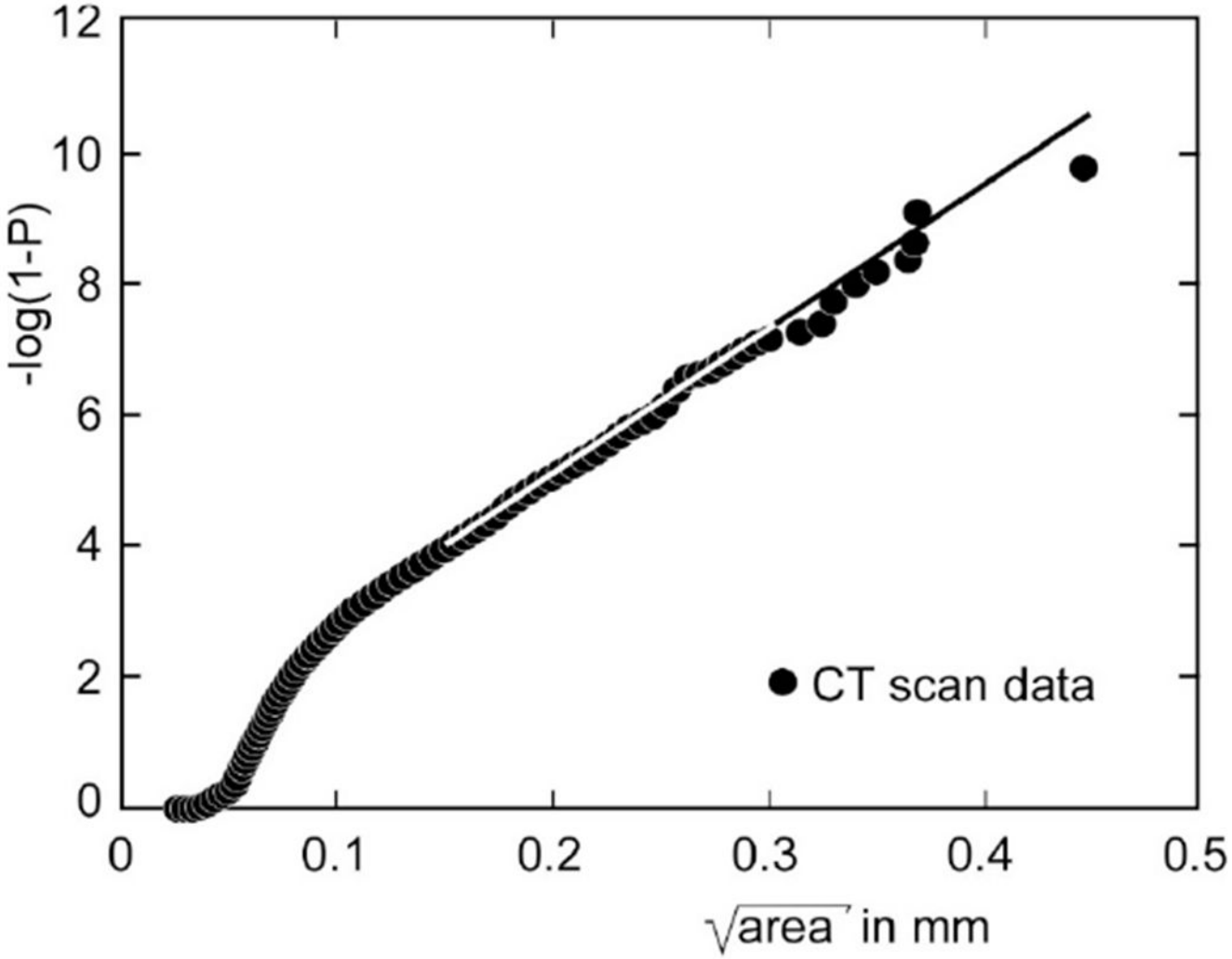

Fig. 32:
Example of an extreme value statistics applied to AM defects, AlSi10Mg; according to [238]; P = probability.

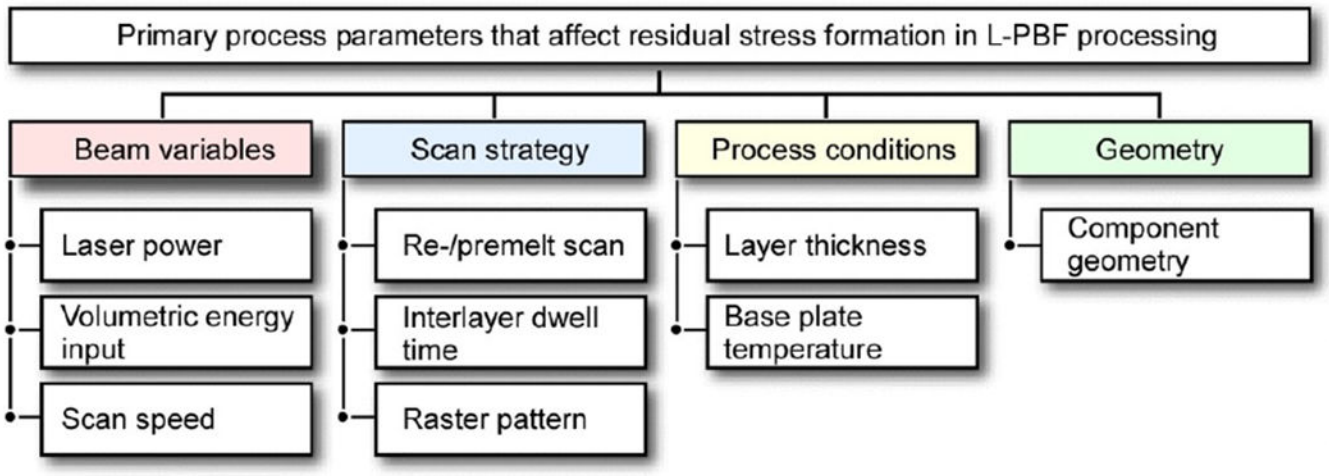

Fig. 33:
Parameters which influence the residual stress magnitude and pattern in AM processed component; according to [23].

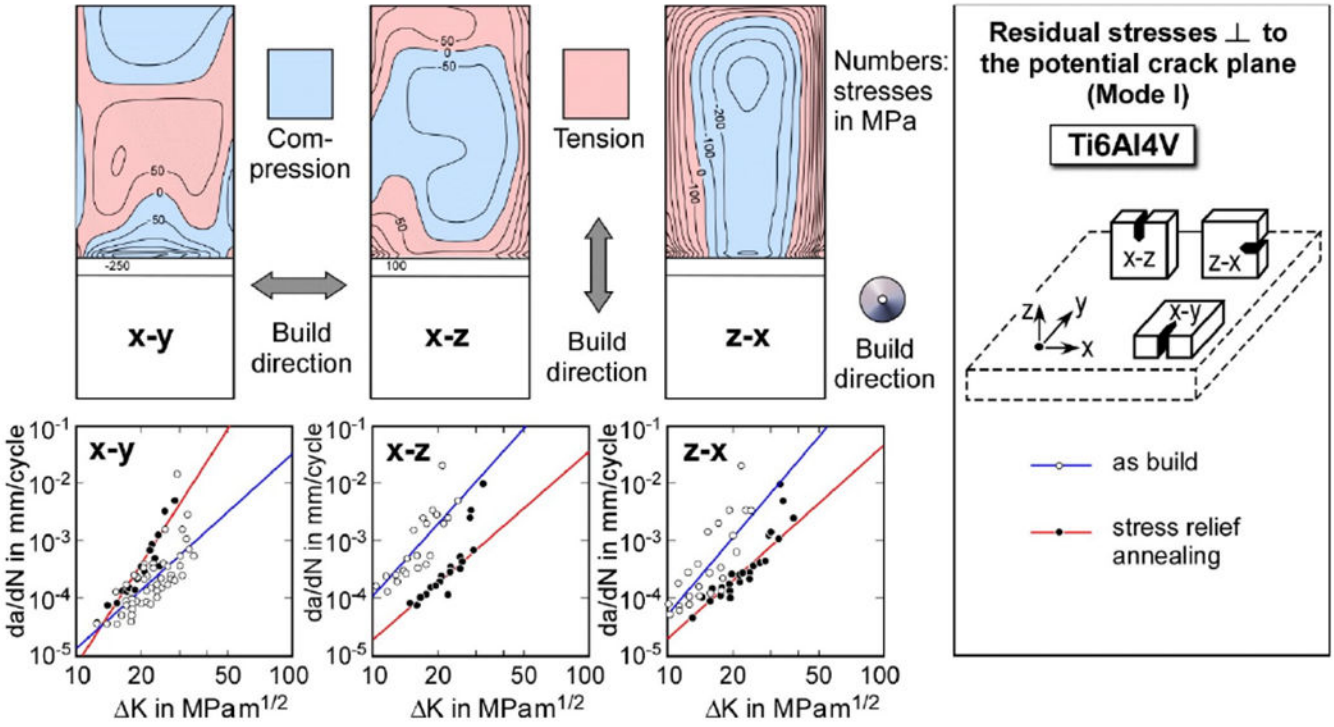

Fig. 34:

Residual stress distribution in L-PBF processed Ti6Al4V as-built at the crack planes in the C(T) specimens build in 3 different orientations and the effects of stress relief heat treatment. The residual stresses were determined by the Contour Method; according to [98].

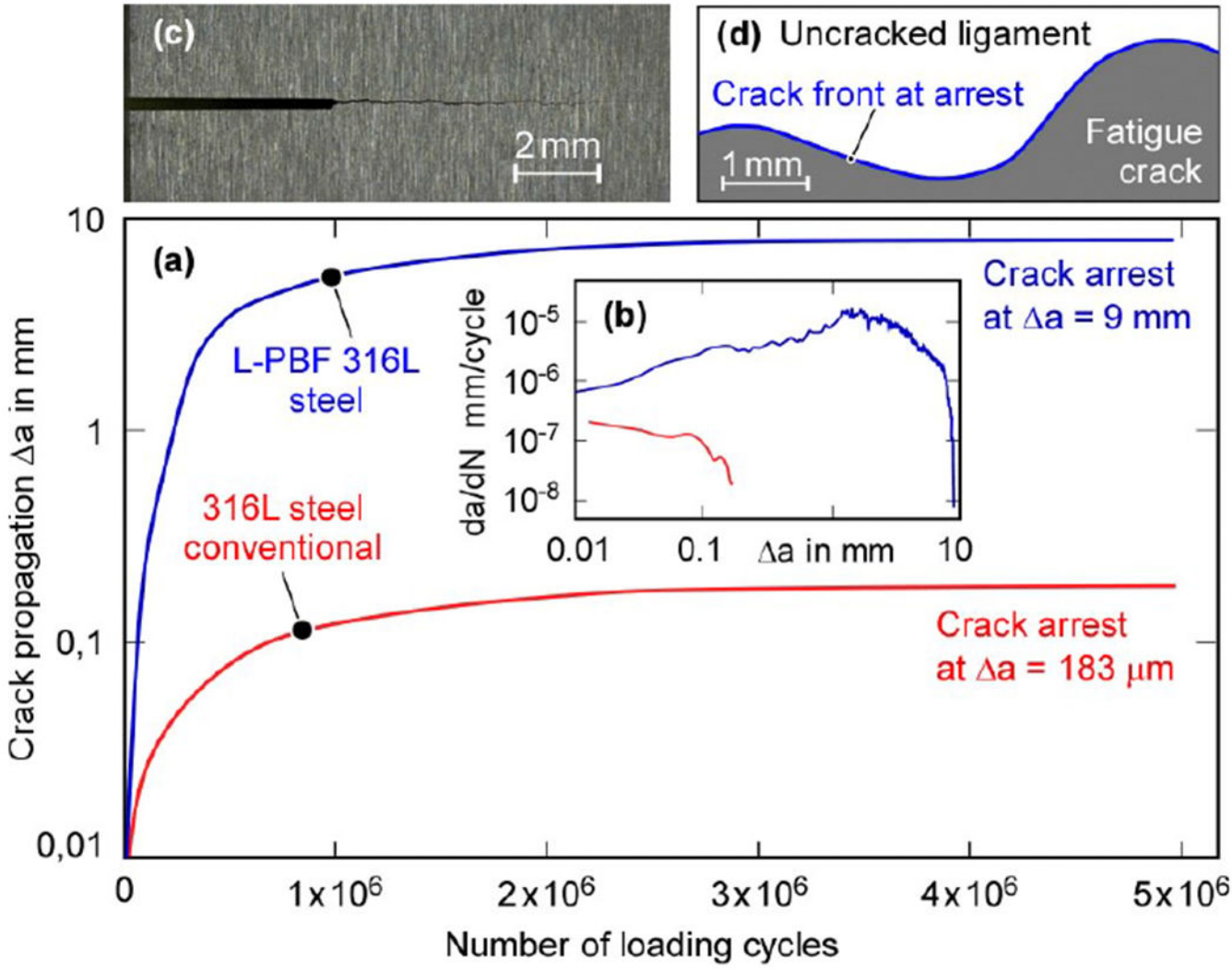

Fig. 35:

Crack propagation in compression pre-cracking for a SEN(B) specimen. (a) Conventional (red curve) and L-PBF (blue curve) processed 316L; (b) crack growth rate vs. crack extension length; (c) Surface view on the resulting fatigue crack for the L-PBF processed specimen; (d) the irregular crack front of the same; according to [264] .

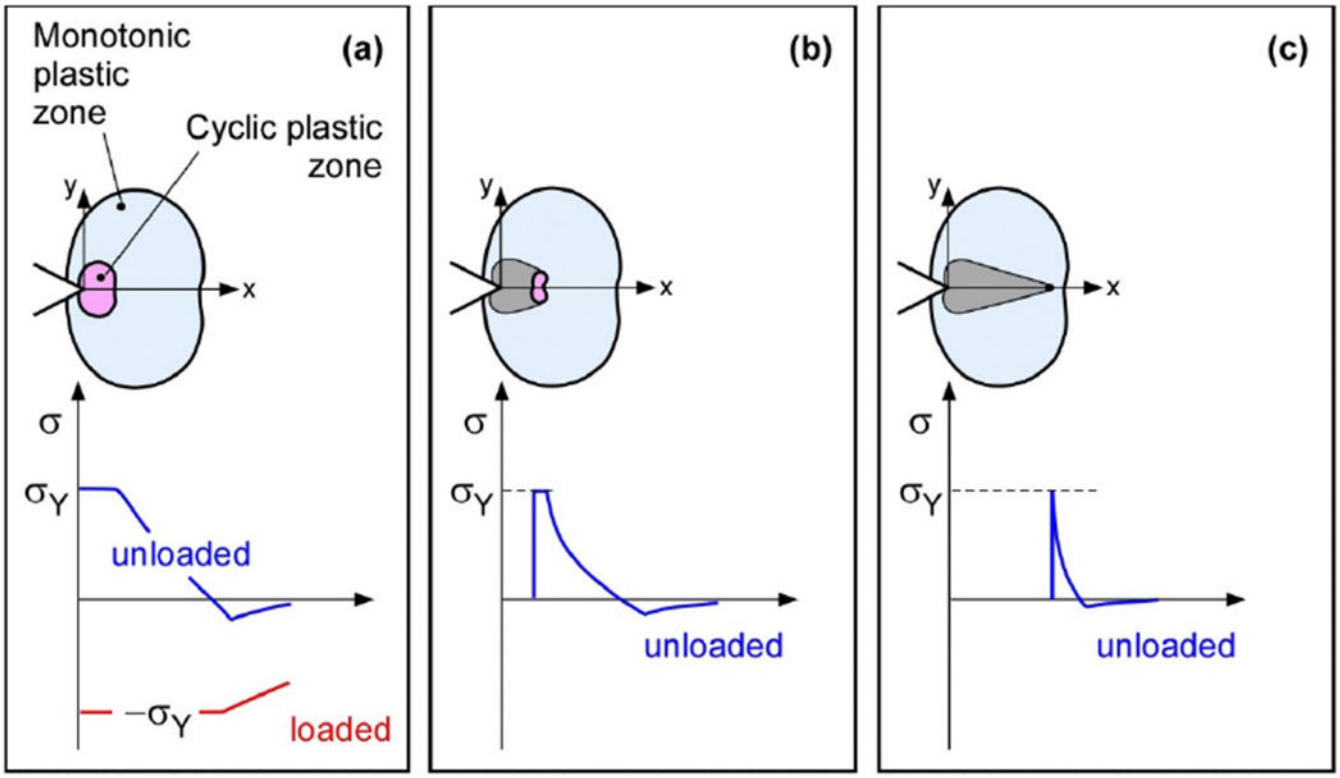

Fig. 36:

Development of the plastic zone and the residual stresses near the notch root in cyclic compression loading. (a) first loading cycle; (b) after small crack extension; (c) at crack arrest; according to [265].

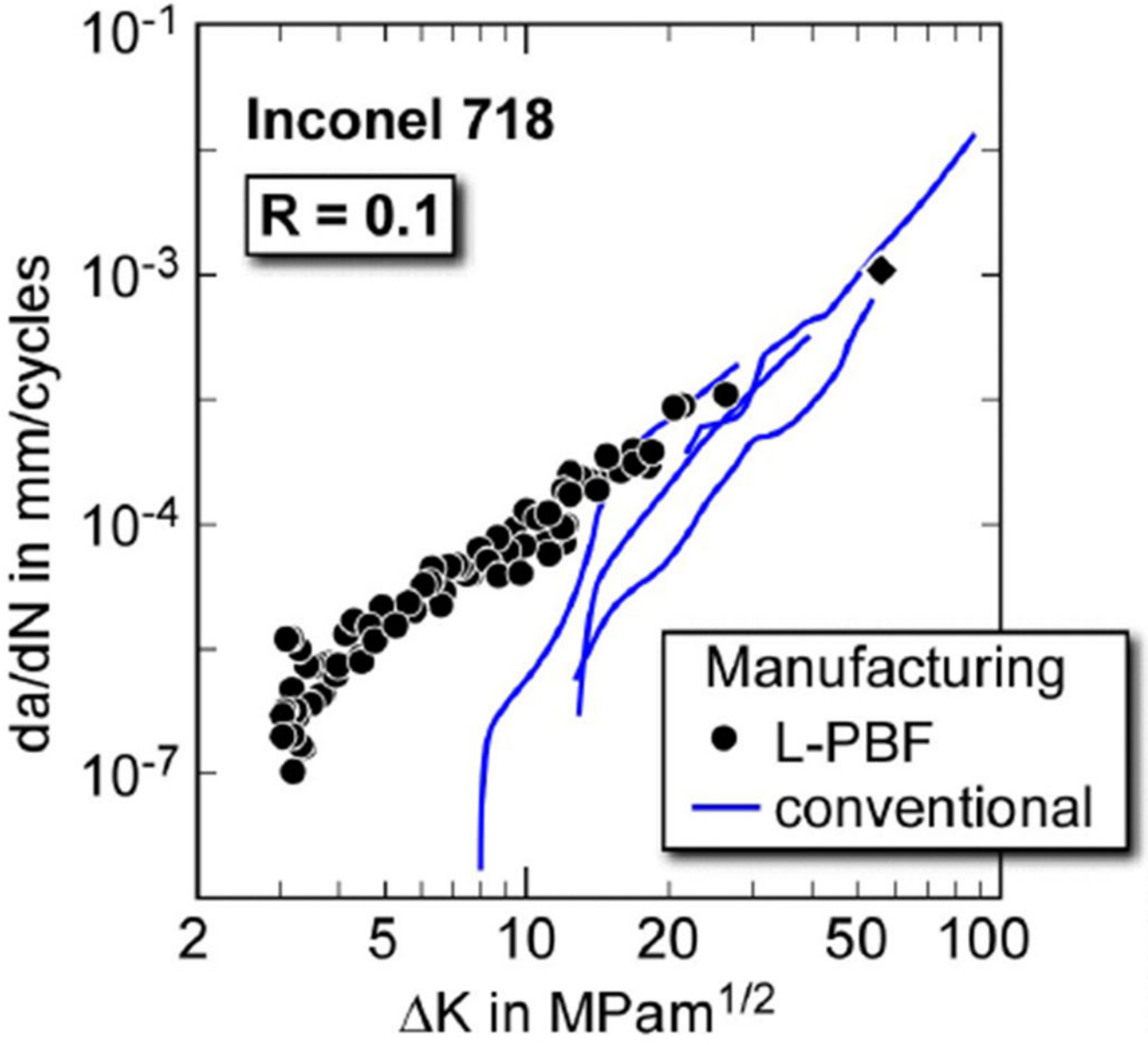

Fig. 37:
Threshold regime of the da/dN-ΔK curve of conventionally and AM processed Inconel 718; according to [279].

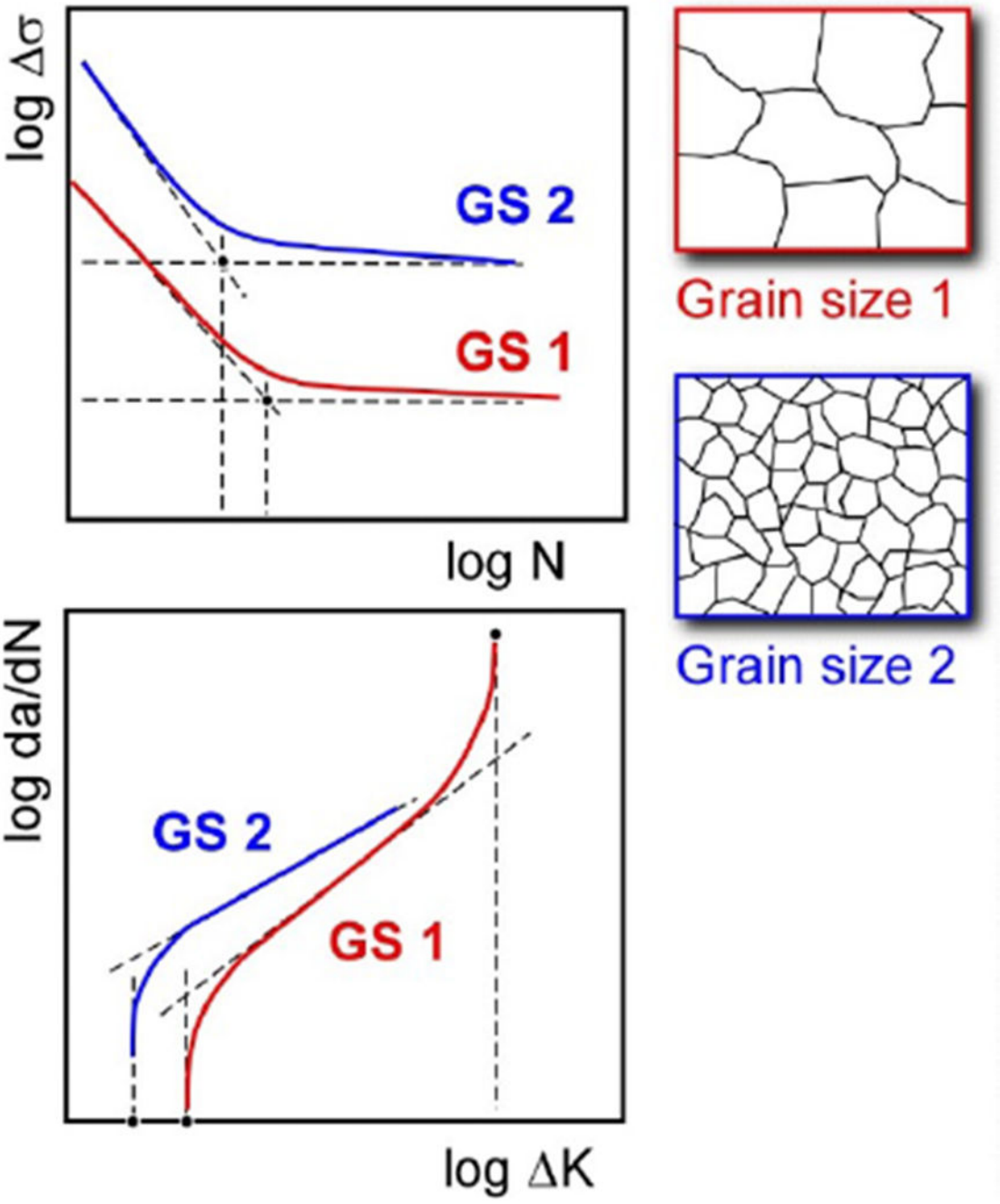

Fig. 38:
Effect of the grain size on the S-N curve and the da/dN-ΔK curve, schematic view; according to [280].

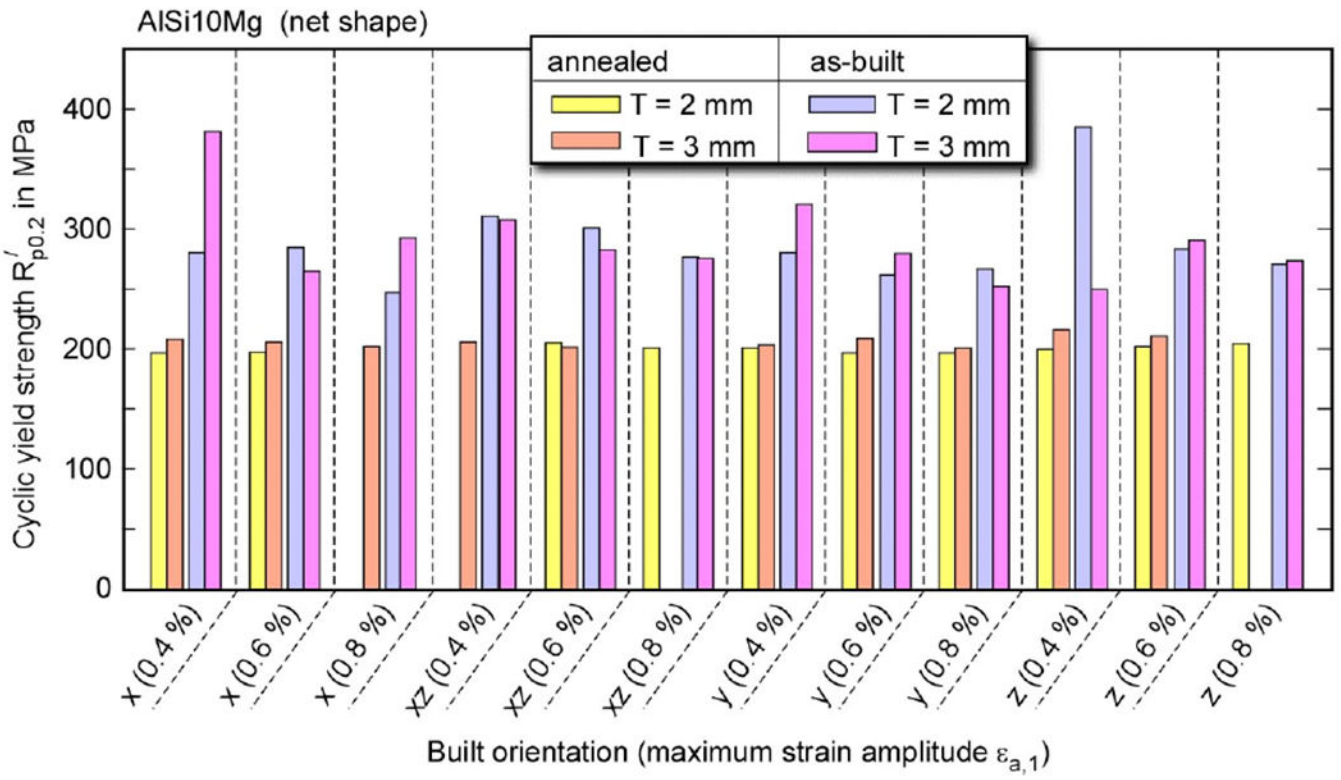

Fig. 39:

Cyclic yield strength for as-built and stress-relief annealed specimens; according to Wagener et al. [295], see also Wagener et al. [296].

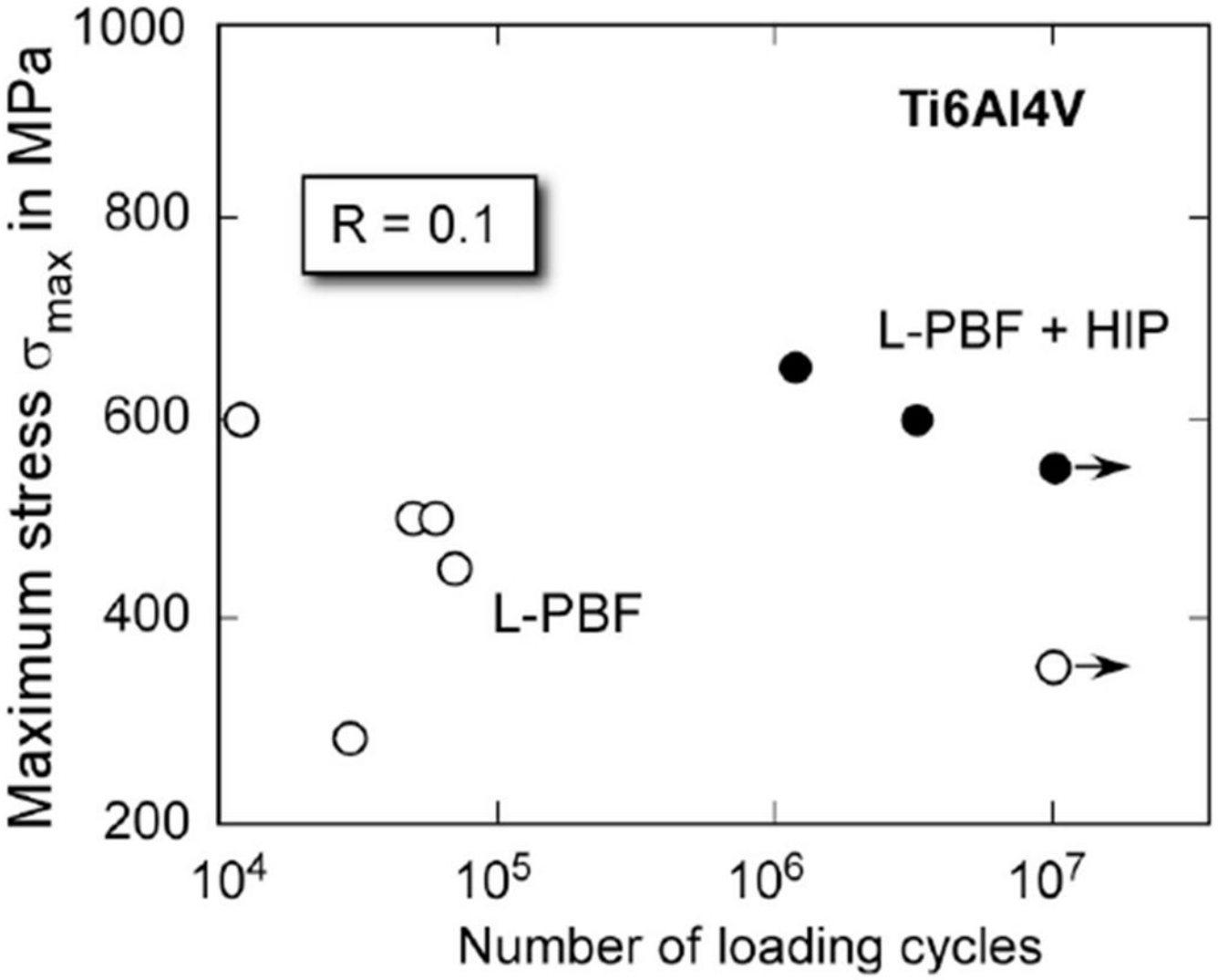

Fig. 40:
Examples for the effect of HIP treatment on the fatigue strength; according to [305].

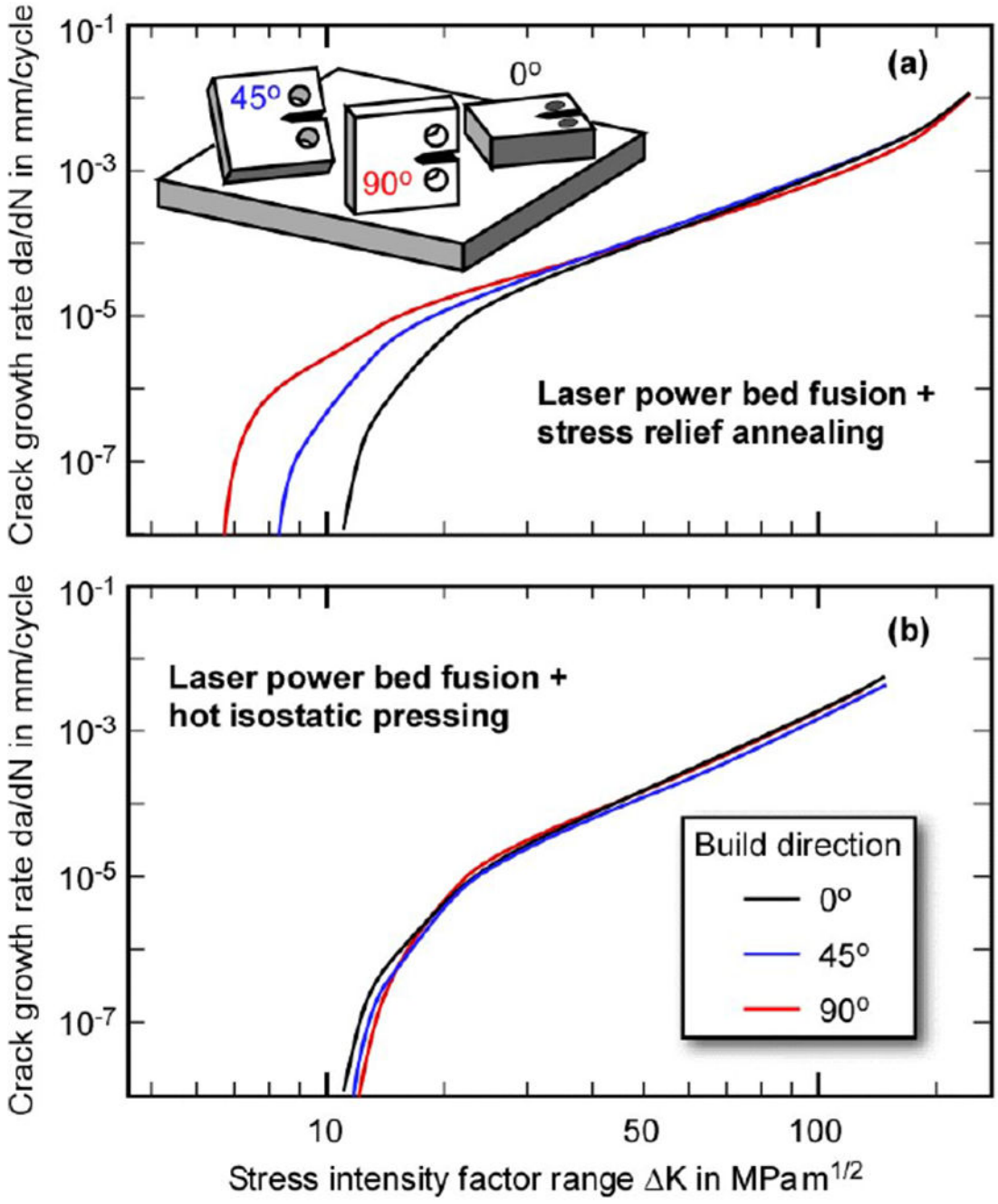

Fig. 41:

Fatigue crack propagation curves of Inconel 625 as a function of the building direction. (a) thermal stress relieved condition; (b) after hot isostatic pressing (HIP, at 1120 °C and 100 MPa for 4 hours); according to [283].

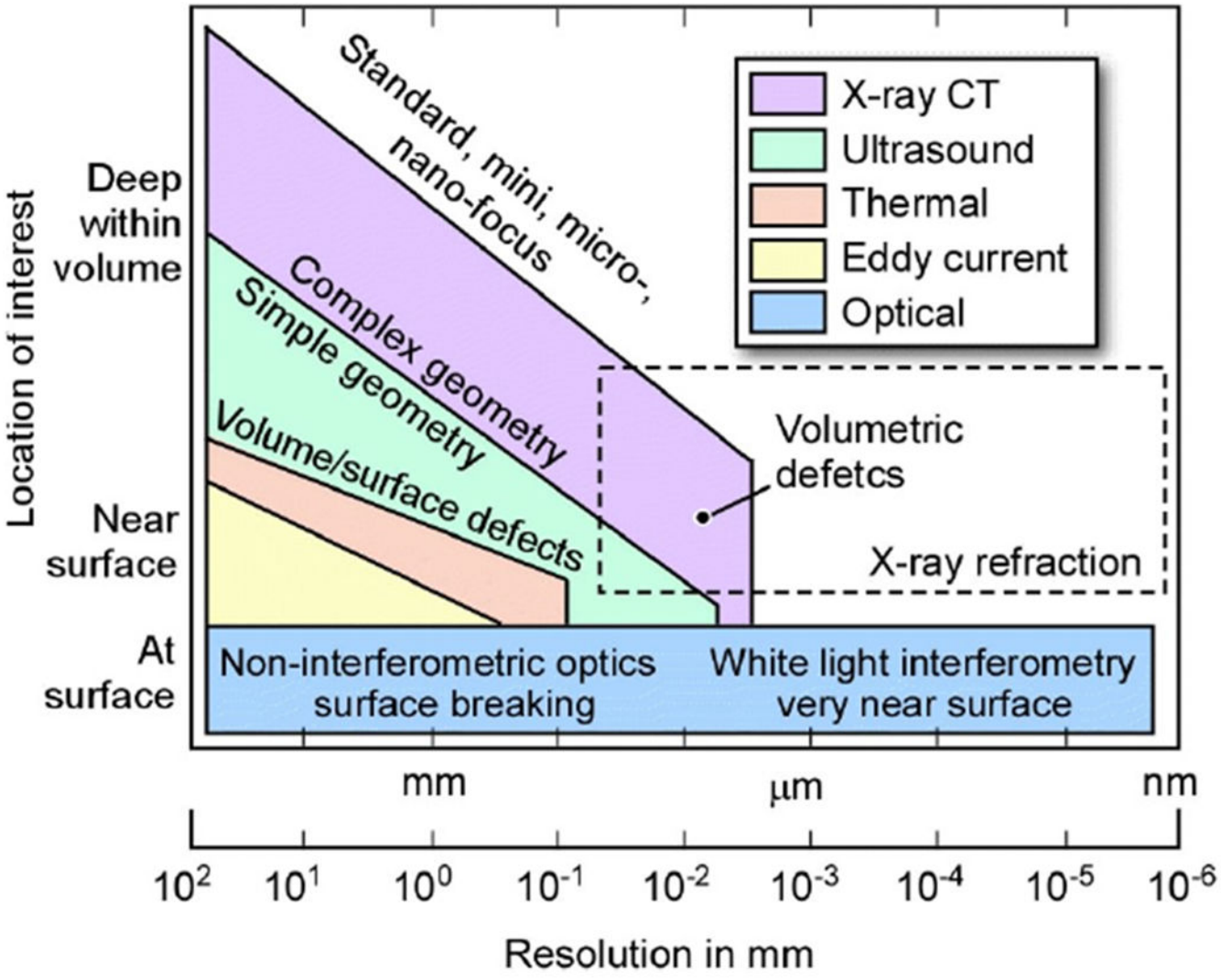

Fig. 42:

Comparison of different NDT techniques with respect to their spatial resolution and the potential location of the defect; according to [29], cf. also [24]; modified.

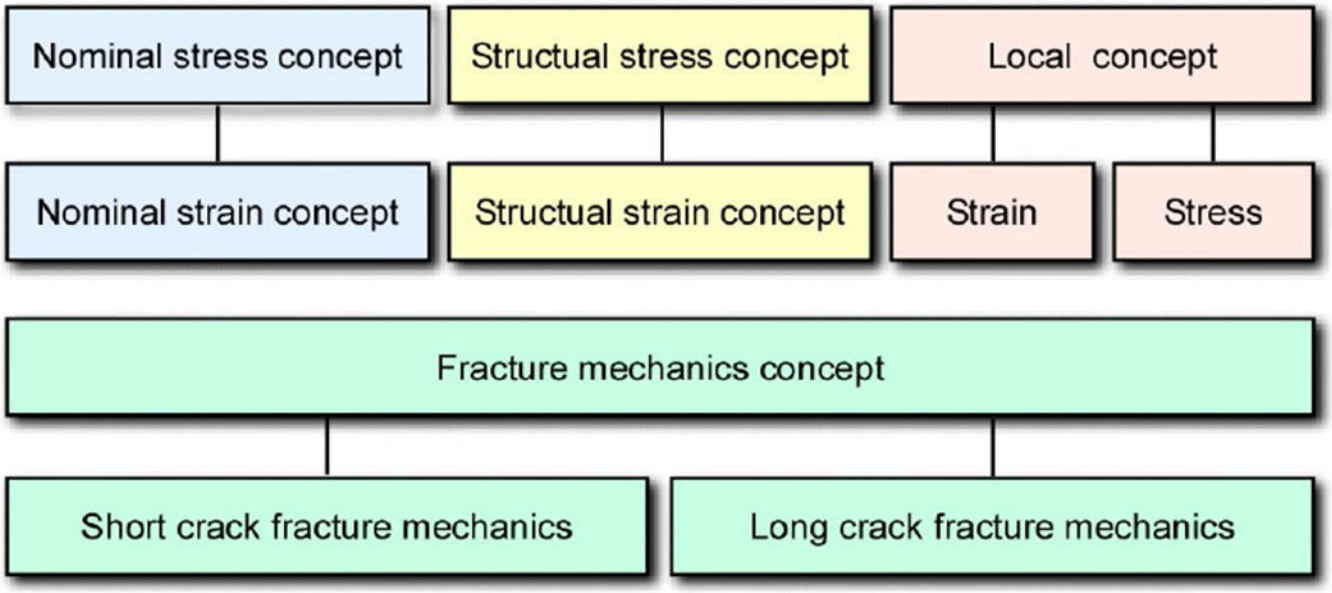

Fig. 43:
Fatigue design concepts; according to [339]; modified.

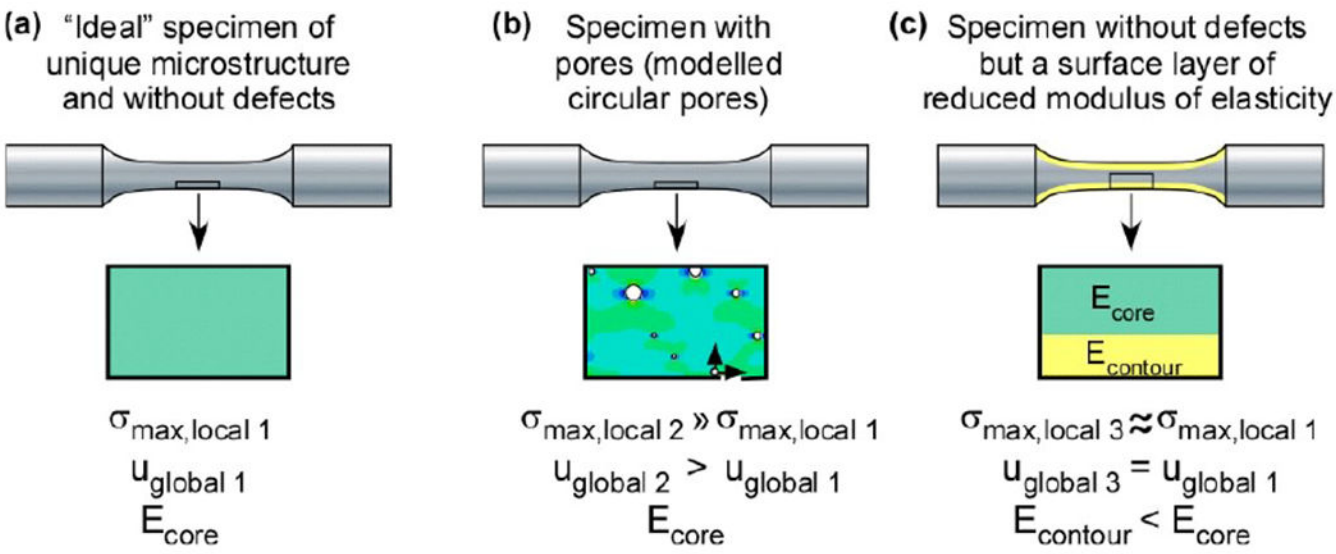

Fig. 44:

Schematic representation of the differences in stresses σ and displacements *u* resulting from different modeling techniques; linear-elastic finite element simulations of AM specimens; (a) "ideal" specimen without defects; (b) specimen with spherical pores near the surface; (c) specimen without imperfections but a surface layer with reduced modulus of elasticity; according to [343].

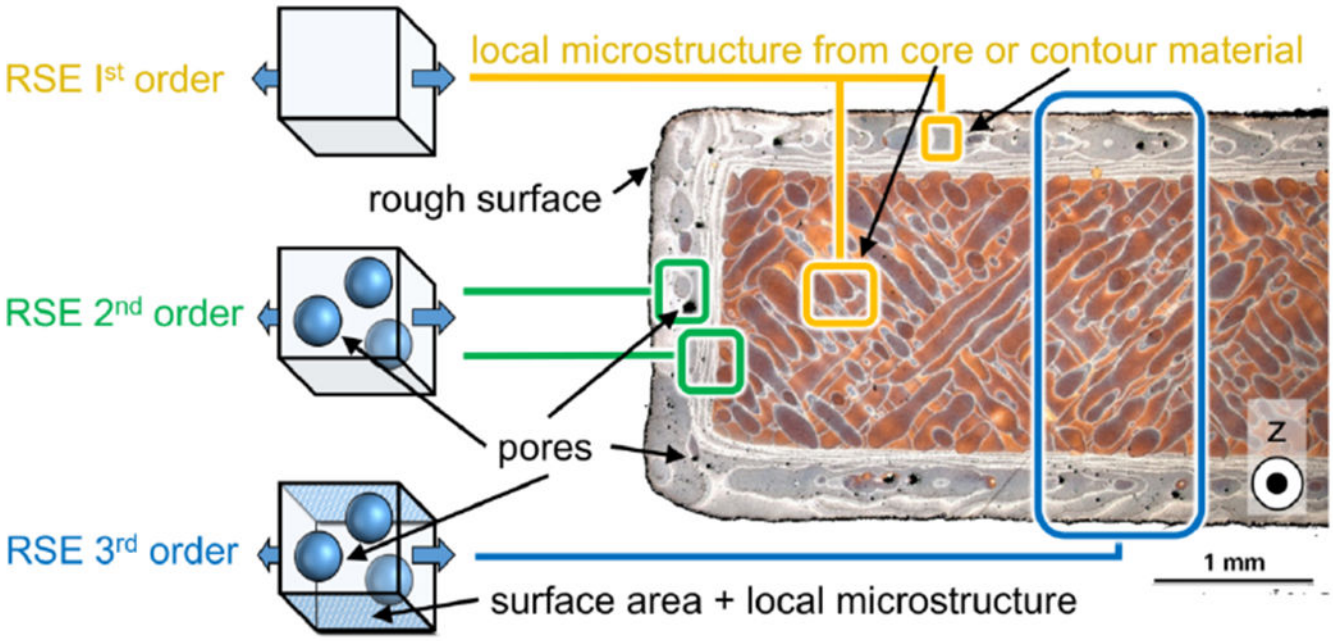

Fig. 45:

Representative Structural Elements including core and contour material; PBF-LB AlSi10Mg; according to [344], see also [345].

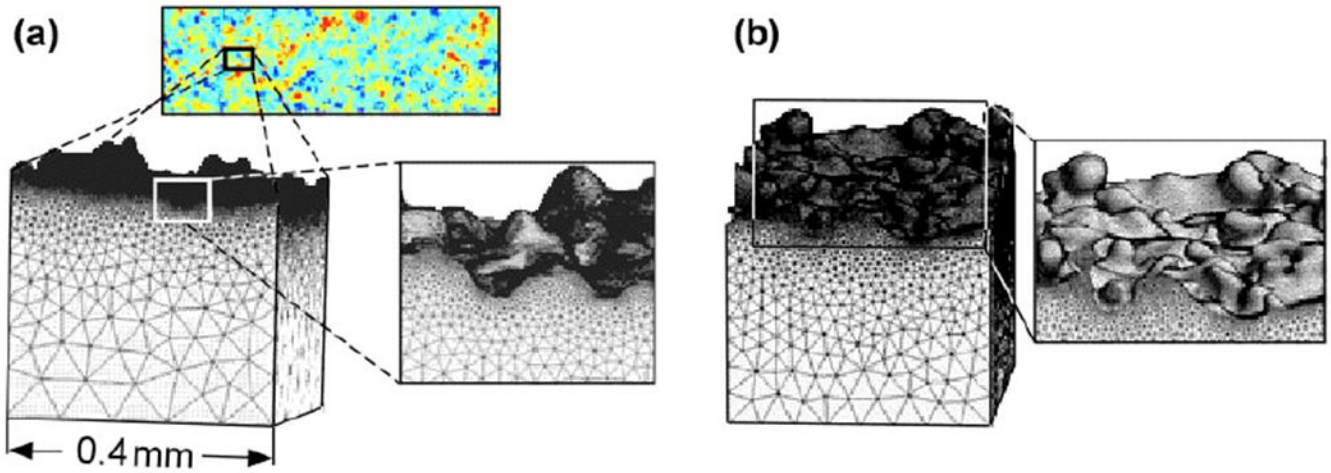

Fig. 46.

(a) FEM-meshed volume generated from a surface scan (profilometry); (b) meshed volume from volume scan (tomography); according to [202].

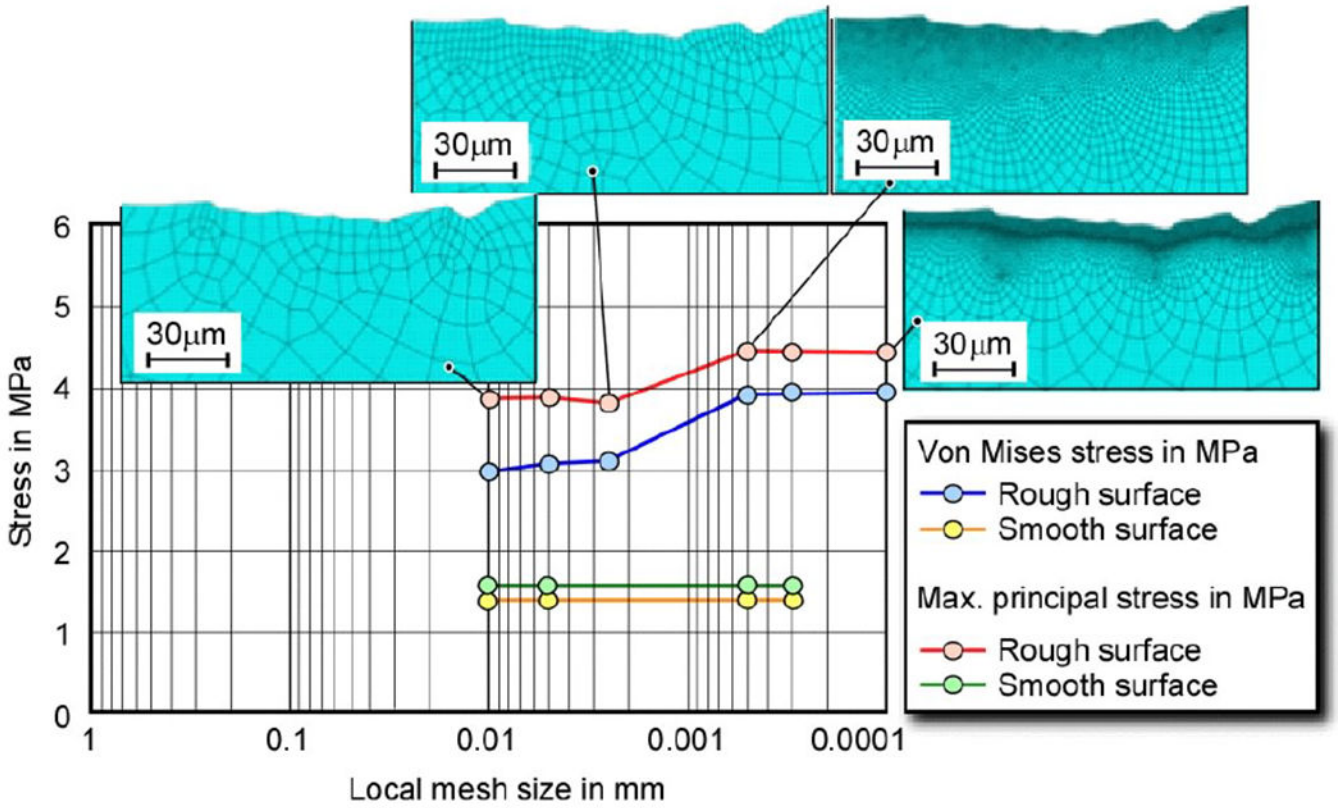

Fig. 47:
Convergence study for finite element modeling of the measured surface roughness; according to [343].

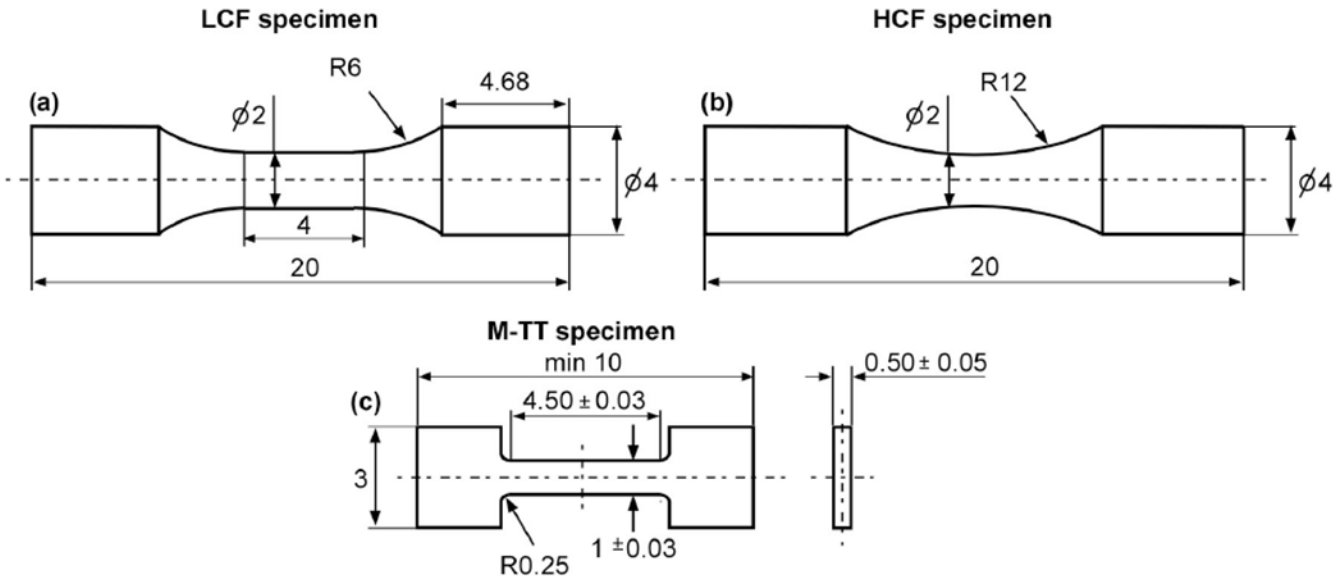

Fig. 48:

Sub-size specimen geometries for small-scale fatigue and tensile testing. (a) low cycle fatigue specimen, (b) high cycle fatigue specimen; (c) M-TT specimen; all dimensions in millimeters.

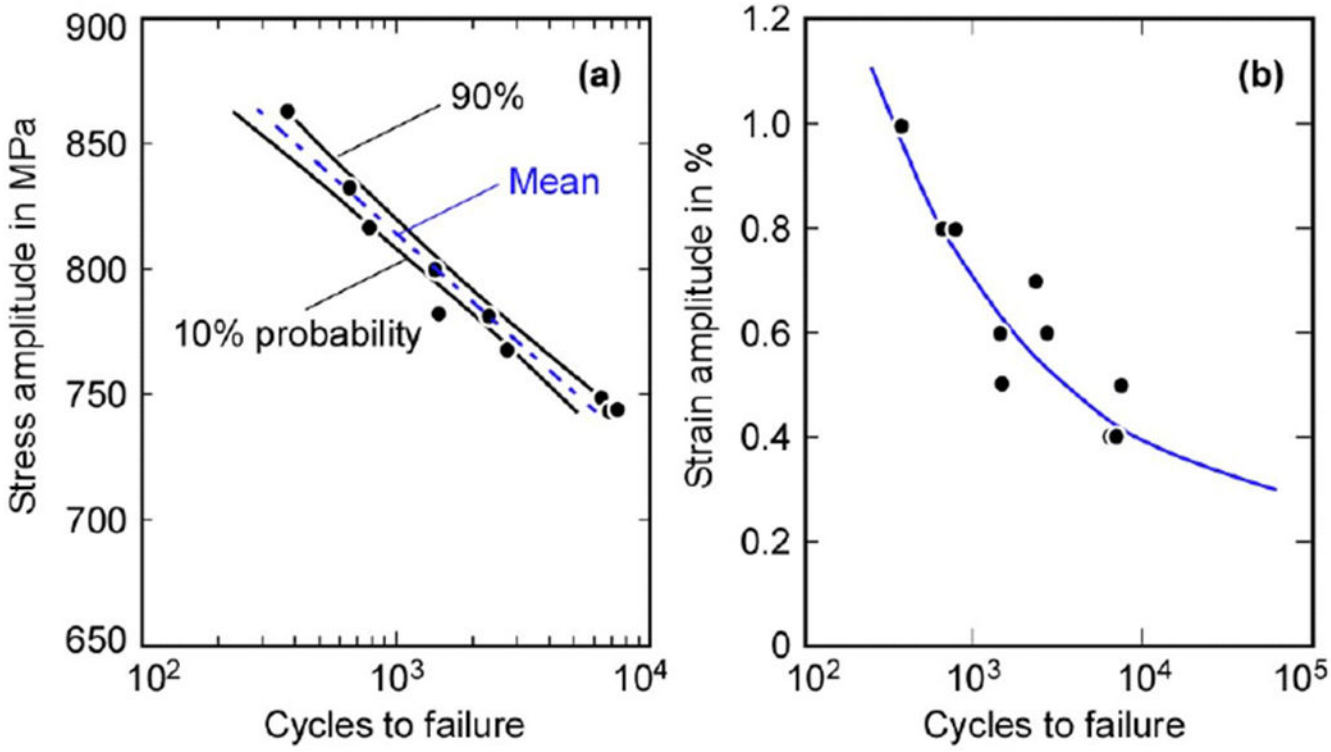

Fig. 49:
(a) S-N and (b) e-N curve obtained by sub-size specimens; material: L-PBF processed Inconel 718; according to COMTES FHT.

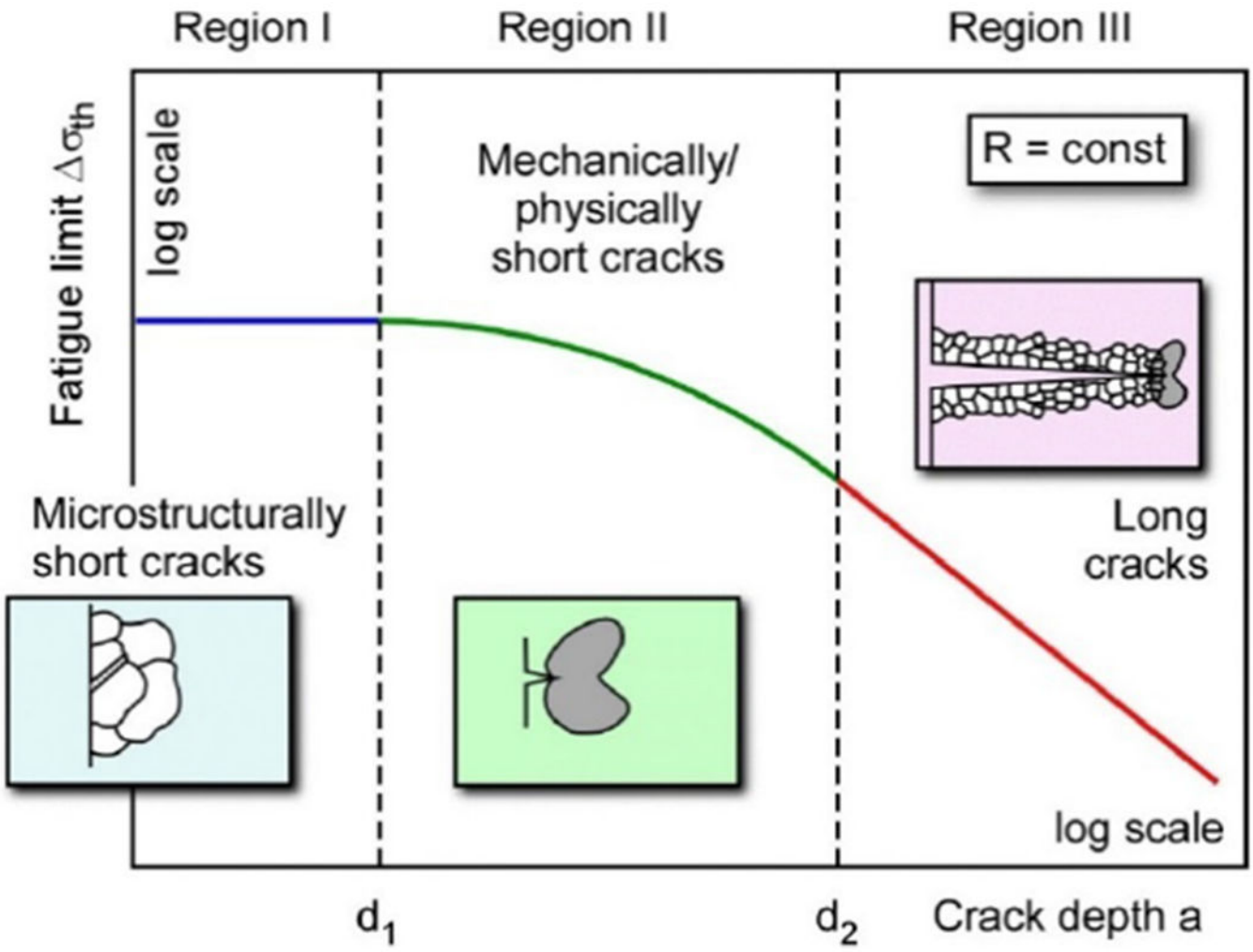

Fig. 50:
Kitagawa-Takahashi (KT) diagram.

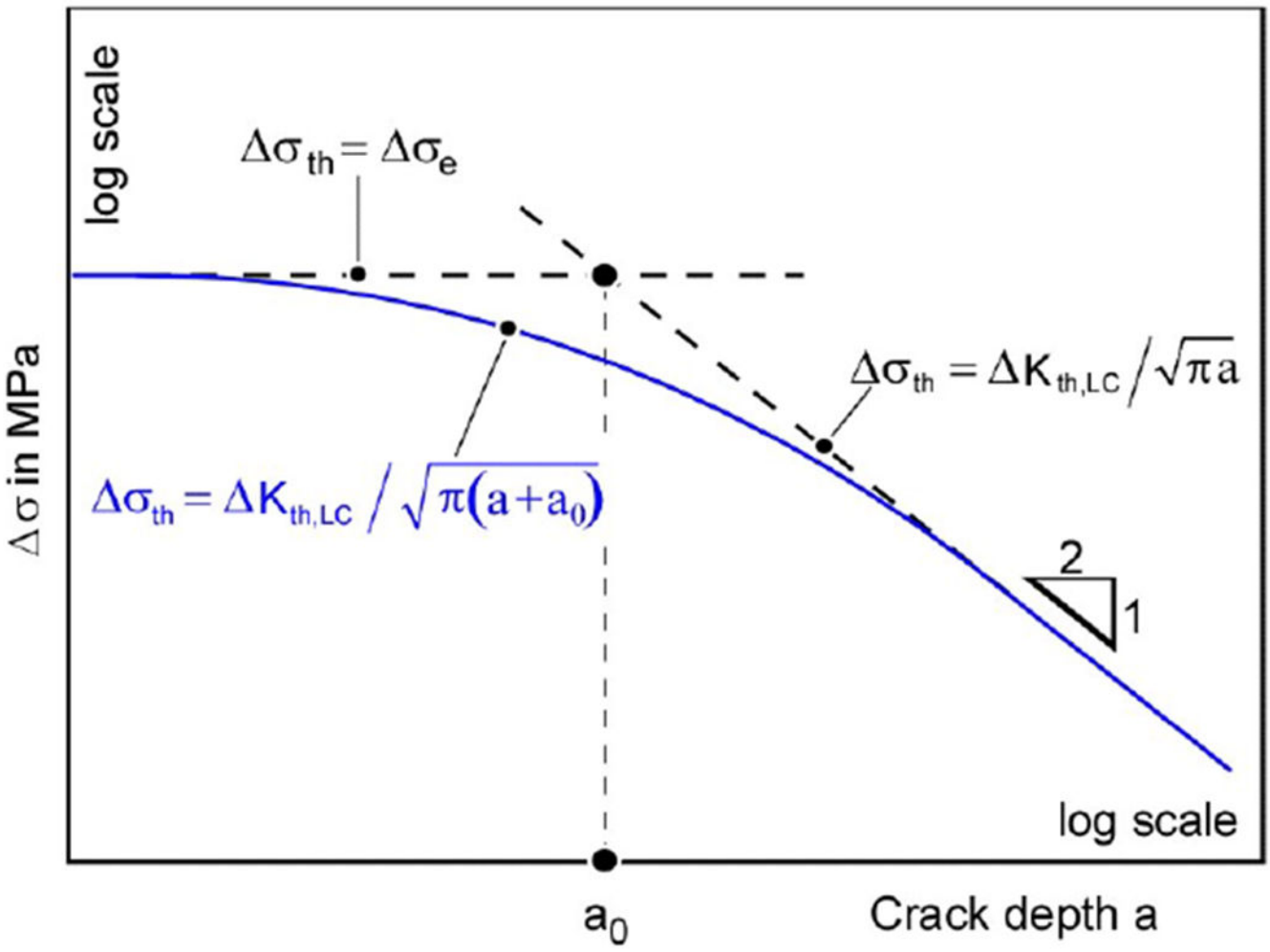

Fig. 51:
Kitagawa-Takahashi (KT) diagram: Description by El Haddad's fictitious crack depth a + a_0; according to [421].

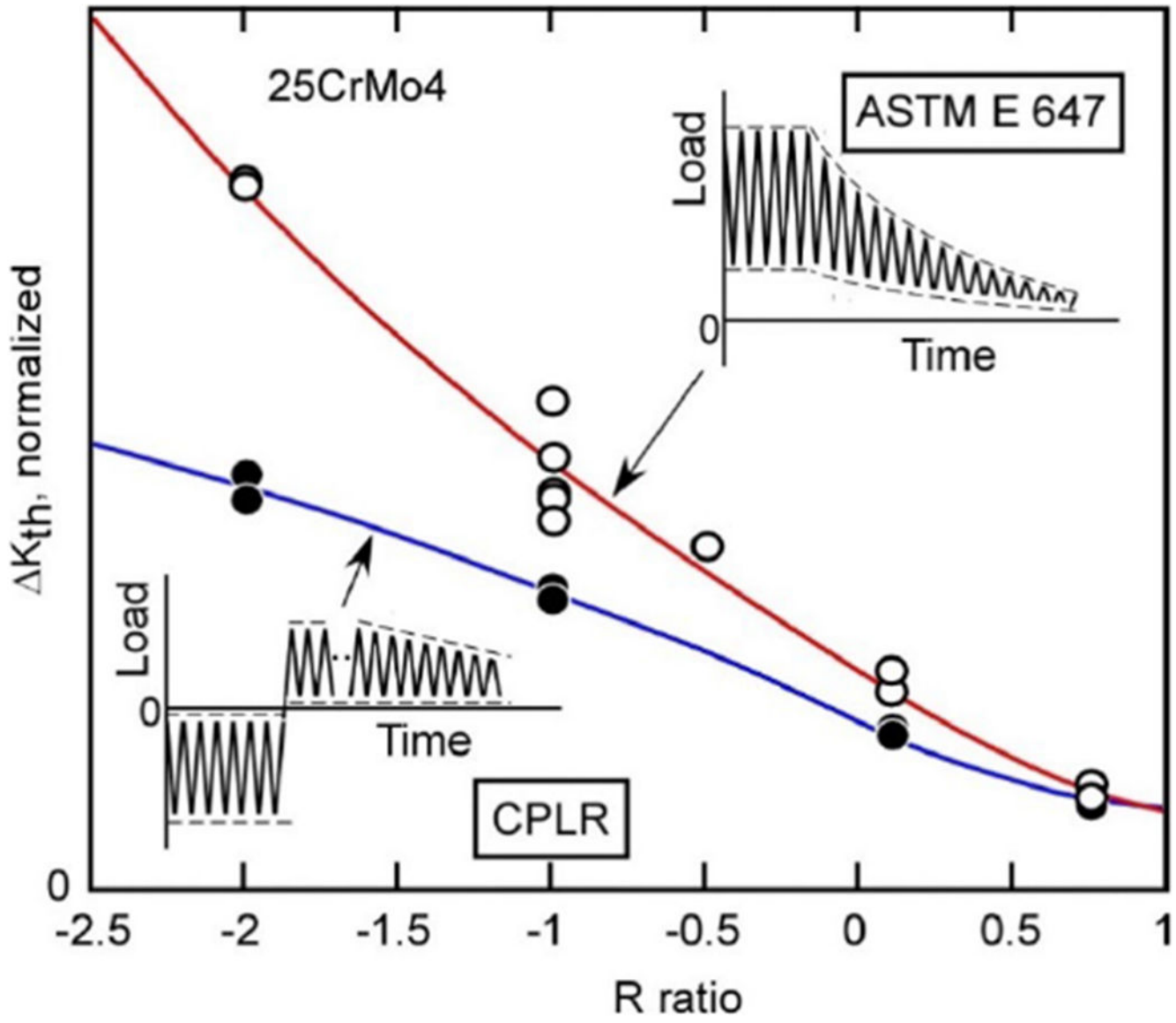

Fig. 52:

Effect of different experimental techniques (load reduction according to ASTM E647 and compression pre-cracking load reduction, CPLR) on the resulting long fatigue crack propagation threshold; material: railway axle steel, according to [384].

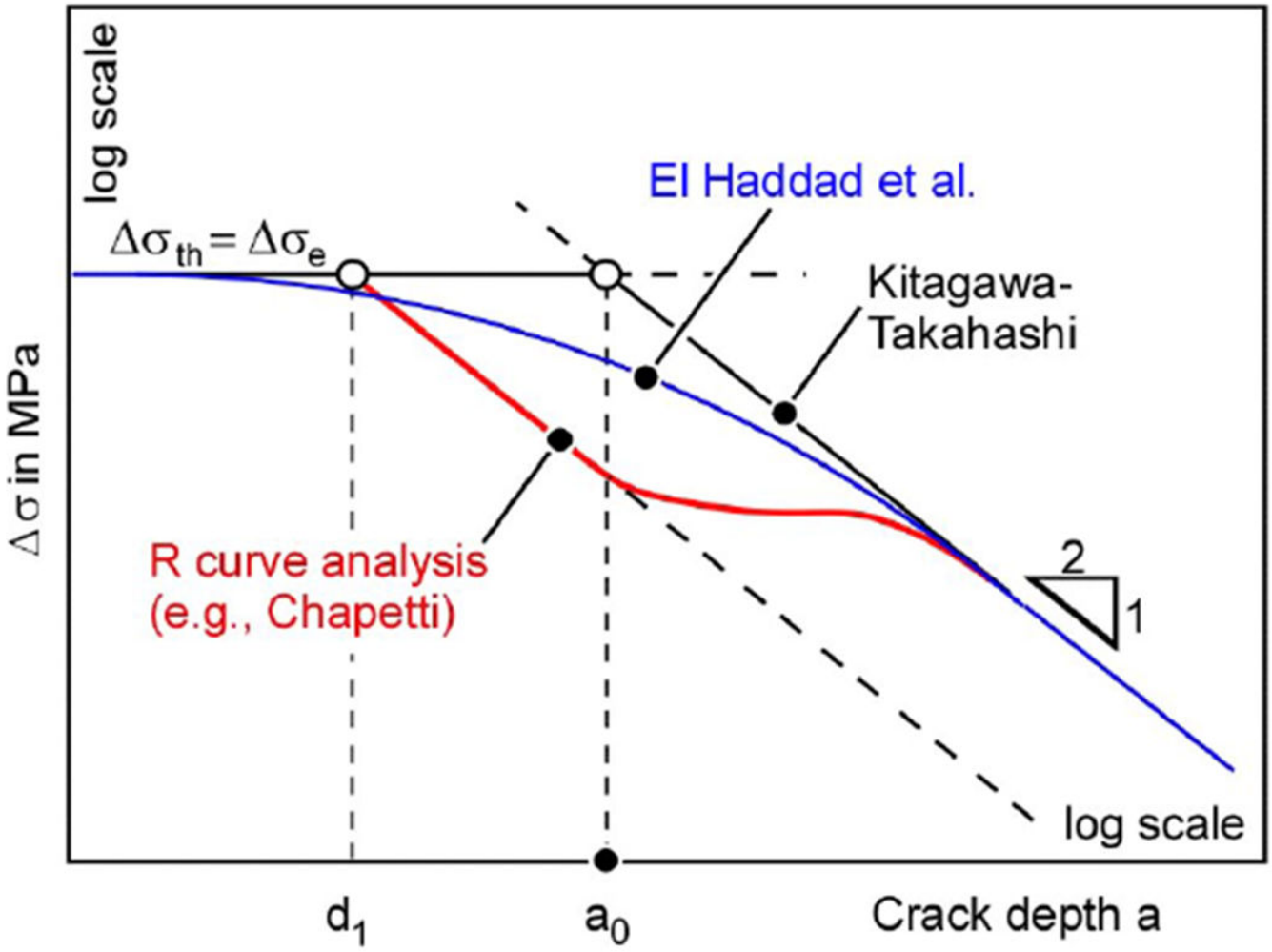

Fig. 53:
Comparison of Kitagawa-Takahashi (KT) diagrams obtained by the basic approach, by El Haddad's fictitious crack depth approach and by cyclic R curve analysis; according to [387].

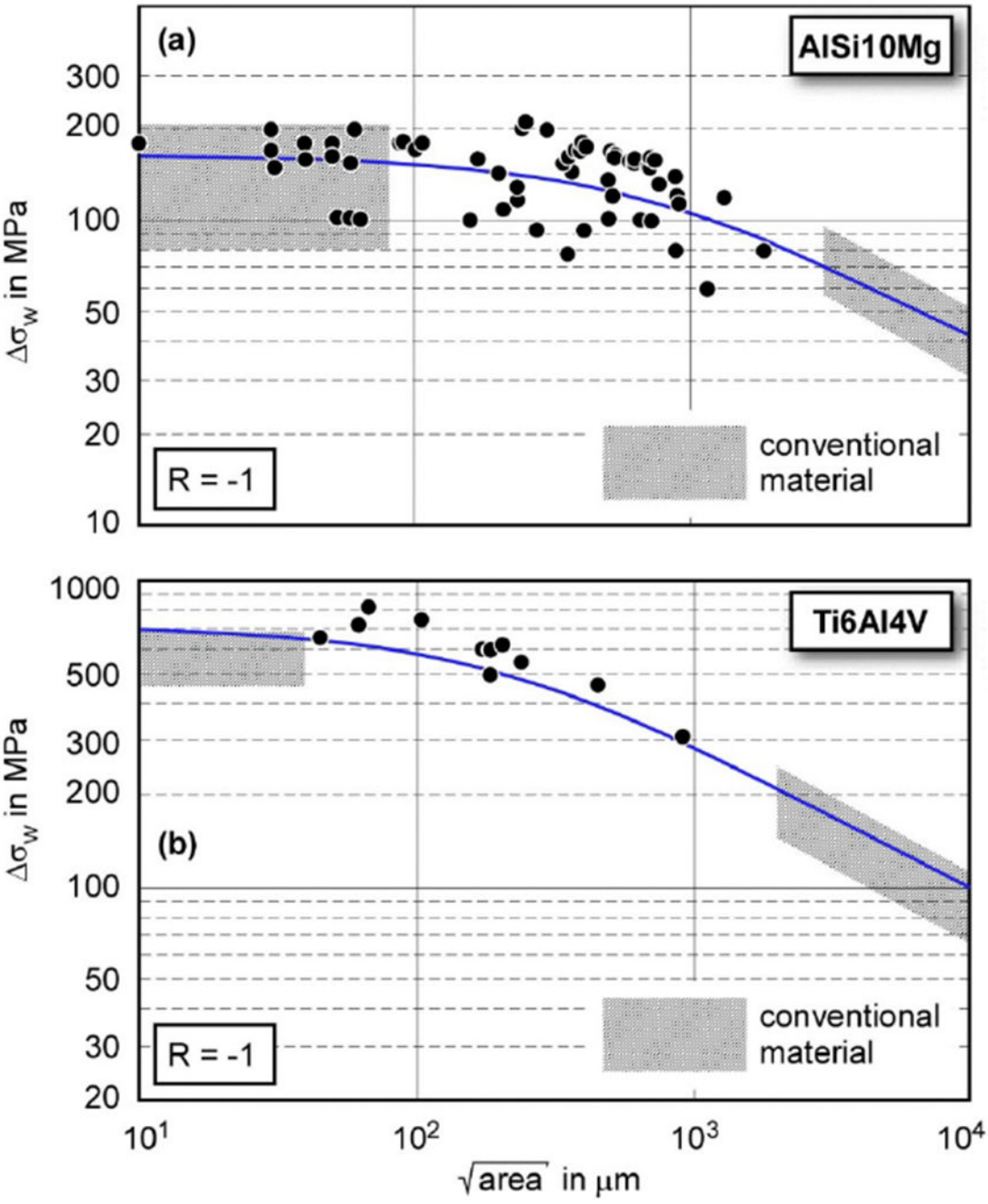

Fig. 54:

KT diagrams obtained from literature data of (a) AM manufactured AlSi10Mg and (b) AM manufactured Ti6Al4V. The points are based on Eqn. (16) with reported data of $\Delta\sigma_e$ and $\Delta K_{th,LC}$ and a_0 was based on Eqn. (13); according to [390].

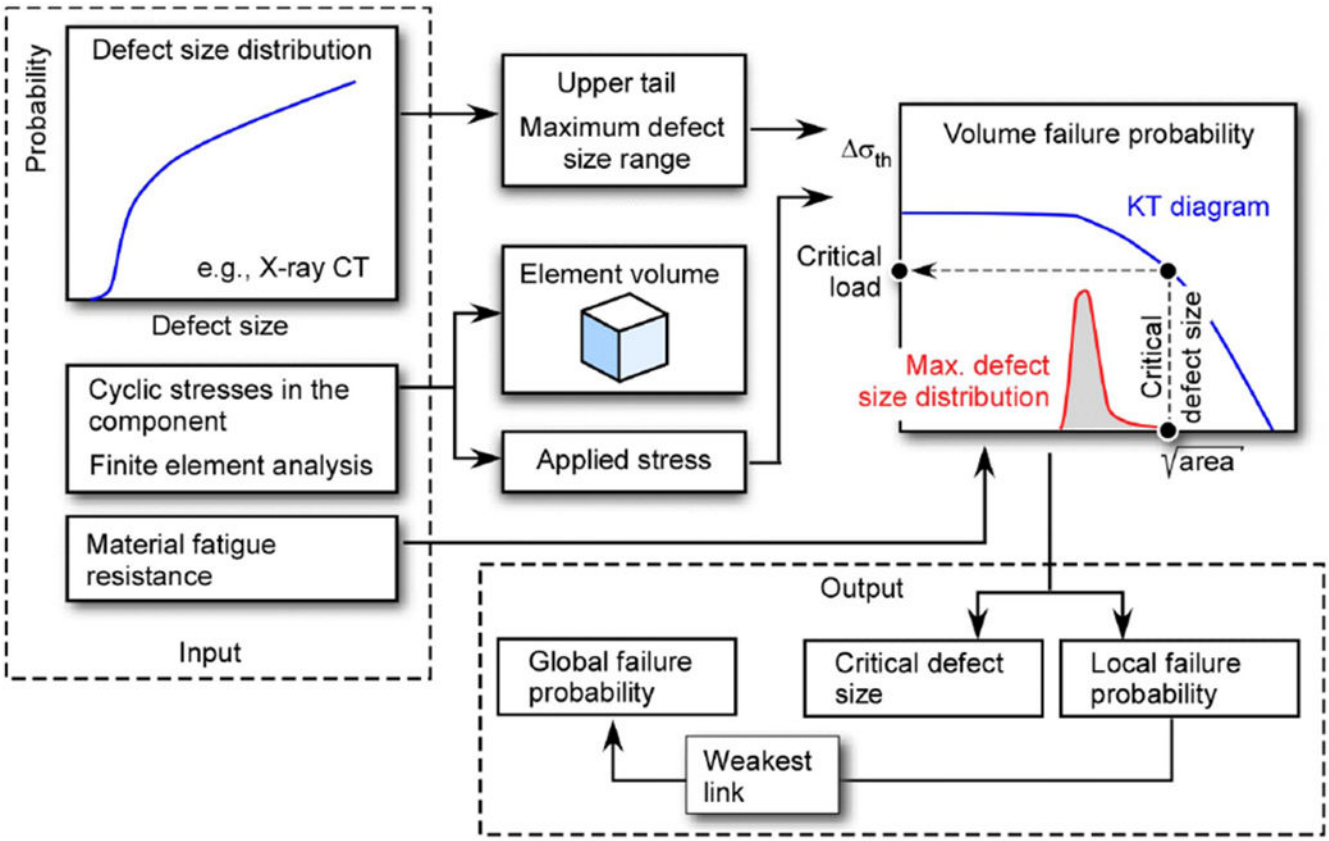

Fig. 55:
Assessment of AM structures; approach of Beretta and Romano, figure according to [161], simplified reproduction.

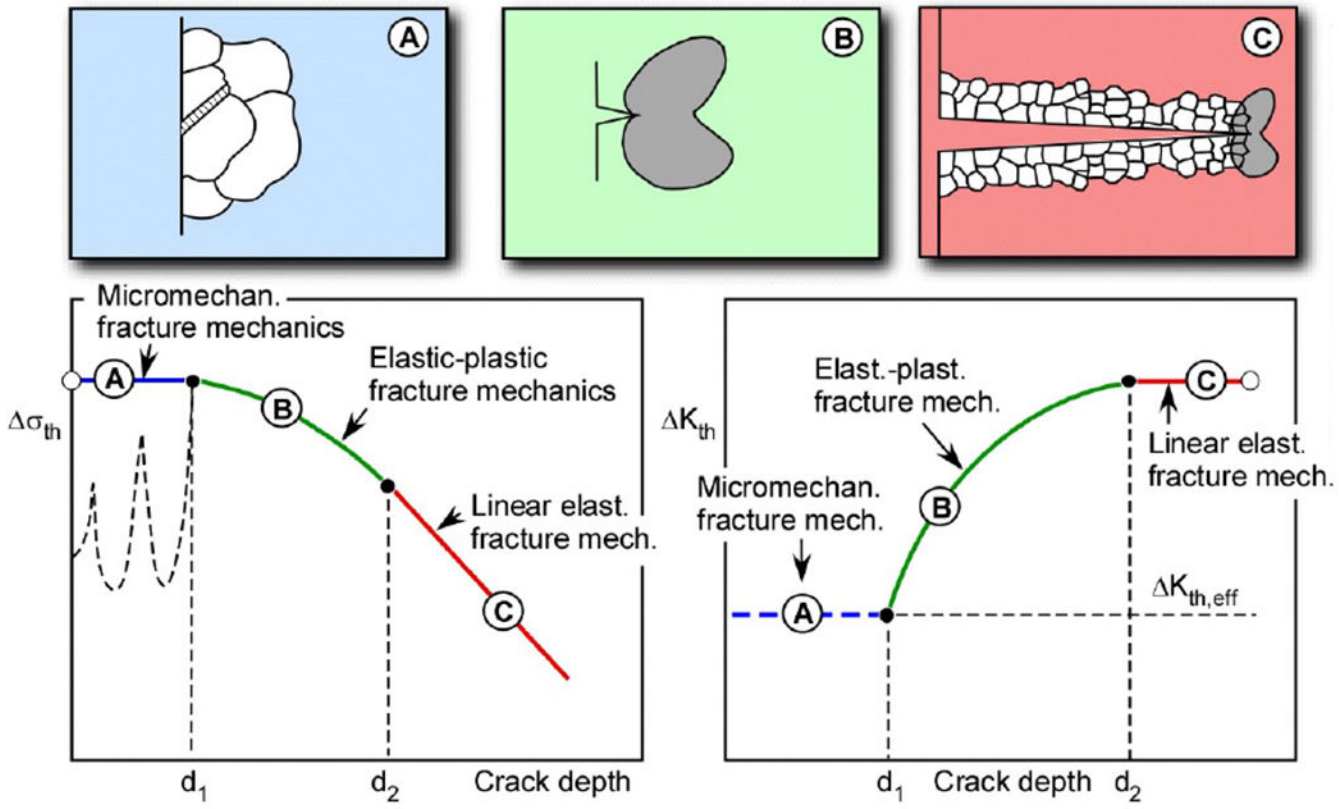

Fig. 56:
Comparison between the KT diagram and the cyclic R curve.

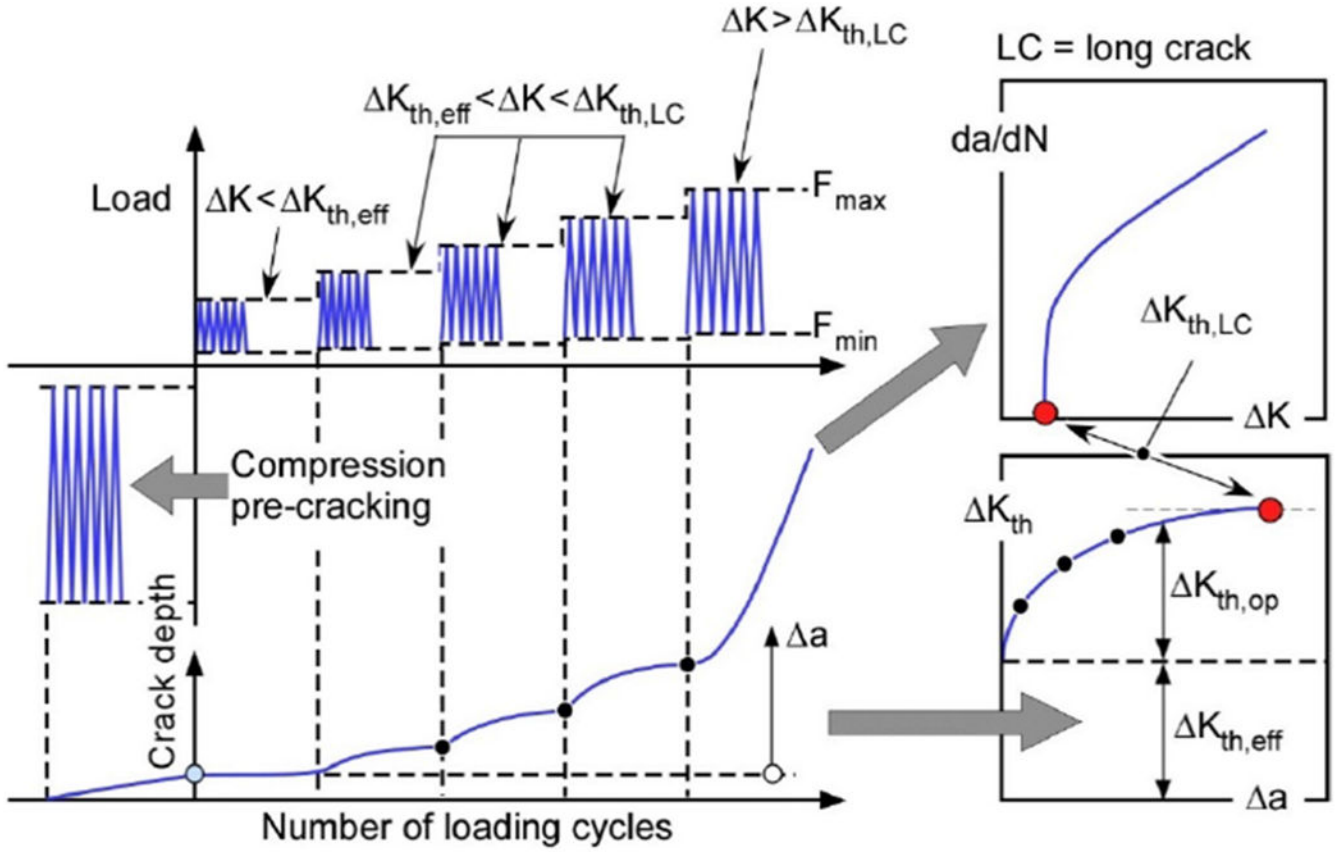

Fig. 57:
Loading scheme of cyclic R-curve determination according to [265].

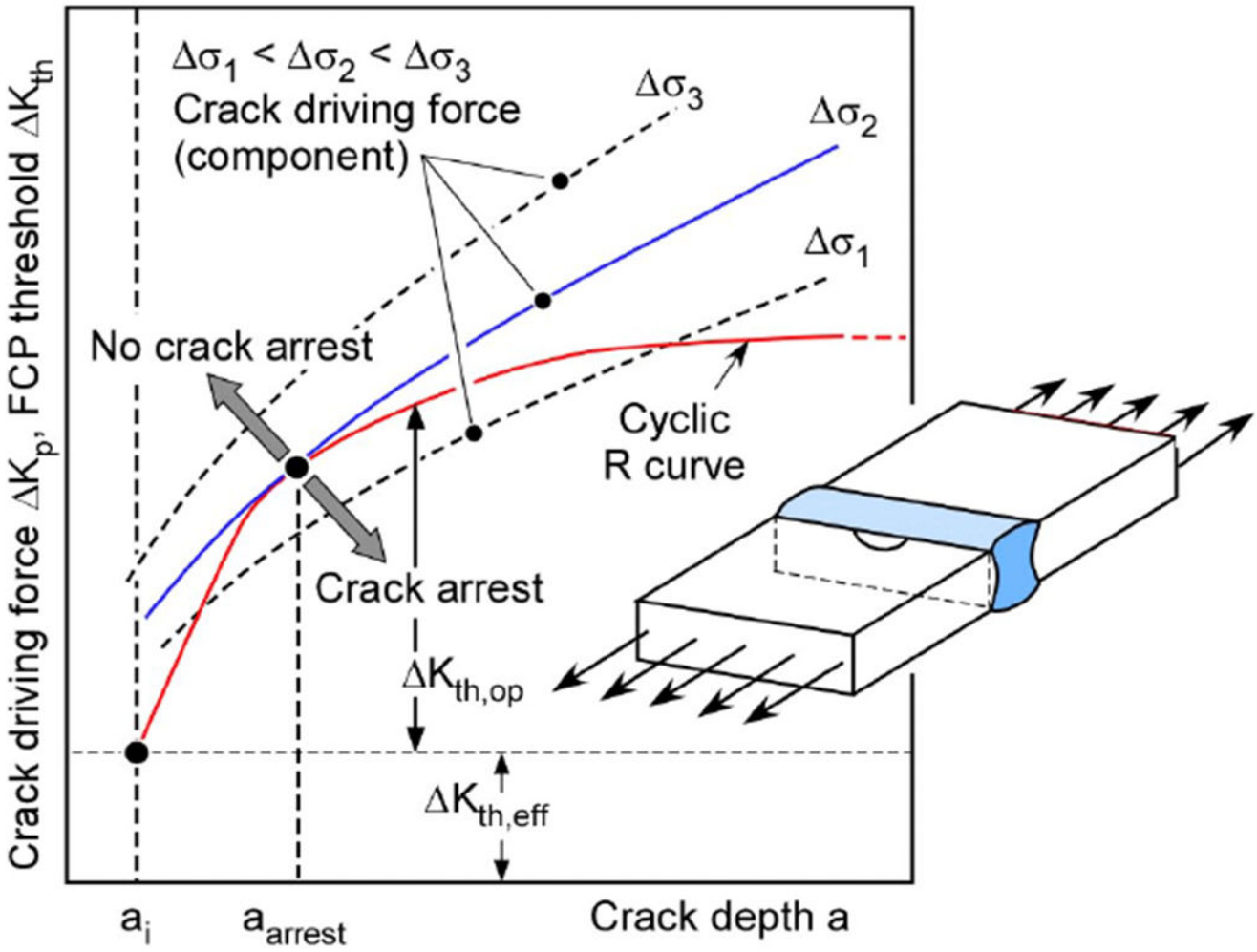

Fig. 58:
Schematic view of a cyclic R-curve analysis.

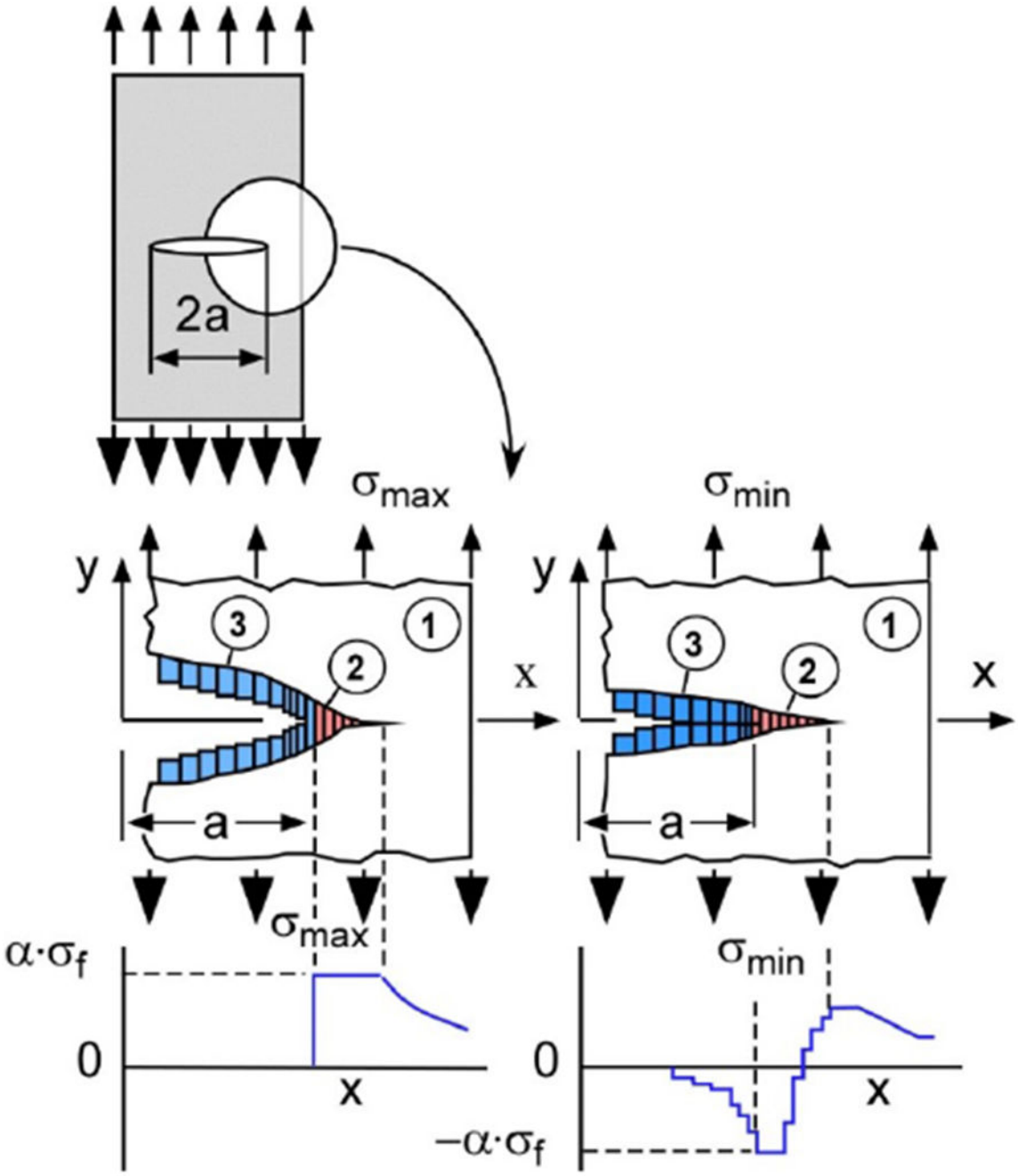

Fig. 59:
Modified strip yield model according to [407].

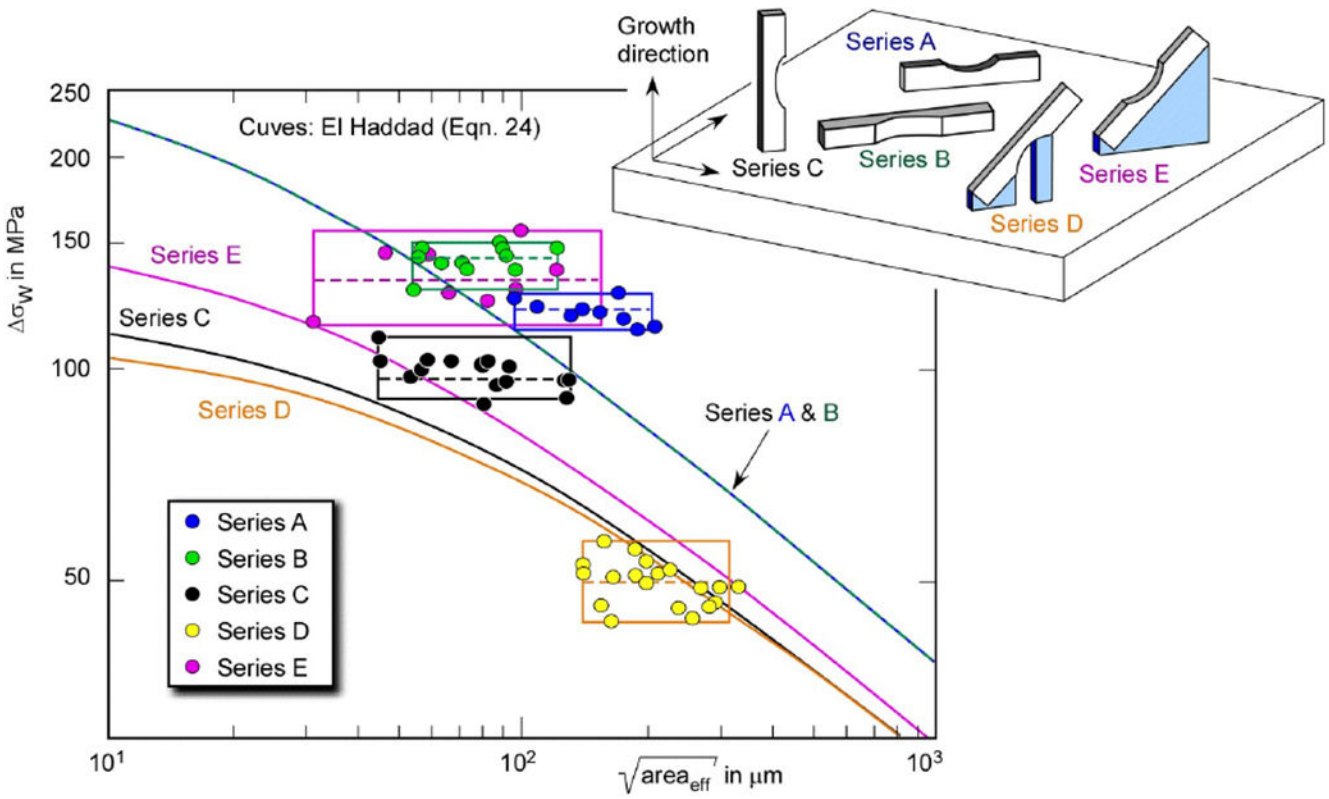

Fig. 60:

Analysis of the fatigue strength for as-built specimens made of L-PBF AlSi10Mg printed in different orientations and tested at R = 0.1 (series C: residual stresses: 140 MPa, series D residual stresses: 72 MPa). The residual stresses were measured at the surface. For series C, a simplified limit condition for elastic shakedown was considered; according to [154].

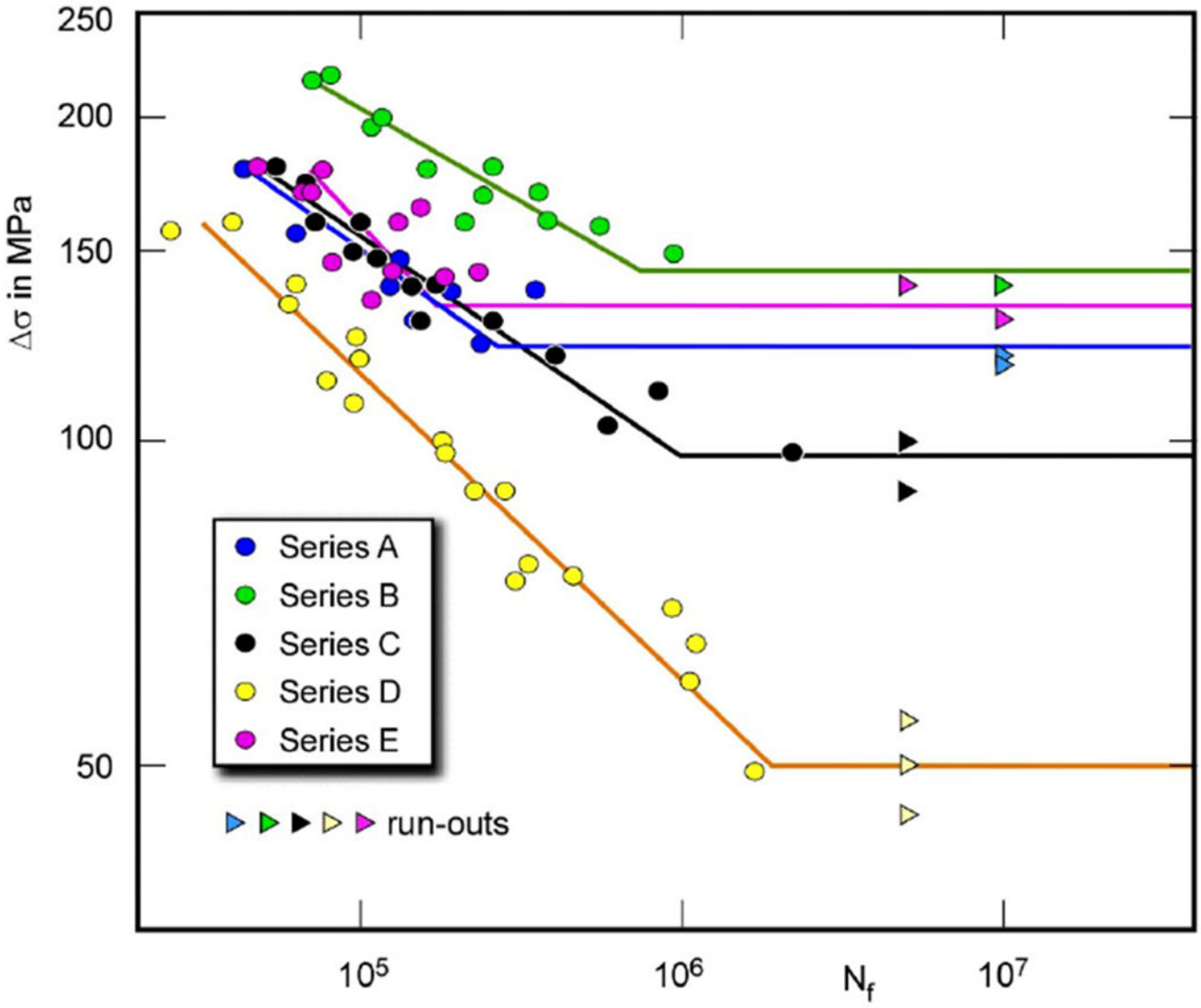

Fig. 61:
Fatigue properties of as-built L-PBF AlSi10Mg specimens tested at R=0.1; S-N diagrams for the different series of Fig. 60; according to [154].